2013

Blast furnace hearth refractory and coke ash mineral interactions

Phillp Drain
University of Wollongong

Blast Furnace Hearth Refractory
And
Coke Ash Mineral Interactions

By

Phillip Brian Drain $B_{(MATERIALS)}E$

A thesis submitted in fulfilment of the
requirements for the award of the degree of

MASTERS OF ENGINEERING
(Materials)

from

UNIVERSITY OF WOLLONGONG
FACULTY OF ENGINEERING

September 2013

Certification

I, Phillip B. Drain, declare that this thesis, submitted in fulfilment of the requirements for the award of Masters of Engineering, in the Department of Engineering, University of Wollongong, is whole my own work unless otherwise referenced or acknowledged. This document has not been submitted for qualifications at any other academic institution.

Phillip Brian Drain

September 2013

Acknowledgments

I would like to acknowledge the support and guidance I have received from my academic supervisor Associate Professor Brian Monaghan throughout this project. For this I am very grateful.

I would like to acknowledge the support and assistance of Dr Robert Nightingale and Dr Michael Chapman. I would like to thank Jim Cummins, Greg Brown and John Spink of BlueScope Steel refractory services for the use of their laboratory and technical advice. I would also like to thank Greg Tillman, Dr Ray Longbottom and Hazem Labib of the University of Wollongong for technical support in terms of sample preparation and analysis.

Finally, I would like to thank my family and friends for all their support and encouragement that helped me get this thesis across the finish line.

Abstract

The by-products of coke dissolution in iron are primarily calcium aluminate minerals known as coke ash. These minerals are unreactive with the iron bath and can therefore deposit onto the blast furnace hearth refractories when they form below the iron-slag interface. This study was focused on understanding the interactions between these coke ash minerals and blast furnace hearth refractories. Improved understanding of these interactions may have implications for the campaign life of the blast furnace hearth refractory materials.

It was found that the aluminosilicate refractory followed the linear rate law and the alumina carbon refractory corresponded to the logarithmic rate law. Thermodynamic modelling was conducted and compared with the spot analysis results and micrographs to determine the phases likely to have formed. It was found that the formation of gehlenite ($Ca_2Al_2SiO_7$) and anorthite ($CaAl_2Si_2O_8$) were more likely in the reactions with the aluminosilicate refractory due to the higher silicon content in the refractory. This corresponds with the observation of this refractory following the linear rate law which is typical of a material which forms a non-protective reaction layer with high porosity or forms liquid phase reaction products. The rates of reaction were found to follow an Arrhenius relationship, demonstrating temperature dependence for the reactions between both hearth refractories and the calcium aluminates. The reaction rate was also observed to increase with the calcium content as predicted by Fick's 1^{st} law of Diffusion. The Kirkendall effect was demonstrated via an inert wire test indicating net mass transport of material into the refractory materials from the calcium aluminates. This suggests that the active species responsible for most the reactions observed was the calcium ion.

Detailed analysis using thermodynamic data was carried out to determine the possible reactions between the calcium aluminates and the refractory minerals. The formation of low liquidus temperature phases (anorthite and gehlenite) and the possible formation of liquid oxide phase were determined to increase the rate of refractory wear and limit the ability of the refractories to form a protective reaction layer. The formation of grossite ($CaAl_4O_7$) and hibonite ($CaAl_2O_{19}$) was found to make the refractory more susceptible to structural and thermal spalling due to the increased stress in the reaction layer cause by the volume change and variation in thermal expansion coefficients of the reaction products.

Contents

List of Tables

List of Figures

Definitions and Notation

mass%	mass percent
Coke Ash	The mineral product remaining after coke dissolution in liquid iron.
[X]	Element X is dissolved in liquid iron
SEM	Scanning Electron Microscope
Liquid Holdup	The amount of liquid slag and iron contained in the deadman coke bed
Hearth Pad	Refractories making up the bottom of the blast furnace hearth
R_q	The root mean square roughness parameter
R_a	Roughness parameter
Lime	CaO
Silica	SiO_2
Alumina	Al_2O_3
CA	$CaO.Al_2O_3$
CA2	$CaO.2Al_2O_3$
CA6	$CaO.6Al_2O_3$
Gehlenite	$Ca_2Al_2SiO_7$ also a member of the melilite group of minerals
Anorthite	$CaAl_2Si_2O_8$ also a member of the plagioclase group of minerals
Corundum	$\sim Al_2O_3$
Hibonite	$CaAl_2O_{19}$
Grossite	$CaAl_4O_7$
Mullite	$Al_6Si_2O_{13}$ commonly shown in the form $3Al_2O_3.2SiO_2$
k_0	Reaction Rate constant

1. Introduction

The blast furnace ironmaking process is currently the principal method of primary iron production and has been in use in its current form for over 100 years. The internal conditions of a blast furnace are difficult to view and measure directly, resulting in significant uncertainty in the understanding of the chemical interactions and structure within the blast furnace. This study is focused on understanding the chemical interactions between the dissolution products of coke and hearth refractories.

1.1. Problem Definition

Blast furnaces are constructed with a water-cooled shell lined with refractory to ensure operational security. The refractory materials used are capable of withstanding the high temperatures and corrosive environment produced within the ironmaking blast furnace. The typical configuration of a blast furnace hearth is composed primarily of micropore carbon refractory protected by layers of aluminosilicate and alumina–carbon refractories as shown in Figure 1.1. These refractory materials may react with the calcium aluminate reaction products known to form on dissolution of coke.

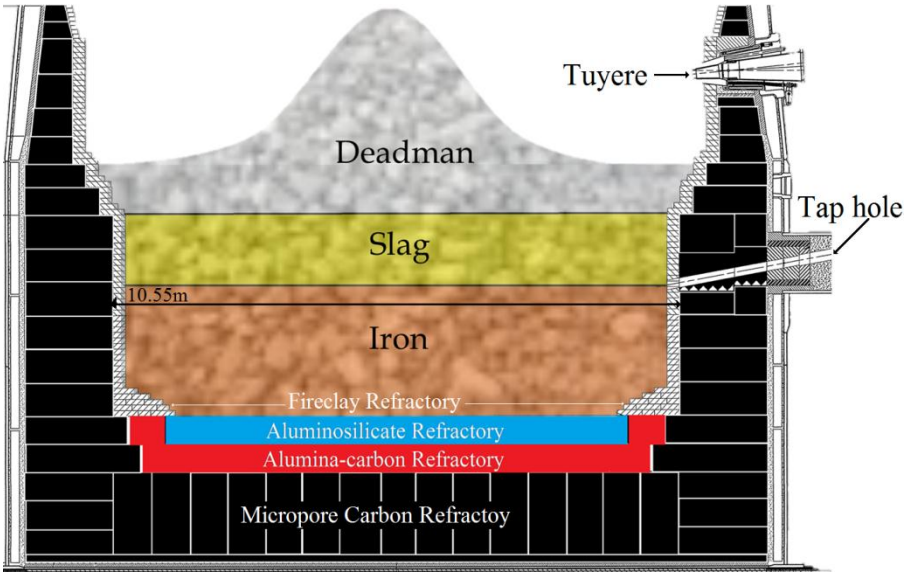

Figure 1.1: No.5 BF Port Kembla Hearth Refractory Design, adapted from [1]. Slag and iron levels within packed bed of coke are shown. Internal diameter of 10.55m at the taphole

The coke is consumed in the blast furnace producing the heat and reducing gas essential for the reduction of iron ore to metallic iron (Fe). It remains solid in the lower zones of the blast furnace providing support for the burden above and maintains the furnace permeability essential for high productivity. This allows liquids to drain to the hearth and ensures that reducing gas can move through the cohesive zone and into the upper shaft as shown in Figure 2.1 [2].

Coke is composed of carbon and up to 15 mass% oxides [3]. Carbon dissolution from the coke into liquid iron can leave an oxide layer at the coke-iron interface. This can occur anywhere coke is contact with liquid iron below the cohesive zone, including the hearth below the iron-slag interface where coke-iron contact is constant. Given that this oxide material in feed coke is approximately 50 mass% SiO_2, this layer was expected to be siliceous. However recent studies by Chapman et al [3, 4, 5, 6] have found that coke ash is comprised largely of calcium aluminates.

In the hearth, below the iron-slag interface, this material is unable to dissolve in the slag or iron and is therefore able to settle on the hearth refractories. In this situation it may be expected that the calcium aluminate coke dissolution products could react with the aluminosilicate and alumina-carbon hearth refractories. These reactions may promote hearth wear and reduce the blast furnace campaign life. Understanding the kinetics of the calcium aluminate - refractory reactions is important for prolonging the campaign life of blast furnace hearth refractories. Characterising and understanding these reactions is the subject of this study.

1.2. Aim

To characterise and evaluate the reactions between refractory and coke ash minerals (calcium aluminates) at temperatures representative of the blast furnace hearth.

1.3. Objectives

- Conduct refractory and calcium aluminate reaction couple tests over a range of different times at temperatures representative of hearth conditions.
- Quantify the size of any reaction layer that forms at the reaction couple interface for the various times and temperatures tested.

1.4. Methodology

Representative samples of the blast furnace hearth refractories (aluminosilicate and alumina-carbon) and synthetic calcium aluminates ($CaO.Al_2O_3$, $CaO.2Al_2O_3$ and $CaO.6Al_2O_3$) of various coke ash compositions will be used for this study. The use of synthesised calcium aluminates eliminates the variability typical of industrial coke ash compositions and the distribution of phases allowing for much better control of the compositions at the reaction interface improving the experimental reliability.

Preparation of the materials will require the reaction interface surface of each material to be polished and the surface roughness measured using the atomic force microscopy. This will ensure the reliability of experimental results by providing a consistent surface contact in each test to be conducted and characterise the surface baseline conditions. The reaction couples will be heated to a temperature (~1500˚C) representative of conditions experienced at the refractory/ coke ash interface in a blast furnaces.

Scanning electron microscopy and energy dispersive spectroscopy will be used to characterise the reaction couples and any product layer formed during the experiment. Measurements of the reaction layer thickness over a range of reaction times for different calcium aluminates and refractories will be analysed to evaluate the reaction kinetics of the refractory - calcium aluminate couples.

2. Literature Review

Due to the broad nature of literature concerning the ironmaking blast furnace, metallurgical coke and refractories, this review is focused on literature concerning a) coke dissolution products below the iron- slag interface in the hearth; b) blast furnace hearth refractories, and c) the associated thermodynamic and kinetic data required for meaningful analysis. A review of relevant mineral systems and diffusion data has also been provided to aid discussion of reactions in these systems.

2.1. The Ironmaking Blast Furnace

The ironmaking blast furnace is a counter current shaft furnace for smelting iron ores to produce liquid iron. Coke and pulverised coal are combusted in the raceway with preheated air injected through the tuyeres to produce heat and reducing gases which drive the smelting process (see Figure 2.1). The raw materials are charged into the top of the furnace via a rotating chute that controls the distribution of materials. The liquid iron and slag collect in the hearth at the bottom of the furnace and are tapped from the furnace at regular intervals. Blast furnace iron production is a continuous process and only fully stops when the burden material is quenched or rundown for refractory relining.

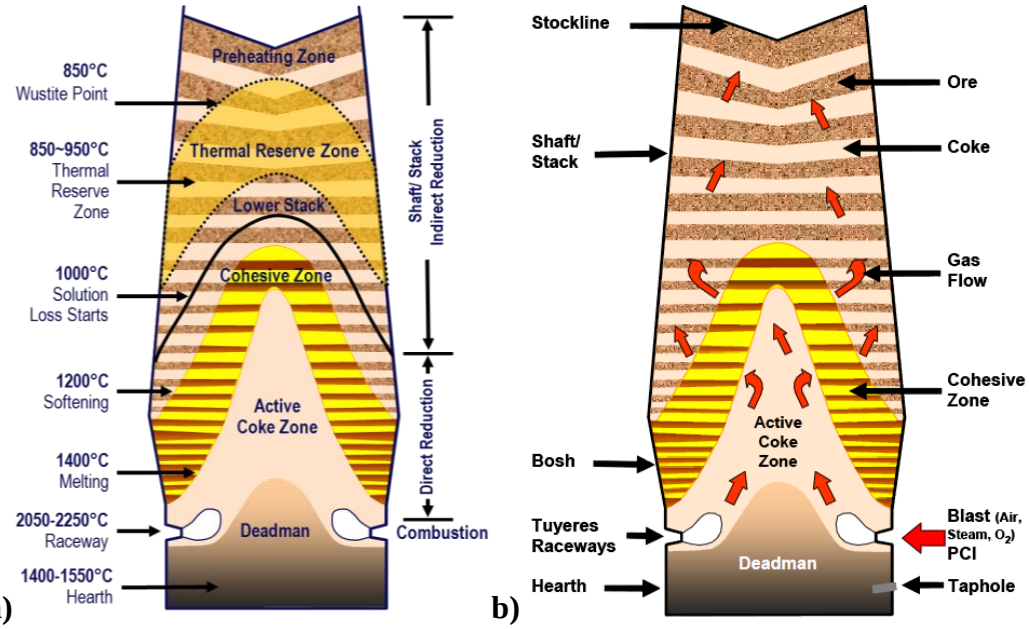

Figure 2.1: Blast furnace a) key reaction zones and b) gas flow, adapted from [7]

The principle blast furnace reaction zones of interest in this study, shown in Figure 2.1, are:

- Deadman (1200°C-1550°C): is a packed coke bed characterised by a slow coke decent rate due to dissolution in iron. This region has limited liquid and gas permeability [2].
- Hearth (1400°C -1550°C): molten metal and slag drain to the hearth through the coke bed where they form immiscible layers before being tapped [2].

2.1.1. Raw Materials

The ironmaking process utilises many ores and beneficiated raw materials. These include:

- *Iron Ores*: primarily haematite (Fe_2O_3) and some magnetite (Fe_3O_4) in both pellet and lump form. These materials and sinter are the primary source of metallic iron.
- *Sinter*: an agglomeration of iron ores, fluxes and coke fines. Sinter contains all these materials bound together and is highly porous so as to improve the kinetics of the reduction reactions.
- *Fluxes*: Limestone (mostly $CaCO_3$) and quartz (SiO_2). Fluxes are used to aid the removal of oxides and impurities from the blast furnace charge and liquid iron.
- *Metallurgical Coke*: is coal that has undergone densification and de-volatilisation. It is composed predominantly of carbon with 10-15 mass% mineral matter. Coke is the primary source of reductant and fuel for combustion at the raceway.
- *Pulverised Coal*: is crushed coal injected via the tuyeres as a fuel source and reductant.

2.1.2. Permeability in a Blast Furnace

The raw materials are screened prior to charging into the furnace in order to control the size distribution of the feed. The feed is then charged in alternating layers of ferrous materials (iron ores and sinter), fluxes and metallurgical coke. Screening and layering of the different raw materials is used to control the permeability of the furnace. This is vital to achieving the high gas and liquid flow rates required for high liquid iron production.

Coke is the only material which remains solid below the cohesive zone where it forms a packed bed that supports the burden above and maintains liquid and gas permeability throughout the lower zone of the furnace. Permeability in this coke bed is maintained by minimising coke degradation via supply of high quality, high strength coke. Efficient blast furnace operation relies on the high permeability to gas and liquids provided by this coke bed which allows the reducing gases to move up through the furnace and the liquid iron and slag to collect in the hearth.

Permeability in the deadman can reduce rapidly due to the degradation of low quality coke. This can occur rapidly in the deadman via mechanical wear and the Boudouard reaction shown in equation 2-1. This reaction is also known as the carbon solution loss or coke gasification reaction.

$$CO_{2\,(g)} + C_{(coke)} = 2CO_{(g)} \qquad \textbf{(2-1)}$$

Deadman permeability restoration is a lengthy process requiring first an improvement in coke quality and time for the deadman to clean via coke dissolution. Eventually all the carbon in the coke is consumed by dissolution in liquid iron leaving behind inorganic mineral matter referred to as coke "ash". Currently it is unknown how these coke ash minerals interact with blast hearth refractory.

2.1.3. Key Reactions in the Blast Furnace Hearth

The reactions that occur in the blast furnace hearth and deadman are of importance for coke ash and blast furnace hearth refractory interactions. These reactions include:

- *Coke dissolution*

Not all the carbon from coke is consumed in the reactions that provide heat and reducing gases. Significant amounts of coke remain as a packed bed in the blast furnace hearth. The majority of the carbon content in this coke is consumed by dissolution in liquid iron as given in equation 2-2. Carbon can also be consumed by reactions with slag as shown in equation 2-3. A significant amount of the remaining mineral matter contained within coke is insoluble in liquid iron.

$$C_{(coke)} = [C] \quad \textbf{(2-2)}$$

$$(SiO_2) + C_{(coke)} = SiO_{(g)} + CO_{(g)} \quad \textbf{(2-3)}$$

Where: [ ] = in solution in Fe

( ) = in solution in slag

- *Dissolution of coke ash mineral matter in slag*

The mineral matter remaining after coke dissolution in molten iron or combustion in the raceway is able to dissolve in the slags formed in the cohesive and active coke zones. This is unable to occur low in the hearth as liquid iron and slag form immiscible layers in the hearth preventing dissolution of the coke ash mineral matter formed below the iron-slag interface (as shown in Figure 1.1).

- *Silica depletion of coke ash mineral matter*

Approximately 90 mass% of coke mineral matter is composed of silica, alumina and lime. However, in a study of Port Kembla coke, it was found that the mineral matter formed during coke dissolution in the lower zone of the blast furnace has been depleted of silica [3, 4, 5, 6]. Silica depletion of coke at high temperatures is well documented by a number of sources, an example of which is shown in Figure 2.2 [8]**.**

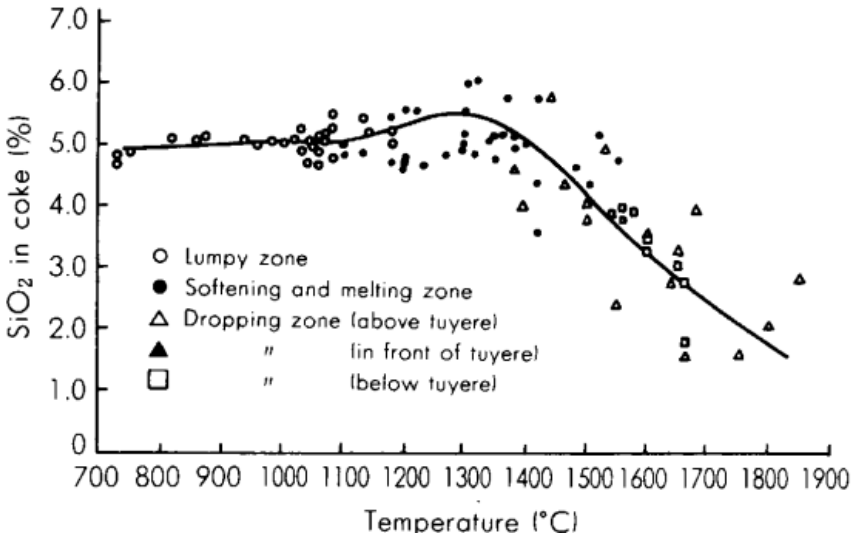

Figure 2.2: The change of SiO_2 content in coke with increasing temperature in a blast furnace [8].

Equations 2-4 to 2-7 show possible reactions by which the silica can be depleted from the mineral matter. Equation 2-4 is considered the dominant reaction by which silica depletion of coke occurs [8-12]. Due to the depletion of silica by these reactions the coke ash mineral layer has been found to be a predominantly calcium aluminate mineral layer.

$SiO_{2(s)} + C_{(s)} = SiO_{(g)} + CO_{(g)}$ **(2-4)** [13-14]

$SiO_{2(s)} + 2[C] = [Si] + 2CO_{(g)}$ **(2-5)** [13-14]

$2SiO_{2(s)} + SiC_{(s)} = 3SiO_{(g)} + CO_{(g)}$ **(2-6)** [13-14]

$SiC_{(s)} + CO_{(g)} = SiO_{(g)} + 2C_{(graphite)}$ **(2-7)** [13-14]

2.1.4. Hearth Liquid Flow

The position of the deadman determines the fluid flow conditions through the blast furnace hearth. Permeability of the deadman controls the balance of forces which determine the buoyancy of the deadman coke bed in the molten iron and slag layers as shown in Figure 2.3 [15]. Liquid flow in the hearth is important as fluid flow affects the rate of coke dissolution and refractory degradation reactions.

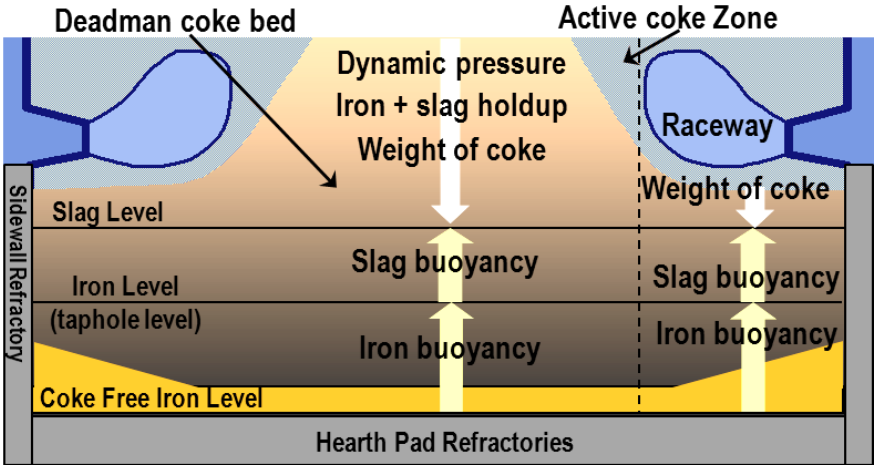

Figure 2.3: Simplified forces acting on the coke bed adapted from [15]

The deadman coke has a significantly lower density than the molten iron and slag producing the upward forces shown in Figure 2.3 . These forces are countered by the dynamic pressure and liquid hold up in the deadman. Liquid hold up is defined as the mass of liquid iron and slag in the deadman above the iron-slag interface. The buoyancy across the blast furnace varies due to the raceway, providing additional upwards force around the furnace circumference. The balance of these different forces can produce the following conditions in the deadman coke bed:

Static Deadman (or Sitting Deadman): occurs when the liquid hold up is high, reducing the buoyancy of the deadman causing it to rest on the hearth pad refractory forming a densely packed, low permeability coke bed as shown in Figure 2.4 a). Low coke bed permeability produces high peripheral liquid flows around the circumference of the hearth. It has been found that a static deadman will cause the coke mineral matter in the peripheral regions of the hearth to be consumed in 2 to 3 days due to the high hot metal flows, while coke mineral matter in the centre of the deadman is consumed significantly slower, taking 15-18 days [8] up to a couple of months [16]. Therefore a static deadman increases the residence time for coke ash minerals in the hearth.

Dynamic Deadman (or Floating Deadman): occurs when the hearth coke bed is no longer completely resting on the hearth pad refractories and forms a loosely packed, high permeability coke bed suspended resulting in a coke free zone. This allows coke particles to move, increasing the removal rate of coke fines, thereby improving permeability. The coke free zone allows the molten iron and slag to flow radially across the hearth reducing the residence time of coke ash mineral matter formed in this region.

Figure 2.4 b) shows a dynamic deadman partly floating due to the higher buoyancy under the raceway which allows a circumferential coke free zone to form. Figure 2.4 c) shows a dynamic deadman with a complete coke free zone formed due to low liquid hold up.

Unique conditions in the BlueScope Steel's No.5 blast furnace hearth during its third campaign produced a static (sitting) deadman in the southern half of the hearth and a dynamic deadman in the northern half [17]. Nightingale [18] has indicated that the southern half of the hearth was the first to experience significant wear later in the campaign. This suggests that longer reaction times for the coke ash and blast furnace hearth refractory interactions have a negative impact on the campaign life of the hearth refractory.

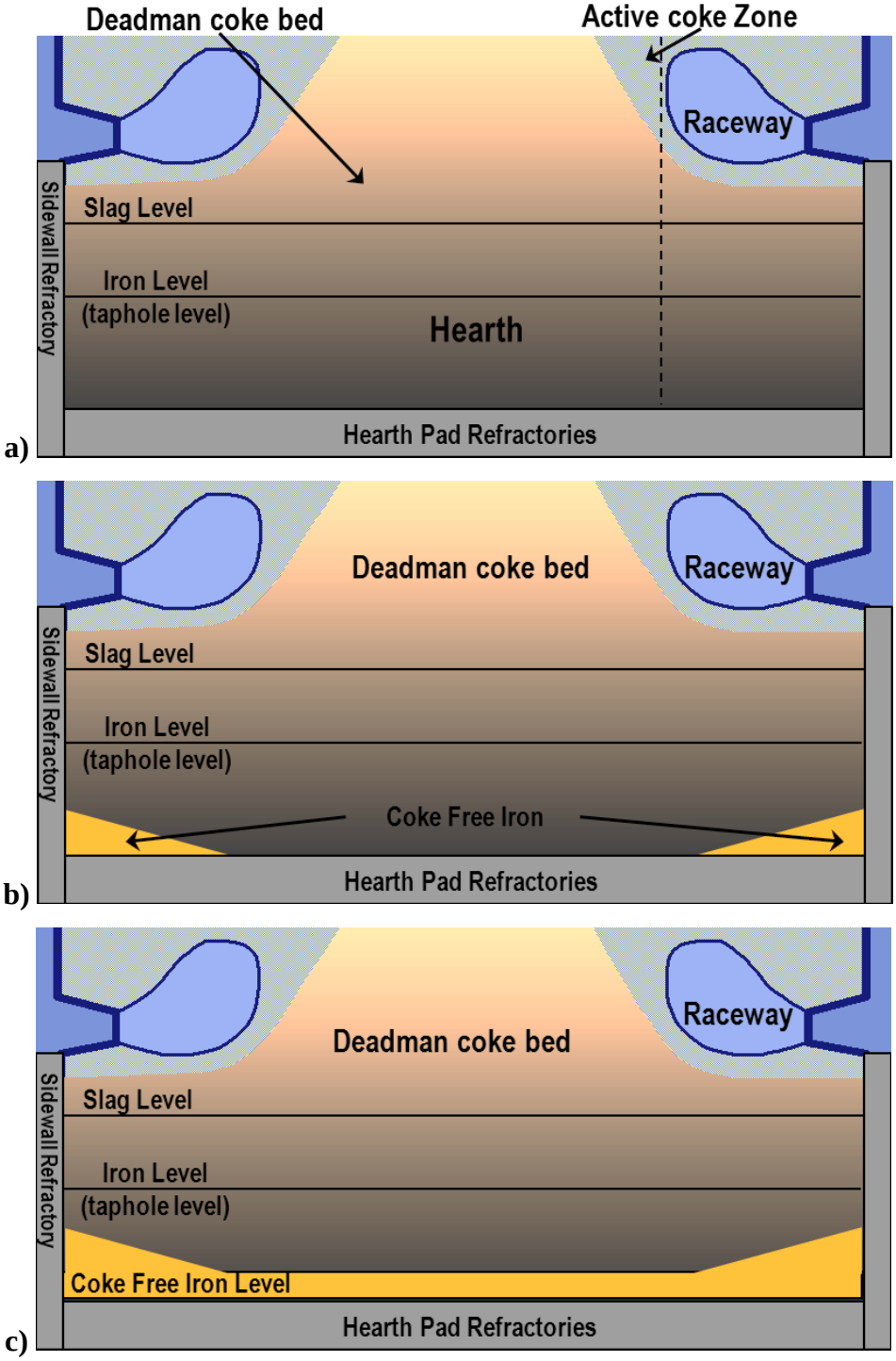

Figure 2.4: Diagrams of a) static/sitting deadman b) dynamic deadman c) dynamic deadman with a complete coke free zone, adapted from [15]

2.2. Coke

Coke is produced by carburisation of a crushed blend of coals by heating to approximately 1400 K in the absence of oxygen. This releases volatile gases and allows a number of phases to soften and deform plastically causing densification and de-volatilisation of the material. The evolution of these gases produces the porous structure characteristic of coke. Using blended coals also allows control of the coke properties. The coking process produces a hard, porous carbon product which is used as a fuel and reductant source in the blast furnace. Over 90% of the total metallurgical coke produced is used in ironmaking blast furnaces [3].

2.2.1. Coke Composition and Mineralogy

Australian cokes contain carbon, 10-15 mass% ash and 0.40-0.45 mass% sulphur [19]. Coke ash is composed of mineral matter an example composition of which is provided in Table 2.1.

Table 2.1: Ash composition of a typical BlueScope Steel coke by mass% of ash (total ash 11.6 mass%)[4]

SiO_2	Al_2O_3	Fe_2O_3	CaO	P_2O_5	MgO	K_2O	TiO_2	Na_2O	Mn_3O_4
54.8	32.3	4.9	2.9	1.42	1	0.51	1.4	0.38	0.05

There are a number of phases present in Australian metallurgical coke. The primary mineral phases are: Quartz (SiO_2, 1.9-33.1 mass%), Mullite ($Al_6Si_2O_{13}$, 2.5-9.7 mass%), Fluorapatite ($Ca_5(PO_4)_3F$, 0.5-5.3 mass%) and an amorphous "mullite like" glassy phase [20-21]. Metallurgical coke also contains minor amounts of cristobalite (~0.1 mass%) and crystalline forms of calcium; oldhamite (CaS ~0.3 mass%), akermanite ($Ca_2Mg_2Si_2O_7$, 0-0.4 mass%) and diopside ($CaMgSi_2O_6$, 0.1-0.4 mass%) [20-21].

2.2.2. Coke Dissolution in Liquid Iron

Coke dissolution is an important reaction as it is required for the carbonisation of the liquid hot metal in the hearth. Liquid iron entering the hearth and deadman region contains more than 2 mass% carbon. The liquid iron dissolves further carbon while permeating through the packed bed of coke in the deadman and hearth of the blast furnace [4].

A simplified representation of liquid iron behaviour is shown in the iron-carbon phase diagram in Figure 2.5. This binary phase diagram shows that the liquidus temperature decreases as the carbon content approaches 4.27 mass% carbon. At this composition the fluidity of the liquid iron will be maximised and the superheat (heat above that required to melt iron) required is minimised.

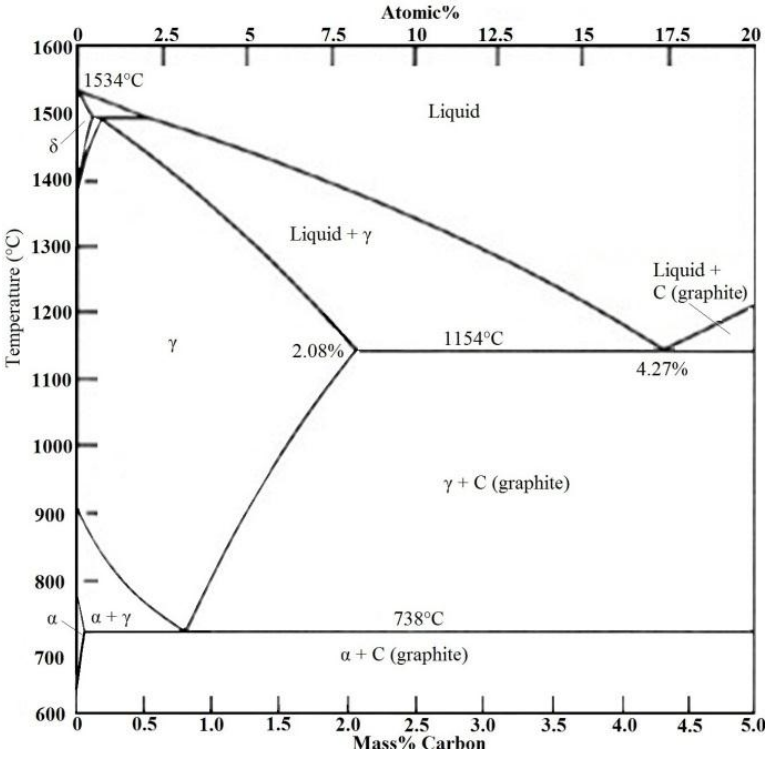

Figure 2.5: Fe-C phase diagram [22]

Carbon dissolution into iron is, in general, considered to be a first order kinetics controlled reaction [4, 23-32]. If the rate-controlling step is mass transfer of carbon from the coke through the adjacent boundary layer into the bulk liquid iron, then for a given area the kinetics of the dissolution reaction can be represented by equation 2-8. From this equation it can be seen that the reaction rate is proportional to the reaction area for the dissolution reaction.

$$\frac{dC_{[C]}}{dt} = \frac{A}{V} k_m([C]_{sat} - [C]_{bulk}) \qquad \textbf{(2-8)}\ [4]$$

Where

$\frac{dC_{[C]}}{dt}$ = rate of carbon dissolution into an iron melt

$[C]_{bulk}$= bulk carbon concentration in melt

$[C]_{sat}$ = carbon concentration at carbon saturation

k_m= mass transfer coefficient (ms^{-1})

A= area of reaction interface (m^2)

V = volume of melt (m^3)

Dissolution of the carbon content from coke produces a by-product layer of oxide mineral matter known as coke ash. This material may accumulate on the surface of the coke [3-6, 33]. This reduces the surface area for the dissolution reaction and therefore the reaction rate. Figure 2.6 shows a schematic representation of the reduction in reaction area interface between coke and liquid iron due to the formation of an oxide layer.

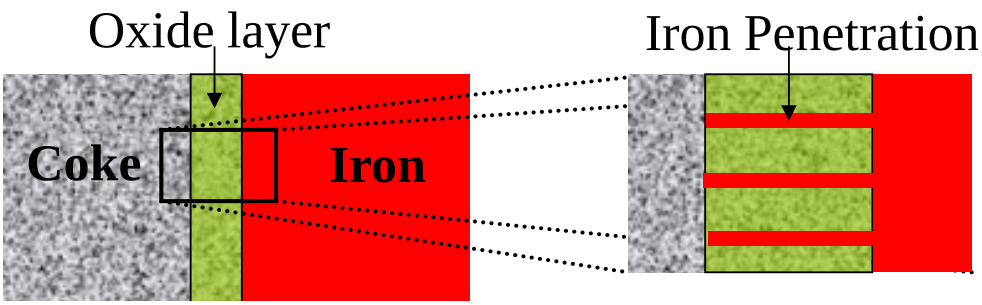

Figure 2.6: Schematic representation of coke dissolution and mineral layer formation [33]

A significant amount of coke dissolution occurs in the hearth. Therefore as the dissolution of coke occurs there is potential for the insoluble components of the inorganic mineral matter to form a layer on the surface of the coke. This coke ash mineral matter can accumulate in a static deadman and come into contact with the hearth refractory.

2.2.3. Mineral Layer Formation

During metallurgical coke dissolution in liquid iron, a mineral layer may form at the coke-liquid iron interface. Although a number of studies on carbon dissolution in iron have been conducted [34-35, 25], the study by Chapman et al [3-6, 33] was the first to study the development of the predominantly calcium aluminates mineral layer at the interface. The absence of silica from the mineral layer can be attributed to the reduction of silica to [Si] or as a loss to the gas phase as $SiO_{(g)}$ as shown in equations 2-4 to 2-7.

Chapman *et al* [3, 4] documented the formation and changing morphology of this mineral layer during coke dissolution in liquid iron. The formation of this mineral layer decreased the rate of coke dissolution [4-5], most likely due to the reduction of the dissolution reaction area. The volume of material in the mineral layer increases with reaction time and the temperature. The study by Chapman et al [4] observed that the mineral layer was enriched with calcium with both increasing reaction temperature and time. The phases identified in the ash layer by Chapman et al [4] study are given in Table 2.2

Table 2.2: The characteristics of calcium aluminates [36-37]

Phase	**Mass.% Al_2O_3**	**Mass.% CaO**	**Molar ratio CaO:Al_2O_3**	**Liquidus (**°C)	**Typical Morphology**
$CaO.6Al_2O_3$	91.8	8.2	0.16	1830	Lath shaped crystals
$CaO.2Al_2O_3$	78	22	0.5	1762	Idiomorphic platelike and Needle like crystals
$CaO.Al_2O_3$	65	35	1.0	1602	Cubic

It is important to note that many of the phases formed in the mineral matter are not soluble in iron but are soluble in blast furnace slags. For this reason the study by Chapman *et al* [4] was focused on dissolution of coke in the hearth below the iron-slag interface where the coke is only in contact with liquid iron. This is an important consideration when characterising the interactions between coke ash and blast hearth refractory minerals.

2.3. Blast Furnace Hearth Refractories

The blast furnace hearth is constructed of a water cooled shell lined with refractory materials capable of withstanding the high temperature and corrosive environment produced within the ironmaking blast furnace. There are a number of different refractories used in the blast furnace hearth as shown in Figure 1.1, these include:

- Fireclays: manufactured from aluminosilicate clays (kaolinite)
- Aluminosilicates: manufactured from andalusite, mullite and bauxite
- Micro-pore carbon: manufactured from anthracite, pitch and graphite
- Alumina-Carbon: manufactured from alumina grains, anthracite and graphite.

The bulk of the blast furnace hearth refractory is constructed of precision machined micro-pore carbon blocks. The non-wetting behaviour of the micro-pore carbon refractories provides excellent resistance to corrosion by liquid and gas penetration. The high thermal conductivity of these refractories produces a high thermal gradient improving the cooling of the protective aluminosilicate and alumina-carbon refractory layers.

The aluminosilicate and alumina-carbon refractories are used to protect the micro-pore carbon from erosion and abrasion by acting as a wear layer at the bottom of the hearth. In some cases a sacrificial layer of fireclay brick is placed over the aluminosilicate and alumina-carbon refractories. This delays exposure of the aluminosilicate and alumina-carbon refractories to extend the refractory in-service life. The design of the hearth refractories is similar in most blast furnaces with the main variations being the specific type of carbon and ceramic refractories used. The aluminosilicate and alumina-carbon refractories at the bottom of the hearth are in direct contact with the coke ash minerals and can potentially react with each other.

2.3.1. Fabrication

Blast furnace hearth refractories are produced by conventional powder processing. This involves mixing beneficiated and processed natural ores with binders followed by uniaxial pressing to form a green refractory material. The properties of the refractories produced are controlled by blending the raw materials to achieve the required composition and by adjusting the particle size distribution to maximise the density of the green refractory. High density in the large green refractory bricks reduces shrinkage and associated stresses when the brick is fired.

Binders such clay, pitch, resins or chemical binders are added to increase the green strength of the pressed block. The low temperature bonds formed from these additives melt or react to form a high temperature bonding phase when the green material is fired. The nature of this bonding phase has a significant influence on the in-service properties of a refractory. This phase may be ceramic (e.g. fine grained alumina or glass) or carbon derived from the pitch or resin binder as in the alumina-carbon refractories used in a blast furnace hearth. Figure 2.7 shows an idealised representation of the fired refractory microstructure containing aggregate (filler) and matrix (bond) phases. The aggregate and matrix are multiphase phase regions. The aggregate is typically a fused grain, tabular grain or sintered grain material with superior properties to the bond phase.

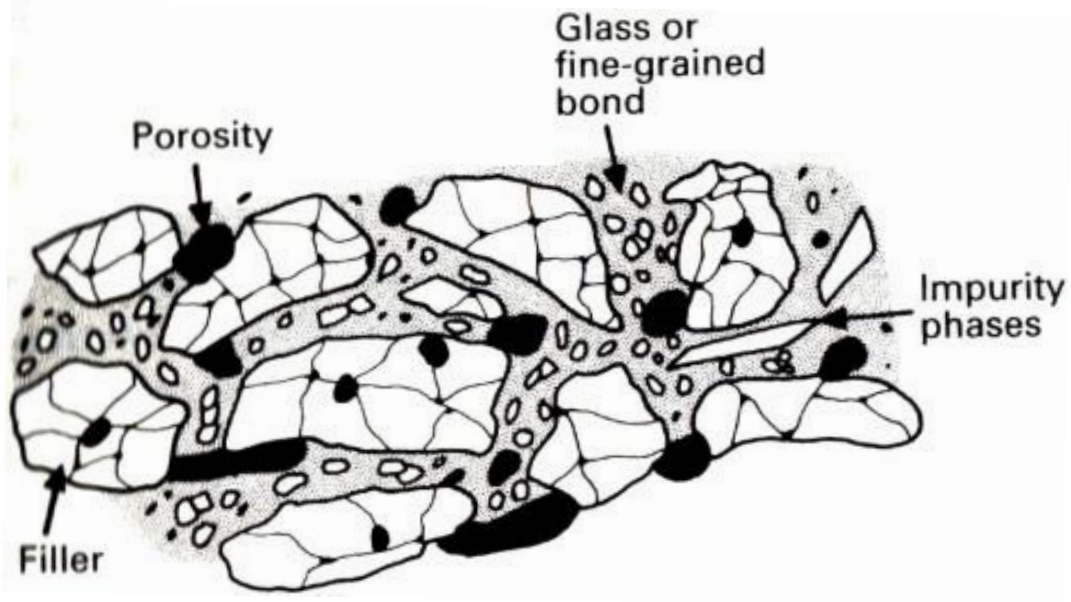

Figure 2.7: Schematic diagram of a refractory microstructure made from powders with a large range of sizes [38].

The aim of refractory fabrication is to produce a refractory that is stable under operational conditions to ensure the in-service properties required are achieved. The properties of a refractory can change throughout their service life as prolonged interactions with the high temperature processing environment drives changes in the composition and the microstructure of the refractory.

2.3.2. Composition and Microstructure

Alumina-Carbon Refractories: The alumina in these refractories provides oxidation resistance and the carbon provides increased thermal conductivity, non-wetting behaviour in contact with slag and slag attack resistance [38]. Since oxides and graphite react on sintering, the bonding phase is formed by pyrolysis of carbon-based binders or the formation of ceramic bonds from clay or other additives. A comparison of two alumina-carbon refractory materials currently in use in different blast furnaces is provided in Table 2.3. The microstructure of an alumina-carbon refractory is shown in Figure 2.8 a).

Table 2.3: Texture and mineralogy of different alumina-carbon refractories [39].

	Texture	**Mineralogy**	**Other Factors**
Material 1	Aggregate grains and fines	White fused alumina to 4 mm, matrix anthracite grains to 200 µm, alumina fines, and sparse graphite.	Overall dark grey colour
Material 2	Aggregate grains in a matrix of fines	White fused alumina to 4mm, matrix coke, anthracite and alumina fines.	Coke grains show concentric shape

Aluminosilicate Refractories: These materials have high oxidation and wear resistance compared to other materials. A comparison of two aluminosilicate refractories currently used in different blast furnaces is provided in Table 2.4. A typical microstructure of a high alumina refractory is shown in Figure 2.8 b).

Table 2.4: Texture and mineralogy of different aluminosilicate refractories [39].

	Texture	Mineralogy	Other Factors
Material 1	Aggregate grains bonded with sintered fines and minor glass.	Fine mullite and glass aggregate up to 3 mm and an amorphous glassy matrix.	Minor iron patches, overall white colour difficult to see aggregate grains
Material 2	Aggregate grains bonded with mullite and glass meshwork.	Primarily fine mullite and glassy phase aggregate grains up to 6 mm and matrix.	No iron patches, overall white colour, hard to distinguish aggregate, dense

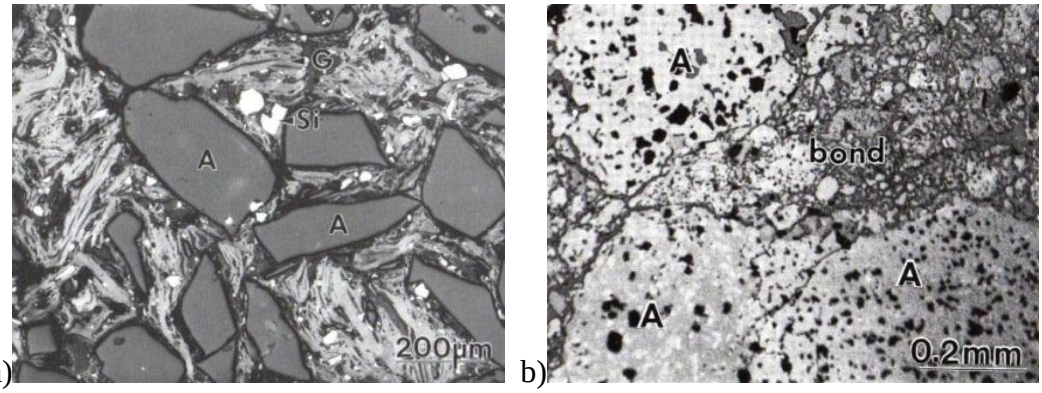

Figure 2.8: a) Microstructure of an alumina-carbon refractory; alumina grains (A), graphite flakes (G), light antioxidant Si metal grains (Si). b) Microstructure of aluminosilicate refractory showing sintered porous alumina aggregate grains (A) bonded with fine alumina, glass and mullite [38].

The compositions of aluminosilicate and alumina-carbon hearth refractories currently in use in a recently relined blast furnace are detailed in Table 2.5[40-41].

Table 2.5: Composition of the aluminosilicate and alumina-carbon refractories in mass% [40-41]

Analyte	Aluminosilicate	Alumina-Carbon
Fe_2O_3	0.62	0.56
SiO_2	28	5.6
Al_2O_3	70.5	75.7
CaO	0.11	0.17
MnO	0.01	-
MgO	0.05	0.07
P_2O_5	0.076	-
K_2O	0.1	0.13
TiO_2	0.32	0.07
Na_2O	0.09	0.26
S	<0.005	-
Cr_2O_3	0.045	-
ZnO	0.005	-
ZrO_2	0.03	-
Total Carbon	-	17.5
SiC	-	1.5

2.4. Refractory and Mineral Systems

Given the refractory compositions detailed in section 2.3.2 and the coke mineral data detailed in section 2.2.3, it is clear that phase diagrams of Al_2O_3, CaO and SiO_2 will be important in understanding the reaction behaviour of the refractory mineral couples. Therefore phase diagrams of these systems have been given in Figures 2.9 to 2.12. There are also various thermodynamic software packages such as MTDATA [42], FactSage [43], Thermo-Calc [44] that can be used to calculate phase equilibria. While all these packages have their own internal architecture for dealing with different phases/species, they are all based on Gibb's free energy minimisation to predict the equilibrium phase stability. A full discussion of the packages would not be appropriate for this literature review.

2.4.1. CaO- Al_2O_3 Binary System

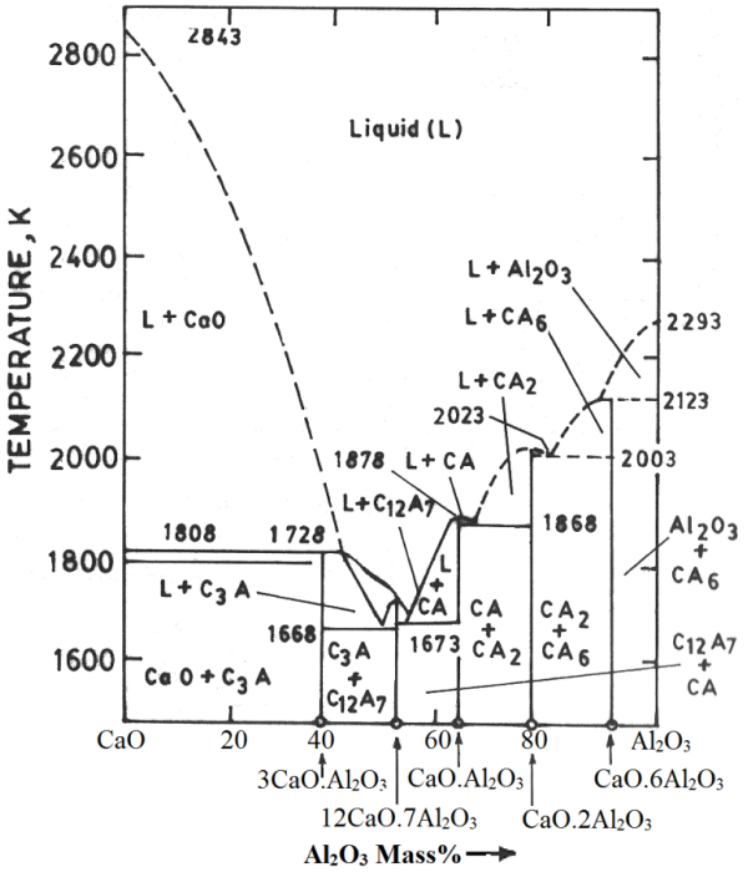

Figure 2.9: Al_2O_3-CaO phase diagram [45]

2.4.2. Al_2O_3-SiO_2 Binary System

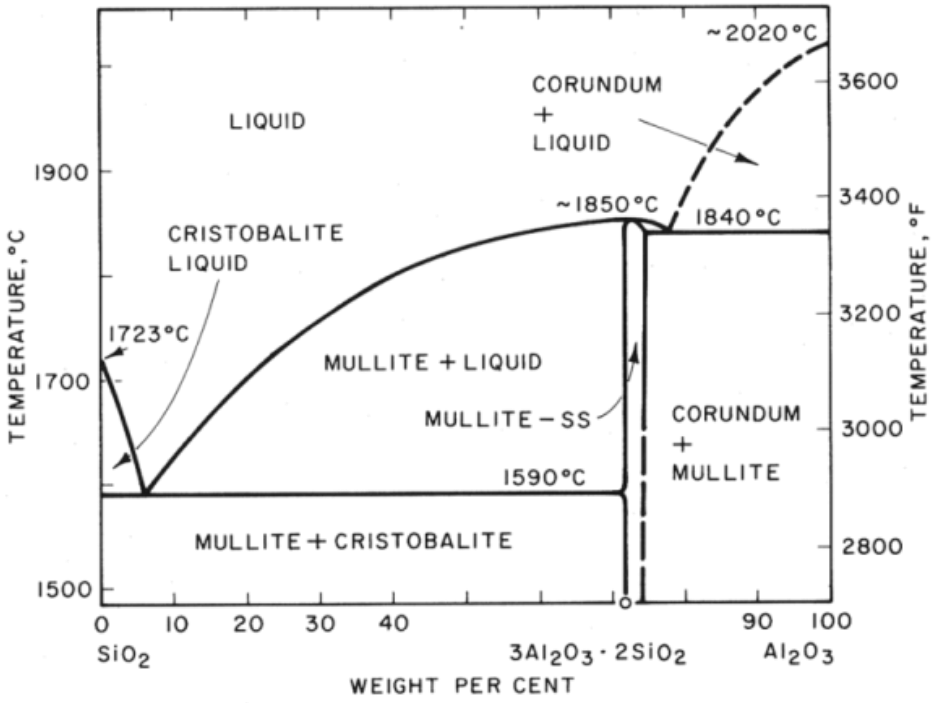

Figure 2.10: Al_2O_3-SiO_2 phase diagram [45]

2.4.1. $CaO\text{-}SiO_2$ Binary System

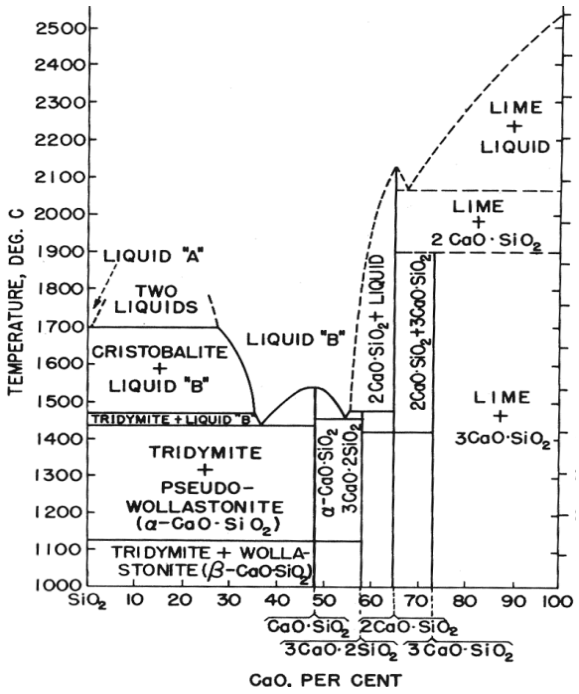

Figure 2.11: SiO_2-CaO phase diagram [46]

2.4.2. $Al_2O_3\text{-}CaO\text{-}SiO_2$ Ternary System

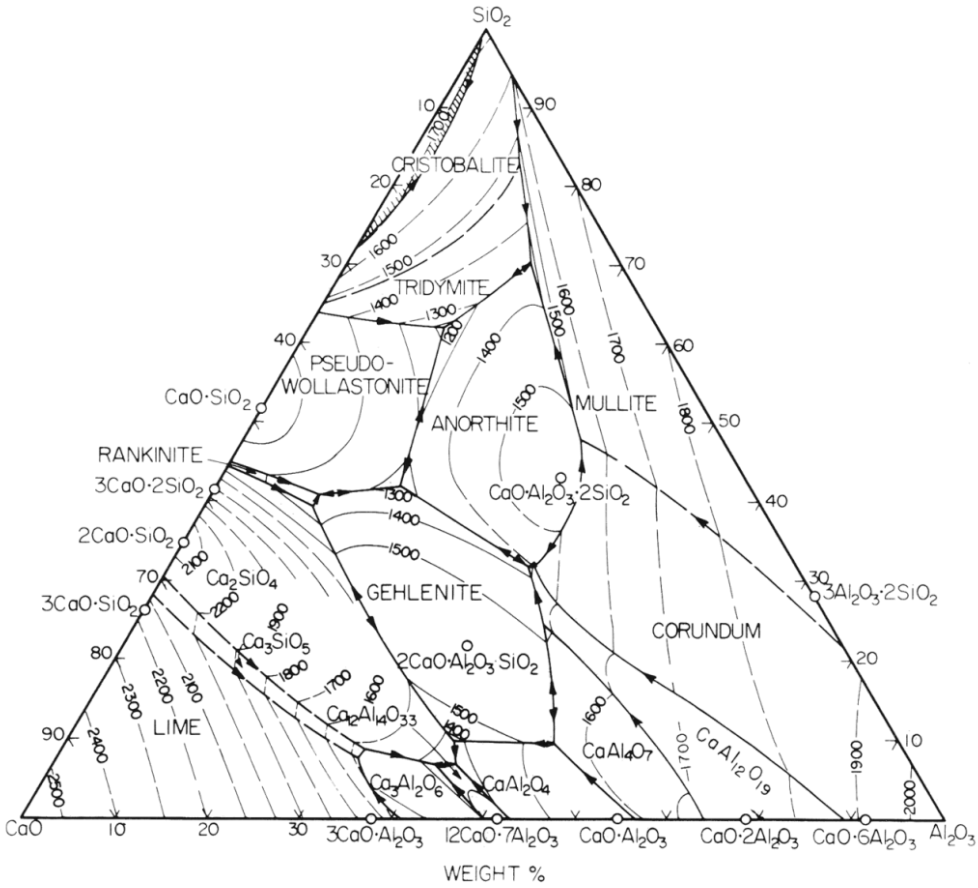

Figure 2.12: Al_2O_3-SiO_2-CaO phase diagram [45]

2.5. Thermodynamics of Refractory and Mineral Matter Reactions

Thermodynamic data for the formation of minerals within the composition range of the materials commonly found in the refractories and calcium aluminates are given in Table 2.6, all other minerals in the Al_2O_3-SiO_2-CaO system have not been considered in this thermodynamic analysis. This data can be used to understand if a reaction is possible. The chemical formula of the calcium aluminates are often simplified as CA = $CaAl_2O_4$, CA2 = $CaAl_4O_7$ and CA6 = $CaAl_{12}O_{19}$.

Table 2.6: Free energy data for reactions in the coke ash and refractory minerals [47-48]

Reaction	**$\Delta G° = \Delta H° - T\Delta S°$ (J/mol)**
$Ca_{(l)} + 1/2O_{2(g)} = CaO_{(s)}$	$\Delta G° = -640200 + 108.6T$
$2Al_{(l)} + 3/2O_{2(g)} = Al_2O_{3(s)}$	$\Delta G° = -1682900 + 323.2T$
$Si_{(l)} + O_{2(g)} = SiO_{2(s,\ \beta\text{-cristobalite})}$	$\Delta G° = -946300 + 197.6T$
$Si_{(s)} + O_{2(g)} = SiO_{2(s,\ quartz)}$	$\Delta G° = -907100 + 175.7T$
$CaO + 6Al_2O_3 = CaAl_{12}O_{19}$	$\Delta G° = -10800 - 47.18T$
$CaO + 2Al_2O_3 = CaAl_4O_7$	$\Delta G° = -17000 - 25.5T$
$CaO + Al_2O_3 = CaAl_2O_4$	$\Delta G° = -18000 - 19.0T$
$3Al_2O_3 + 2SiO_2 = 3Al_2O_3 \cdot 2SiO_2$	$\Delta G° = 8600 - 17.4T$
$Al_2O_3 + SiO_2 = Al_2O_3 \cdot SiO_2$	$\Delta G° = -8800 + 3.9\ T$

*Note all values are for the formation of solids

2.6. Kinetics of Refractory and Mineral Matter Reactions

2.6.1. Kinetics in Solid State Oxide Systems

In general, high temperature solid phase reactions are often controlled by diffusion of one component into the other [49]. Under such circumstances the rate of flux can be given by Fick's 1st and 2nd laws [50]; shown in equations equation 2-9 and equation 2-10.

$$J = -D\frac{\partial C}{\partial x} \qquad \textbf{(2-9) [50]}$$

$$\frac{x}{\partial t} = \frac{\partial}{\partial x}\left(D\frac{\partial C}{\partial x}\right) \qquad \textbf{(2-10) [50]}$$

If D is independent of concentration it can written as

$$\frac{\partial x}{\partial t} = D\frac{\partial^2 x}{\partial t^2} \qquad \textbf{(2-11) [50]}$$

where:

J = flux across interface ($molm^{-2}s^{-1}$)

D= Diffusion coefficient of ion species (m^2s^{-1})

C= concentration

x= distance across interface

t= time

In the CaO – Al_2O_3 and CaO – SiO_2 systems it has been found that Ca^{2+} is the dominant diffusing species [51-52]. Tagai *et al* found the Ca^{2+} ions were able to diffuse through layers of different calcium aluminates to bulk Al_2O_3 [53]. In the Al_2O_3 – SiO_2 system, counter diffusion occurs where both the Al^{3+} and Si^{2+} ions diffuse [51-52]. A study by Mohamed and Sharp found that the activation energy for the formation of $CaAl_2O_4$ was in the same range as the self-diffusion of Ca^{2+} into CaO [54-55].

The diffusion coefficients for Al^{3+}, Ca^{2+} and Si^{2+} cations in solid alumina at 1397˚C are shown in Table 2.7. A direct comparison of this data clearly shows Ca^{2+} has the highest diffusivity in alumina confirming the tabulated data by Hao and Tanaka [51].

Table 2.7: The diffusion coefficients of Al^{3+}, Ca^{2+} and Si^{2+} cations in alumina (99.85 mass%) at 1397˚C from [56] and calculated from data provided in [57] using equation 2-16.

$\mathbf{D_{Al}}$	~1.0 x 10^{-13} cm^2/s
$\mathbf{D_{Ca}}$	3.10 x 10^{-9} cm^2/s
$\mathbf{D_{Si}}$	~7.51 x 10^{-12} cm^2/s

Figure 2.13 shows a comparative plot of the self-diffusion coefficients for the cations in Al_2O_3 and CaO. From this plot it can be seen that the rate of Ca^+ diffusion within CaO is also significantly higher than Al^{3+} in Al_2O_3. It is therefore expected that Ca^{2+} and Si^{2+} cations will have greater mobility in the refractory.

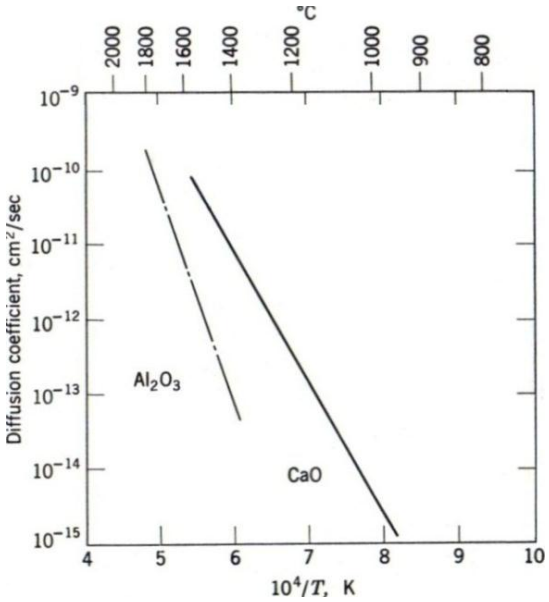

Figure 2.13: Comparative plot of diffusion coefficients for cations in Al_2O_3 and CaO [50]

2.6.2. Temperature Dependence

Diffusion coefficients and rate constants are temperature dependant variables which may be calculated using a form of the Arrhenius equation shown below.

$$D = D_0 e^{\left(-\frac{Q}{RT}\right)} \qquad \textbf{(2-12)} \text{ [50]}$$

where:

R = 8.314 $JK^{-1}mol^{-1}$ Q = Activation energy ($Jmol^{-1}$)

T = Temperature (K) D = Diffusion coefficient (cm^2/s)

D_0 = Diffusion Frequency Factor (cm^2/s)

2.6.3. Area of Reaction Interface

The contact area between the refractory and coke ash minerals is a key parameter in all kinetic control regimes detailed previously. The contact area will be affected by:

- Refractory and coke ash mineral matter porosity
- Surface roughness of both materials
- Phase changes at the interface causing volume or surface texture changes
- Pressure applied at the interface
- Formation of any liquid phases
- The size and distribution of aggregate and matrix phases at the refractory interface

2.6.4. Kinetic Models in Solid State Oxide systems

During reaction there is the possiblity of a product layer forming and a number of models have been developed to describe this behaviour [66, 67]. The key ones with respect to refractory behaviour are defined below.

Linear Rate Law: is an emprical model applicable to systems where product formation is independent of the reaction layer thickness. This occurs when the reaction layer has high porousity, cracking, spalling or consists of a liquid phase. The rate of reaction is directly proportional to time as shown in equations 2-13 & 2-14.

$$\frac{dx}{dt} = k_{lin}t \qquad \textbf{(2-13)}\ [58\text{-}59]$$

$$x = k_{lin}t + A \qquad \textbf{(2-14)}\ [58\text{-}59]$$

where:

k_{lin} = is the linear rate constant — x = reaction layer thickness

t = time — A = is a constant

Parabolic Rate Law: is a model applicable to systems where the rate controlling step is the diffusion of cations to the reaction interface. This can be derived from Fick's First Law of diffusion assuming uniform diffusivity throughout a continuous reaction layer (i.e. single phase) as shown in equation 2-15 and 2-16.

$$\int_0^x x dx = \int_0^t k_{para} dx \qquad \textbf{(2-15)} \text{ [58-59]}$$

$$x^2 = 2k_{par}t + B \qquad \textbf{(2-16)} \text{ [58-59]}$$

where:

k_{para} = is the parabolic rate constant — x = reaction layer thickness

t = time — B = is a constant

Logarithmic Rate law: is a model mainly applicable to systems with thin product layers formed at relatively low temperatures.

$$x = k_{log} log t + C \qquad \textbf{(2-17)} \text{ [58-59]}$$

where:

k_{log} = is the logarithmic rate constant — x = reaction layer thickness

t = time — C = is a constant

Combinations of these laws are used to describe the kinetics of more complex systems (e.g. duel phase systems). Figure 2.14 shows schematically the difference the rate of reaction layer formation for each of these models.

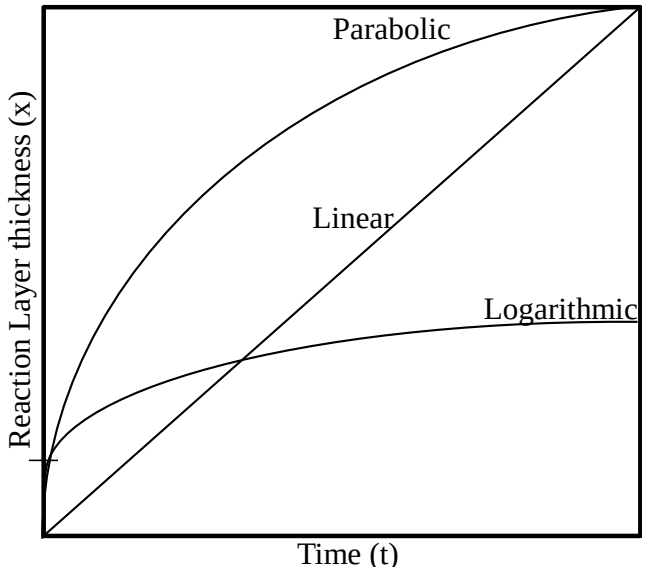

Figure 2.14: Comparative plot of the different kinetic models for the reaction layer formation. Adapted from [58].

2.7. Refractory Degradation Mechanisms in the Blast Furnace Hearth

A review of refractory degradation mechanisms is provided in this section based on the publications of Lee *et al* [38, 60], Pilbrico company of Japan [61] and Jones [62].

Abrasion: resulting from friction between the hearth coke bed and refractory. Observations from the excavation of a Port Kembla blast furnace hearth observed more wear on the side of the hearth with a static deadman [18]. This indicates that an increase in the contact between the solid coke bed and the hearth refractory results in higher wear rates due to increase abrasion or reactions between the materials or a combination of both.

Erosion: wear of hearth refractories due to high liquid metal flows across the hearth refractory is well documented by industry. Detailed computational fluid dynamic models have been developed to predict hearth erosion [63, 64].

Thermal shock and fatigue: can occur due to thermal cycling of the hearth refractory due to variations in iron flow and water supply to the hearth cooling system [38]. High variation in the thermal profile through a refractory will create regions of high stress which can initiate cracking of the refractory. Cracking of blast furnace refractory due to thermal cycling has been observed in industry [18].

Creep: may occur due to the high temperatures and stresses on the hearth refractory [38]. This can occur due to process instability creating high hearth temperatures or failure of hearth cooling systems.

Reduction: Silica is unstable in the presence of carbon at high temperatures. This may result in refractory loss due to the reduction of SiO_2 to $SiO_{(g)}$ (equation 2-3) and the oxidation of carbon containing refractories to form $CO_{(g)}$ and $CO_{2(g)}$ (equation 2-1).

$$(SiO_2) + C_{(coke)} = SiO_{(g)} + CO_{(g)}$$

$$CO_2\ (g) + C_{(coke)} = 2CO\ (g)$$

Corrosion due to solid- solid reactions: The high rate of solid-state diffusion at the in-service temperatures of refractories can cause localised composition changes and bonding of materials at the interface [52, 60]. The localised composition changes can result interfacial phase and subsequent volume changes at the interface leading to structural spalling of the region [65]. Composition changes can also cause low melting point or liquid phases to form resulting in further degradation of the refractory due to liquid penetration.

Corrosion due to hot gas penetration/ condensed phase corrosion: Hot gases can be absorbed into refractories penetrating pores and cracks until the thermal gradient causes the gases to condense forming a liquid (or solid) within the refractory pores. This condensed phase may provide some protection from further penetration by blocking pores in the hot face. However these filled pores may cause damage when subjected to thermal cycling creating a freeze-thaw cycle. In addition to this penetrating gases can undergo chemical reactions with the refractory resulting in localised dissolution.

Corrosion due to liquid penetration: the reduction of interfacial tension is the driving force that allows corrosive liquids and gases to penetrate into refractories pores. The wetting behaviour of a material is determined by the balance of the interfacial tensions (γ) between the different phases (liquid/solid = γ_{SL}, liquid/vapour = γ_{LV} and solid/vapour = γ_{SV}). Figure 2.15a) shows liquid penetration (pore wetting) due to high γ_{SV} and low γ_{SL} and γ_{LV}. Figure 2.15a) shows a non-wetting solid where the γ_{SL} is greater than the γ_{LV} and γ_{SV} and therefore liquid/solid surface is minimised.

a) 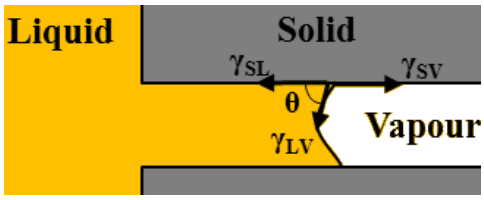

b) 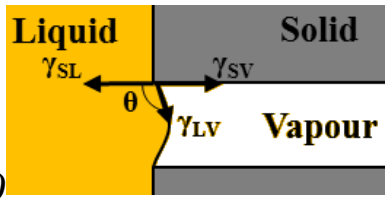

Figure 2.15: a) Wetting of a refractory pore ($\theta<90°$) b) a non-wetting solid ($\theta\geq90°$) [61]

Liquid penetration is controlled by the degree and type of porosity (open or closed), chemical resistance of matrix phase, degree of direct bonding, liquid viscosity and the wettability of the refractory [60]. Liquid penetration can undergo freeze-thaw cycles due to variations in liquid composition and thermal gradients allowing penetration over time. There are two basic patterns:

1) ***Deep penetration*** (Figure 2.16a) via pores or by dissolution of the matrix phase. This tends to loosen the aggregate grains at the hot face and can result in structural spalling.
2) ***Limited penetration*** (Figure 2.16b) to the hot face of the refractory producing a fairly uniform dissolution of the hot face. This occurs in direct bonded and low porosity refractories.

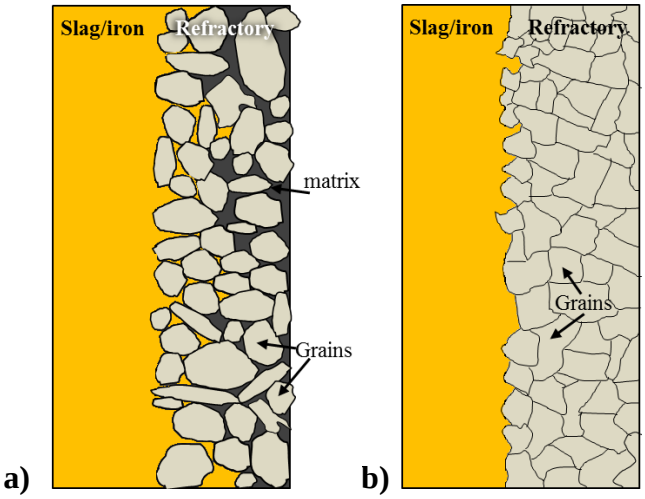

Figure 2.16: Penetration mechanisms, adapted from [61]

Corrosion due to dissolution: Corrosion can be caused by the dissolution of a refractory in a liquid such as slag. These reactions are either chemical reaction or mass transport (diffusion and liquid flow) controlled. In most cases, at the high temperatures of the blast furnace hearth, mass transport is the slower process and hence it controls the overall dissolution rate. As detailed previously in 2.6.1 the flux across an interface (i.e. the dissolution rate) in a mass transport controlled system can be determined using equation 2-10 [50]. It can be seen from equation 2-10 that both a larger interfacial area and concentration would increase the dissolution rate.

Corrosion due to indirect dissolution: is characterised by the formation of one or more solid products at the interface. This introduces two more steps in the dissolution process:

1) The formation of the product at the solid/product interface
2) The dissolution of the product at the product/liquid interface

After the formation of the reaction (product) layer steady state conditions may be achieved where the thickness of the reaction layer remains constant as the refractory is consumed. The rate of indirect refractory dissolution is given by equation 2-18. It can be seen from this equation that indirect dissolution is a mixed control system that is dependent on the rate of solid state diffusion to reaction layer and the dissolution rate into the liquid phase.

$$\frac{d\Delta Y}{dt} = \left(\frac{k_p}{\Delta Y}\right) + k_l \qquad \textbf{(2-18)} \text{ [60]}$$

Where:

ΔY = rate of refractory consumed to form product (m/s)

k_p = rate constant associated with the formation of the product

k_l = rate constant associated with the product dissolution

2.1. Summary

On review of the literature relating to the interactions between coke ash minerals and hearth refractories, no studies on this topic was found. However, a number of related studies into the effect of calcium aluminates on refractory wear in cement kilns and the degradation of alumina-carbon refractories via carbon dissolution into iron melts [66] were found.

Recent findings by Chapman et al [3-6, 33] determined the coke ash consisted predominately of calcium aluminates. Historically the coke ash was expected to be siliceous due to the high silica content in coke. The implications of a different coke ash composition on the thermodynamics and kinetics of any reactions with hearth refractories are significant. Understanding these interactions is critical for predicting and extending the blast furnace campaign life.

3. Experimental Method

3.1. Reaction Couple Experiments

The interactions between coke ash and blast furnace hearth refractories were investigated using blast furnace hearth refractory and synthetic coke ash reaction couples. These reaction couples were reacted under argon at temperatures representative of the blast furnace hearth using the experimental configuration outlined in Figure 3.1. The interfaces of these reaction couples and any reaction products were characterised using scanning electron microscopy, energy dispersive spectroscopy and image analysis software. Further, the mass change (if any) as a result of the experiment was calculated using Equation 3-1.

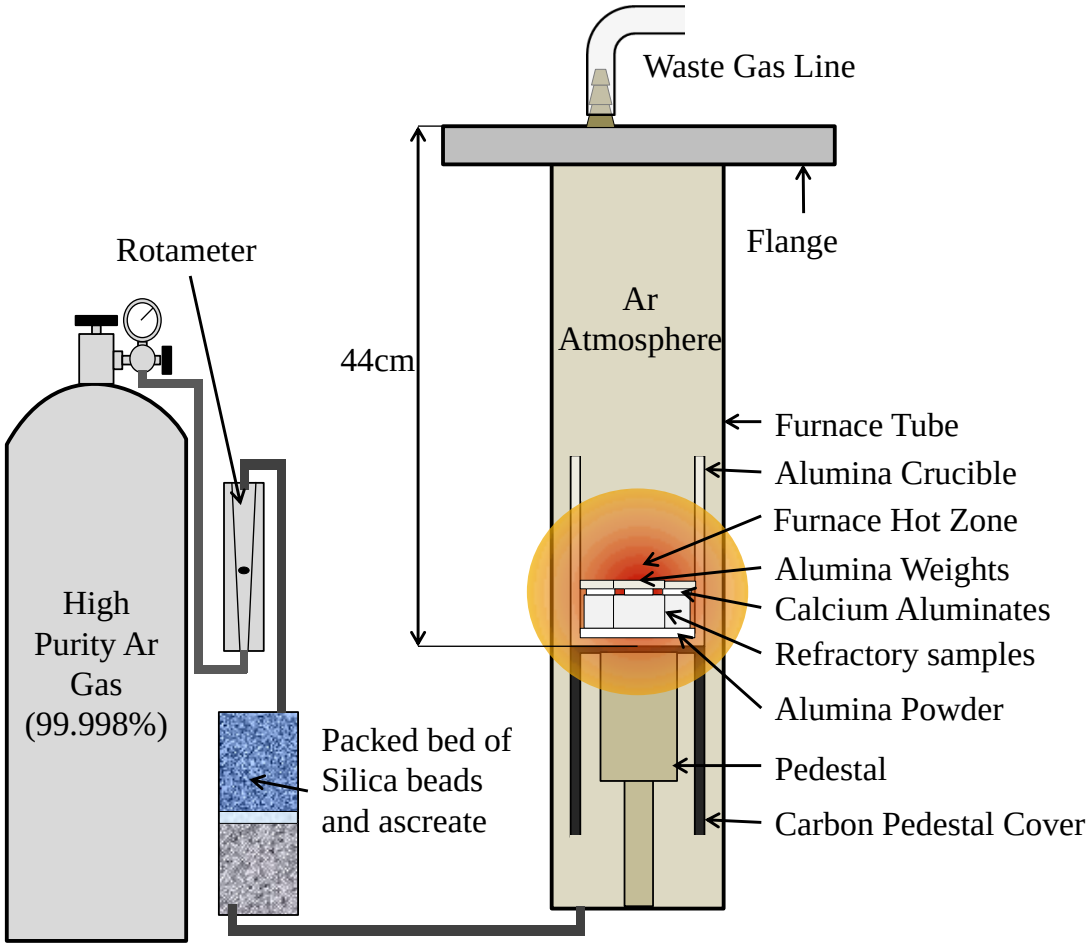

Figure 3.1: Gas Scrubbing and high temperature furnace experimental setup schematic

$$\%\Delta \boldsymbol{Mass} = \frac{\boldsymbol{Mass_{before}} - \boldsymbol{Mass_{after}}}{\boldsymbol{Mass_{before}}} \times \mathbf{100} \qquad \textbf{(3-1)}$$

3.1.1. Reaction Couple and Crucible Configuration

The polished surfaces of refractory and calcium aluminate disc were coupled together with the calcium aluminate positioned on top as shown in Figure 3.2 a). Three reaction couples were placed in an alumina crucible (99.8%Al_2O_3, 74mm high, 62mm internal diameter, 2mm wall thickness). A small amount of tabular alumina powder was used to cover the bottom of the crucible to prevent sticking. An alumina weight (approximately 15g) was placed on top of each reaction couple. A schematic diagram of the crucible configuration is shown in Figure 3.2 b).

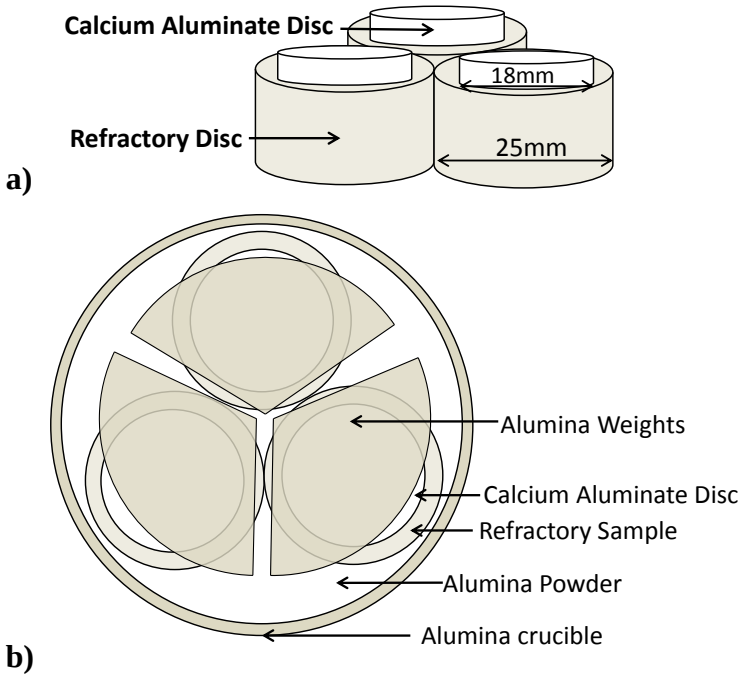

Figure 3.2: Schematic diagrams of a) Reaction couples and b) crucible configuration

Refractory samples of dissimilar compositions (refer to section 3.3 for refractory details) were not heated together as a trial experiment found that cross contamination occurred. The cross contamination is shown by the blackening of the refractories and calcium aluminates in Figure 3.3.

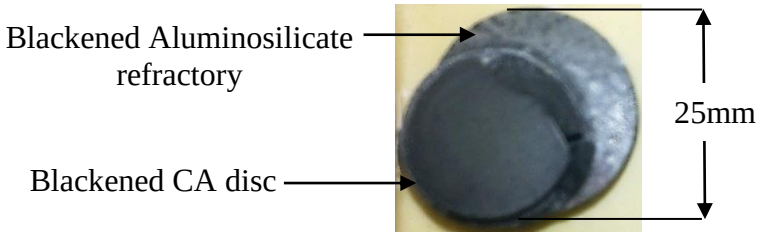

Figure 3.3: cross contamination of the Aluminosilicate/ CA reaction couple after heating in crucible with an Alumina-Carbon refractory

3.1.2. Reaction Couple Furnace Configuration

The reaction couples were positioned in the vertical tube furnace (Figure 3.1). The carbon pedestal cover shown in Figure 3.1 was used to gather oxygen within the furnace tube thereby minimising oxidation of the Alumina-Carbon refractories at elevated temperatures. The furnace was purged with high purity Argon gas (99.998%) for 1 hour prior to heating. A flow rate of 1 litre/min was maintained throughout the heating cycle. To assess the integrity of the gas seal and furnace system a carbon crucible was heated to a furnace set point of 1520°C for 4 hours under these conditions and the mass of the crucible before and after was measured. A mass loss of 0.01% was observed confirming a non-oxidising atmosphere had been achieved.

3.1.3. Experimental Heating Schedule

The schematic of the heating schedule used in these experiments is shown in Figure 3.4. The heating and cooling rates were selected to prevent thermal shock of the alumina furnace tube.

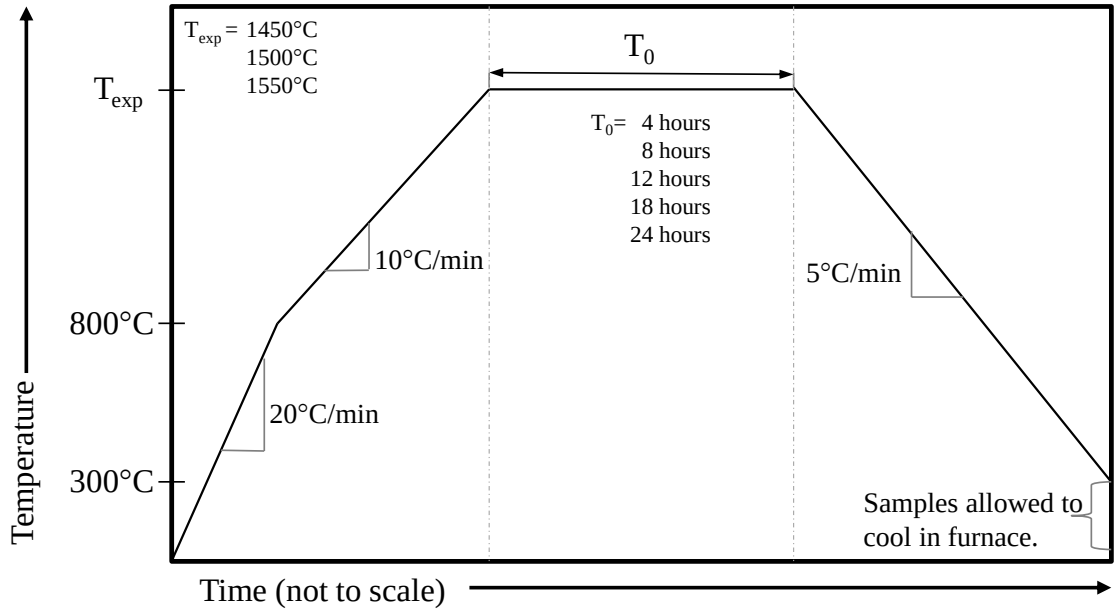

Figure 3.4: Experimental Temperature Schedule

3.1.4. Experimental Matrix

The developed experimental matrix is given in Table 3.1 - Table 3.2, where calcium aluminates CA = $CaO.Al_2O_3$, CA2 = $CaO.2Al_2O_3$, CA6 = $CaO.6Al_2O_3$. The compositions of the refractories used are the same as those given in the literature review section in Table 2.5.

Table 3.1: Experimental Matrix testing the effect of time on reaction kinetics

Reaction Couple	Reaction Times				
	4 hours	**8 hours**	**12 hours**	**18 hours**	**24 hours**
Aluminosilicate - CA	1500°C	1500°C	1500°C	1500°C	1500°C
Aluminosilicate - CA2	1500°C	1500°C	1500°C	1500°C	1500°C
Aluminosilicate - CA6	1500°C	1500°C	1500°C	1500°C	1500°C
Alumina Carbon - CA	1500°C	1500°C	1500°C	1500°C	1500°C
Alumina Carbon - CA2	1500°C	1500°C	1500°C	1500°C	1500°C
Alumina Carbon - CA6	1500°C	1500°C	1500°C	1500°C	1500°C

Table 3.2: Experimental Matrix testing the effect of temperature on reaction kinetics

Reaction Couple	Reaction Temperatures			
	1450°C	**1500°C**	**1530°C**	**1550°C**
Aluminosilicate - CA	4 hours	4 hours	4 hours	N/A
Aluminosilicate - CA2	4 hours	4 hours	4 hours	4 hours
Aluminosilicate - CA6	4 hours	4 hours	N/A	4 hours
Alumina Carbon - CA	4 hours	4 hours	4 hours	N/A
Alumina Carbon - CA2	4 hours	4 hours	4 hours	4 hours
Alumina Carbon - CA6	4 hours	4 hours	N/A	4 hours

Note: CA was not tested at 1550°C to avoid excessive bonding to the crucible weights.

3.1.5. Experimental Repeatability

To assess the repeatability of the experimental method the CA6 reaction couple experiments were repeated three times at 1450°C for 4 hours. All the repeat experiments yielded the same results as the original experimental results. For both refractories it was found that the CA6 did not form a physical bond at the interface and no other physical or chemical changes were observed, with the only exception of CA6 blackening in the presence of the Alumina - Carbon refractory. The Alumina - Carbon refractories tested under these conditions all experienced similar mass losses in the range of 3.00% to 3.87%. No mass loss was observed in any Aluminosilicate reaction couple repeats.

3.1.6. Experimental Outcomes

Key outputs of the experimental program are given in Table 3.3.

Table 3.3: Reaction couple experimental outputs

	Analysis as a function of			
Analysis	**Temperature**	**Time**	**Refractory Material**	**Calcium Aluminate**
Mass Loss	Yes	Yes	Yes	Yes
Bonding observed	Yes	Yes	Yes	Yes
Reaction Layer thickness	Yes	Yes	Yes	Yes
Reaction Layer Composition	Yes	Yes	Yes	Yes
Composition Change across reaction interface	Yes	Yes	Yes	Yes
Elemental Mapping	Yes	Yes	Yes	Yes

3.2. Reaction Couple Furnace Temperature Calibration

The experimental sample temperature was calibrated using the same setup used for the reaction couple experiments with the inclusion of a thermocouple as shown in Figure 3.5. The temperature calibration conditions are further detailed in Table 3.4.

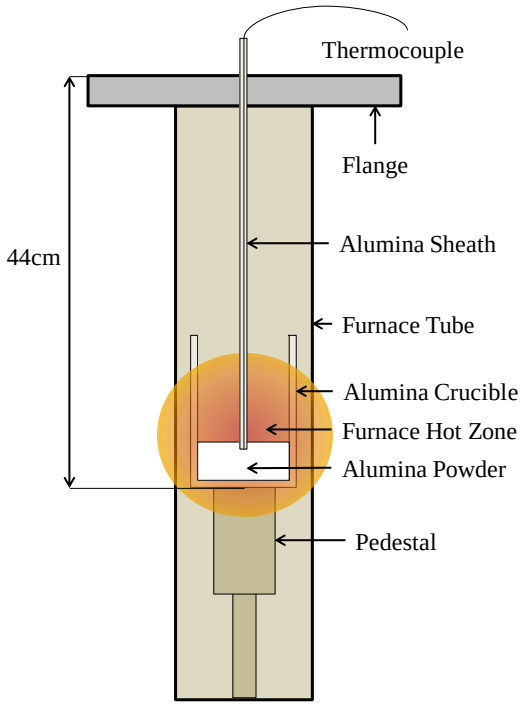

Figure 3.5: High temperature furnace calibration setup schematic

Table 3.4: Vertical tube furnace temperature calibration conditions.

Thermal Mass / Sample	285g (alumina powder + crucible)
Thermocouple	Type R (R1FEB06) in an alumina sheath
Hot zone position	44cm below the furnace top flange
Atmosphere	Argon gas (1.0 L/min)
Controller Temperature range	1350°C - 1650°C

The furnace was ramped up to a controller temperature of 1350°C and held until the thermocouple temperature stabilised. The controller set-point was increased in intervals of 50°C after allowing 10 to 20 minutes for the thermocouple temperature to stabilise at each controller set point. The sample temperature and furnace set point were logged and plotted in Figure 3.6. Equation 3-2 was established using the calibration data to predict the sample temperature from the furnace set point controller. It is this calculated sample temperature that is quoted in all the experiments.

Sample Temperature (°C) = 0.9891 x Controller temperature (°C) – 53.447 **(3-2)**

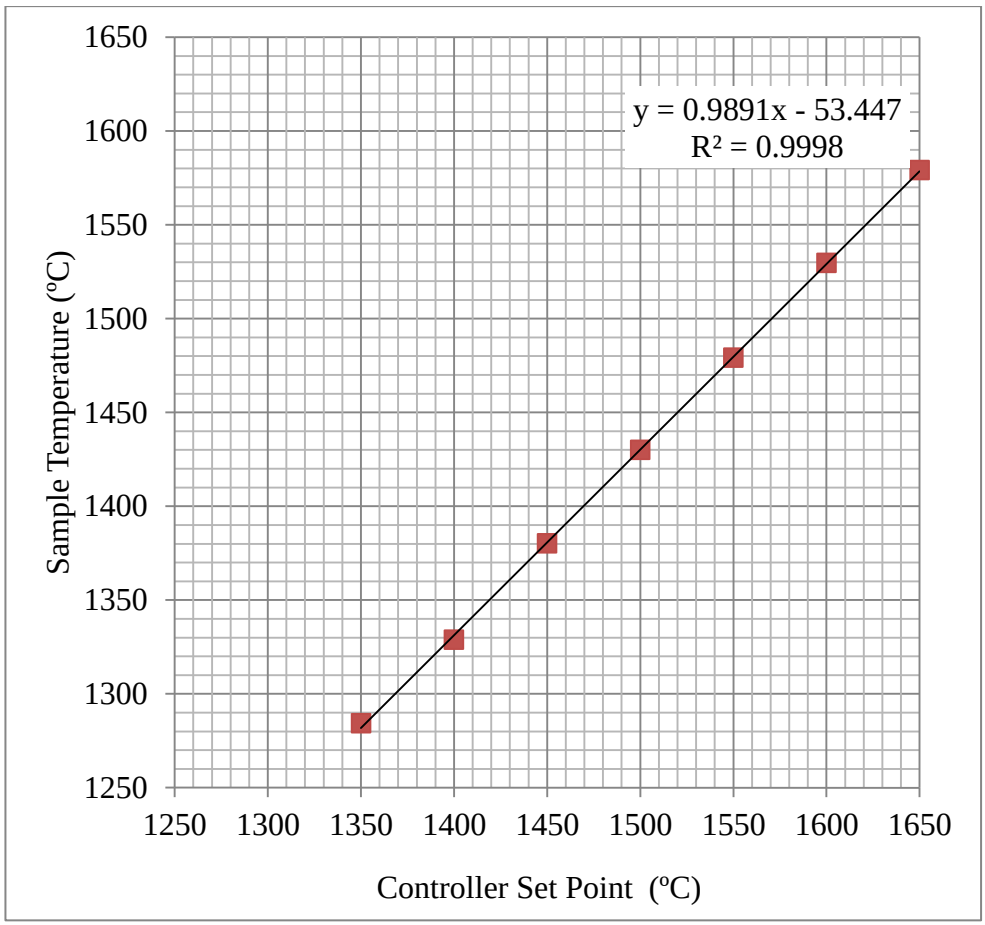

Figure 3.6: High temperature vertical tube furnace calibration carried out on 2/8/2010

3.3. Preparation of Refractories

3.3.1. Coring and Cutting of Samples

Samples of the Aluminosilicate and Alumina-Carbon hearth refractories approximately 230mm x 110mm x 70mm in size were obtained, as shown in Figure 3.7. A diamond tipped core drill was used to remove nine cores (labelled from A to I) from each refractory brick as shown in Figure 3.7 c). These 24 - 26mm diameter cores were cut into four 15mm lengths and one 10mm length, labelled from 1 to 5 as shown in Figure 3.7 d).

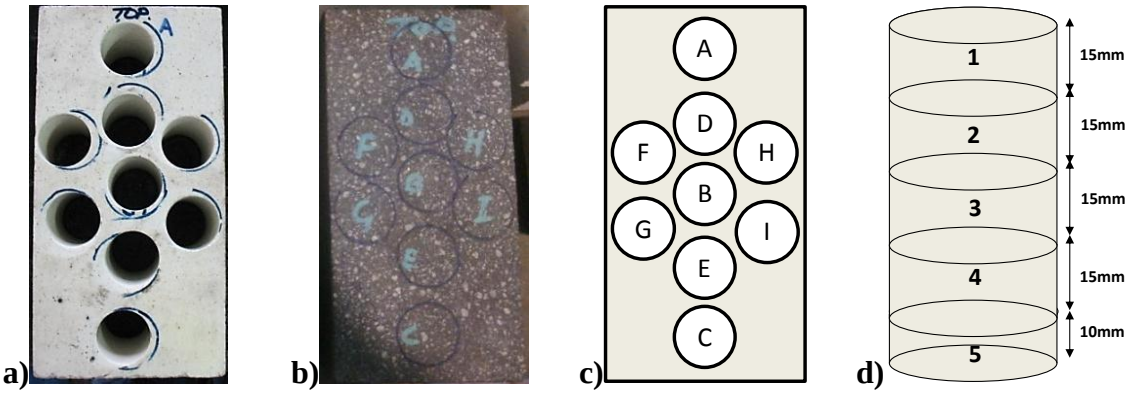

Figure 3.7: a) Aluminosilicate sample b) Alumina-carbon sample c) Core positions (A – I) d) sample positions in cores (1-5)

The bricks were cross sectioned and visually inspected for defects such as laminations that may affect the uniformity of the refractory microstructure. No laminations or other defects were observed from these visual inspections.

3.3.2. Sample Cleaning

The samples were ultrasonically cleaned in distilled water after coring and cutting to remove any contaminants from the cutting process. Each refractory sample was cleaned for 15 minutes before the distilled water was changed and cleaned for a further 15 minutes. The Alumina-Carbon refractory and Aluminosilicate refractory were cleaned separately to avoid cross contamination. The samples were dried at 110°C for a week in an oven before storing in a desiccator until required.

3.3.3. Grinding and Polishing of Refractories

The Alumina-Carbon and Aluminosilicate refractory samples were ground and polished on a Struers Rotopol 1 and Pedemat auto polisher to 3µm using the polishing schedules outlined in Table 3.5 and Table 3.6 respectively. Between each of the fine grinding (FG) and diamond polishing (DP) steps the refractory samples were cleaned with ethanol in the ultrasonic cleaner for 10 minutes to remove fines in the surface pores of the refractory. New grinding and polishing disc were used for each refractory to avoid cross contamination.

Table 3.5: Fine grinding and polishing for the Alumina-Carbon refractory samples

Step	**FG1**	**FG2**	**DP1**
Surface	Diadisc	MD-Largo	MD-Dac
Abrasive	Diamond	DP-suspension	DP-suspension
Grain Size	40µm	9µm	3µm
Lubricant	Water	Struers Green*	Struers Green*
RPM	150	150	150
Force (N)	40	30	30
Time (min)	Until Planar	10	5

Table 3.6: Fine grinding and polishing for the Aluminosilicate refractory samples

Step	**FG1**	**FG2**	**FG3**	**DP1**
Surface	Diadisc	DP-Pan	MD-Largo	MD-Dac
Abrasive	Diamond	DP-suspension	DP-suspension	DP-suspension
Grain Size	40µm	15µm	3µm	3µm
Lubricant	Water	Struers Green*	Struers Green*	Struers Green*
RPM	150	150	150	150
Force (N)	40	40	40	40
Time (min)	Until Planar	10	10	8

*****Struers Green is a water based lubricant

After polishing the aluminosilicate based refractory samples were heated to 1100°C in air for 2.5 hours in a muffle furnace to "burn off" residual diamond particles or oils entrapped in the pores of refractory surface. The samples were allowed to cool in furnace and then stored in a desiccator until required. The polishing methods detailed in Table 3.5 and Table 3.6 were selected to achieve minimal surface contamination of the refractories and a surface roughness less than 3µm.

3.3.4. Microstructure Characterisation

In a study by Drain [65] both refractory materials were characterised by taking a number of samples from different locations in the refractory brick as shown in Figure 3.8. It was found that the microstructure was independent of the position within the refractory brick. No large defects or variations in microstructure (e.g. laminations) were observed throughout the Alumina-Carbon and Aluminosilicate refractories. These findings corresponded with refractory characterisation carried out by BlueScope Steel (Table 2.4). An example of the micrographs produced is shown in Figure 3.9.

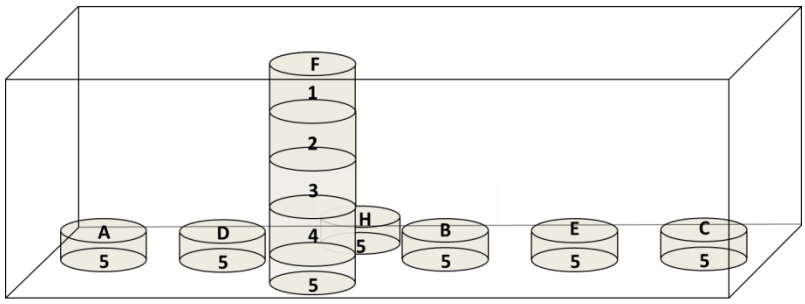

Figure 3.8: Refractory characterisation sample positions

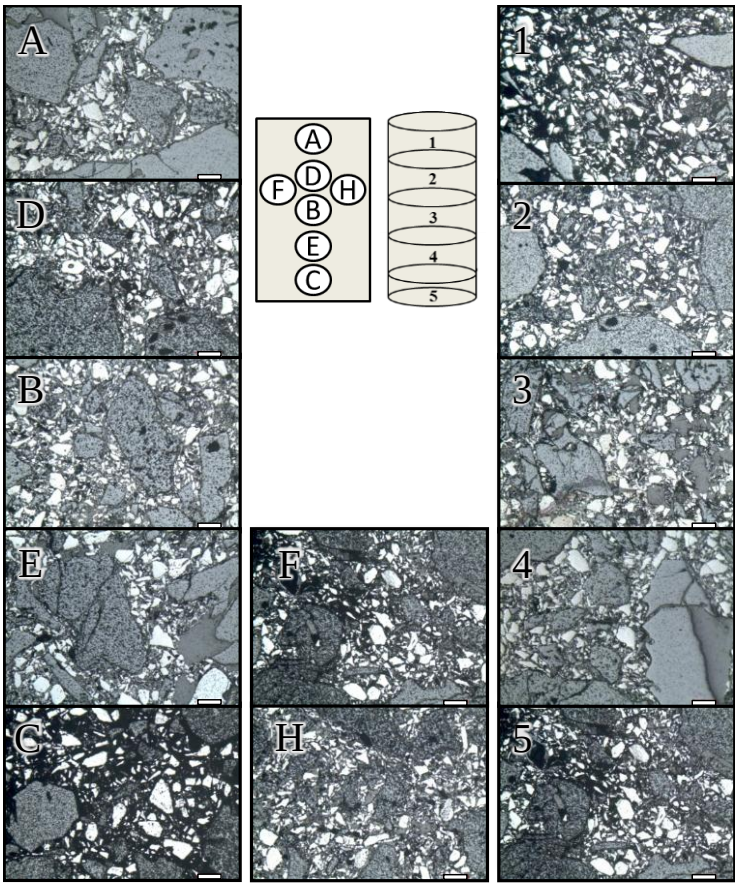

Figure 3.9: Alumina-Carbon refractory at different locations throughout the refractory bulk. Scale bar = 200µm

3.3.5. Composition Characterisation

In a study by Drain [65] energy dispersive spectroscopy (EDS) spot analysis (Table 3.7 and Table 3.8) was used to identify the composition of each phase observed in both hearth refractories in Figure 3.10. It was found that the Alumina-Carbon refractory contained large fused alumina grains surrounded by a matrix of graphite, anthracite grains and alumina fines. The Aluminosilicate refractory was comprised of mullite grains and glass aggregate in a mullite matrix phase.

a) 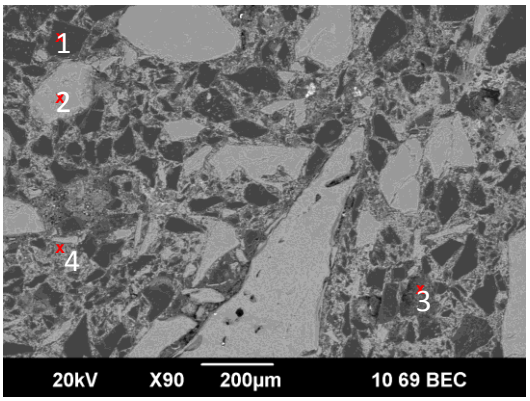

b) 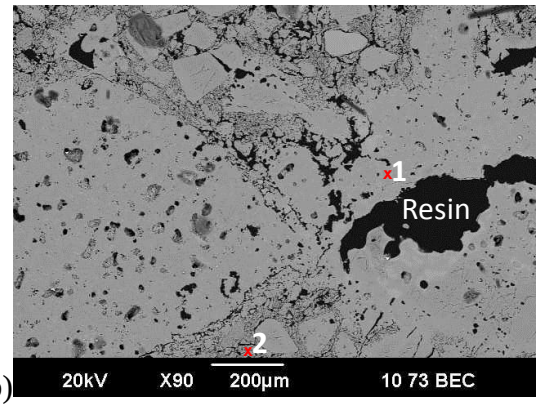

Figure 3.10: Micrographs of a) Alumina-Carbon & b) Aluminosilicate refractory. Scale = 200µm. Numbers indicate EDS spot analysis positions in Table 3.7 and Table 3.8.

Table 3.7: Alumina-Carbon refractory EDS spot analysis results reported as oxides

EDS Position		C	Al_2O_3	SiO_2	Identified Phase
1	Mass%	100			Graphite
	Mol%	100			
2	Mass%	23.9	76.0		Alumina Grain
	Mol%	72.8	27.2		
3	Mass%	66.4	15.4	18.2	Anthracite Grain
	Mol%	92.4	2.5	5.1	
4	Mass%	34.8	45.7	19.5	Matrix Phase
	Mol%	78.9	12.2	8.9	

Table 3.8: Aluminosilicate refractory EDS spot analysis results reported as oxides

EDS Position		Al_2O_3	SiO_2	FeO	Identified Phase
1	Mass%	66.7	31.7	1.6	Mullite
	Mol%	54.3	43.8	1.8	
2	Mass%	94.0	6.0		Corundum/ matrix phases
	Mol%	90.2	9.8		

3.4. Preparation of Calcium Aluminates

3.4.1. Calcium Aluminate Synthesis

A number of single-phase calcium aluminates were required for this study to produce a series of coke 'ash' minerals of known composition. The method detailed in Chapman [3, 4] was used to synthesise the calcium aluminates using the raw materials given in Table 3.10. Calcium carbonate ($CaCO_3$) was used as the source of CaO. The decomposition of $CaCO_3$ to CaO at 900°C allows the desired calcium aluminate phase to be produced.

Table 3.9: Base powders used for synthesis of calcium-aluminate phases [3, 4].

Material	Alumina	Calcium Carbonate
Chemical Formula	Al_2O_3	$CaCO_3$
Molecular weight (g/mol)	101.96	100.09
Supplier	Sigma-Aldrich	Chem-Supply PTY LTD
Purity	>99.7 mass%	99.0 mass%
Particle Size	<10μm	Not Available

The alumina and calcium carbonate powders were mixed in appropriate quantities (detailed in Table 3.10) with deionised water (~500ml) to produce slurry. The slurry was filtered using a 75mm bucher filter and a Filtech 2850-70 filter paper (equivalent to a Whatman #6) resulting in an approximately 3μm particle retention. The filter cake powders were then placed in a drying oven at 110^{o}C for 24 hours.

Table 3.10: Raw material powder quantities for calcium aluminate synthesis.

		CA	**CA2**	**CA6**
Mass (g) required per 100g of Calcium aluminate	Al_2O_3	64.52	78.43	91.59
	CaO*	35.49	21.57	8.41
	$CaCO_3$	63.33	38.50	15.20

*CaO derived from calcination of $CaCO_3$

The dried powders were mixed with distilled water to achieve 4 mass% moisture content before being pressed in a steel die at 650kN in 5-6 gram batches. These green blocks were then fired using a muffle furnace. The heating schedule used is given in Figure 3.11.

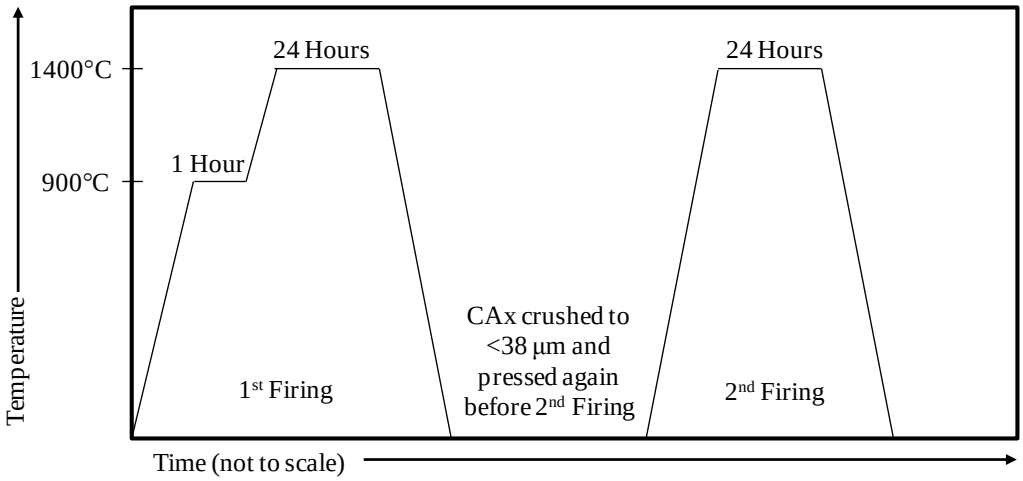

Figure 3.11: Firing schedule for synthesis of calcium aluminates [3, 4].

After heat treating the material was then cooled and crushed in a ring grinder. The ring grinder was cleaned prior to use with calcium aluminate powder of the phase to be crushed to reduce contamination. The materials were then mechanically screened to produce a fine powder with a particle size less than 38µm. The -38µm calcium aluminate powder was pressed again at 4 mass% moisture and fired for 24 hours at 1400°C. The calcium aluminates were then allowed to cool in furnace after which they were crushed and screened again to produce a fine powder with a particle size less than 38µm.

A sample of each calcium aluminate powder produced was tested for homogeneity using XRD. The XRD patterns for each of the synthesised calcium aluminates are presented in

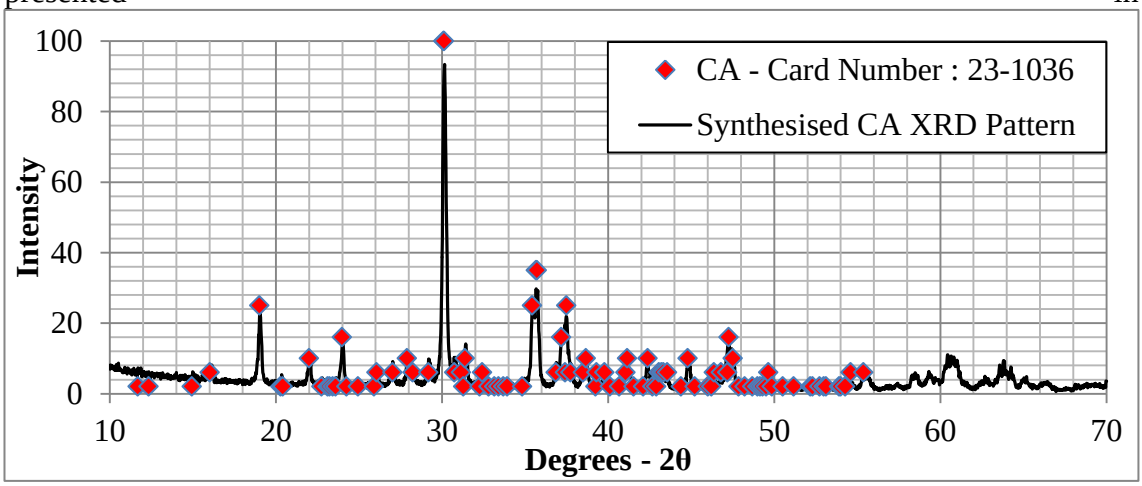

Figure 3.12 to Figure 3.14. For all the calcium aluminates synthesised the material produced was of the single phase desired with very low impurity content.

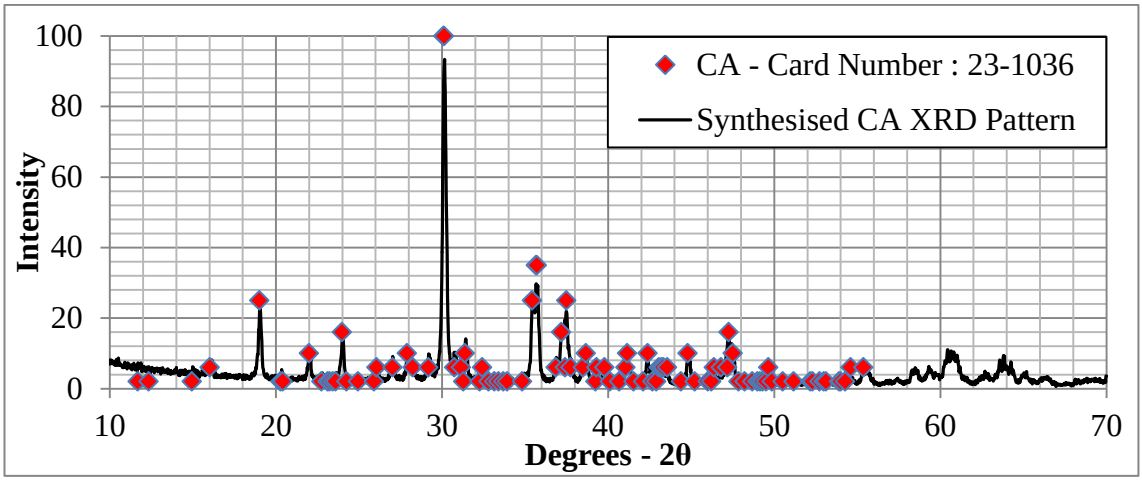

Figure 3.12: XRD pattern for the synthesised CA ($CaAl_2O_4$), card number 23-1036

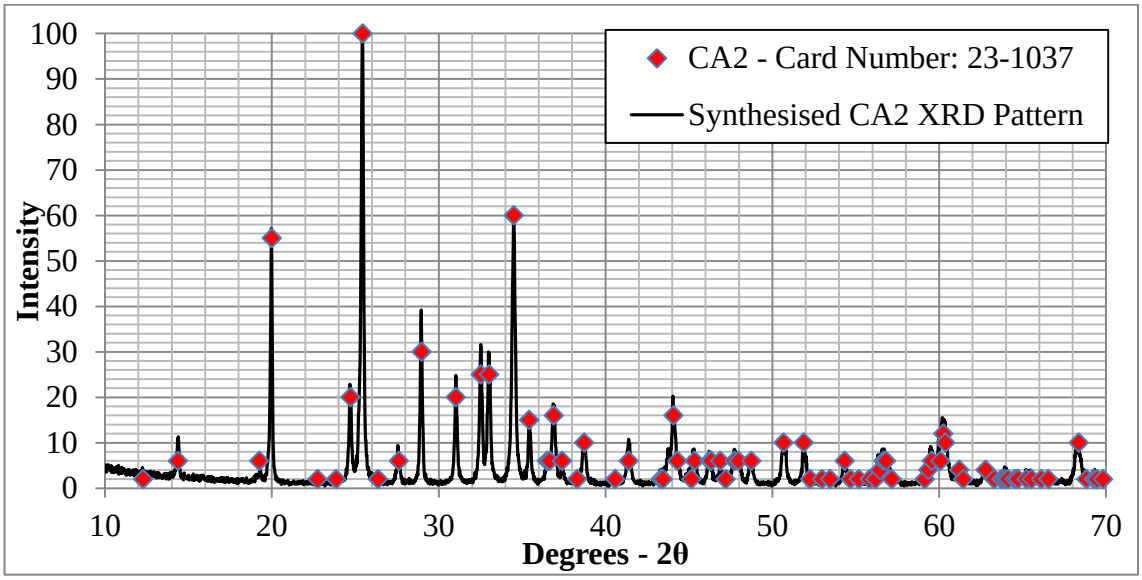

Figure 3.13: XRD pattern for the synthesised CA2 ($CaAl_4O_7$), card number 23-1037

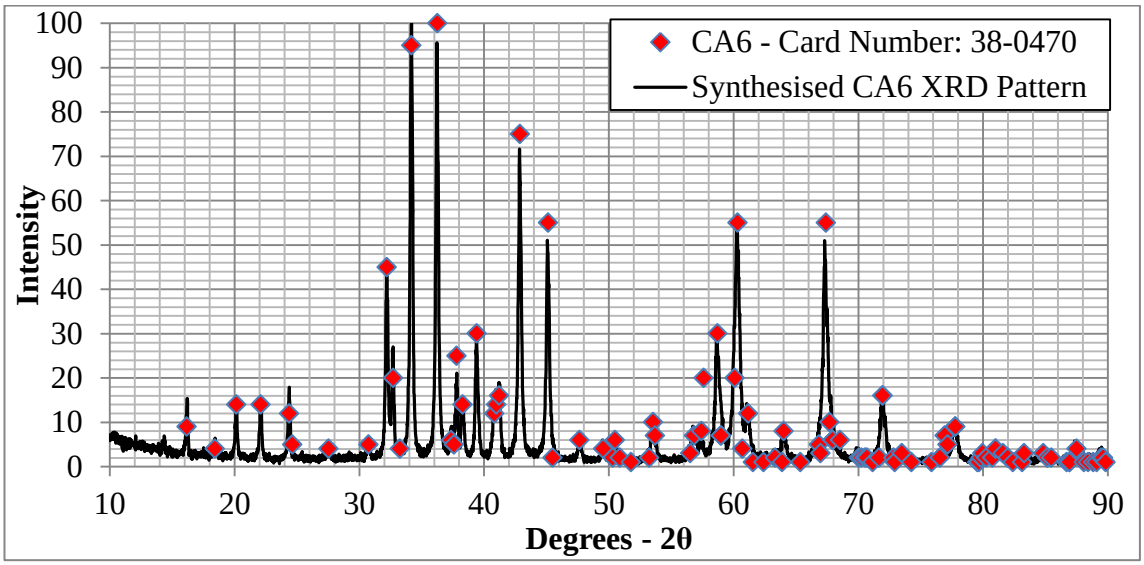

Figure 3.14: XRD pattern for the synthesised CA6 ($CaAl_{12}O_{19}$), card number 38-0470

3.4.2. Preparation of Calcium Aluminate Reaction Couple Disks

The calcium aluminate disks were produced from the synthesised CA, CA2 and CA6 powders with a moisture level of 4 mass%. The required powder was pressed in a 25mm diameter circular steel die at a pressure of 650kN for 30 seconds. A muffle furnace was used to fire the CA2 and CA6 discs at a furnace temperature of 1625°C for 4 hours. The CA discs were fired at 1550°C for 4 hours in a high temperature vertical tube furnace for more accurate temperature control due to concerns of melting. After firing the calcium aluminate disks were ground and polished to 1µm using the Struers Rotopol rotary polisher. The calcium aluminate discs were glued directly onto the sample holder (see Figure 3.15).

Figure 3.15: CA6 disks (23.9mm diameter) attached to sample holder

The disks were made planar using the grinding and polishing schedule outlined in Table 3.11 to remove a crosshatch pattern marked on the surface with a 4B pencil. Between each of the grinding and polishing steps the disks were cleaned with cotton wool soaked in detergent, rinsed with deionised water and dried using ethanol and a warm air dryer.

Table 3.11: Fine grinding and polishing schedule for the calcium aluminate disks

Step	**FG1**	**FG2**	**DP1**	**DP2**	**DP3**
Surface	Diadisc	DP-Pan	DP-Pan	DP-Dur	DP-Dur
Abrasive	Diamond	DP-suspension	DP-suspension	DP-suspension	DP-suspension
Grain Size	40µm	15µm	6µm	3µm	1µm
Lubricant	Distilled	Struers	Struers	Struers	Struers

	Water	Green	Green	Green	Green
RPM	150	150	150	150	150
Force (N)	100	250	250	200	200
Time (min)	Until Planar	6	5	5	5

After polishing the disks were separated from the sample holder by dissolving the glue in acetone. Once detached the disks were heated to 1100°C in air for 2.5 hours in a muffle furnace to "burn off" residual diamond particles or hydrocarbons entrapped in the surface pores of the calcium aluminate disk. The disks were allowed to cool in furnace and then stored in a desiccator until required.

3.5. Measurement of the Reaction Couple Interfacial Surface Roughness

3.5.1. Contact Atomic Force Microscopy

Contact atomic force microscopy (AFM) produces a roughness profile by measuring the deflection of a cantilever tip moving across the sample surface as shown in Figure 3.16. These profiles can be compiled to produce a three dimensional height profile over the scanned area.

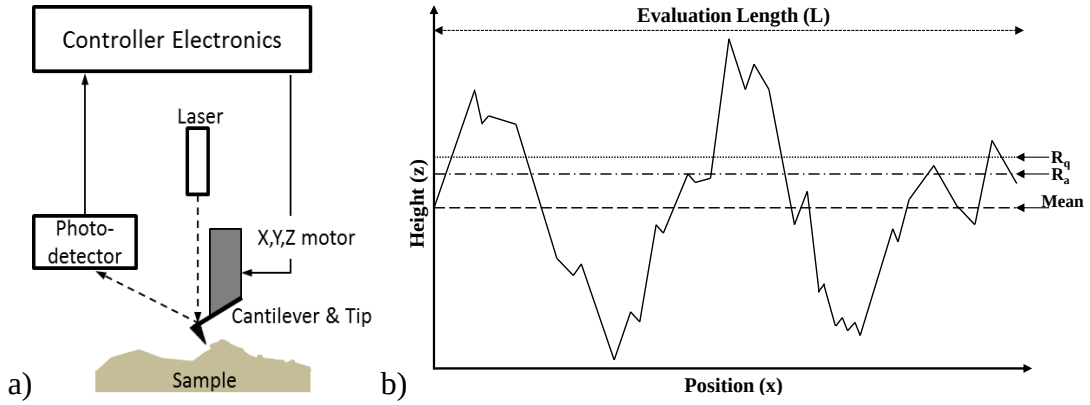

Figure 3.16: AFM schematic and roughness profile. Adapted from [67, 68].

There are two methods of using the raw profile data to calculate an average roughness parameter for the area of interest. The first of these methods is the root mean square (RMS) roughness parameter (R_q) which is calculated using equation (3-3)

$$R_q = \sqrt{\frac{1}{L}\int_0^L Z^2(x)dx} \qquad \textbf{(3-3)}\ [68]$$

Where:

L = evaluation Length

Z = height

x = distance along measurement

The second of these methods is the arithmetic mean roughness parameter (R_a) which is calculated using equation (3-4)

$$R_a = \frac{1}{L}\int_0^L |Z^2(x)|dx \qquad \textbf{(3-4)}\ [68]$$

3.5.2. Roughness Analysis using the Atomic Force Microscope

Measurements of surface roughness were made using contact AFM for each refractory and calcium aluminate after polishing. The measurements and micrographs were taken over a 15μm square area on the polished surface of each material as shown in Figure 3.17. The regions of the scanned area containing pores (darker regions of AFM micrographs) were excluded from the analysis to avoid skewing the results for the materials with higher degrees of porosity.

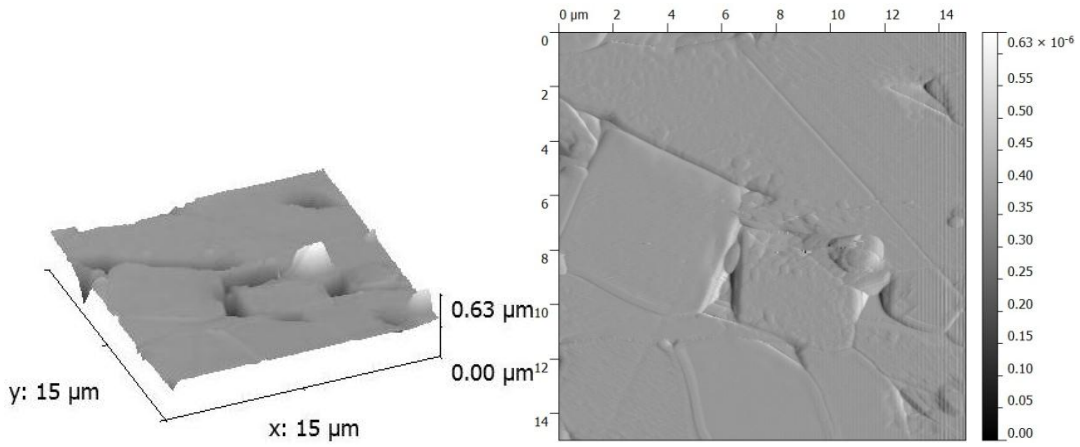

Figure 3.17: AFM micrographs of the polished Aluminosilicate refractory surface. The darker shaded regions show pores in the refractory. The x-y axes are 15μm and the z axis is 0.63μm.

The root mean square (R_q) and arithmetic mean (R_a) roughness parameters were obtained for each 15μm square area analysed. The average and standard deviation of

these parameters were calculated for each material and are given in Table 3.12. All the roughness data and atomic force micrographs can be found in Appendix I.

Table 3.12: Atomic Force Microscopy Average Roughness Measurements

	Root Mean Square Roughness R_q (µm)		**Arithmetic Mean Roughness R_a (µm)**	
Material	**Mean**	**Standard Deviation**	**Mean**	**Standard Deviation**
Carbon Matrix	0.2628	11.2%	0.213	12.6%
Alumina grains	0.0547	27.2%	0.0423	31.2%
Aluminosilicate	0.0419	41.5%	0.0273	60.8%
CA	0.0489	13.5%	0.0359	14.8%
CA2	0.0341	12.3%	0.0207	19.8%
CA6	0.7940	13.7%	0.6308	13.6%

Polishing was carried out to achieve a standard surface to enable direct comparison of the various reaction couples. AFM analysis of the surface roughness of each material may assist in the analysis of the reaction kinetics. It can be seen from Table 3.12 that the roughness for the materials is less than 1µm which confirms the desired polish was achieved. However there is significant variation in roughness of each material due to different properties and porosity of each material tested.

The CA, CA2, Aluminosilicate refractory and alumina grains of the Alumina-Carbon refractory were all found to have roughness measurements in the same order of magnitude. The Alumina-Carbon refractory matrix and CA6 were found have roughness measurements significantly higher than the other materials measured.

The high roughness measured for the Alumina-Carbon refractory matrix is the result of the polishing schedule used preferentially polishing the harder alumina grains while excessive amounts of the soft carbonaceous matrix material was removed result in a high roughness in the matrix regions or the refractory. Since the main reactions of interest are likely to occur with the alumina grains, a low roughness of the alumina grains is likely of higher importance to this study.

The polished CA6 was also found to have a much higher roughness than the other materials. The higher porosity of the CA6 disc (discussed in Section 3.7) and the

faceted surface produced by the multi-granular structure shown in Figure 3.18 has resulted in the high roughness on the polished surface of this disc.

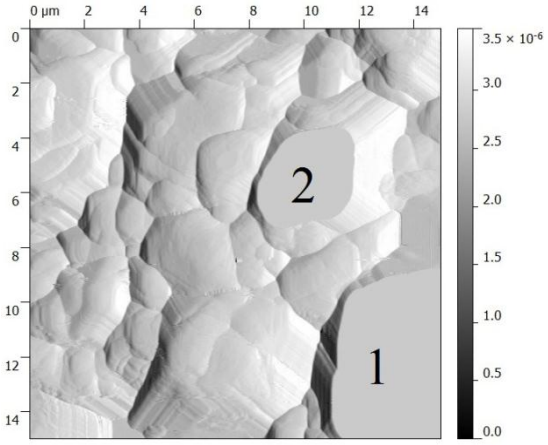

Figure 3.18: Contact AFM of the polished CA6 surface. Polishing has produced the facets labelled 1 and 2.

3.5.3. Calibration of the Atomic Force Microscope

The atomic force microscope (AFM) was calibrated prior to conducting the roughness analysis. The AFM was calibrated by scanning a 10µm x 10µm pitch grating with 180nm deep pits (provided with the AFM) and completing the following three steps:

- Check for consistent spacing measurements between pits on the largest scan size.
- Check the dimensions in the X & Y directions at scan sizes of 440V and 100V fall within 2% of the actual value (10 + 0.2µm).
- Establish the depth of the pits in the grating measurements are 180mn ± 1nm.
- Enter any corrections required into the microscope software.

The AFM calibration method used is detailed further in "Scanning probe microscopy training notebook" by Thornton et al [67].

3.6. Characterisation of Heat Treated Reaction Couple Materials

To assess the effect of temperature on the different reaction couple materials (Aluminosilicate, Alumina-Carbon, CA, CA2 and CA6) individual samples were heated in an argon atmosphere to a sample temperature of 1450°C for 3 hours and cooled in furnace using the experimental setup shown in Figure 3.1. The mass change of each material during heat treatment was calculated using Equation 3-1. No significant mass loss occurred in the calcium aluminates or Aluminosilicate refractory as the measured mass loss (Table 3.13) was less than the measurement error of the balance used.

Table 3.13: Heat Treated Refractory and Calcium Aluminate mass loss data

Material	Mass before Heat Treatment	Mass after Heat Treatment	Δ Mass%
Alumina-Carbon	18.661g	17.980g	3.65 mass%
Aluminosilicate	17.097g	17.095g	0.01 mass%
CA	2.582	2.567	0.58 mass%
CA2	2.325g	2.322g	0.13 mass%
CA6	3.790g	3.792g	-0.05 mass%

Optical and scanning electron microscopy was conducted to characterise the structure and chemical composition of each material after heat treatment. No chemical changes, reaction products or structural changes were observed in any of the materials. The microscopy and EDS results are further detailed in the study by Drain [65].

3.6.1. Heat Treated Alumina-Carbon Refractory Changes

The Alumina-Carbon refractory was the only material observed to have lost mass as shown in Table 3.17. A comparison of the as-received micrographs (Figure 3.9 and Figure 3.10) and the heat treated micrograph (Figure 3.19) found no reaction products formed or structural changes occurred during heat treatment of the Alumina-Carbon refractory. EDS spot analysis (Table 3.14) found the composition of the alumina and graphite grains were comparable to the pre-heat treated compositions (Table 3.7).

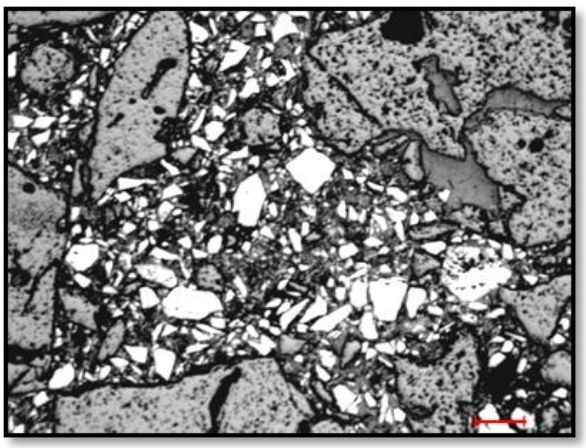

Figure 3.19: Optical micrographs of the heat treated Alumina-Carbon refractory. Scale bar is 200µm.

Table 3.14: Heat Treated Alumina Carbon Refractory EDS spot analysis results

EDS Position		C	Al_2O_3	Identified Phase
1	Mass%	19.96	80.14	Alumina Grain
	Mol%	67.91	80.04	
2	Mass%	100		Graphite
	Mol%	100		

Elemental mapping (Figure 3.20) of the heat treated refractory found that the distribution of aluminium and carbon was comparable to the pre-heat treatment refractory. However silicon depletion of the matrix phase near the surface was identified, this may contribute to the mass loss observed in this material.

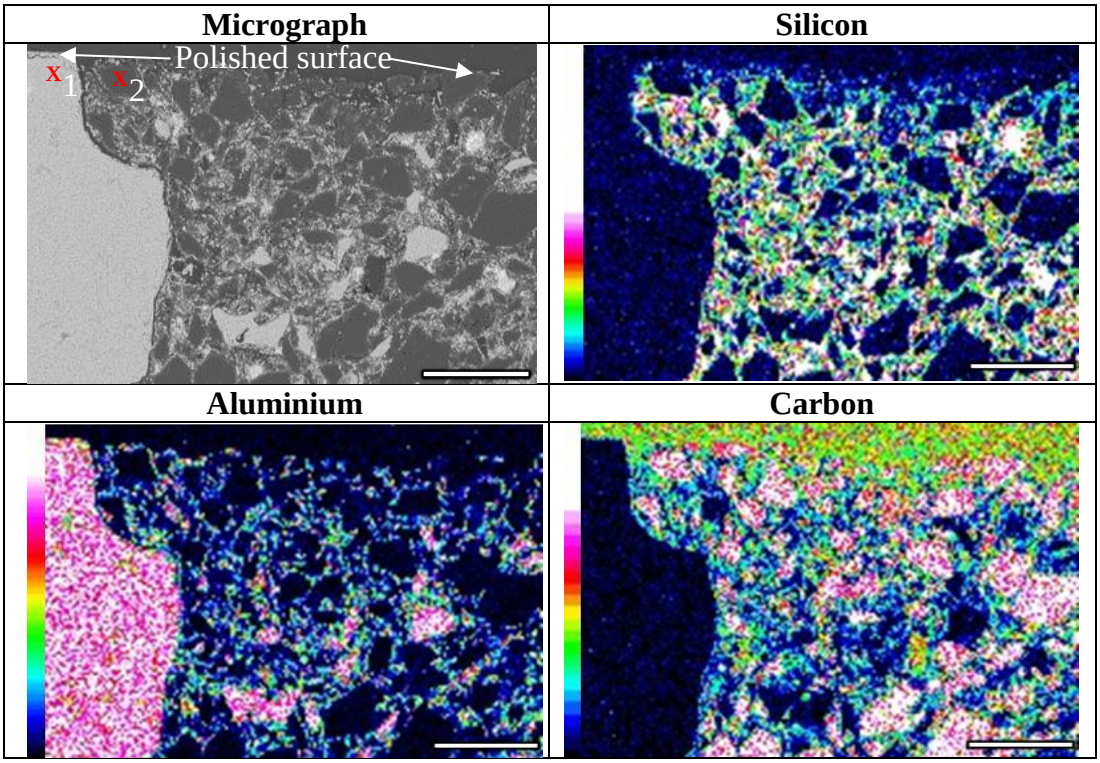

Figure 3.20: SEM micrograph and EDS elemental X-ray maps showing element distributions within the heat treated Alumina-Carbon refractory. EDS spot analysis locations are marked and identified using numbers. The scale bar is 200µm.

Refractory literature reviewed in Section 2.3.3 indicates that some oxides such as SiO_2 used in refractories can become unstable at high temperatures in the presence of carbon. The reactions used to describe the silica depletion of the coke ash can also be used to describe SiO_2 reduction reactions in the Alumina-Carbon refractory (Equations 2-4, 2-6 and 2-7), reproduced below [13, 14].

$$SiO_{2(s)} + C_{(s)} = SiO_{(g)} + CO_{(g)}$$

$$2SiO_{2(s)} + SiC_{(s)} = 3SiO_{(g)} + CO_{(g)}$$

$$SiC_{(s)} + CO_{(g)} = SiO_{(g)} + 2C_{(graphite)}$$

The proximity of the silicon depletion to the refractory surface where any $SiO_{(g)}$ formed is able to diffuse out of the refractory suggests reactions (2-4), (2-6) and (2-7) are likely mechanisms of the silicon depletion and mass loss observed.

3.7. Measurement of Bulk Density and Apparent Porosity

The bulk density and apparent porosity of each refractory and calcium aluminate were determined using the methods detailed in AS1774.5-2001: Refractories and refractory materials – Physical test methods - Method 5: The determination of density, porosity and water absorption (Appendix II). The bulk density and apparent porosity is determined by measuring the dry mass, the mass of the sample saturated with distilled water and the mass of the sample suspended in distilled water and using Equations 3-5 and 3-6. Six samples of each material used in this study were used to determine the average bulk density and porosity of each material as shown in Table 3.17.

$$D_B = \frac{m_D}{m_S - m_i} \times D_i \qquad \textbf{(3-5)}$$

$$P_a = \frac{m_S - m_D}{m_S - m_i} \times 100 \qquad \textbf{(3-6)}$$

Where:

D_B= Bulk Density

m_D= mass of dried sample

m_S= mass of sample vacuum impregnated with distilled water and weighed in air

m_i= mass of sample vacuum impregnated with distilled water and weighed while immersed in distilled water

D_i= density of distilled water at the test temperature (standard lab conditions)

P_a= Apparent Porosity

Table 3.15: Average density and porosity of refractories and calcium aluminates.

Materials	Bulk Density (g/cm^3)		Apparent Porosity (%)	
	Average	Standard Deviation	Average	Standard Deviation
CA ($CaO{\cdot}Al_2O_3$)	2.73	3.66%	2.23	26.00%
CA2 ($CaO{\cdot}2Al_2O_3$)	2.82	0.71%	0.38	39.47%
CA6 ($CaO{\cdot}6\ Al_2O_3$)	2.20	8.64%	29.51	1.63%
Aluminosilicate Refractory	2.57	0.39%	13.74	3.20%
Alumina-Carbon Refractory	2.72	0.74%	10.60	4.15%

*Average and standard deviation of six samples for each material

3.8. Microscopy Preparation of Reaction Couples

After the experimental heating schedule was completed the reaction couples were cold mounted and vacuum impregnated using epofix resin and hardener mixed in a ratio of 25:3. Care was taken to avoid disturbing the contact between the refractory and calcium aluminates during the mounting process. After 24 hours the mounted samples were removed from the moulds and cleaned with detergent and ethanol. The mounted samples were then cut using the Struers Accutom 50 cutting machine with a diamond blade such that the interface between the refractory and calcium aluminate was clearly visible as shown in Figure 3.21 b).

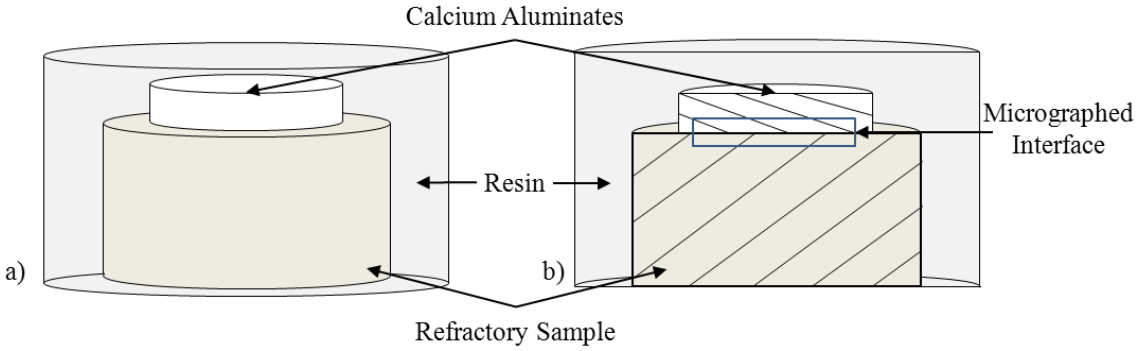

Figure 3.21: Reaction couple a) Cold mounted b) Cold mounted and cross sectioned

The samples were then cold mounted and vacuum impregnated in epofix resin with the surface of interest (cross sectional surface) facing the bottom of the mould. The samples were allowed to set for 24 hours before being removed from the moulds. Once mounted the experimental samples were prepared as per the grinding and polishing procedure outlined in Table 3.16.

Once polished the samples were ultrasonically cleaned in ethanol for 10 minutes and dried. Silver paint was used to create conductive strips down the side of each sample prior to carbon coating for use in SEM.

Table 3.16: Automatic grinding and polishing schedule for mounted refractory samples

Step	FG1	FG2	FG3	DP1
Surface	Diadisc	MD-Allegro	MD-Largo	MD-Dac
Abrasive	Diamond	DP-suspension	DP-suspension	DP-suspension
Grain Size	40µm	9µm (only)	3µm (A/S) or 9µm (A/C)	3µm (both)
Lubricant	Water	Struers Green (water based)	Struers Green (water based)	Struers Green (water based)
RPM	150	150	150	150
Force (N)	40	30	30	30
Time (min)	Until Planar	5	10	8 (A/S) or 5 (A/C)

EDS analysis was conducted using the JEOL JEM LA 6490 SEM to determine any change in composition of the calcium aluminate or the refractory was determined using elemental mapping, spot analysis and area analysis of the different phases observed. Line analysis across the interface between the calcium aluminate and refractory was also conducted.

3.9. Measurement of Reaction Layer

The SEM micrographs and ImageJ software were used to measure the thickness of the reaction layer observed in many of the reaction couples. This was done by opening the micrograph file with ImageJ and using the straight line selection to draw a line across the reaction layer approximately perpendicular to the interface as shown in Figure 3.22. The length of the line drawn is recorded in the results table by selecting ‘Measure’ in the ‘Analyze’ menu or by using the shortcut ‘Ctrl+M’.

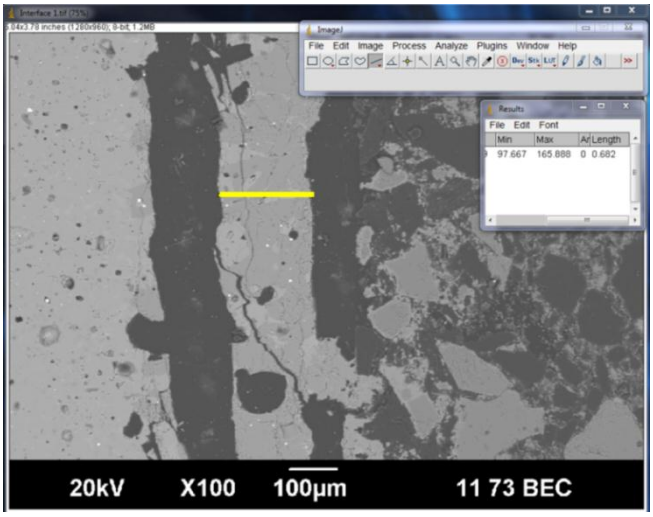

Figure 3.22: ImageJ measurement of reaction layer thickness (yellow line).

Thirty thickness measurements were recorded for each micrograph in addition to the length of the scale bar. The ImageJ length measurements were converted to micrometres using the measurement taken of the 100µm scale bar used in the SEM micrographs. This was done for three different micrographs of each reaction couple interface. This produces a large dataset of 90 reaction layer thickness measurements for each reaction couple. The average and standard deviation of each data set were then calculated and are reported in section 4.13.

3.9.1. Calibration of the Scanning Electron Microscope Scale Bar

The optical microscope scale was calibrated using a 10µm increment graticule in both the x and y directions as shown in Figure 3.23. There was found to be a +5% error in the 200µm optical microscope scale bar which was measured to 190µm using the graticule in both the horizontal and vertical directions.

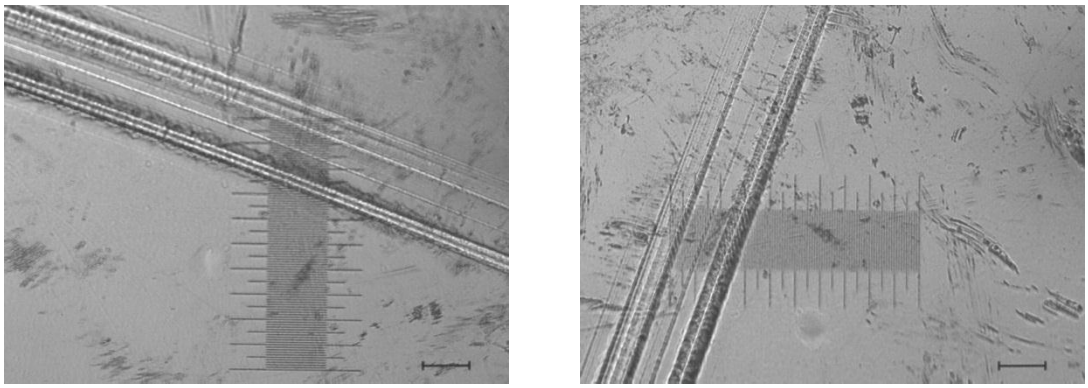

Figure 3.23: 10µm increment graticule used to calibrate Optical Microscope in the X & Y directions. Scale bar = 200µm.

The SEM scale bar was calibrated by measuring the distance between two pores easily identified in both the SEM and optical micrographs (identified by the red line in Figure 3.25). Size of a phase in a reaction couple sample with a calibrated optical microscope and comparing the size measured with the same dimension measured using the SEM as shown in Figure 3.24.

a) 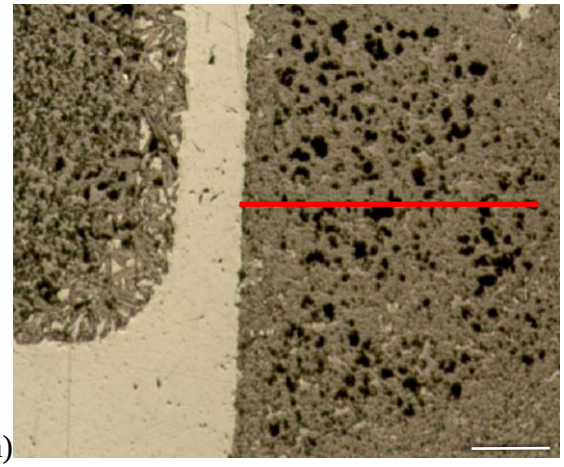 b) 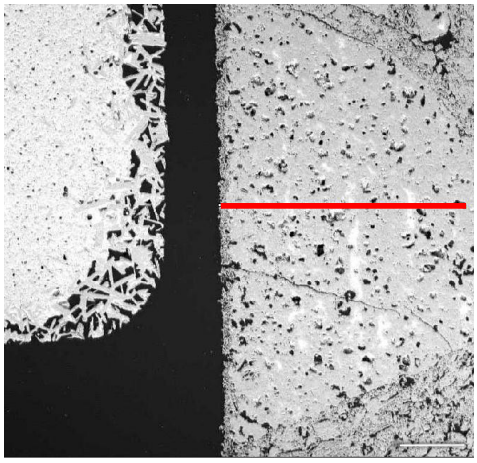

Figure 3.24: a) optical micrograph with phase measured to be 724µm wide (scale bar = 190µm) b) SEM micrograph with measured width of phase of 747µm (scale bar = 200µm)

The alumina grain in Figure 3.24 a) was found to be 724µm wide using the calibrated optical micrograph scale bar. The width of the same alumina grain was then measured to be 747µm using the SEM micrograph shown in Figure 3.24 b). The SEM scale bar was calculated to be 194µm as shown:

$$\frac{Calibrated\ Optical\ Measurement}{SEM\ Measurement} \times scale\ bar\ length = \ actual\ scale \qquad \textbf{(3-7)}$$

$$\frac{724\mu m}{747\mu m} \times 200\mu m = \ 194\mu m$$

Therefore the SEM scale bar has a measurements must be scaled up by 3% for an accurate measurement.

3.9.2. Reaction Layer Measurement Error

The measurement error was found by using the ImageJ software to measure the length of the scale bar on SEM micrographs 100 times. It was found that the measurements ranged from 92.9% to 105.0% of the average with a standard deviation of 2.2%. Using a six sigma approach to cover 99.99% of measurements than measurement error is ±6.6% (i.e. three standard deviations to each side of the mean). This a measure of the error associated with visually selecting the start and end points on a micrograph.

3.9.3. Identification of the Original Reaction Couple Interface

During initial testing it became clear that the location of the original refractory - calcium aluminate interface would need to be established for some of the longer time experiments. The original interface location was marked by placing a platinum wire in between the refractory and calcium aluminates at the interface of the reaction couple. The wire was place in a trench scored into the surface of both materials as shown in Figure 3.25.

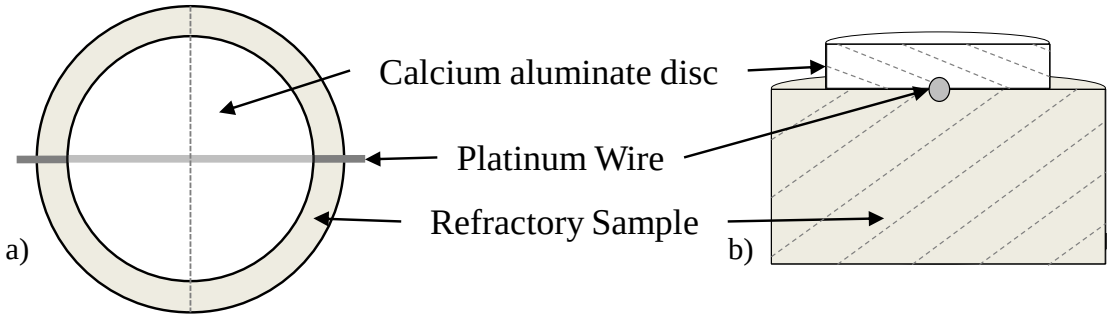

Figure 3.25: Schematic of platinum wire positioned between the refractory and calcium aluminate discs. a) Plan view b) Cross section

Identification of the original interface using platinum wire was only carried out on the CA and CA2 reaction couples tested for 18 hours at 1500°C.

4. Results

In this chapter the results of the experimental and thermodynamic modelling work are presented in four parts:

- *Summary of results* – provides an overview of all experimental results
- *Temperature effect on reaction couple kinetics* – provides measurements and micrographs detailing the influence of increasing reaction temperatures on mass change, reaction layer thickness and reaction phases formed.
- *Time effect on reaction couple kinetics* – provides measurements and micrographs detailing the influence of increasing reaction times on mass change, reaction layer thickness and reaction phases formed.
- *Phase Stability Diagrams* – produced using MTDATA software

All phases identified using EDS analysis in Table 4.1 to Table 4.7 are based on the assumption that for the given temperature and composition the phase can be predicted using the phase diagram in Figure 2.12.

4.1. Summary of Results

- A reaction layer was observed at the interface between the calcium aluminates (CA and CA2) and refractories (Alumina - Carbon and Aluminosilicate)
- The reaction layer thickness was found to increase with time, temperature and the CaO content of the calcium aluminates.
- The variation in thickness measurements increased with both time and temperature. This is due to the growth of a needle like lath phase and the increased spalling of material at the interface.
- Under most of the conditions tested, the Alumina - Carbon refractory produced thicker reaction layers compared to the Aluminosilicate refractory. However it was observed that the calcium aluminates only reacted with the alumina grains in the refractory and not the carbonaceous matrix.
- It was observed that the formation of a reaction layer caused cracking and spalling of material at the reaction couple interface. The spalled material consisted of newly formed phases at the interface as well as some unreacted material sheared from the calcium aluminate and refractory.

- The CA6 composition was observed to have increased porosity at the interface. The high porosity region was found to have lower CaO composition then the bulk CA6.
- The Alumina - Carbon refractory was found to react at lower temperatures with the calcium aluminates than the Aluminosilicate refractory.
- Calcium depletion of the CA and CA2 near the refractory interface was observed to increase with both time and temperature. Calcium enrichment of the refractories near the interface was observed to increase with time and temperature.
- Silicon enrichment of the reaction layer was observed in both the Aluminosilicate refractory and alumina-carbon refractory. Silicon enrichment was found to increase with time and temperature.
- The Aluminosilicate refractory was observed to become very porous near the interface at the longer reaction times. EDS analysis of the remaining material found a change in the composition corresponding to a change from mullite material to corundum. This change of phase and lost material from the refractory suggests a liquid phase high in silica (e.g. anorthite or gehlenite) may have formed during testing leaving behind the porous structure observed.

4.2. Temperature Effect on Reaction Couple Kinetics

4.2.1. Mass Change Measurements

The temperature series reaction couples with a measured mass loss (calculated using Equation 3-1) are given in Figure 4.1. Only the Alumina - Carbon refractory reaction couples experienced a mass greater than the 0.5% error associated with measurement scales. All mass change results are given in Appendix III.

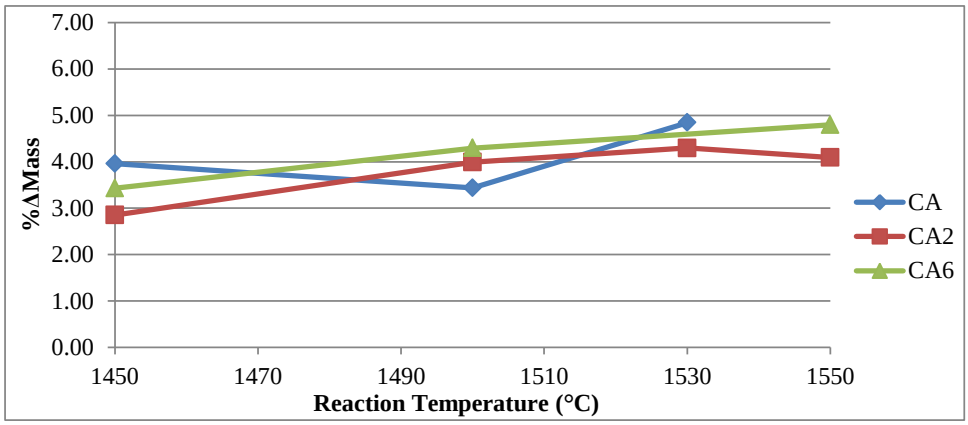

Figure 4.1: Mass loss results for the Alumina - Carbon refractory reaction couples from 1450°C to 1550°C.

4.2.2. SEM Micrographs

Three SEM micrographs of the interface were produced for each reaction couple in the temperature series. All SEM micrographs produced are given in Appendix V. Figure 4.2 and Figure 4.3 show a micrograph selected from each reaction couple in the temperature series.

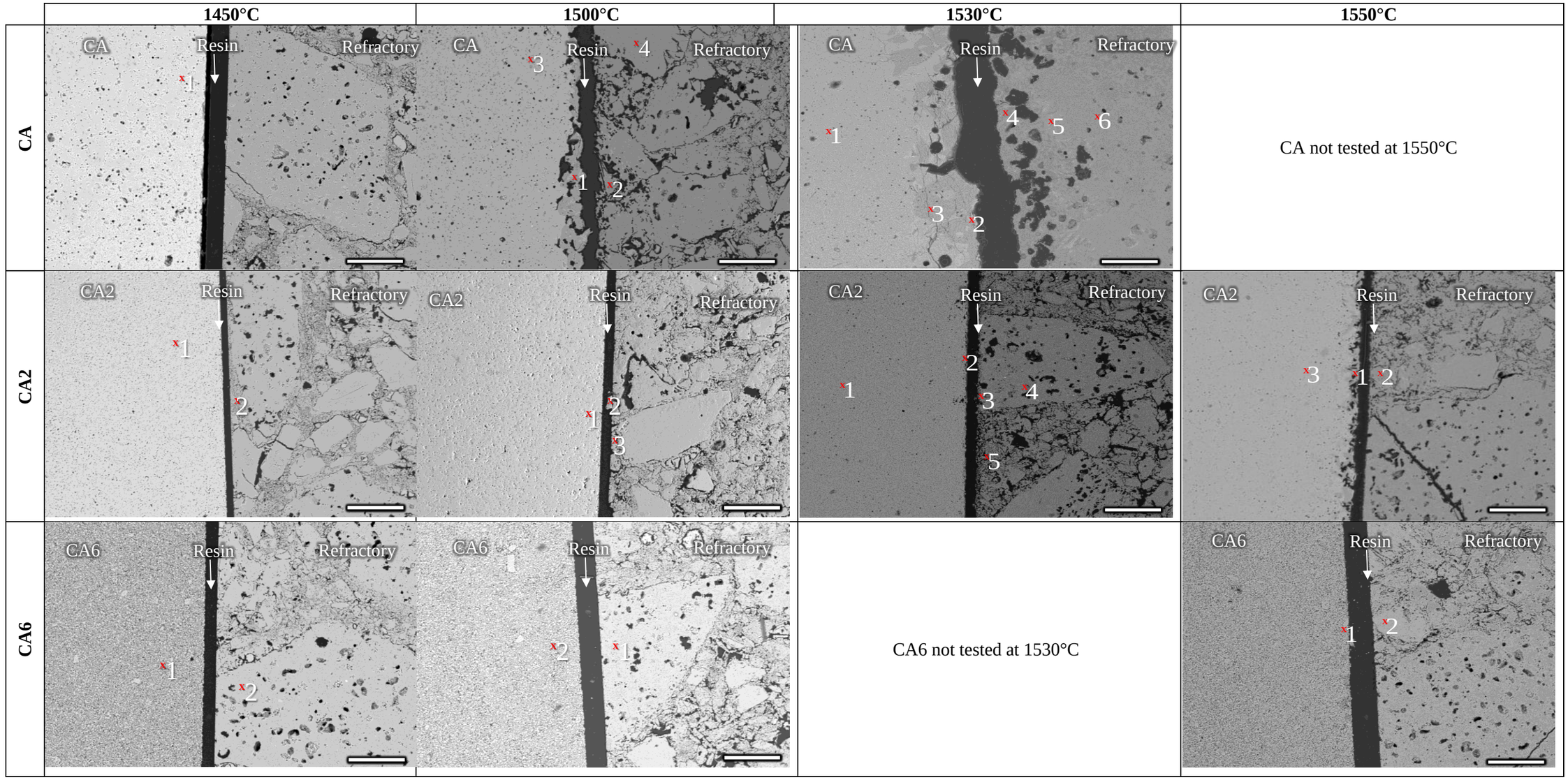

Figure 4.2: SEM micrographs of the interface between the Aluminosilicate Refractory and calcium aluminates after heating to various reaction temperatures. The numbers on each micrograph represent spot analysis points given in Table 4.1. Reaction time = 4 hours. Scale bar = 200µm

Table 4.1: Aluminosilicate refractory temperature series reaction couples EDS spot analysis results, at 4 hours reaction time.

	Units	1450°C					1500°C					1530°C					1550°C				
		No.	Al_2O_3	CaO	SiO_2	Phase	No.	Al2O3	CaO	SiO2	Phase	No.	Al2O3	CaO	SiO2	Phase	No.	Al2O3	CaO	SiO2	Phase
CA	Mass%	1	64.6	35.4		CA	1	77.2	15.4	7.4	Hibonite	1	60.0	40.0		CA	CA not tested at 1550°C				
	Mol%		50.6	49.9				65.6	23.8	10.6			45.2	54.8							
	Mass%						2	63.3	4.6	32.1	Mullite	2	39.7	39.8	20.6	Gehlenite					
	Mol%							50.2	6.6	43.2			27.0	49.2	23.8						
	Mass%						3	64.5	35.5		CA	3	73.1	26.7	0.2	Hibonite					
	Mol%							49.9	50.0				59.9	0.3	39.8						
	Mass%						4	67.5	1.75	30.8	Mullite	4	99.7	0.0	0.3	Corundum					
	Mol%							54.9	2.6	42.5			99.5	0.1	0.4						
	Mass%											5	30.9	14.4	54.7	Gehlenite					
	Mol%												20.6	17.5	61.9						
	Mass%											6	64.7	6.0	29.3	Mullite					
	Mol%												51.7	8.7	39.6						
CA2	Mass%	1	78.8	21.2		CA2	1	77.9	22.12		CA2	1	80.6	19.41		CA2	1	91.6	8.4		CA6
	Mol%		67.1	32.9				65.9	34.06				69.6	30.45				85.8	14.3		
	Mass%	2	87.9		12.0	Corundum	2	100			Alumina Grain	2	80.6	19.41		CA2	2	75.2		24.8	Mullite
	Mol%		81.1		18.9			100					69.6	30.45				64.1		35.9	
	Mass%						3	67.0		32.9	Mullite	3	86.2		13.8	Corundum	3	78.0	22.0		CA2
	Mol%							54.6		45.4			78.7		21.3			66.1	33.9		
	Mass%											4	75.6		24.4	Mullite					
	Mol%												64.6		35.4						
	Mass%											5	74.9		25.2	Mullite					
	Mol%												63.7		36.3						
CA6	Mass%	1	90.7	9.3		CA6	1	76.7		23.3	Mullite Grain	CA6 not tested at 1530°C					1	90.4	9.6		CA6
	Mol%		84.3	15.7				66.0		34.0								83.8	16.2		
	Mass%	2	73.8		26.2	Mullite Grain	2	91.0	9.0		CA6						2	73.1		26.9	Mullite
	Mol%		62.4		37.6			84.8	15.2									61.6		38.4	

	1450°C	1500°C	1530°C	1550°C
CA	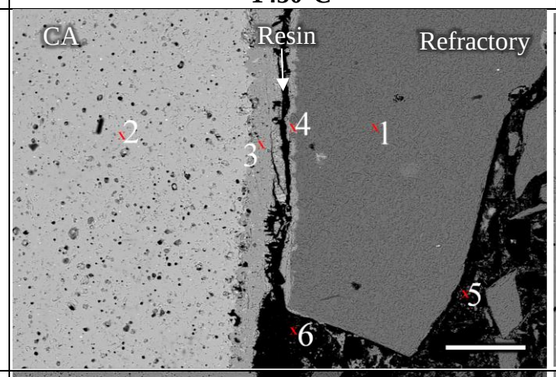	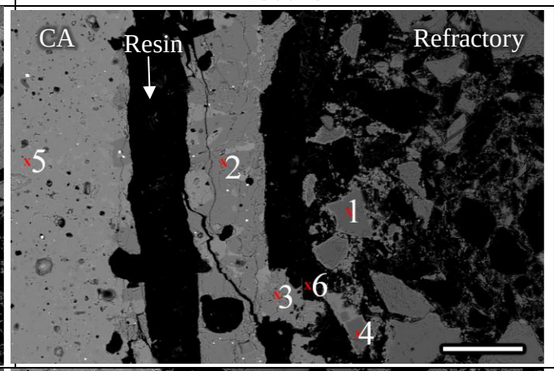	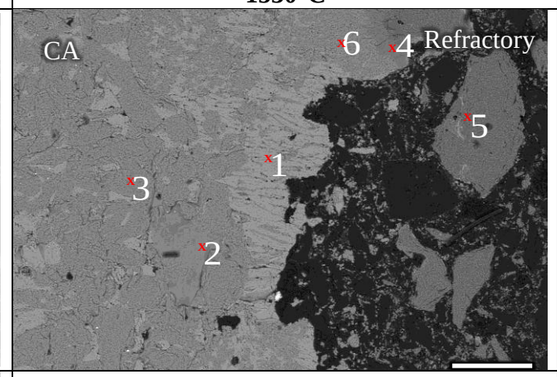	CA not tested at 1550°C
CA2	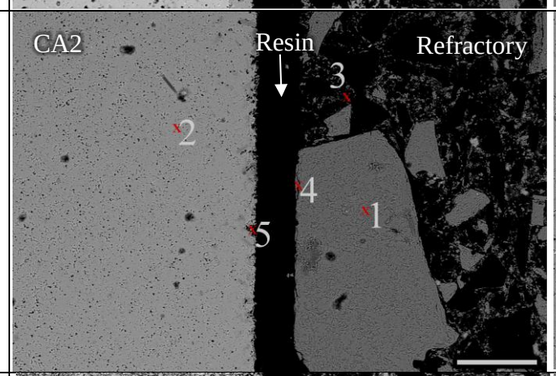	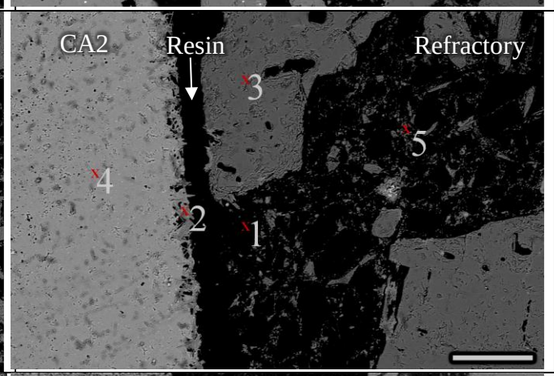	CA2 not tested at 1530°C	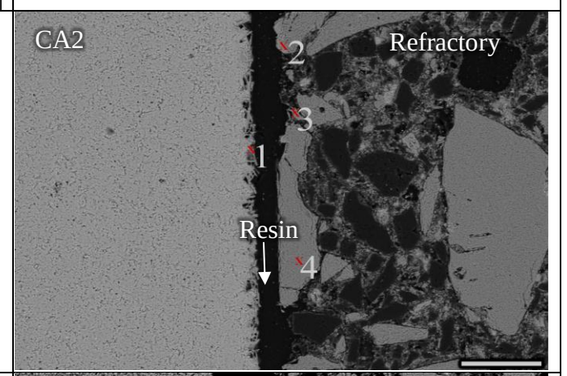
CA6	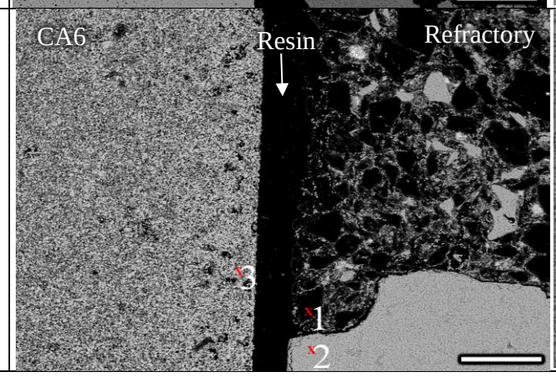	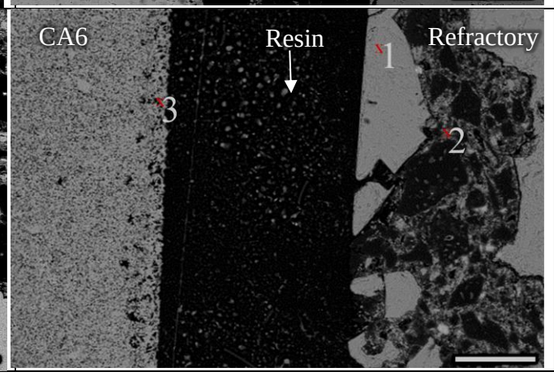	CA6 not tested at 1530°C	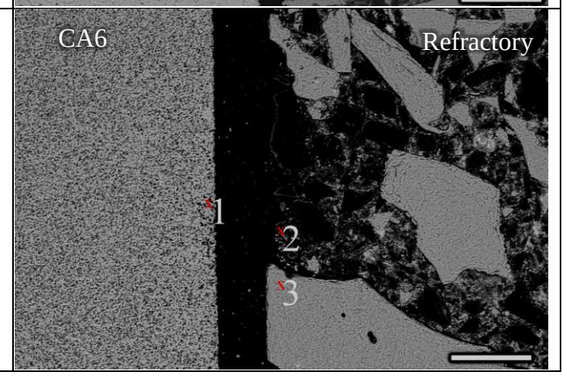

Figure 4.3: SEM micrographs of the interface between the Alumina - Carbon Refractory and calcium aluminates after heating to various reaction temperatures. The numbers on each micrograph represent spot analysis points given in Table 4.2. Reaction time = 4 hours. Scale bar = 200µm

Table 4.2: Alumina-Carbon refractory temperature series reaction couples EDS spot analysis results, at 4 hours reaction time.

	Units	1450°C						1500°C						1530°C						1550°C					
		No.	C	Al_2O_3	CaO	SiO_2	Phase	No.	C	Al_2O_3	CaO	SiO_2	Phase	No.	C	Al_2O_3	CaO	SiO_2	Phase	No.	C	Al_2O_3	CaO	SiO_2	Phase
CA	Mass%	1		100			Alumina grain	1		100			Alumina Grain	1		76.7	22.7	0.6	Hibonite	CA not tested at 1550°C					
	Mol%			100						100						64.4	34.7	0.9							
	Mass%	2		65.8	33.9	0.3	CA	2		79.1	20.9		CA2	2		35.5	42.5	22.0	Gehlenite						
	Mol%			39.3	60.2	0.4				67.6	32.4					23.7	51.5	24.8							
	Mass%	3		77.3	20.5	2.2	CA2	3		79.0	21.0		CA2	3		64.6	35.4		CA						
	Mol%			65.4	31.5	3.2				67.4	32.6					50.1	49.9								
	Mass%	4		79.0	21.0		CA2	4		100			Alumina Grain	4		76.1	21.8	2.2	Hibonite						
	Mol%			67.4	32.6					100						63.8	33.1	3.1							
	Mass%	5	34.9	17.6		47.5	Carbon matrix	5		65.3	34.7		CA	5		99.8	0.0	0.2	Corundum						
	Mol%		75.1	4.5		20.4				50.9	49.1					99.6	0.1	0.3							
	Mass%	6	91.9	1.4	2.854	3.8	Graphite	6		98.0		1.9	Anthracite												
	Mol%		98.4	0.2	0.652	0.8				99.6		0.4													
CA2	Mass%	1		100			Alumina Grain	1	98.1	0.8	1.0	0.2	Anthracite Grain	CA2 not tested at 1530°C						1		84.7	15.3		Hibonite
	Mol%			100					99.7	0.1	0.2	0.1										75.3	24.7		
	Mass%	2		79.0	21.0		CA2	2		89.7	8.7	1.6	corundum							2		92.1	7.9		corundum
	Mol%			67.35	32.7					82.9	14.6	2.5										86.5	13.5		
	Mass%	3	73.8	6.2	2.0	18.0	Anthracite Grain	3		100.0	0.0		Alumina grain							3		92.3	7.7		corundum
	Mol%		93.9	0.9	0.6	4.6				100.0	0.0											86.9	13.2		
	Mass%	4		100			Alumina Grain	4		78.7	21.3	0.1	CA2 / Hibonite							4		100			Alumina grain
	Mol%			100						67.0	32.9	0.1										100			
	Mass%	5		80.5	19.5		Hibonite	5	40.9	49.8	0.1	9.2	Carbon Matrix												
	Mol%			69.5	30.6				84.1	12.1	0.0	3.8													
CA6	Mass%	1	100				Graphite	1		100			Alumna Grain	CA6 not tested at 1530°C						1		93.0	7.0		CA6
	Mol%		100							100												87.9	12.1		
	Mass%	2		100			Alumina Grain	2	36.5	14.9	0.1	48.5	Carbon Matrix							2	98.0	2.0			Graphite
	Mol%			100					76.1	3.7	0.0	20.2									99.8	0.2			
	Mass%	3		91.6	8.4		CA6	3		91.7	8.3		CA6							3		100			Alumina Grain
	Mol%			85.7	14.3					85.9	14.1											100			

4.2.3. Reaction Layer Thickness Measurements

The average reaction layer thickness and standard deviation was determined using 90 thickness measurements from each of the reaction couples (Appendix IV). The thickness measurements were produced using three different SEM micrographs of the reaction couple interface (Section 4.2.2 and Appendix V). The average thickness $\pm$ 1 standard deviation for each reaction couple are given in Figure 4.4 and Figure 4.5.

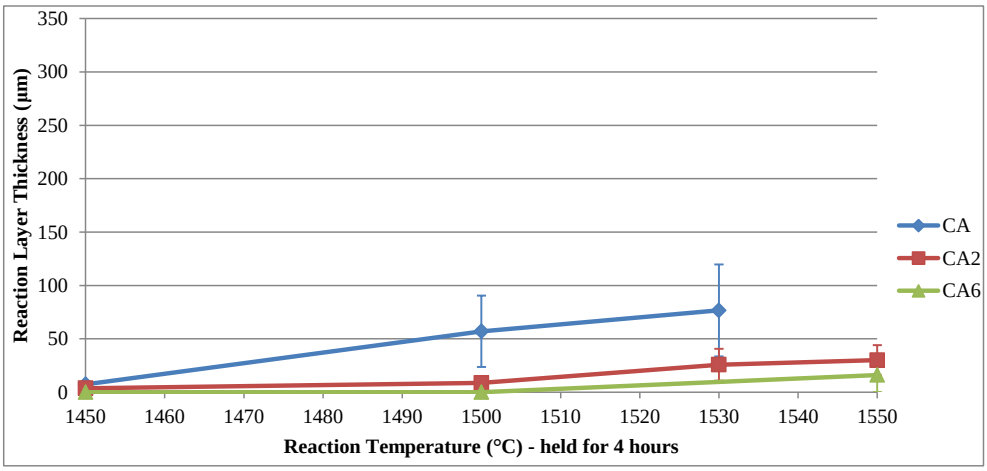

Figure 4.4: Reaction layer thickness by temperature for all the aluminosilicate refractory reaction couples.

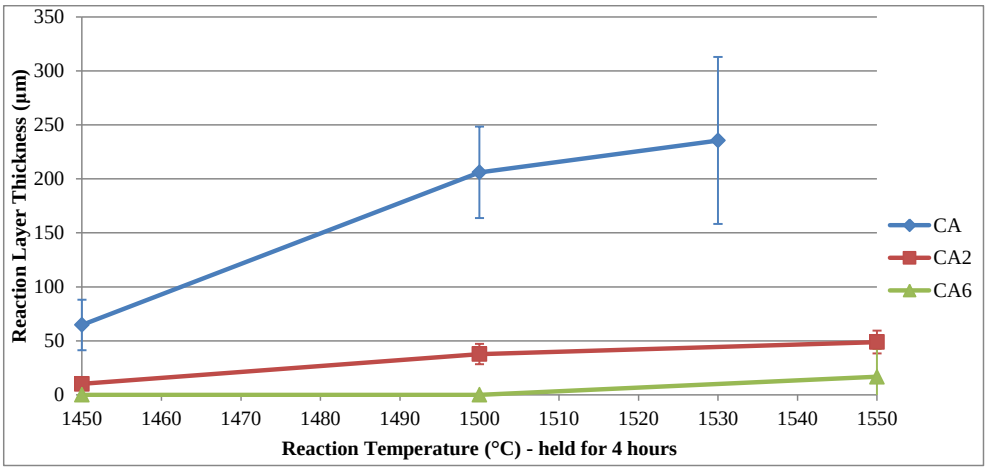

Figure 4.5: Reaction layer thickness by temperature for all the alumina-carbon refractory reaction couples.

It can be seen from Figure 4.4 and Figure 4.5 that the reaction layer thickness increased with reaction temperature and CaO content of the calcium aluminate. A comparison of the trends (Figures 4.4 and Figure 4.5) for each refractory show the Alumina - Carbon refractory reaction layer thickness was greater than the Aluminosilicate refractory under the same conditions.

Variation in the thickness measurements are due to difficulty in determining the start and finish position of the reaction layer as well as discontinuities and porosity in the reaction layer. The lath – needle like structure of the CA6 reaction layers formed also increased the variation of thickness measurement results.

4.2.4. Elemental Analysis of the Reaction Layer

Elemental X-ray mapping of a range of elements often found in refractory materials (Al, Ca, C, Cr, Fe, K, Mg, Mn, Na, O, P, Ti, Zn and Zr) was conducted at the interface in the reaction couples using the SEM. The elemental maps with measureable concentration profiles (aluminium, silicon and calcium) elemental maps are shown in Figure 4.6 to Figure 4.11. The elemental maps for Cr, Fe, Mg, Mn, Na, O, P, Ti, Zn and Zr were conducted however these have not been reported here due to the absence of any significant concentration profile across the interface.

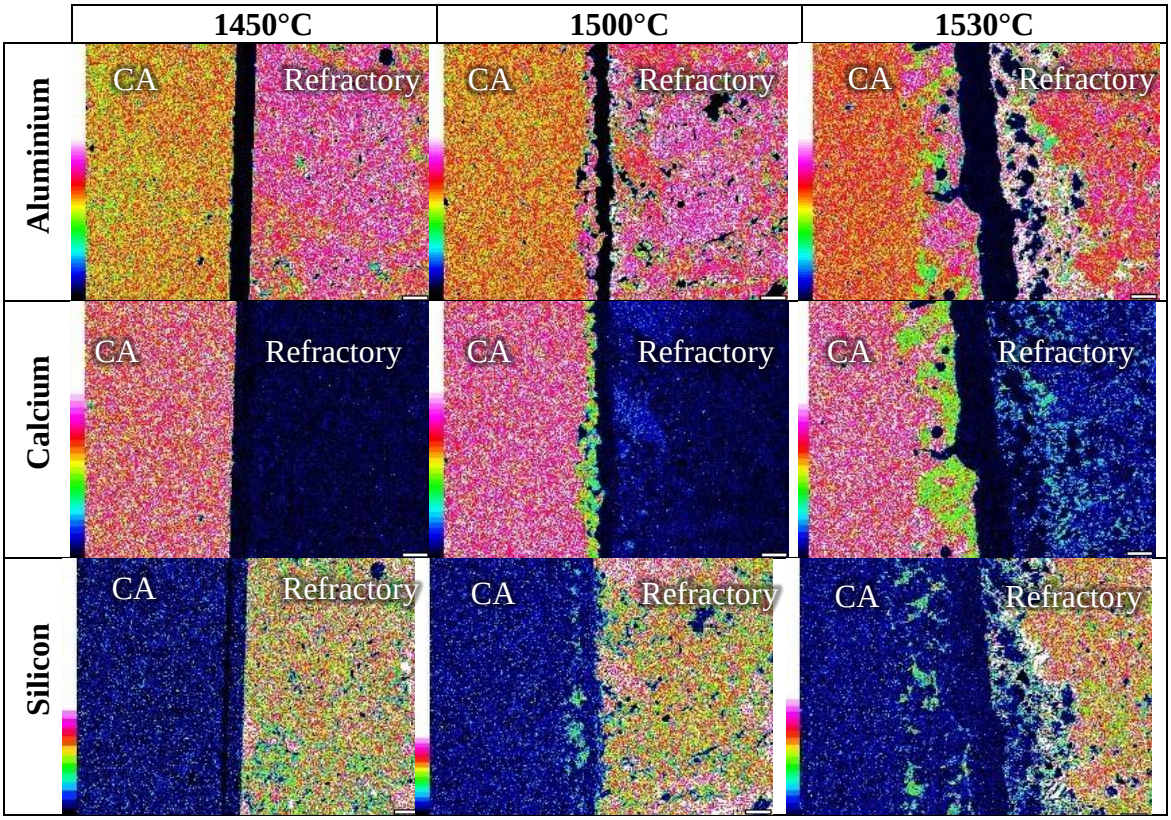

Figure 4.6: Elemental Mapping of the CA - Aluminosilicate interface. A colour concentration scale is provided on the left of each micrograph. Reaction time = 4 hours. Scale bar = 100µm

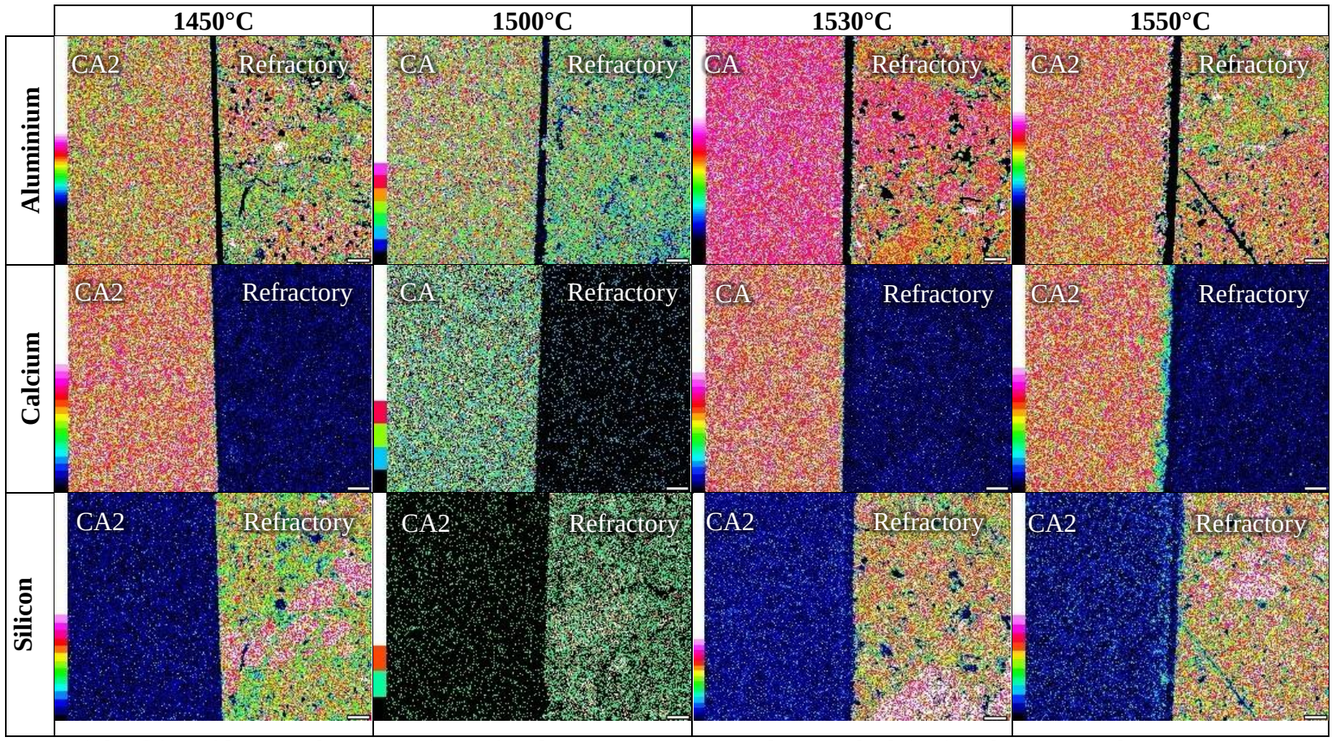

Figure 4.7: Elemental Mapping of the CA2 - Aluminosilicate interface. A colour concentration scale is on the left of each micrograph. Reaction time = 4 hours. Scale bar = 100µm

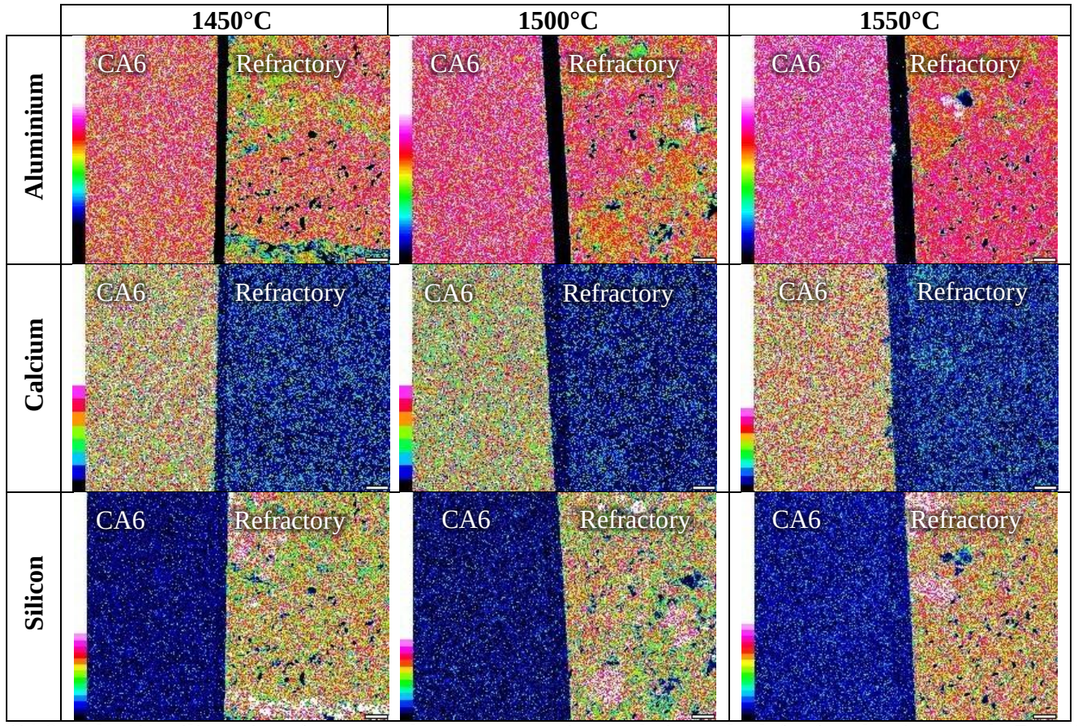

Figure 4.8: Elemental Mapping of the CA6 - Aluminosilicate interface. A colour concentration scale is on the left of each micrograph. Reaction time = 4 hours. Scale bar = 100µm

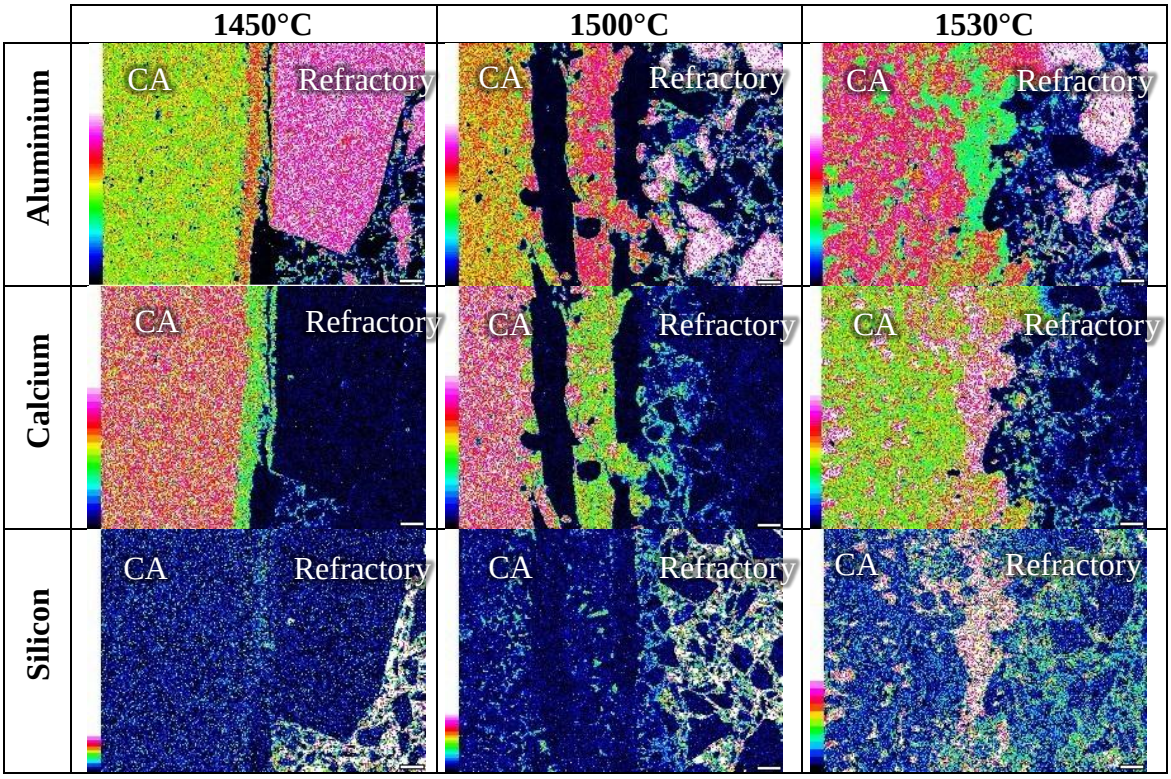

Figure 4.9: Elemental Mapping of CA – Alumina - Carbon interface after 4 hours. A colour concentration scale is on the left of each micrograph. Scale bar = 100µm

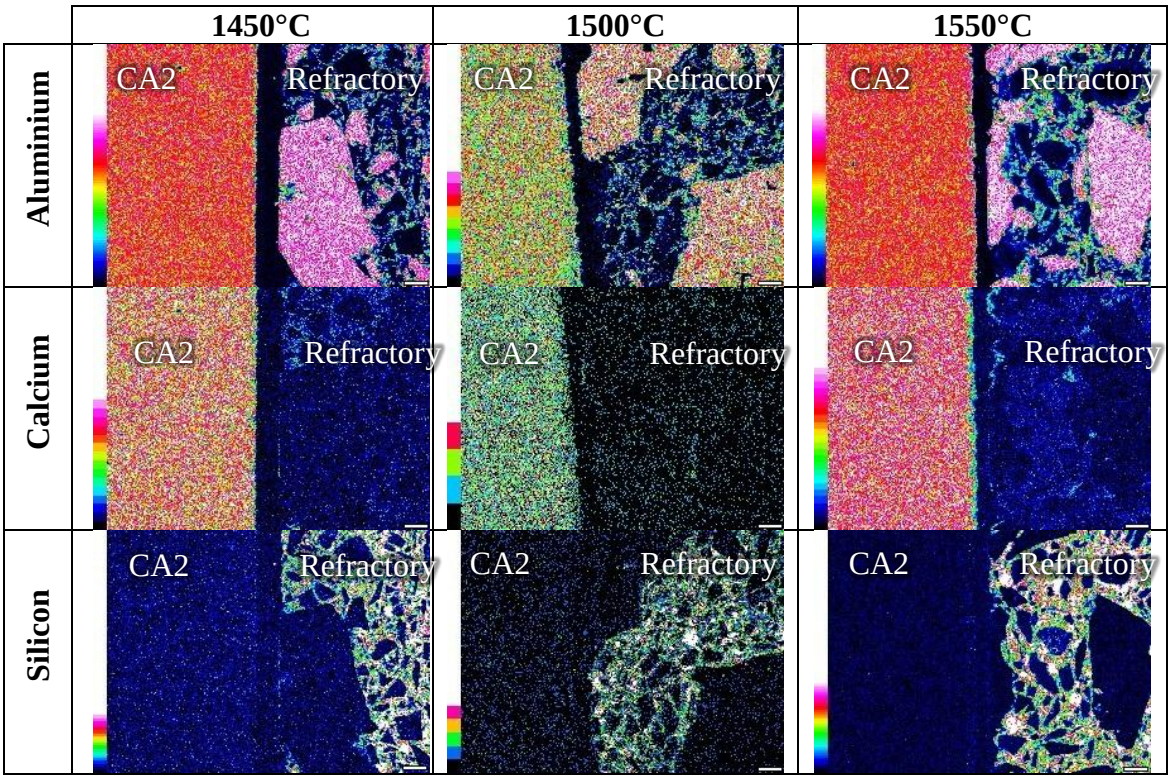

Figure 4.10: Elemental Mapping of CA2 – Alumina - Carbon interface after 4 hours. A colour concentration scale is on the left of each micrograph. Scale bar = 100µm

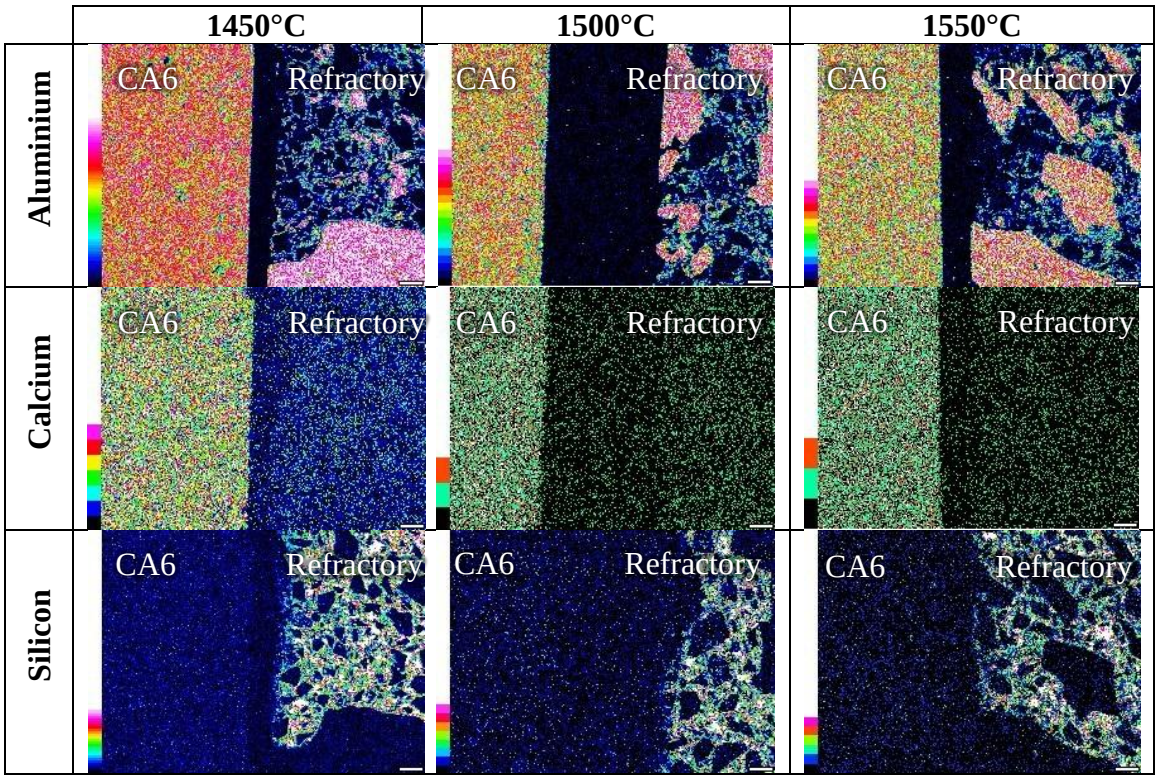

Figure 4.11: Elemental Mapping of CA6 – Alumina - Carbon interface after 4 hours. A colour concentration scale is on the left of each micrograph. Scale bar = 100µm

EDS spot analysis composition (Table 4.1 and Table 4.2) and the ternary $Al_2O_3 – SiO_2 –$ CaO phase diagram (Figure 2.12) was used to determine the likely phases formed in the reaction layer of the different couples as shown in Table 4.3.

Table 4.3: Reaction Layer phases consistent with EDS compositions observed in the Temperature Series Reaction couples in Figure 4.2 and Figure 4.3.

Reaction Couple		**˚C**	**Reaction Layer Phase (s)**
Aluminosilicate	CA	1500	CA2/ Hibonite ($CaAl_{12}O_{19}$)
Aluminosilicate	CA	1530	Hibonite ($CaAl_{12}O_{19}$) , Gehlenite ($2CaO{\cdot}Al_2O_3{\cdot}SiO_2$)
Aluminosilicate	CA2	1550	CA6 / Corundum
Alumina - Carbon	CA	1450	CA2/ Hibonite ($CaAl_{12}O_{19}$)
Alumina - Carbon	CA	1500	CA2
Alumina - Carbon	CA	1530	CA2/ Hibonite ($CaAl_{12}O_{19}$)
Alumina - Carbon	CA2	1450	CA2/ Hibonite ($CaAl_{12}O_{19}$)
Alumina - Carbon	CA2	1500	CA6/ Corundum
Alumina - Carbon	CA2	1550	CA6/ Corundum

4.3. Time Effect on Reaction Couple Kinetics

4.3.1. Mass Change Measurements

The time series reaction couples with a measured mass loss (calculated using Equation 3-1) are given in Figure 4.12. Only the Alumina - Carbon refractory reaction couples experienced a mass greater than the measurement error of the scales used of 0.5%. All mass change results are given in Appendix III.

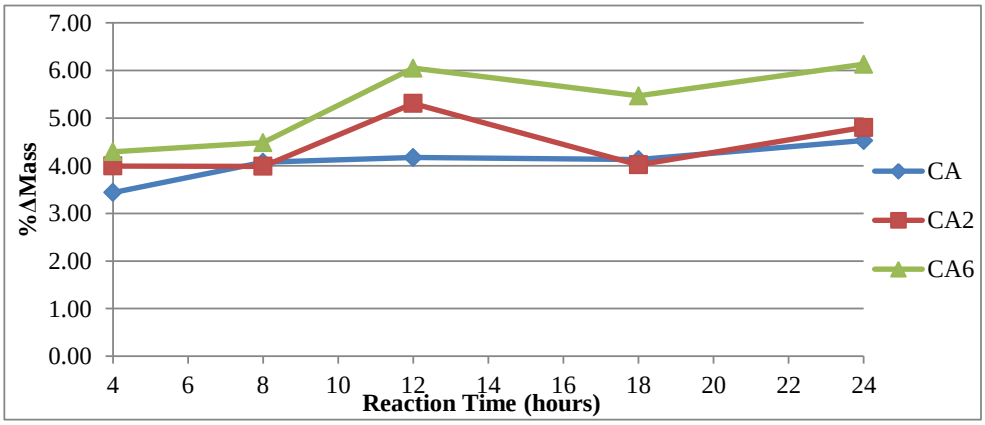

Figure 4.12: Mass loss results for the Alumina - Carbon refractory reaction couples from 4 hours to 24 hours.

4.3.2. SEM Micrographs

Three SEM micrographs of the interface were produced for each reaction couple in the time series (Appendix V). Figure 4.13 and Figure 4.16 show a micrograph selected form each reaction couple in the time series.

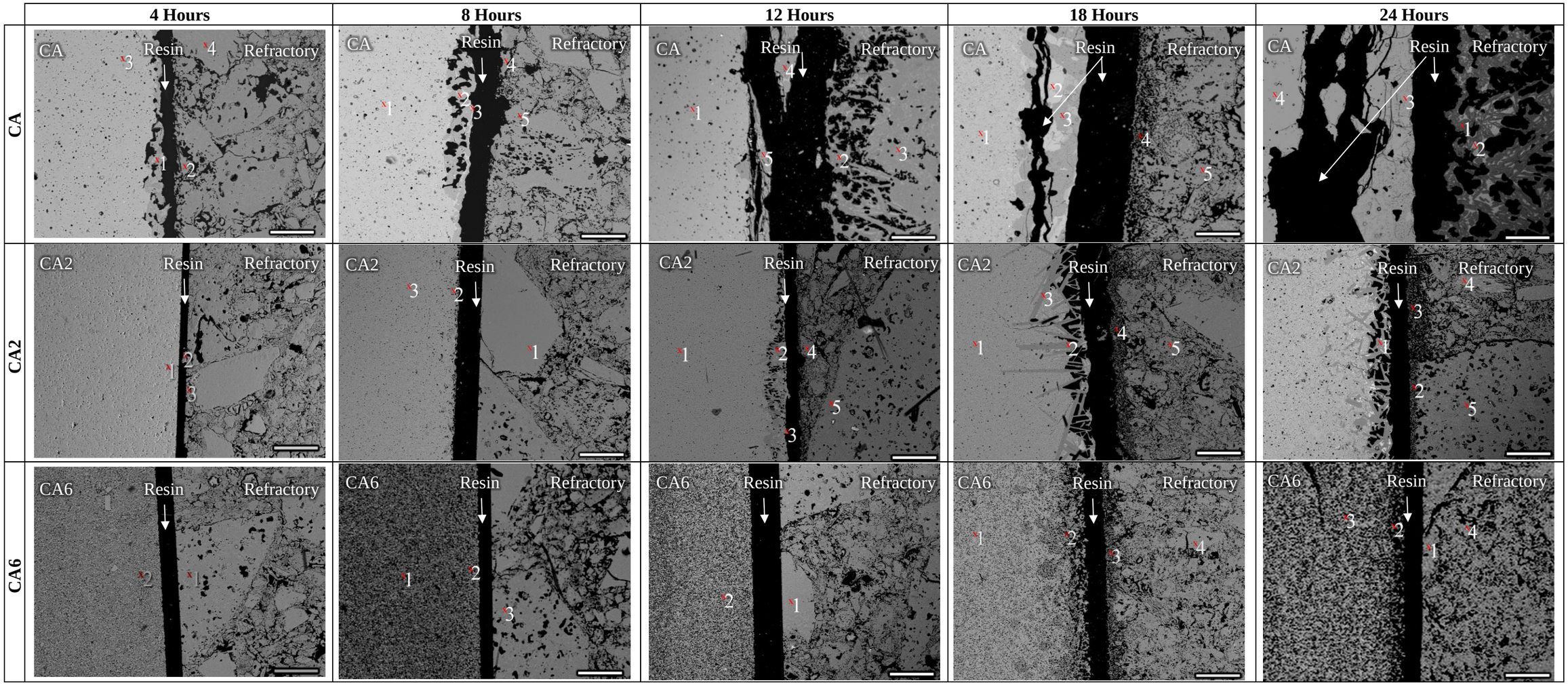

Figure 4.13: SEM micrographs of the interface between the Aluminosilicate Refractory and calcium aluminates after heating to 1500°C for various reaction times. The numbers on each micrograph represent spot analysis points given in Table 4.4. Scale bar = 200µm

Table 4.4: Aluminosilicate refractory time series reaction couples EDS spot analysis results at 1500°C reaction temperature.

	Spot No.	Units	4 Hours				8 Hours				12 Hours				18 Hours				24 Hours			
			Al_2O_3	CaO	SiO_2	Phase	Al_2O_3	CaO	SiO_2	Phase	Al_2O_3	CaO	SiO_2	Phase	Al_2O_3	CaO	SiO_2	Phase	Al_2O_3	CaO	SiO_2	Phase
CA	1	Mass%	77.2	15.4	7.4	Hibonite	65.3	34.7		CA	63.5	36.5		CA	67.8	32.2		CA	100.0			Corundum
		Mol%	65.6	23.8	10.6		50.9	49.1			48.9	51.1			53.7	46.3			100.0			
	2	Mass%	63.3	4.6	32.1	Mullite	73.8	26.2		CA2/ grossite	76.8	5.9	17.3	Corundum	67.8	32.2		CA	37.7	18.3	44.0	Anorthite
		Mol%	50.2	6.6	43.2		60.8	39.3			65.7	9.1	25.1		53.7	46.3			25.9	22.8	51.3	
	3	Mass%	64.5	35.53		CA	38.2	22.5	39.3	Gehlenite	71.3		28.7	Mullite	79.5	20.5		CA2	80.3	19.6	0.1	CA2/ Grossite
		Mol%	49.9	50.0			25.8	25.9	48.3		59.4		40.6		68.0	32.0			69.2	30.6	0.2	
	4	Mass%	67.5	1.8	30.8	Mullite	83.4	11.3	5.3	Corundum	78.8	21.2		CA2	100.0			corundum	66.8	33.1	0.1	CA
		Mol%	54.9	2.6	42.5		74.3	17.1	8.7		67.2	32.8			100.0				52.6	47.3	0.1	
	5	Mass%					65.4	33.1	1.6	Mullite	79.0	21.0.		CA2	67.8		32.2	Mullite				
		Mol%					52.6	45.1	2.3		67.5	32.6			55.4		44.6					
CA2	1	Mass%	77.9	22.1		CA2	57.8		42.2	Mullite	78.13	21.9		CA2	79.5	20.5		CA2	91.4	7.8	0.8	Corundum / CA6
		Mol%	65.9	34.1			44.6		55.4		66.27	33.7			68.1	31.9			85.4	13.3	1.3	
	2	Mass%	100			Alumina Grain	91.9	8.2		CA6	89.01	2.4	8.6	Corundum	92.3	7.7		CA6	100.0	0.0		Corundum
		Mol%	100				86.1	13.9			81.90	3.8	14.3		86.8	13.2			100.0	0.0		
	3	Mass%	67.1		32.9	Mullite	77.8	22.2		CA2	61.81	12.1	26.1	CA2 / Hibonite	92.3	7.7		CA6	100.0	0.0		Corundum
		Mol%	54.6		45.4		65.8	34.2			47.67	15.8	36.5		86.8	13.2			99.9	0.1		
	4	Mass%									75.55	24.4		Mullite	100.00			Corundum	59.5	1.2	39.3	Mullite
		Mol%									64.57	35.5			100.00				46.4	0.6	51.9	
	5	Mass%									70.73	29.3		Mullite	75.6		24.4	Mullite	74.8	0.9	24.3	Mullite
		Mol%									58.74	41.2			64.6		35.4		56.3	42.4	1.3	
CA6	1	Mass%	76.7		23.3	Mullite Grain	93.3	6.7		CA6 / corundum	68.2	0.4	31.4	Mullite Grain	91.4	8.6		CA6	75		25	Mullite
		Mol%	66.0		34.0		88.5	11.5			55.8	0.6	43.6		85.5	14.5			63.9		36.13	
	2	Mass%	91.0	9.0		CA6	91.2	8.8		CA6 / corundum	89.5	8.5	2.0	Corundum	100			Corundum	42.1	16.9	41.0	Corundum
		Mol%	84.8	15.2			85.1	14.9			82.6	14.3	3.2		100				29.6	21.6	48.5	
	3	Mass%					77.1		23.0	Mullite					100			Corundum	85.4	10.6	4.0	Corundum
		Mol%					66.4		33.6						100				76.6	17.4	6.1	
	4	Mass%													73.7		26.3	Mullite	72.3	0.1	27.6	Mullite
		Mol%													62.3		37.8		60.6	0.1	39.3	

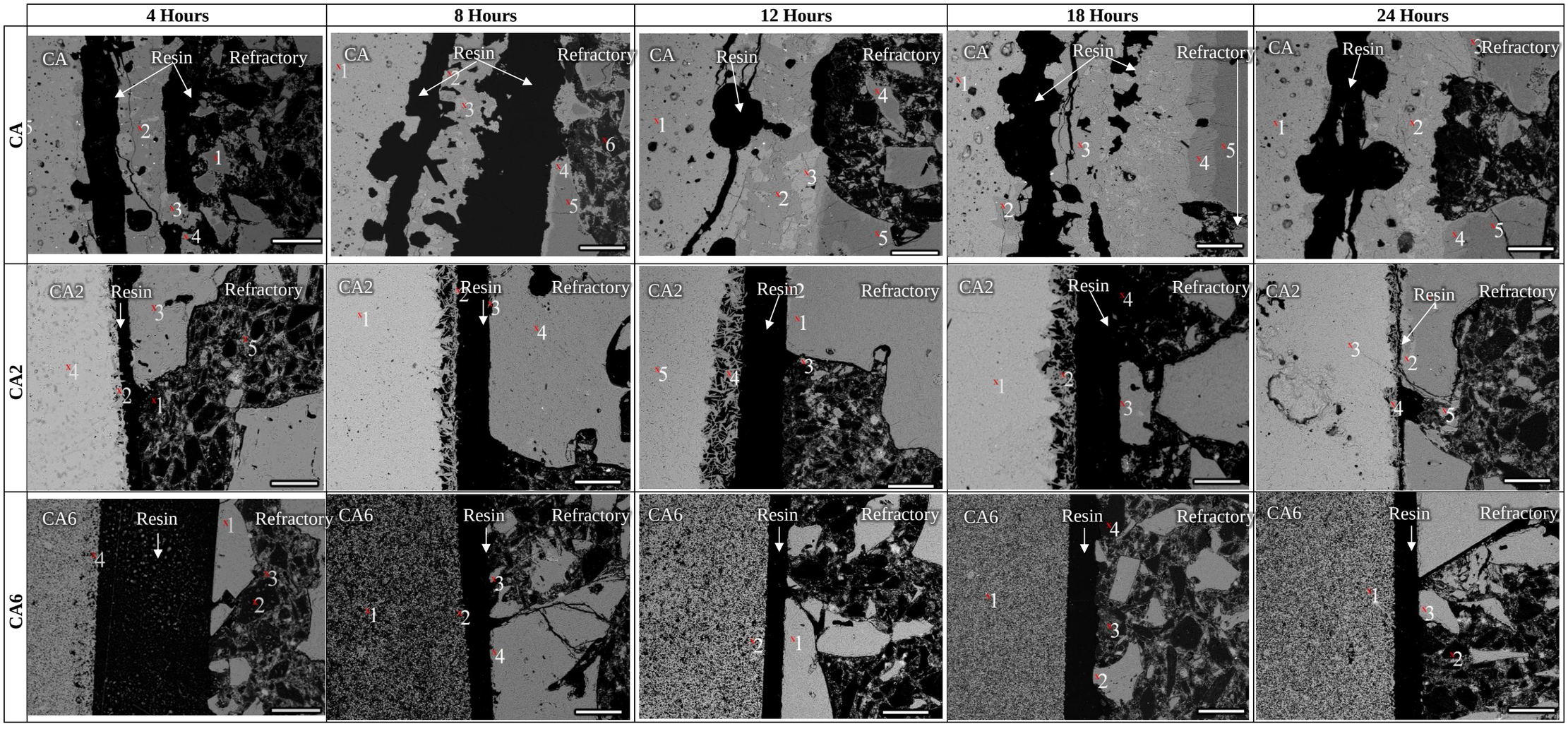

Figure 4.14: SEM micrographs of the interface between the Alumina - Carbon Refractory and calcium aluminates after heating to 1500°C for various reaction times. The numbers on each micrograph represent spot analysis points given in Table 4.5. Scale bar = 200µm

Table 4.5: Alumina-Carbon refractory time series reaction couples EDS spot analysis results at 1500°C reaction temperature.

	Spot No.	Units	4 Hours				8 Hours				12 Hours				18 Hours				24 Hours			
			C	Al_2O_3	CaO	SiO_2	C	Al_2O_3	CaO	SiO_2	C	Al_2O_3	CaO	SiO_2	C	Al_2O_3	CaO	SiO_2	C	Al_2O_3	CaO	SiO_2
CA	1	Mass%		100				65.5	34.5			67.2	32.9			63.2	36.8			63.9	36.1	0.0
		Mol%		100				51.1	48.9			52.9	47.1			48.6	51.4			49.3	50.7	0.0
	2	Mass%		79.1	20.9			78.4	21.6			80.0	20.0			80.0	20.0			81.6	18.4	
		Mol%		67.6	32.4			66.7	33.3			68.7	31.3			68.8	31.3			70.9	29.1	
	3	Mass%		79.0	21.0			65.3	34.7			41.9	39.2	18.9		79.9	20.2			91.5	8.5	
		Mol%		67.4	32.6			50.9	49.1			28.8	49.1	22.1		68.6	31.5			85.5	14.5	
	4	Mass%		78.8	21.2			79.3	20.7			92.8	7.2			92.4	7.6			92.2	7.8	
		Mol%		67.1	32.8			67.9	32.1			87.7	12.4			87.0	13.0			86.6	13.4	
	5	Mass%		65.3	34.7			100.0	0.0			100				100.0				100.0		
		Mol%		50.9	49.1			100.0	0.0			100				100.0				100.0		
CA2	1	Mass%	98.1	0.8	1.0	0.2		63.7	31.8			100.0				91.4	8.6			100.0		
		Mol%	99.7	0.1	0.2	0.1		67.5	32.5			100.0				85.5	14.6			100.0		
	2	Mass%		89.7	8.7	1.6		91.7	8.3			98.2	1.8			92.4	7.6			93.4	6.6	
		Mol%		82.9	14.6	2.5		85.9	14.1			96.8	3.2			87.0	13.0			88.6	11.4	
	3	Mass%		100.0	0.0			91.9	8.1			91.4	8.6			100.0				79.8	20.2	
		Mol%		100.0	0.0			86.2	13.8			85.5	14.6			100.0				68.5	31.5	
	4	Mass%		78.7	21.3	0.1		99.9	0.1			91.6	8.5		100.0					89.4	10.6	
		Mol%		67.0	32.9	0.1		99.7	0.3			85.6	14.4		100.0					82.3	17.7	
	5	Mass%	40.9	49.8	0.1	9.2						79.6	20.4							92.7	7.3	
		Mol%	84.1	12.1	0.0	3.8						68.3	31.8							87.5	12.5	
CA6	1	Mass%		100				91.4	8.6			100				92.0	8.0			93.4	6.6	
		Mol%		100				85.4	14.6			100				86.4	13.4			88.7	11.3	
	2	Mass%	99	0.2	0.8			91.2	8.8			91	8.9			100			98.1	1.9		
		Mol%	99.8	0.0	0.2			85.0	15.0			84.8	15.2			100			99.8	0.2		
	3	Mass%	36.5	14.9	0.1	48.5		100							46.6	27.0		26.3		100		
		Mol%	76.1	3.7	0.0	20.2		100							84.7	5.8		9.6		100		
	4	Mass%		91.7	8.3			100							98.0	2.0						
		Mol%		85.9	14.1			100							99.8	0.2						

Table 4.6: Alumina-Carbon refractory temperature series reaction couples EDS spot analysis results

	Spot No.	4 Hours	8 Hours	12 Hours	18 Hours	24 Hours
CA	1	Alumina Grain	CA	CA	CA	CA
	2	CA2	CA2	CA2	CA2	CA2
	3	CA2	CA	Gehlenite	CA2	CA6
	4	CA2	CA2	CA6	CA6/ corundum	CA6
	5	CA	Corundum	Alumina Grain	Alumina Grain	Alumina Grain
CA2	1	Anthracite Grain	CA2	Alumina Grain	CA6	Alumina Grain
	2	corundum	CA6	corundum	CA2	CA6
	3	Alumina grain	CA6	CA6	Alumina Grain	CA2
	4	CA2 / Hibonite ($CaAl_{12}O_{19}$)	Corundum	CA6	Graphite	CA6
	5	Carbon Matrix		CA2		CA6
CA6	1	Alumna Grain	CA6	Corundum	CA6	Corundum
	2	Anthracite Grain	CA6	CA6	Alumina Grain	Graphite grain
	3	Carbon Matrix	Corundum		Anthracite grain	Corundum
	4	CA6	Corundum		Graphite grain	

4.3.3. Reaction Layer Thickness Measurements

The average reaction layer thickness and standard deviation was determined using 90 thickness measurements from each of the reaction couples (Appendix IV). The thickness measurements were produced using three different SEM micrographs of the reaction couple interface (Section 4.3.2 and Appendix V). The average thickness $\pm$ 1 standard deviation for each reaction couple are given in Figure 4.15 and Figure 4.16.

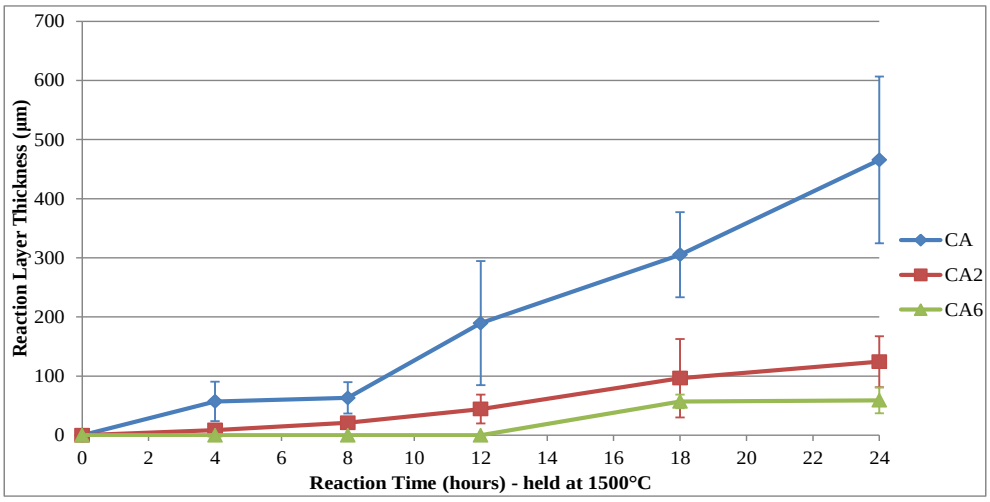

Figure 4.15: Reaction layer thickness by time for all the aluminosilicate reaction couples.

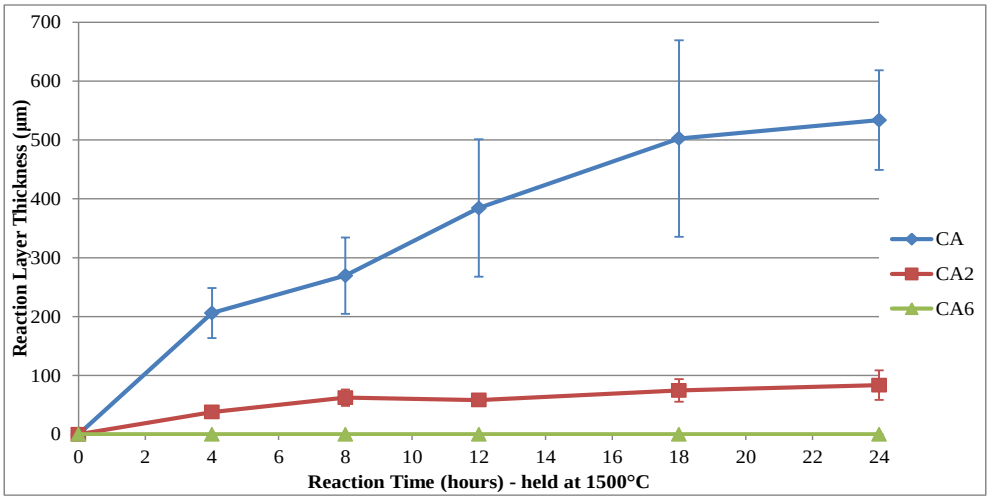

Figure 4.16: Reaction layer thickness by time for all the alumina-carbon reaction couples.

4.3.4. Elemental Analysis of the Reaction Layer

Elemental X-ray mapping of a range of elements often found in refractory materials was conducted at the interface in the reaction couples using the SEM. The aluminium, silicon and calcium elemental maps are shown in Figure 4.17 to Figure 4.22.

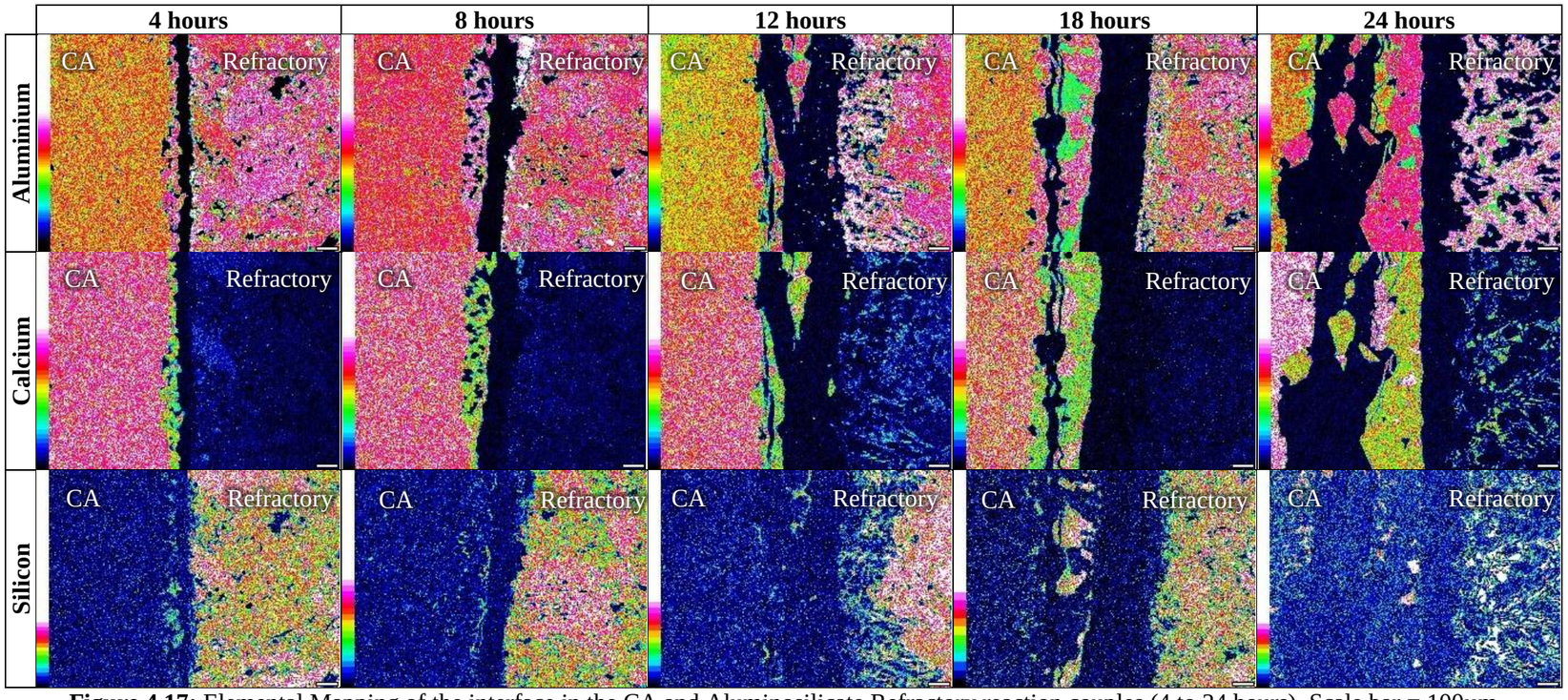

Figure 4.17: Elemental Mapping of the interface in the CA and Aluminosilicate Refractory reaction couples (4 to 24 hours). Scale bar = 100µm

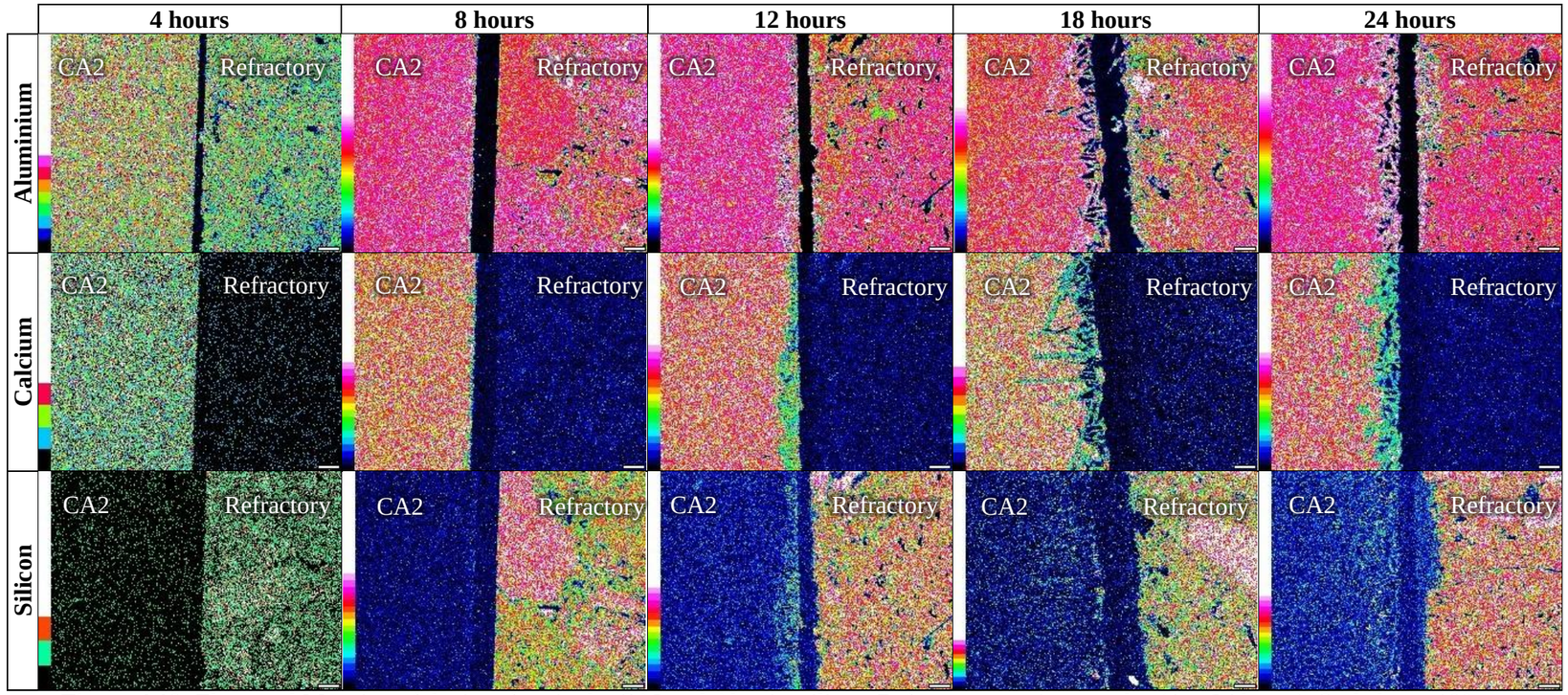

Figure 4.18: Elemental Mapping of the interface in the CA2 and Aluminosilicate Refractory reaction couples (4 to 24 hours). Scale bar = 100µm

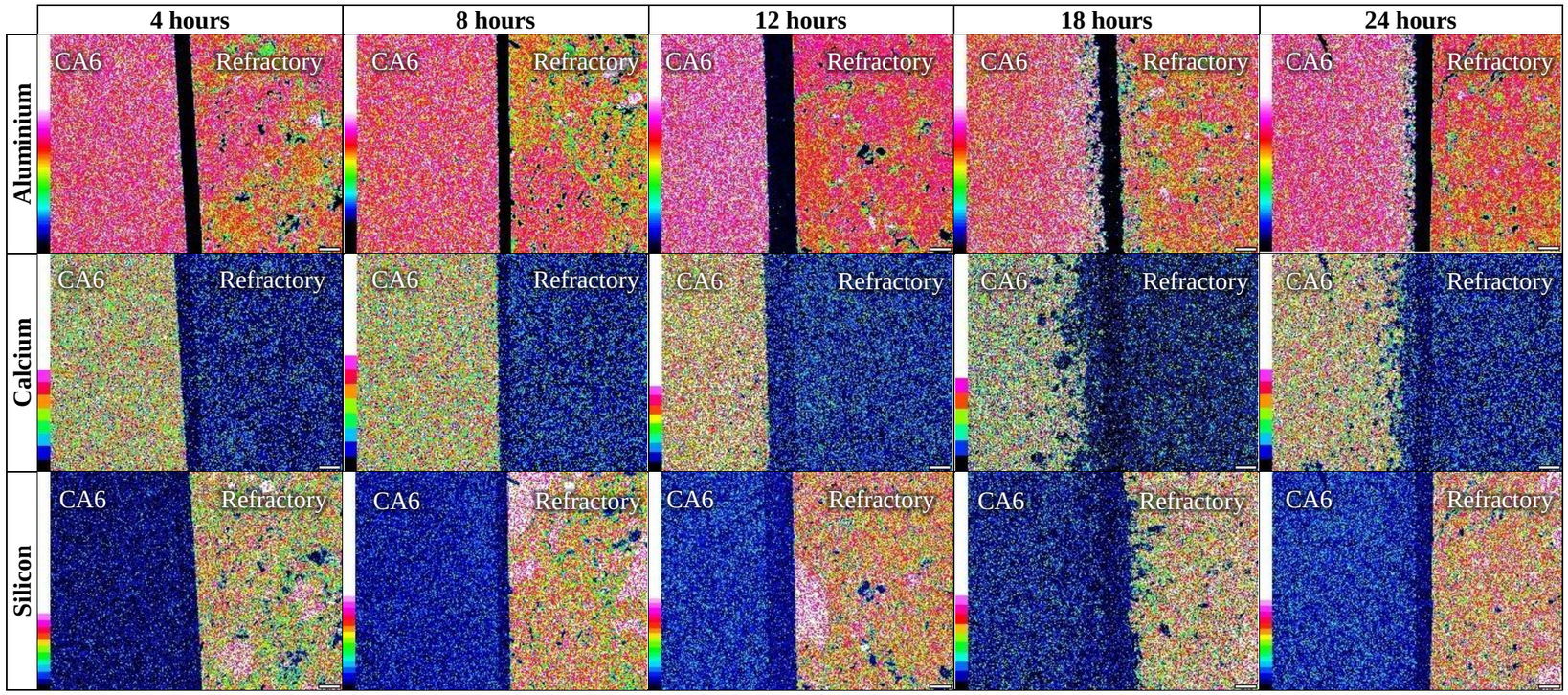

Figure 4.19: Elemental Mapping of the interface in the CA6 and Aluminosilicate Refractory reaction couples (4 to 24 hours). Scale bar = 100µm

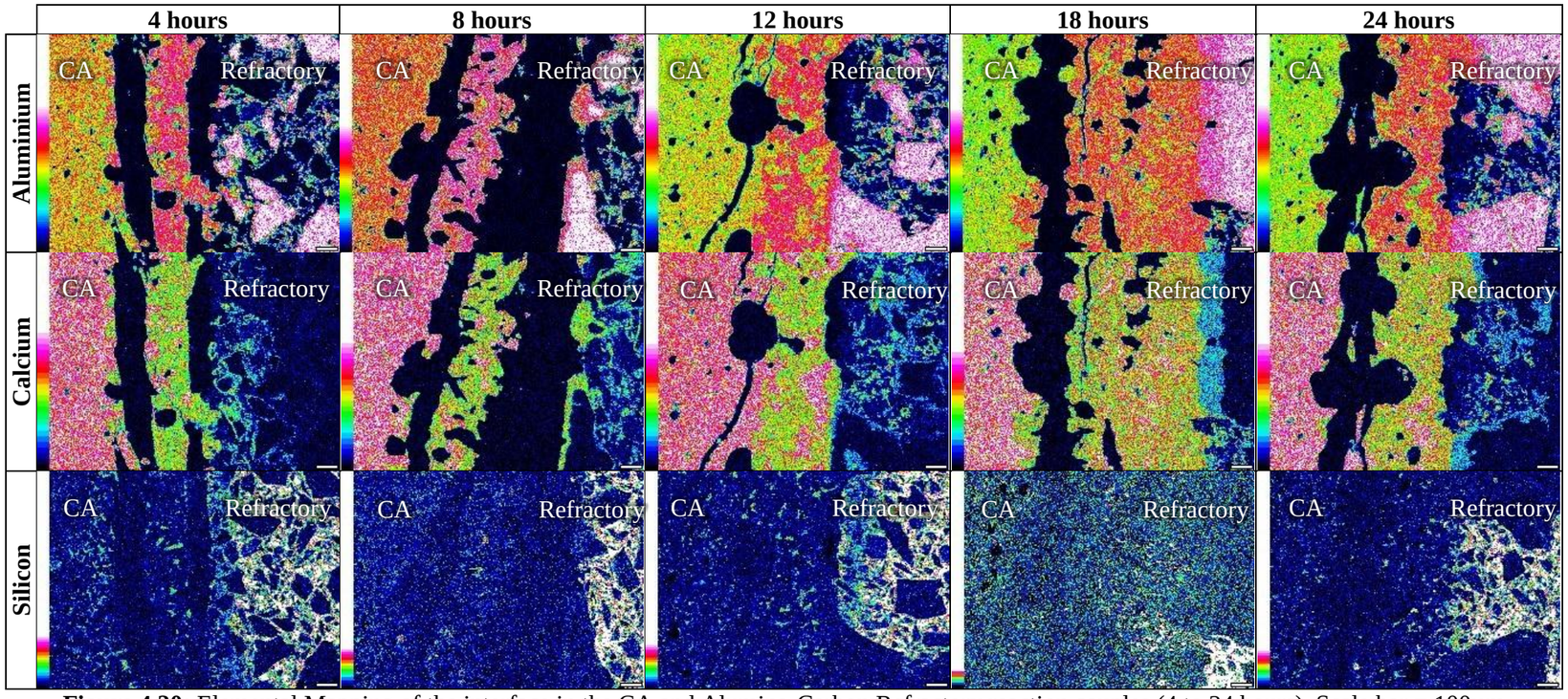

Figure 4.20: Elemental Mapping of the interface in the CA and Alumina-Carbon Refractory reaction couples (4 to 24 hours). Scale bar = 100µm

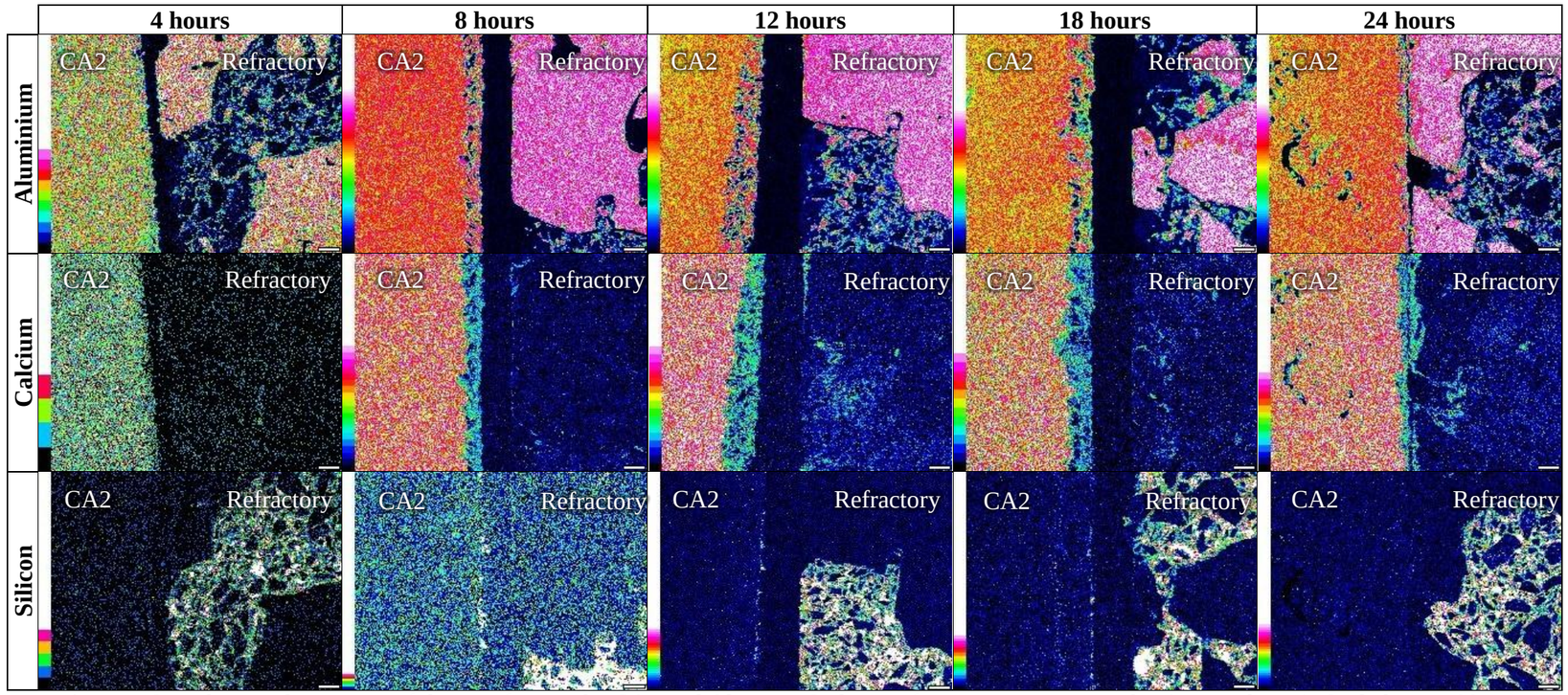

Figure 4.21: Elemental Mapping of the interface in the CA2 and Alumina-Carbon Refractory reaction couples (4 to 24 hours). Scale bar = 100µm

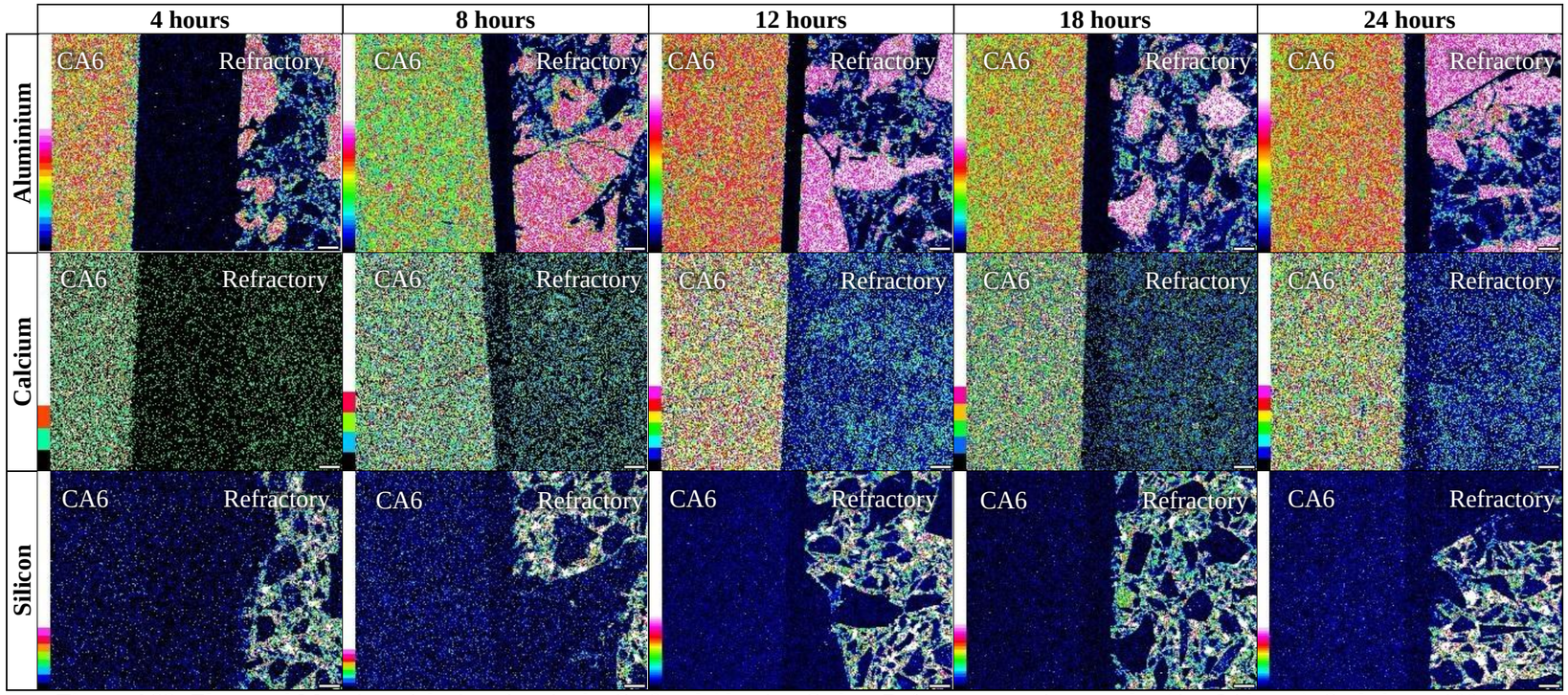

Figure 4.22: Elemental Mapping of the interface in the CA6 and Alumina-Carbon Refractory reaction couples (4 to 24 hours). Scale bar = 100µm

Table 4.7 details the phases identified in the reaction layer of each reaction using energy dispersive spectroscopy analysis (Tables 4.4 – Table 4.6).

Table 4.7: Reaction Layer phases consistent with EDS compositions observed in the Time Series Reaction couples in Figure 4.15 and Figure 4.16.

Reaction Couple Materials		**Time (Hours)**	**Reaction Layer Phase(s)**
Aluminosilicate	CA	4	CA2/ Hibonite ($CaAl_{12}O_{19}$)
Aluminosilicate	CA	4	CA2/ Hibonite ($CaAl_{12}O_{19}$) Gehlenite ($2CaO{\cdot}Al_2O_3{\cdot}SiO_2$)
Aluminosilicate	CA	8	CA2/ Hibonite ($CaAl_{12}O_{19}$) Gehlenite ($2CaO{\cdot}Al_2O_3{\cdot}SiO_2$)
Aluminosilicate	CA	12	CA2, Corundum
Aluminosilicate	CA	18	CA, CA2, Corundum
Aluminosilicate	CA	24	Corundum, Anorthite, Grossite ($CaAl_4O_7$)
Aluminosilicate	CA2	8	CA6
Aluminosilicate	CA2	12	CA2/ Hibonite ($CaAl_{12}O_{19}$), Corundum
Aluminosilicate	CA2	18	CA6, Corundum
Aluminosilicate	CA2	24	CA6, Corundum
Alumina - Carbon	CA	4	CA2
Alumina - Carbon	CA	4	CA2/ Hibonite ($CaAl_{12}O_{19}$)
Alumina - Carbon	CA	8	CA2, Corundum
Alumina - Carbon	CA	12	CA2/ Hibonite ($CaAl_{12}O_{19}$) Gehlenite ($2CaO{\cdot}Al_2O_3{\cdot}SiO_2$)
Alumina - Carbon	CA	18	CA2, CA6
Alumina - Carbon	CA	24	CA2, CA6
Alumina - Carbon	CA2	4	CA6, Corundum
Alumina - Carbon	CA2	8	CA6, Corundum
Alumina - Carbon	CA2	12	CA6
Alumina - Carbon	CA2	18	CA6
Alumina - Carbon	CA2	24	CA6

4.4. Experimental Observations

Visual changes observed during testing of the reaction couples test are presented in Table 4.8.

Table 4.8: Reaction Couple visual observations

	Alumina - Carbon	**Aluminosilicate**
Refractory	no visible change	The refractory matrix browned while mullite grains remained white
Calcium Aluminate	Blackened	no visible change
Interface	refractory surface became cloudy	Refractory did not brown at the interface
Example Reaction couple	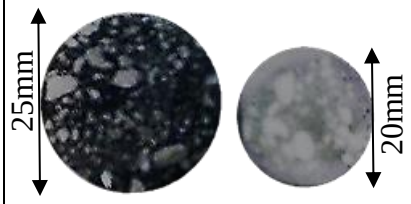	

At the highest reaction temperature and longer reaction times (18 and 24 hours), deformation due to the formation of a reaction layer in the CA and CA2 discs was observed. CA6 needles were observed at the edges of the CA and CA2 discs where there was contact with the refractory. A glassy phase was observed on the alumina weights and on the edges of the reaction couples after testing the Alumina - Carbon refractory with CA and CA2 as shown in Figure 4.23. The formation of this glassy phase was not observed after the testing of the Aluminosilicate refractory.

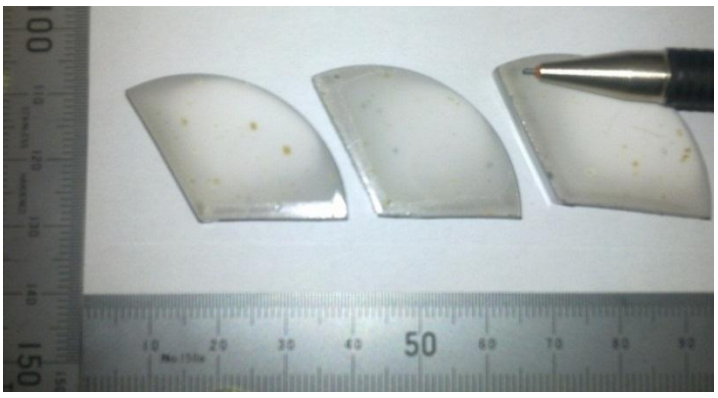

Figure 4.23: Glassy phase observed on the alumina weights after reaction couple testing.

EDS analysis was of the alumina weights and the glassy phase formed is shown in Table 4.9. The high silica content of the glassy phase indicates that the glassy phase was deposited in the furnace during the reaction time between the Alumina - Carbon refractory and the calcium aluminate reaction couples. The formation of this phase accounts for some of the mass loss observed during the testing of the Alumina - Carbon reaction couples. The source of all the components of this phase is from the refractories or calcium aluminates.

Table 4.9: EDS Analysis of alumina weights and the observed glassy phase.

Oxide	**Alumina Weights** (Mass %)	**Glassy Phase** (Mass %)
Al_2O_3	99.7	24.75
FeO	0.01	0.00
SiO_2	0.18	60.84
Na_2O	0.01	9.26
MgO	0.10	3.91
K_2O	0.00	1.25

During testing of alumina-carbon refractory a fibrous material was also observed to accumulate in the furnace tube between the hot zone the end cap and near the waste gas outlet line from the furnace. This fibrous material was collected for analysis as shown in Figure 4.24.

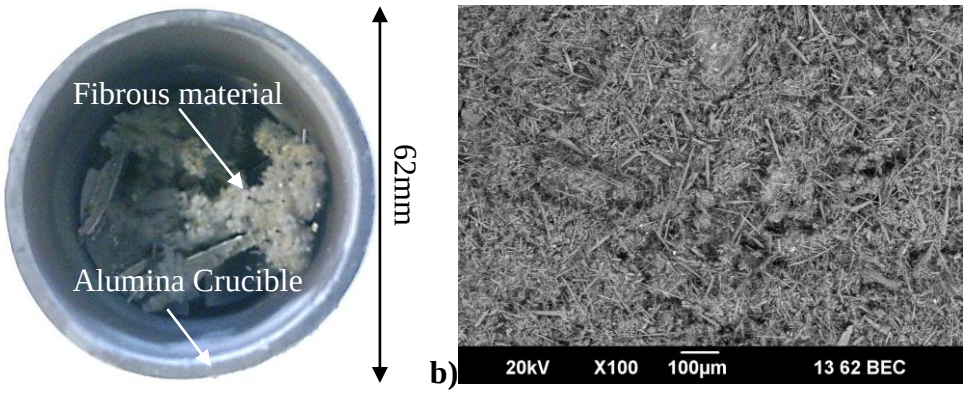

Figure 4.24: a) Fibrous material collected from above the hot zone in the furnace by knocking down into a crucible (bench top photograph of crucible once removed from the tube furnace). b) SEM Micrograph of fibrous material collected.

EDS analysis was conducted on the fibrous material collected and the composition was found to be 13.92 mass% carbon and 86.08 mass% alumina. XRD analysis of the fibrous material was carried out and best match for the fibrous material was identified as aluminium oxide-carbide (Al_4O_4C) (6.52 mass% carbon) as shown in Figure 4.25. A number of major peaks between 30°and 45° were not identified. Given the fibrous nature of the fibrous nature of the material found and the SiO_2 loss observed in the alumina carbon refractories the presence of SiO_2 may be the source of these peaks.

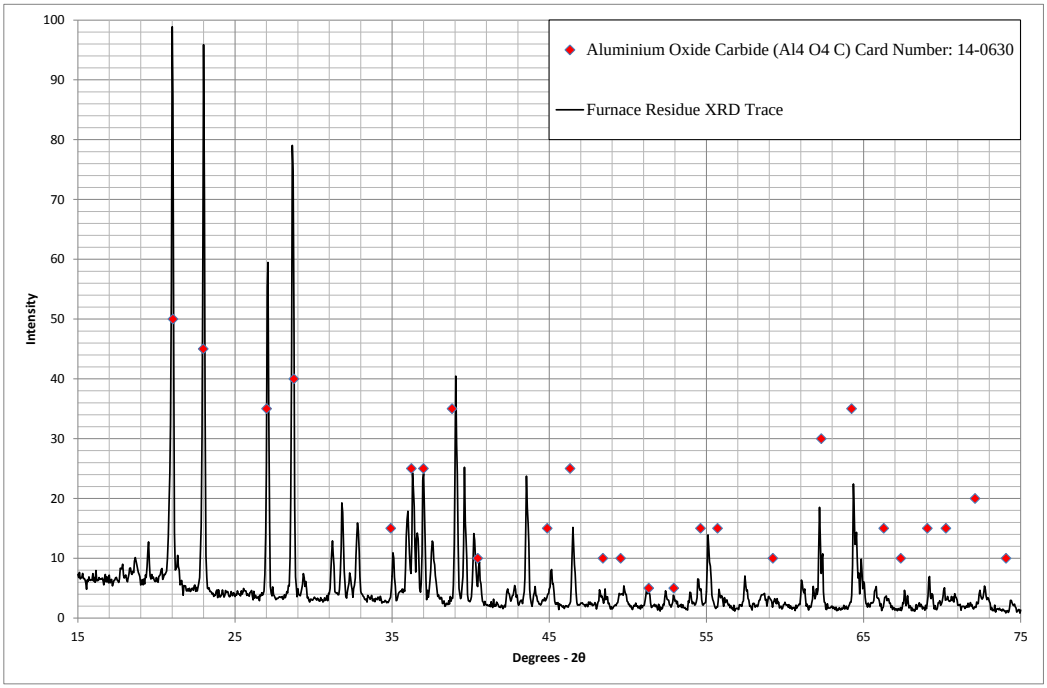

Figure 4.25: XRD trace for the fibrous material (Al_4O_4C) collected from above the hot zone in the vertical tube furnace after reaction couple testing.

4.5. Phase Stability Diagrams

Thermodynamic modelling of the principle oxide constituents in the refractories and calcium aluminate reaction couples was conducted to assess the reactivity of each reaction couple tested. The thermodynamic modelling software MTDATA was used to produce the isopleth in Figure 4.26 and the phase stability diagrams in Figure 4.26 and Figure 4.28. This was done based on the data in Table 2.5 but simplified to only include the principle oxide constituents (Table 4.10). Carbon was not included as the appropriate databases were not available.

Table 4.10: Material compositions used to model phase stability diagrams

Material	Al_2O_3	CaO	SiO_2
Aluminosilicate Refractory	71.57		28.43
Alumina grains*	93.11		6.89
CA	64.22	35.78	
CA2	78.21	21.79	
CA6	91.5	8.5	

*aggregate in the Alumina - Carbon refractory

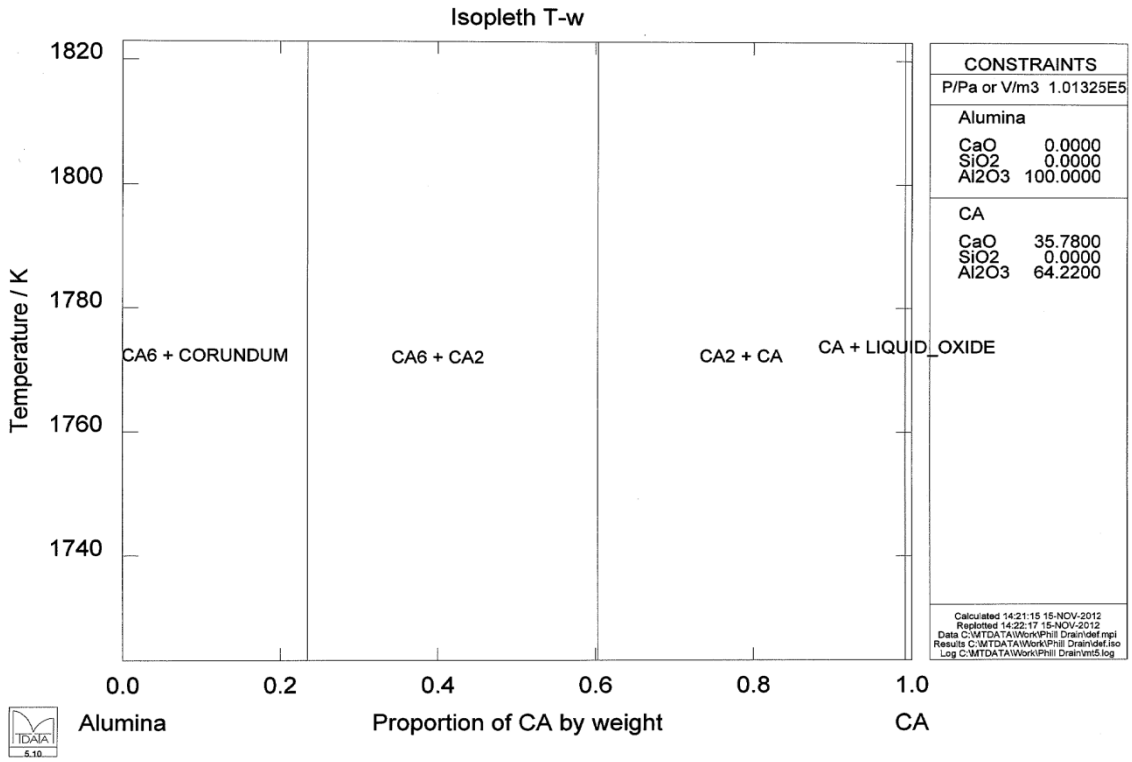

Figure 4.26: Alumina Carbon – calcium aluminate reaction 1500°C Isopleth

	1450°C	1500°C	1550°C	Key
CA	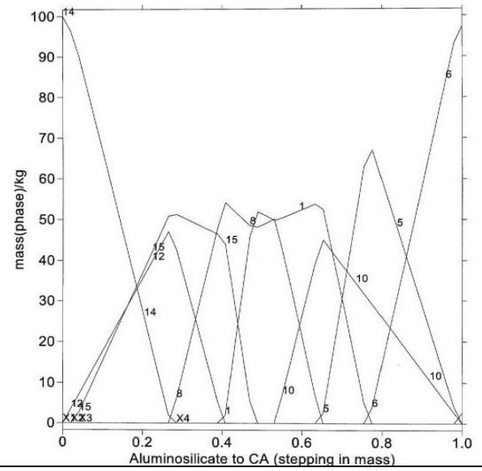	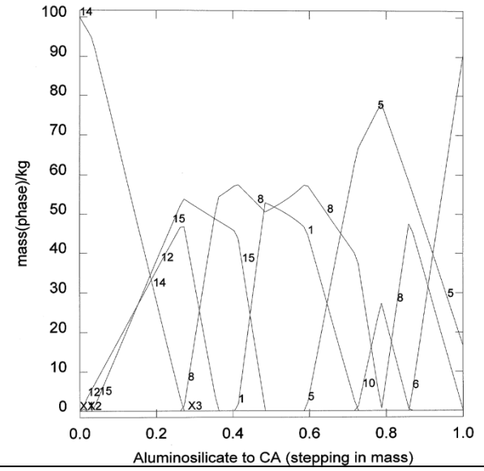	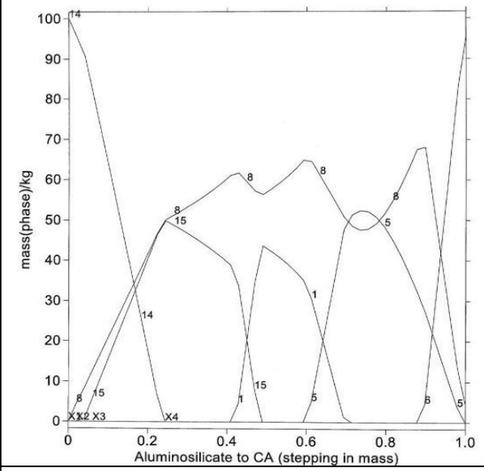	1 = CA6 2 = CF 3 = C2F 4 = C3A 5 = CA2 6 = CA 7 = C12A7 8 = Liquid oxide 9 = Liquid oxide 10 = Melilite 11 = Clinopyroxene 12 = Plagioclase H 13 = Spinel 14 = Mullite 15 = Corundum 16 = Pseudo Wollastonite 17 = Hatrurite 18 = Rankinite 19 = Wollastonite 20 = α – C2S 21 = α – prime C2S 22 = Protopyroxene 23 = Olivinge 24 = Halite 25 = Halite 26 = Cristobalite 27 = Quartz 28 = Tridymite
CA2	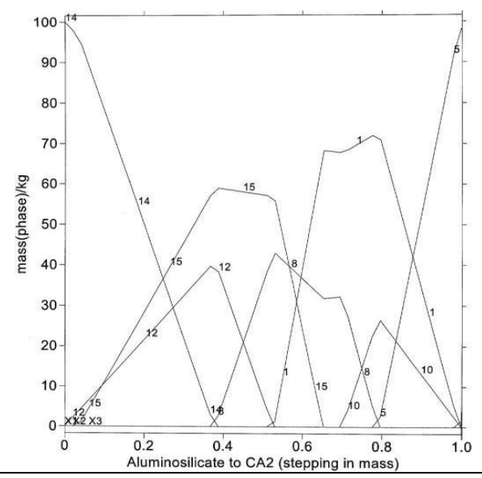	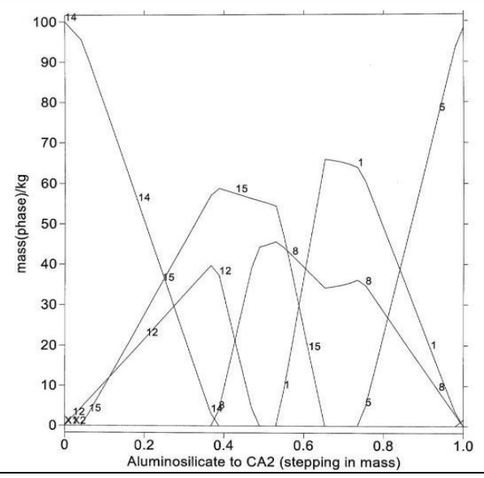	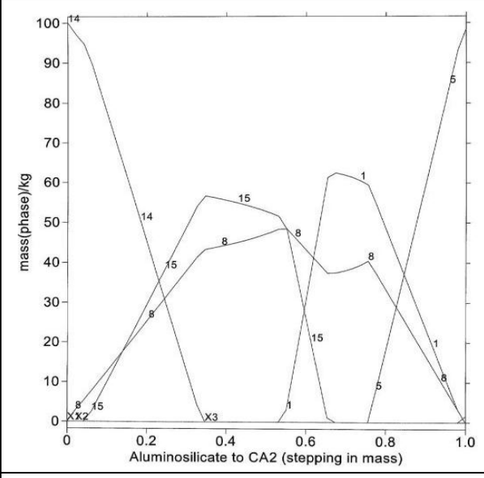	
CA6	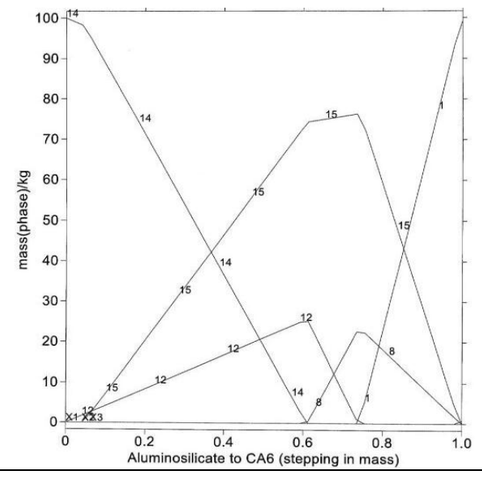	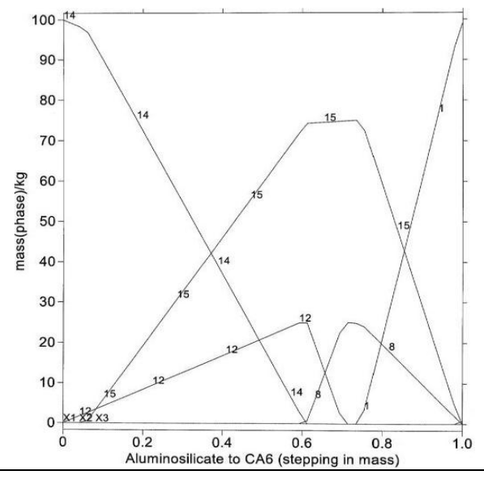	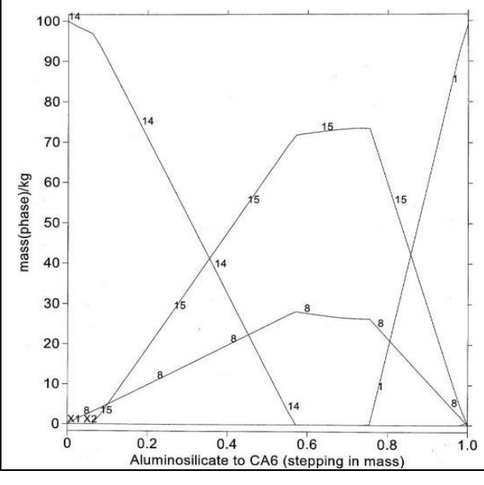	

Figure 4.27: Aluminosilicate – calcium aluminate reaction phase stability diagrams, assumed pressure of 101.325 kPa

	1450°C	1500°C	1550°C	Key
CA	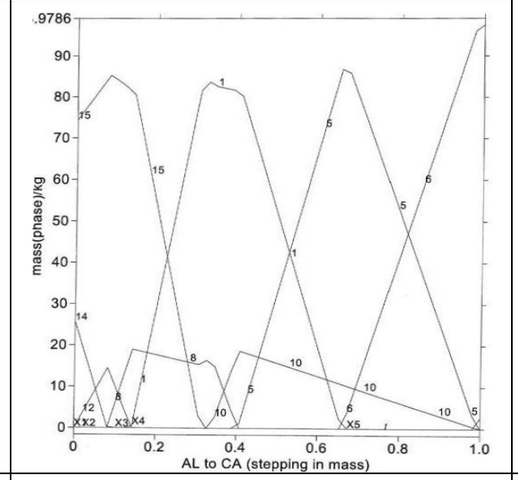	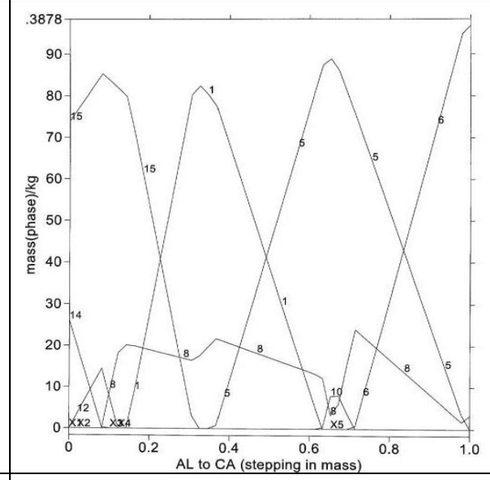	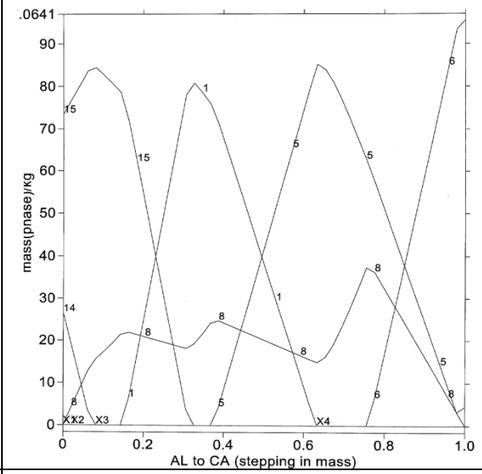	1 = CA6 2 = CF 3 = C2F 4 = C3A 5 = CA2 6 = CA 7 = C12A7 8 = Liquid oxide 9 = Liquid oxide 10 = Melilite 11 = Clinopyroxene 12 = Plagioclase H 13 = Spinel 14 = Mullite 15 = Corundum 16 = Pseudo Wollastonite 17 = Hatrurite 18 = Rankinite 19 = Wollastonite 20 = α – C2S 21 = α – prime C2S 22 = Protopyroxene 23 Olivinge 24 = Halite 25 = Halite 26 = Cristobalite 27 = Quartz 28 = Tridymite
CA2	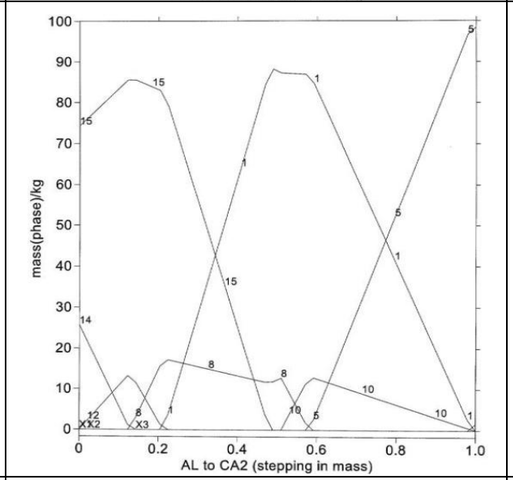	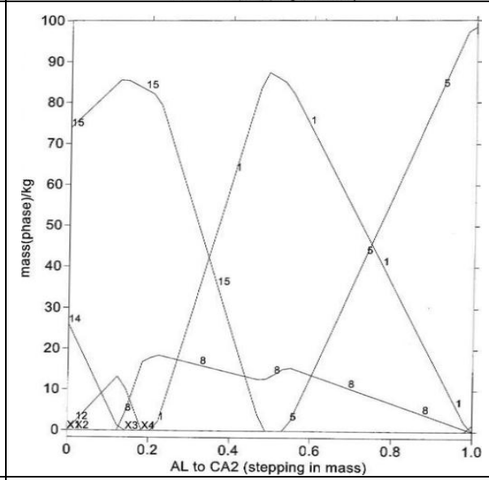	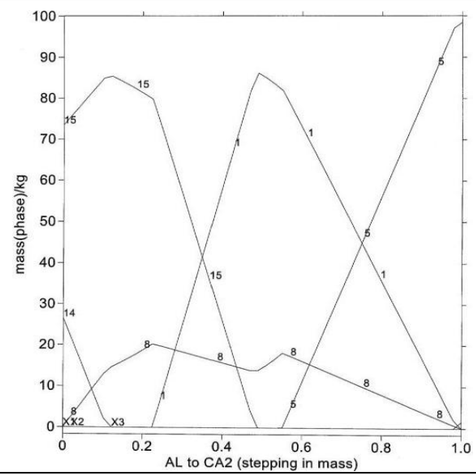	
CA6	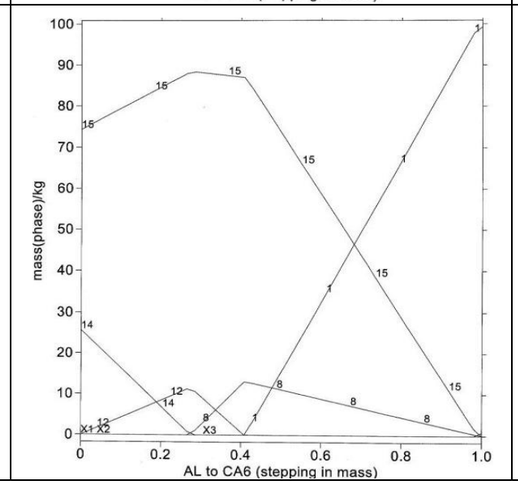	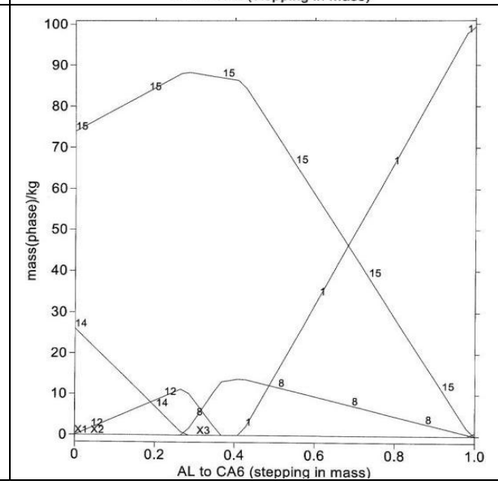	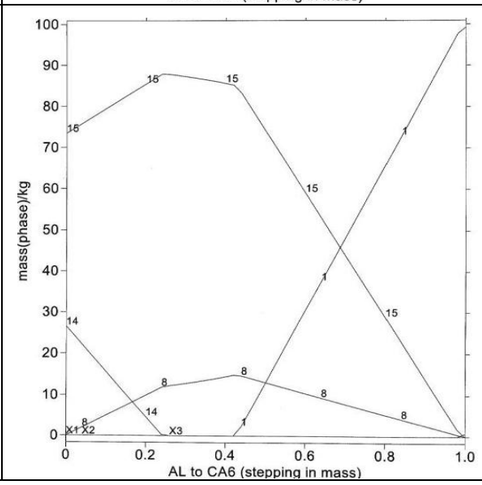	

Figure 4.28: Alumina Carbon – calcium aluminate reaction phase stability diagrams, assumed pressure of 101.325 kPa

5. Discussion

In this chapter the thermodynamics of the reactions between the hearth refractories and coke ash minerals are discussed. The reaction phases observed are compared with those predicted by the phase stability diagrams produced from the MTDATA thermodynamic modelling software. The influences of various phases on the reaction kinetics were discussed, in particular the formation of liquid and low liquidus temperature phases.

The kinetics of these reactions is also discussed in this chapter, the approach utilised was to review the reaction layer thickness data and determine the corresponding kinetic model which applies from the literature. The inert wire experiment was used to discuss the Kirkendall effect for the net direction of mass transfer in the reaction couples.

5.1. Thermodynamics of Hearth Refractory and Coke Ash Interactions

The phase stability diagrams (Figure 4.27 - Figure 4.28) predict the equilibrium phases present at the various reaction couple interfaces. Since the reaction couples were not expected to be at equilibrium, a comparison of the observed and predicted phases was conducted for each reaction couple (Table 5.1 to Table 5.12). The absence of some predicted phase is likely due to the reaction kinetics limiting the phase formation. This analysis was done to determine if there was any similarity between the experimental and thermodynamic modelling results which could be used to predict the phases observed.

The phases identified in Tables 5.1 to Table 5.12 are based on the composition-temperature phase diagram. There is some uncertainty around the phases identified when compositions were close to the phase boundaries. This is due to uncertainty in the EDS analysis and the phase identification being conducted on cold post experimental samples. It was not possible to carry this out in situ at the experimental temperature. For all the reaction couple systems studied there is the potential for liquid phase formation, particularly in the higher CaO calcium aluminates and high temperature reaction couples, as shown in Figures 4.27 and Figure 4.28. It was also observed from these phase stability diagrams that the Aluminosilicate refractory was more likely to form liquid oxides.

5.1.1. Reaction Couple Phase Formation with Temperature

A comparison of the phases observed in the Aluminosilicate – Calcium Aluminate reaction couples and phases predicted by the phase stability diagrams in Figure 4.27 and Figure 4.28 are given in Table 5.1 to Table 5.3.

Table 5.1: Predicted and observed interfacial phases in Aluminosilicate – CA reactions by Temperature. Reaction time = 4 hours.

Predicted Phases	1450°C	1500°C	1530°C
CA ($CaO.Al_2O_3$)	✓	✓	✓
CA2 ($CaO.2Al_2O_3$)	×	✓	✓
Melilite ($2CaO.Al_2O_3.SiO_2$)	×	×	✓
CA6 ($CaO.6Al_2O_3$)	×	×	×
Liquid oxide (~ $CaO.Al_2O_3.SiO_2$)	×	×	×
Corundum (Al_2O_3)	×	×	✓
Plagioclase ($CaO.Al_2O_3.2SiO_2$)	×	×	×
Mullite ($3Al_2O_3.2SiO_2$)	✓	✓	×

✓ = phase observed, × = phase not observed, not predicted = phase not predicted

Table 5.2: Predicted and observed interfacial phases in Aluminosilicate – CA2 reactions by Temperature. Reaction time = 4 hours.

Predicted Phases	1450°C	1500°C	1530°C	1550°C
CA2 ($CaO.2Al_2O_3$)	✓	✓	✓	✓
Melilite ($2CaO.Al_2O_3.SiO_2$)	×	Not predicted	Not predicted	Not predicted
CA6 ($CaO.6Al_2O_3$)	×	×	×	×
Liquid oxide (~ $CaO.Al_2O_3.SiO_2$)	×	×	×	×
Corundum (Al_2O_3)	✓	✓	✓	×
Plagioclase ($CaO.Al_2O_3.2SiO_2$)	×	×	×	Not predicted
Mullite ($3Al_2O_3.2SiO_2$)	✓	✓	✓	✓

✓ = phase observed, × = phase not observed, not predicted = phase not predicted

Table 5.3: Predicted and observed interfacial phases in Aluminosilicate – CA6 reactions by Temperature. Reaction time = 4 hours.

Predicted Phases	1450°C	1500°C	1550°C
CA6 ($CaO.6Al_2O_3$)	✓	✓	✓
Liquid oxide (~ $CaO.Al_2O_3.SiO_2$)	×	×	×
Corundum (Al_2O_3)	×	×	×
Plagioclase ($CaO.Al_2O_3.2SiO_2$)	×	×	Not Predicted
Mullite ($3Al_2O_3.2SiO_2$)	✓	✓	✓

✓ = phase observed, × = phase not observed, not predicted = phase not predicted

A composition corresponding to the original refractory was observed at or close to the interface in all of the reaction couples tested, this is likely due to the reaction not consuming all the refractory. At the higher reaction temperatures (1500°C and 1530°C) the formation of CA2 in the Aluminosilicate-CA reaction couples was observed. This is most likely due the higher reaction rates at higher temperatures as predicted by the Arrhenius equation (2-12). The only CA6 observed at any temperature in the Aluminosilicate reaction couples was unreacted CA6 at the interface of the CA6 reaction couples.

The formation of Corundum was only observed at 1530°C in the CA reaction couple and was not observed at all in the CA6 reaction couple. Corundum was observed in all the CA2 reaction couples, with the exception of 1550°C. Melilite ($2CaO.Al_2O_3.SiO_2$) was only observed at 1530°C in the Aluminosilicate-CA reaction couple. It can be seen from the phase stability diagrams in Figure 4.27 that Melilite is unstable at temperatures of 1500°C and above in the CA2 reaction couples and in all CA6 reaction couples. The absence of Melilite at the lower temperatures may be due to slow reaction kinetics.

Plagioclase ($CaO.Al_2O_3.2SiO_2$) was not observed at any reaction temperature (it was observed at longer reaction times, see section 5.1.2). However one set of spot analysis results (Aluminosilicate-CA2 at 1530°C position 3 in Figure 4.2) had a composition (86.22 Mass% Al_2O_3, 13.78 Mass% SiO_2) corresponding very closely to the phase boundary between Corundum and Anorthite (Plagioclase) on the Al_2O_3-SiO_2-CaO ternary phase diagram (Figure 2.12).

In Figure 4.6 elemental mapping of the Aluminosilicate - CA 1500°C reaction couple there was evidence of a high silicon phase in the reaction layer. This may be either Melilite or Plagioclase, suggesting these phases may have been present at 1500°C.

Liquid oxides were not observed in any reaction couple. This may be a result of no liquid oxides forming since the reaction couples were not at equilibrium or the liquid oxides becoming unstable when the samples were cooled to room temperature. Although the liquid oxides were not measured directly there are some other indicators of a liquid phase formation including: densification, pore penetration, curvature of phases formed and/ or the surrounding pores. The observation of phases with compositions corresponding to the liquid oxides, when at the reaction temperatures, also indicates that liquid oxides may have formed.

The liquid oxide phase has a composition of approximately 35 mass% SiO_2, 32 mass% Al_2O_3 and 33 mass% CaO. This composition is located between Melilite and Plagioclase on the ternary phase diagram (Figure 2.12). The presence of both Melilite and Plagioclase in the Aluminosilicate-CA reaction couple indicates a composition corresponding to the liquid oxide phase may have formed. In addition to this, the micrographs for the Aluminosilicate – CA reaction couple at 1500°C and 1530°C (Figure 4.2) appear to have dense curved reaction product phases and large rounded pores that may have been formed by liquid formation. It is important to note that pore formation can be caused by volume changes as well as liquid formation, however the rounded/ curved nature of the pores suggests liquid formation may be the cause.

Unreacted Mullite (i.e. corresponding to original refractory microstructure in Figure 3.10b) was observed close to the interface in all reaction couples with the exception of the 1530°C CA reaction couple. In the 1530°C CA reaction couple the mullite in this reaction couple had reacted to form corundum. The absence of many of the phases predicted by the phase stability diagrams in Figure 4.27 is most likely due to slow reaction kinetics and the phases may form at longer reaction times (section 5.12). The difficulty in the analysis due to uncertainty and localised nature of EDS spot analysis and the inability to conduct analysis in situ at the experimental temperatures may also contribute to the absence of certain phases from the results

A comparison of the phases observed in the Alumina Carbon – Calcium Aluminate reaction couples and phases predicted by thermodynamic analysis given in the phase stability diagrams in Figure 4.27 and Figure 4.28 are given in Table 5.4 to Table 5.6.

Table 5.4: Predicted and observed interfacial phases in Alumina Carbon – CA reactions by Temperature.

Predicted Phases	**1450°C**	**1500°C**	**1530°C**
CA ($CaO.Al_2O_3$)	×	×	✓
CA2 ($CaO.2Al_2O_3$)	✓	✓	✓
Melilite ($2CaO.Al_2O_3.SiO_2$)	×	×	Not Predicted
CA6 ($CaO.6Al_2O_3$)	×	×	×
Liquid oxide (~ $CaO.Al_2O_3.SiO_2$)	×	×	×
Corundum (Al_2O_3)	✓	✓	✓
Plagioclase ($CaO.Al_2O_3.2SiO_2$)	×	×	Not Predicted
Mullite ($3Al_2O_3.2SiO_2$)	×	×	×

✓ = phase observed, × = phase not observed, not predicted = phase not predicted

Table 5.5: Predicted and observed interfacial phases in Alumina Carbon – CA2 reactions by Temperature.

Predicted Phases	**1450°C**	**1500°C**	**1550°C**
CA2 ($CaO.2Al_2O_3$)	×	×	×
Melilite ($2CaO.Al_2O_3.SiO_2$)	×	Not Predicted	Not Predicted
CA6 ($CaO.6Al_2O_3$)	×	✓	✓
Liquid oxide (~ $CaO.Al_2O_3.SiO_2$)	×	×	×
Corundum (Al_2O_3)	✓	×	✓
Plagioclase ($CaO.Al_2O_3.2SiO_2$)	×	×	Not Predicted
Mullite ($3Al_2O_3.2SiO_2$)	×	×	×

✓ = phase observed, × = phase not observed, not predicted = phase not predicted

Table 5.6: Predicted and observed interfacial phases in Alumina Carbon – CA6 reactions by Temperature.

Predicted Phases	1450°C	1500°C	1550°C
CA6 ($CaO.6Al_2O_3$)	✓	✓	✓
Liquid oxide (~ $CaO.Al_2O_3.SiO_2$)	×	×	×
Corundum (Al_2O_3)	✓	✓	✓
Plagioclase ($CaO.Al_2O_3.2SiO_2$)	×	×	Not predicted
Mullite ($3Al_2O_3.2SiO_2$)	×	×	×

✓ = phase observed, × = phase not observed, not predicted = phase not predicted

The formation of CA2 was observed at all temperatures in the Alumina Carbon - CA reaction couples, indicating a faster rate of reaction than observed in the Aluminosilicate reaction couples. Although CA6 was not observed, a needle like morphology was observed in the Alumina - Carbon – CA2 reaction couple micrographs (Figure 4.3) at temperatures of 1500°C and 1550°C, this may be evidence of CA6 (as described in Table 2.2). Unreacted Corundum from the alumina grains in the refractory was observed at most temperatures.

No compositions corresponding to Melilite ($2CaO.Al_2O_3.SiO_2$) or Plagioclase ($CaO.Al_2O_3.2SiO_2$) were observed in the Alumina Carbon reaction couples at any of the temperatures. High silicon concentrations were observed in the reaction layer using elemental mapping of the Alumina – Carbon - CA reaction couples at 1500°C (Figure 4.9 to Figure 4.11). This indicates Melilite, Plagioclase or liquid oxide which all have high silicon compositions may have formed.

A phase with a composition corresponding to Melilite (Gehlenite - $2CaO.Al_2O_3.SiO_2$) was observed in the 1530°C reaction couple using both spot analysis (Figure 4.3, spot analysis position 2) and elemental mapping (Figure 4.9). Melilite at 1530°C is not stable and was not predicted in the phase stability diagrams, however this phase may have formed from cooling of the liquid oxide phase as the sample was cooled to room temperature for microscopy.

Liquid oxides were not observed in any Alumina - Carbon reaction couple, the possible reasons for this have discussed previous for the aluminosilicate reaction couples. The formation of a high silicon phase composition corresponding to liquid oxide may have formed at the experimental temperature as indicated by the presence of other high silicon phases such as Melilite and Plagioclase. Densification can be observed in the micrographs of the Alumina – Carbon - CA reaction couples (Figure 4.3). The observed low porosity reaction layers that engulf small amounts of unreacted Calcium Aluminates may be due to densification caused by a liquid phase forming and filling the pores in the reaction layer.

No mullite ($3Al_2O_3.2SiO_2$) was observed in any of the Alumina - Carbon reaction couples under the conditions tested. This is most likely due to the assumption used in the thermodynamic modelling that the refractory is of a uniform composition when the Alumina - Carbon refractory is a dual phase system. It was observed that the reactions and bonding only occurred where the Calcium Aluminates were in contact with the alumina grains. The SiO_2 content of the refractory is contained within the carbonaceous matrix phase, which was observed to have minimal reaction with the Calcium Aluminates. Therefore the assumption of SiO_2 reacting with the Calcium Aluminates and alumina grains to form mullite ($3Al_2O_3.2SiO_2$) may not be accurate. The modelling was repeated assuming the reaction occurred between the Corundum (alumina grains in the refractory) and the Calcium Aluminates. The isopleth produced (Figure 4.26) shows that Mullite was no longer predicted as a product in the reaction layer.

5.1.2. Reaction Couple Phase Formation with Time

The time dependency for the formation of the various phases predicted by the phase stability diagrams (Figure 4.27 and Figure 4.28) was tested as shown in Tables 5.7 to 5.9. It was found that some phases take a significant amount of time to form due to slow reaction kinetics. The formation of CA6, Melilite, Plagioclase and Corundum were all found to be time dependant.

Table 5.7: Predicted and observed interfacial phases in Aluminosilicate – CA reaction couples by Time.

Predicted Phases	4 hours	8 hours	12 hours	18 hours	24 hours
CA ($CaO.Al_2O_3$)	×	×	×	✓	✓
CA2 ($CaO.2Al_2O_3$)	✓	✓	✓	✓	✓
Melilite ($2CaO.Al_2O_3.SiO_2$)	×	✓	×	×	×
CA6 ($CaO.6Al_2O_3$)	×	×	×	×	×
Liquid oxide($CaO.Al_2O_3.SiO_2$)	×	×	×	×	×
Corundum (Al_2O_3)	×	✓	✓	✓	✓
Plagioclase ($CaO.Al_2O_3.2SiO_2$)	×	×	×	×	✓
Mullite ($3Al_2O_3.2SiO_2$)	✓	✓	✓	×	×

✓ = phase observed, × = phase not observed, not predicted = phase not predicted

Table 5.8: Predicted and observed interfacial phases in Aluminosilicate – CA2 reaction couples by Time.

Predicted Phases	4 hours	8 hours	12 hours	18 hours	24 hours
CA2 ($CaO.2Al_2O_3$)	✓	✓	✓	×	×
CA6 ($CaO.6Al_2O_3$)	×	✓	✓	✓	✓
Liquid oxide($CaO.Al_2O_3.SiO_2$)	×	×	×	×	×
Corundum (Al_2O_3)	✓	✓	✓	✓	✓
Plagioclase ($CaO.Al_2O_3.2SiO_2$)	×	×	×	×	×
Mullite ($3Al_2O_3.2SiO_2$)	✓	✓	✓	×	×

✓ = phase observed, × = phase not observed, not predicted = phase not predicted

Table 5.9: Predicted and observed interfacial phases in Aluminosilicate – CA6 reaction couples by Time.

Predicted Phases	4 hours	8 hours	12 hours	18 hours	24 hours
CA6 ($CaO.6Al_2O_3$)	✓	✓	✓	✓	×
Liquid oxide($CaO.Al_2O_3.SiO_2$)	×	×	×	×	×
Corundum (Al_2O_3)	×	×	×	✓	✓
Plagioclase($CaO.Al_2O_3.2SiO_2$)	×	×	×	×	×
Mullite ($3Al_2O_3.2SiO_2$)	✓	✓	✓	✓	✓

✓ = phase observed, × = phase not observed, not predicted = phase not predicted

In Table 5.7 the presence of CA at the interface at the longer reaction times of 18 and 24 hours is due to spalling of unreacted material bonded to the reaction layer. The formation of CA2 occurs at all reaction times for the Aluminosilicate - CA reaction couples. CA6 does not form in these reaction couples at any of the reaction times tested. This is most likely due to the high concentration of calcium at the interface forming all the CaO rich phases first. CA6 formed after 8 hours in the Alumninosilicate-CA2 reaction couples and can be seen as the needle structure in Figure 4.13.

Corundum formed at shorter reaction times in the CA and CA2 reaction couples than the CA6 reaction couples. Fick's 1st law of diffusion (Equation 2-9 reproduced below) shows that the lower concentration of CaO in the CA6 compared to CA and CA2 (17 mol% compared to 50 mol% and 33 mol% respectively) results in a smaller ∂C and therefore a lower flux (J) (i.e. rate of mass transfer across an interface in $mol.m^{-2}.s^{-1}$) i.e. a slower rate of reaction.

$$J = -D\frac{\partial C}{\partial x}$$

Melilite ($2CaO.Al_2O_3.SiO_2$) was observed at 8 hours in the Aluminosilicate-CA reaction couple but it was not observed at longer reaction times using spot analysis. Plagioclase ($CaO.Al_2O_3.2SiO_2$) was only observed at a reaction time of 24 hours in the Aluminosilicate - CA reaction couple. High silicon phases observed in elemental mapping of the all Aluminosilicate reaction couples (Figure 4.19 to Figure 4.21) indicates high silicon phases such as Melilite or Plagioclase may have formed in the reaction layer for these reaction couples.

High silicon phases observed in the elemental maps of the Aluminosilicate - CA2 reaction couples from 12 hours onward indicates that high silicon phases such as Plagioclase may have formed in the reaction layer. High silica phases observed close to the phase boundaries with Gehlenite (Hibonite in Figure 4.13 & Table 4.2: CA2, 12 hours, spot no. 3) and Anorthite (Corundum in Figure 4.13 & Table 4.2: CA6, 24 hours, spot no. 2) were measured. Given the inherent uncertainty in EDS analysis and the inability to conduct EDS in situ at the experimental temperatures the presence of phases with silica compositions close to phase boundaries suggest the formation of Melilite, Plagioclase and liquid oxide may have occurred but were not identified.

Table 5.10: Predicted and observed interfacial phases in Alumina - Carbon – CA reaction couples by Time.

Predicted Phases	4 hours	8 hours	12 hours	18 hours	24 hours
CA ($CaO.Al_2O_3$)	×	✓	×	×	×
CA2 ($CaO.2Al_2O_3$)	✓	✓	✓	✓	✓
Melilite ($2CaO.Al_2O_3.SiO_2$)	×	×	✓	×	×
CA6 ($CaO.6Al_2O_3$)	×	×	✓	✓	✓
Liquid oxide($CaO.Al_2O_3.SiO_2$)	×	×	×	×	×
Corundum (Al_2O_3)	✓	✓	✓	✓	✓
Plagioclase ($CaO.Al_2O_3.2SiO_2$)	×	×	×	×	×
Mullite ($3Al_2O_3.2SiO_2$)	×	×	×	×	×

✓ = phase observed, × = phase not observed, not predicted = phase not predicted

Table 5.11: Predicted and observed interfacial phases in Alumina - Carbon – CA2 reaction couples by Time.

Predicted Phases	4 hours	8 hours	12 hours	18 hours	24 hours
CA2 ($CaO.2Al_2O_3$)	×	×	×	×	×
CA6 ($CaO.6Al_2O_3$)	✓	✓	✓	✓	✓
Liquid oxide($CaO.Al_2O_3.SiO_2$)	×	×	×	×	×
Corundum (Al_2O_3)	×	✓	✓	✓	✓
Plagioclase ($CaO.Al_2O_3.2SiO_2$)	×	×	×	×	×
Mullite ($3Al_2O_3.2SiO_2$)	×	×	×	×	×

✓ = phase observed, × = phase not observed, not predicted = phase not predicted

Table 5.12: Predicted and observed interfacial phases in Alumina - Carbon – CA6 reaction couples by Time.

Predicted Phases	4 hours	8 hours	12 hours	18 hours	24 hours
CA6 ($CaO.6Al_2O_3$)	✓	✓	✓	✓	✓
Liquid oxide($CaO.Al_2O_3.SiO_2$)	×	×	×	×	×
Corundum (Al_2O_3)	✓	✓	✓	✓	✓
Plagioclase ($CaO.Al_2O_3.2SiO_2$)	×	×	×	×	×
Mullite ($3Al_2O_3.2SiO_2$)	×	×	×	×	×

✓ = phase observed, × = phase not observed, not predicted = phase not predicted

The formation of CA2 in the Alumina – Carbon - CA reaction couple was observed to occur at all reaction times tested. CA6 was found to form from 12 hours in the Alumina Carbon - CA reaction couple and at all reaction times in the Alumina – Carbon - CA2 reaction couple. The formation of Corundum was observed to occur in all reaction couples at reactions of 8 hours or longer.

Melilite ($2CaO.Al_2O_3.SiO_2$) was only observed in the Alumina - Carbon - CA reaction couple at 12 hours and Plagioclase was not observed in any of the reaction couples. However elemental mapping (Figure 4.20 – Figure 4.22) indicates high silicon phases are present in the reaction layer from 4 hours in the Alumina – Carbon - CA reaction couple (Figure 4.20) and 8 hours in the Alumina - Carbon-CA2 reaction couple (Figure 4.21). These high silicon phases may be Melilite or Plagioclase as both phases have high silicon contents.

Liquid oxides were not observed at any reaction time. This may be a result of no liquid oxides forming since the reaction couples were not at equilibrium or the liquid oxides becoming unstable when the samples were cooled to room temperature. The formation of liquid oxides is indicated by:

- The presence of high silicon phases shown by elemental mapping and the presence of Melilite indicates that phases with a composition corresponding to the liquid oxide phase are likely to have formed.
- The formation of high density reaction layers with rounded pores (Figure 4.16) in the Alumina – Carbon - CA reaction couples
- Densification in the Alumina - Carbon - CA2 reaction couples by the liquid phase filling gaps between the CA6 needles appears to have occurred at the 18 hour reaction time (Figure 4.16).

5.1.3. Phase Identification and Energy Dispersive Spectroscopy Error

In addition the phase identification issues discussed in section 5.1.1 and 5.1.2 there is also a general issue with EDS analysis itself. EDS compositions can have significant uncertainties as a result of the electron beam generating characteristic spectrums of "unseen" elements or phases due to sub surface beam penetration or the beam overlapping a phase boundary of a two phase region (e.g.. the matrix phase regions of each refractory) . This uncertainty combined with compositions that represent a phase near a phase boundary transition can result in a mis-identification of the phase. Ideally these phase identification problems would be overcome by carrying out x-ray diffraction analysis. The nature of the samples in general, and the reaction interface in particular, precluded such analysis.

5.1.4. Alumina - Carbon Refractory Mass Loss

The literature indicates that some oxides such as SiO_2 used in refractories can become unstable at high temperatures in the presence of carbon [66]. The reactions used to describe the silica depletion of the coke ash may also be used to describe SiO_2 reduction reactions in the Alumina - Carbon refractory, as shown by equations 2-4, 2-6 and 2-7 [13-14] reproduced below.

$$SiO_{2(s)} + C_{(s)} = SiO_{(g)} + CO_{(g)}$$

$$2SiO_{2(s)} + SiC_{(s)} = 3SiO_{(g)} + CO_{(g)}$$

$$SiC_{(s)} + CO_{(g)} = SiO_{(g)} + 2C_{(graphite)}$$

The proximity of the silicon depletion to the refractory surface where any $SiO_{(g)}$ formed and is able to diffuse out of the refractory, suggests reactions 2-4, 2-6 and 2-7 are likely mechanisms of the silicon depletion and weight loss observed.

5.2. Kinetics of Hearth Refractory and Coke Ash Interactions

The relative rates of reaction for each reaction couple can be seen in Figure 4.4 – Figure 4.5 and Figure 4.15 – Figure 4.16. It was found that the reaction rates increased with CaO content in the calcium aluminates and were higher in the Alumina - Carbon refractory. The kinetics of formation of a reaction product on a surface is commonly analysed by considering the counter diffusion of cations through the layer as detailed in section 2.6. The growth of the reaction layer can be represented by the linear, logarithmic and parabolic rate laws given in section 2.6.7. These models will be used to understand the kinetics of the refractory – calcium aluminate reactions.

5.2.1. Aluminosilicate Refractory Reaction Kinetics

The reactions at 1500°C between the Aluminosilicate refractory and the Calcium Aluminates (CA, CA2 & CA6) were tested for linear, parabolic and logarithmic kinetic behaviour (equation 2-14, 2-16 and 2-17 respectively). The R^2 values were used as the discriminating parameter for deciding best fit in Figure 5.1 to Figure 5.9. The regression lines and equations as well as their respective R^2 values are given in each figure. Since x^2 was plotted for the parabolic rate law tests a linear regression fit is expected. The R^2 values of 0.945 (Figure 5.2) and 0.940 (Figure 5.5) for the CA and CA2 reaction couples indicates a good fit of the experimental data to the regression line for the linear rate law (equation 2-16) [58, 59].

$$x = k_{lin}t + A$$

The linear rate law test also had more points within one standard deviation of the regression fits then the tests for the logarithmic and parabolic rate laws for all the Calcium Aluminates tested. This suggests the linear rate law model has the smallest error for the Aluminosilicate – Calcium Aluminate systems tested. The CA6 reaction couples had poor fits to the logarithmic, linear and parabolic rate laws with R^2 values of 0.672, 0.682 and 0.687 respectively. The poor fit is due to the very small reaction layer observed and small data set caused by the reaction layer only forming at the longer reaction times.

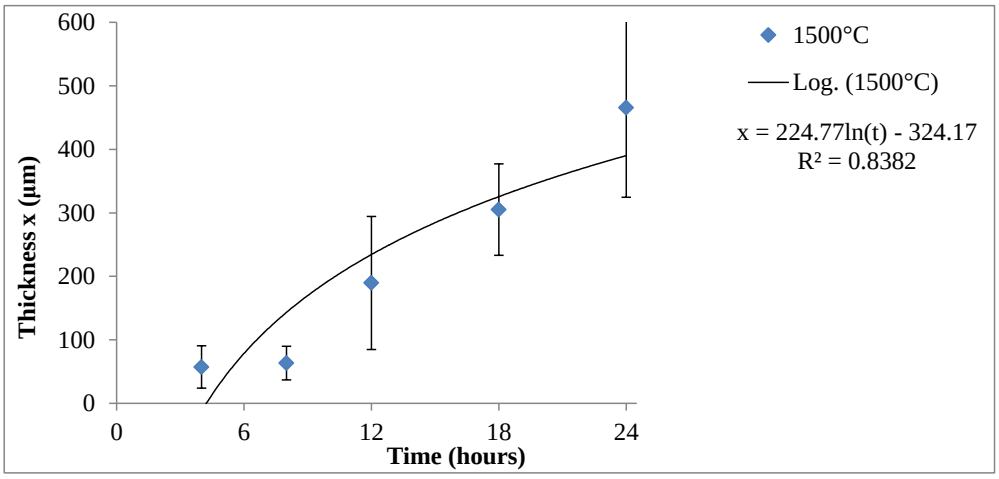

Figure 5.1: Aluminosilicate – CA reaction couples thickness by time. The solid line represents the best fit to the logarithmic rate law.

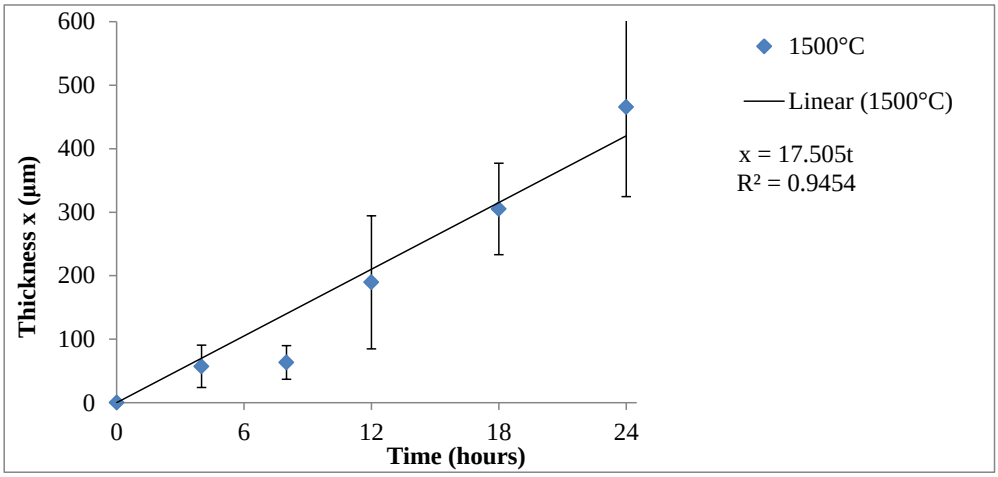

Figure 5.2: Aluminosilicate – CA reaction couples thickness by time. The solid line represents the best fit to the linear rate law.

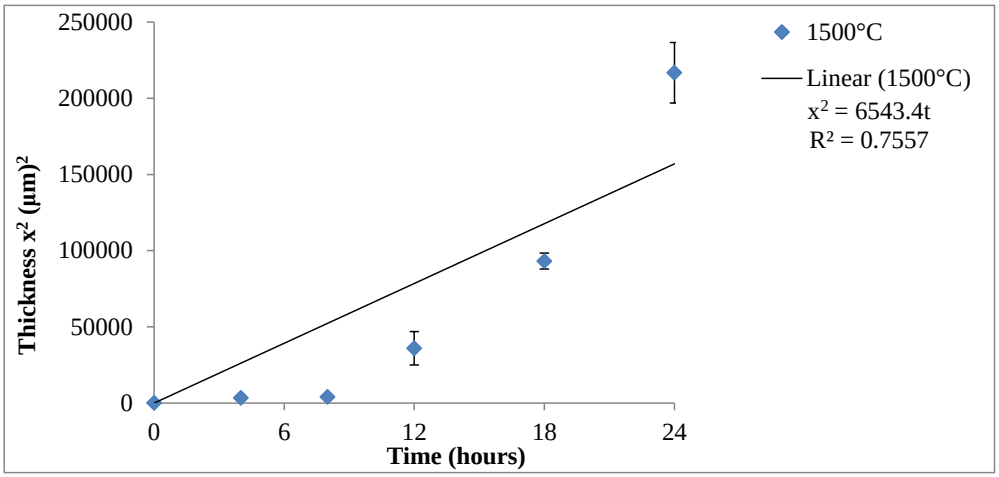

Figure 5.3: Aluminosilicate – CA reaction couples thickness by time. The solid line represents the best fit to the parabolic rate law.

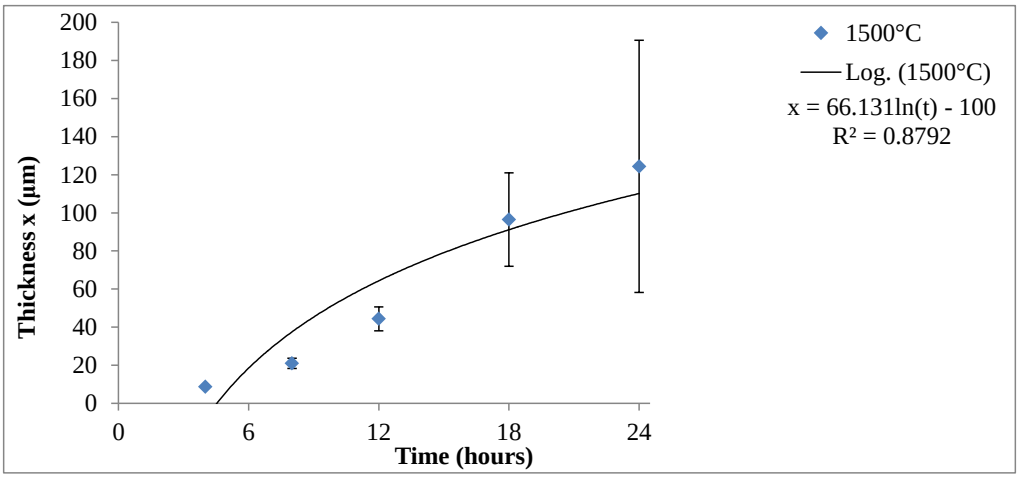

Figure 5.4: Aluminosilicate – CA2 reaction couples thickness by time. The solid line represents the best fit to the logarithmic rate law.

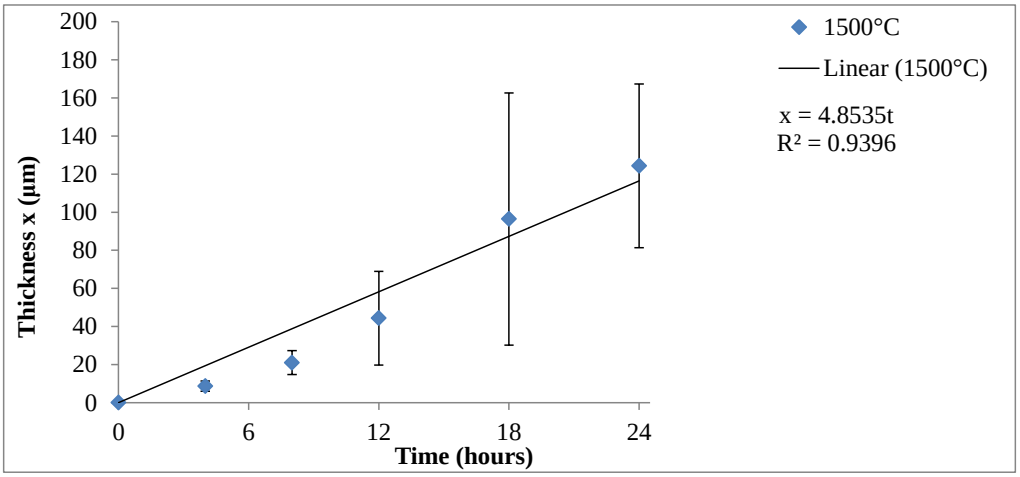

Figure 5.5: Aluminosilicate – CA2 reaction couples thickness by time. The solid line represents the best fit to the linear rate law.

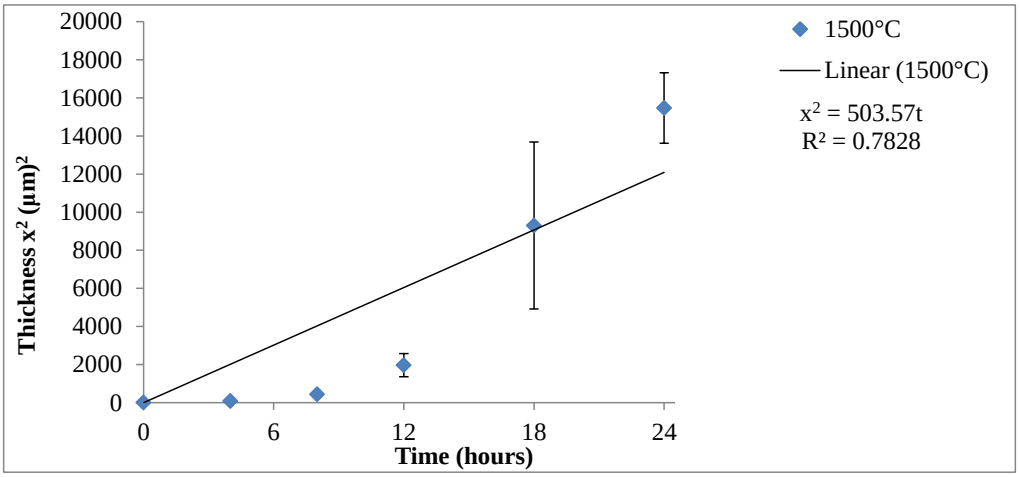

Figure 5.6: Aluminosilicate – CA2 reaction couples thickness by time. The solid line represents the best fit to the parabolic rate law.

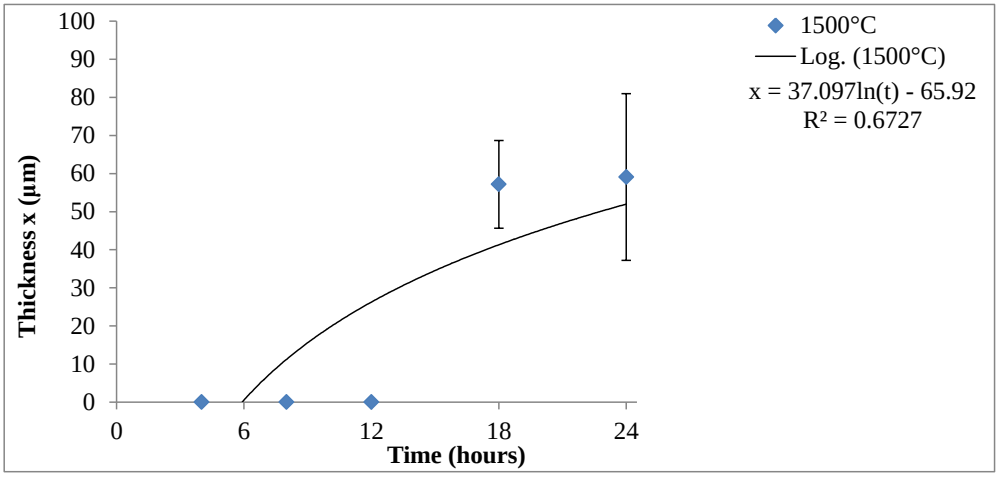

Figure 5.7: Aluminosilicate – CA6 reaction couples thickness by time. The solid line represents the best fit to the logarithmic rate law.

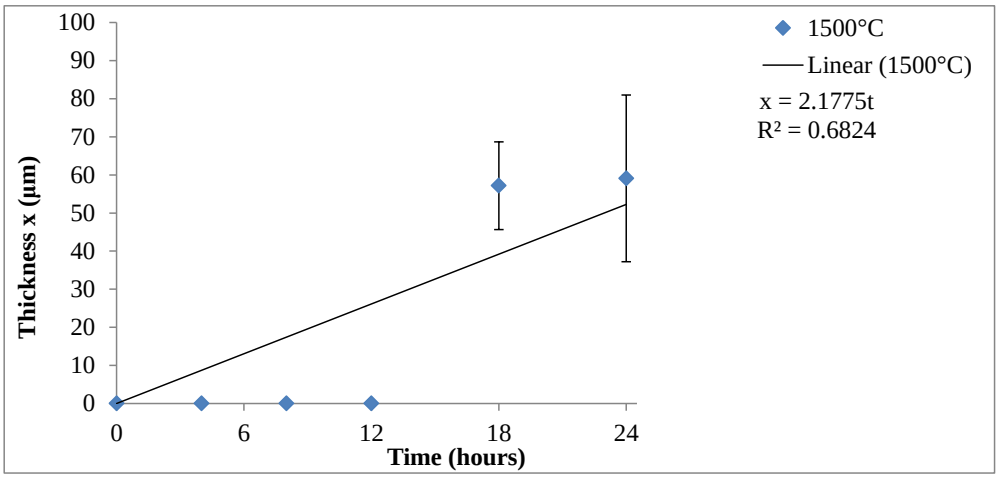

Figure 5.8: Aluminosilicate – CA6 reaction couples thickness by time. The solid line represents the best fit to the linear rate law.

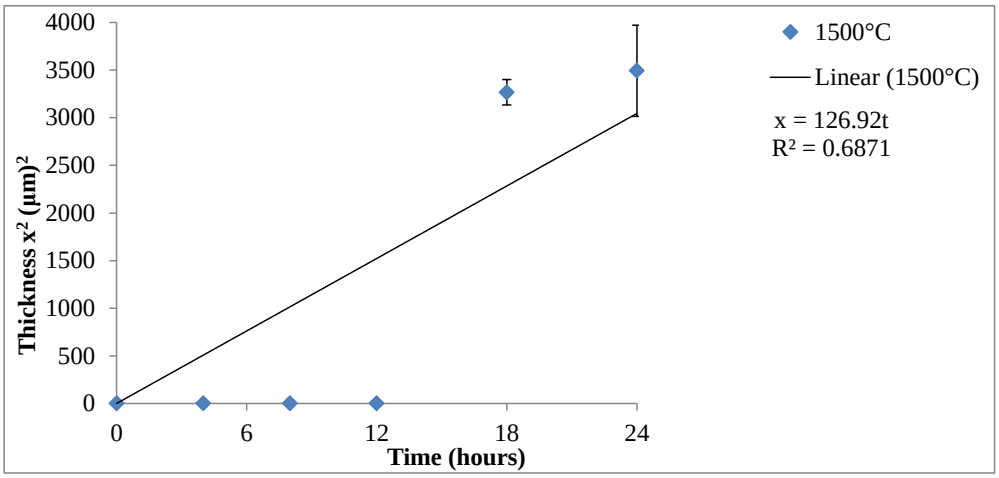

Figure 5.9: Aluminosilicate – CA6 reaction couples thickness by time. The solid line represents the best fit to the parabolic rate law.

Linear reaction kinetics in solid state systems occur when the reaction layers have high porosity, cracking, spalling or consist of a liquid phase. These defects prevent the reaction layer from slowing the reaction kinetics. The CA and CA2 reaction couples were observed to form reaction layers with high porosity at temperatures of 1500°C or greater as shown in Figure 4.2 and Figure 4.15. Spalling and cracking of the reaction layer was also observed at longer reaction times (>12 hours) as seen in Figure 4.15. The formation of rounded pores and the measurement of phase compositions corresponding to Anorthite ($CaO.Al_2O_3.2SiO_2$) and Gehlenite ($2CaO.Al_2O_3.SiO_2$) (Table 4.2), which are liquids at the reaction temperatures, suggests that liquid phases may also have been present.

The CA6 – Aluminosilicate reaction were found to have a poor fit to the logarithmic, linear and parabolic rate laws. This poor fit is likely due to the errors associated with measuring the small thickness and the smaller number of thickness measurements. Measurement of the reaction layer in the CA6 – Aluminosilicate reaction couples was difficult as the boundary of the reaction layer was not clearly defined with little contrast visible between the bulk CA6 and the calcium depleted zone in the SEM micrographs (Figure 4.13). The reaction layer boundary was measured from the point where an increase in porosity was visible in the micrographs.

The CA6 – Aluminosilicate reaction couples were observed to form a much smaller reaction layer consisting mostly of a high porosity region near the interface depleted of calcium. This is consistent with the trend of decreasing reactivity with increasing alumina content of the Calcium Aluminates. The likely cause of the reducing reactivity is due to the lower concentration gradient (∂C) reducing the driving force for diffusion (as shown in equation 2-9 [50]) as the alumina content increases.

$$J = -D\frac{\partial C}{\partial x}$$

Since the flux (J) the amount of mass transferred per unit area per unit time, the rate of reaction with CA6 is dependent on the surface contact. Although CA6 did achieve a surface finish with a roughness of 1μm or less (Table 3.12), it was also found to have a much higher roughness compared to the other calcium aluminates and consequently would have a smaller contact area in the reaction couples than the other materials.

A common approach to predicting the effect of temperature on the product layer formation is to use an Arrhenius relationship detailed in equation 2-16 [58-59]

$$k = k_0 e^{\left(-\frac{E}{RT}\right)}$$

From equation 2-16 it can be seen that increasing temperature increases *k* exponentially. Thus the growth rate of the reaction layer increases with temperature, as observed in Figure 4.4. This is due to the increased mobility of the diffusion cations in the Calcium Aluminates and Aluminosilicate at higher temperatures [58-59]. Estimations of the k_0 and E values (given in Table 5.1) were obtained from analysis of the slope in Figure 5.4 and Figure 5.6. However, given the limited data, these values have a high uncertainty associated with them and should only be considered indicative.

Table 5.13: k_0 and Activation Energy for reaction layer formation for all CA_x - Aluminosilicate reaction couples.

Calcium Aluminate	k_0	E
CA	$3.24\times 10^{24}\ \mu m s^{-1}$	797 kJ mol^{-1}
CA2	$8.22 \times 10^{16}\ \mu m s^{-1}$	556 kJ mol^{-1}
CA6	$1.298 \times 10^{11}\ \mu m s^{-1}$	365 kJ mol^{-1}

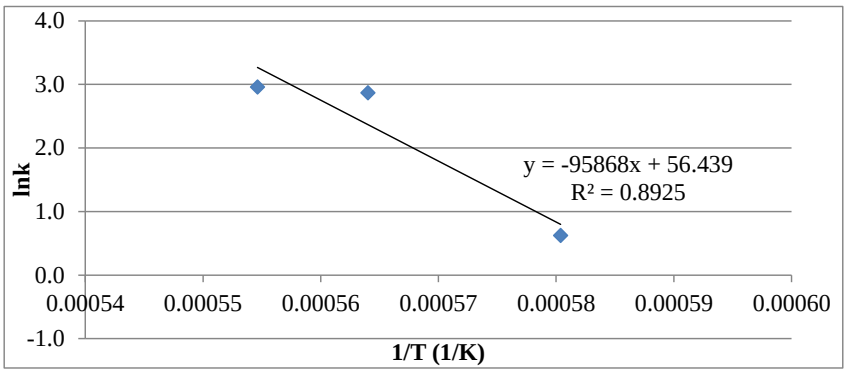

Figure 5.10: Arrhenius plot for the linear rate constant k_0 in the Aluminosilicate – CA reaction couples

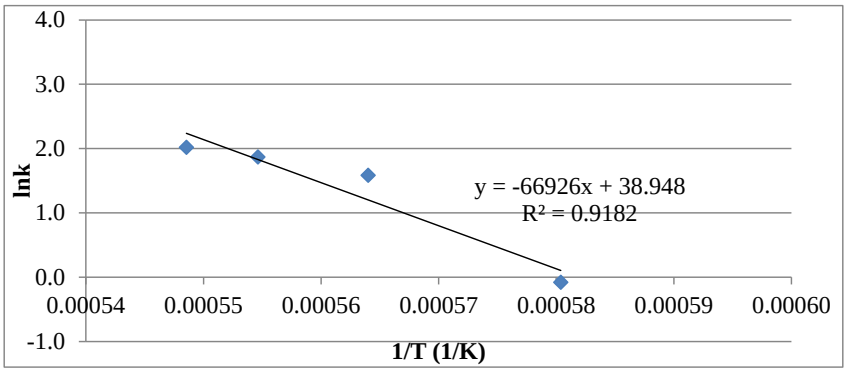

Figure 5.11: Arrhenius plot for the linear rate constant k_0 in the Aluminosilicate – CA2 reaction couples

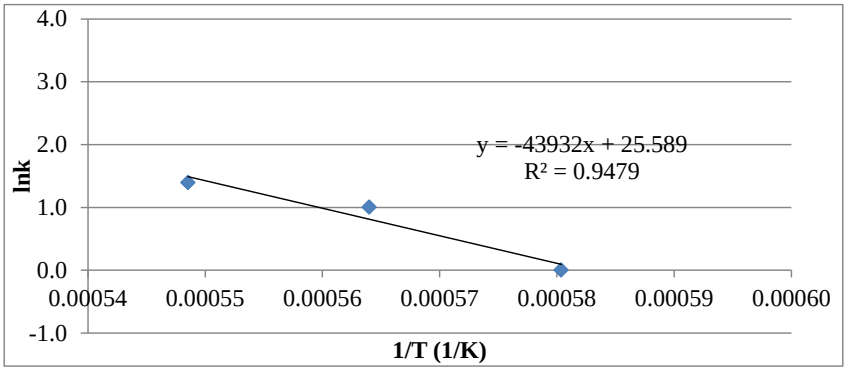

Figure 5.12: Arrhenius plot for the linear rate constant k_0 in the Aluminosilicate – CA6 reaction couples

5.2.2. Alumina-Carbon Refractory Reaction Kinetics

The reactions between the Alumina-Carbon refractory and the Calcium Aluminates (only CA & CA2 as no reaction was observed with CA6) were also tested for linear, parabolic and logarithmic kinetic behaviour (equation 2-14, 2-16 and 2-17 respectively). The R^2 values and the number of points within one standard deviation were used as the discriminating parameter for deciding best fit in Figure 5.13 to Figure 5.18. The regression lines, error bars and equations as well as their respective R^2 values are given in each figure. Since x^2 was plotted for the parabolic rate law tests a linear regression fit is expected. It was determined that the logarithmic rate law (equation 2-17) [58, 59] had these best fit for both the CA and CA2 with R^2 values of 0.9542 (Figure 5.13) and 0.8203 (Figure 5.16). Although the R^2 values for the parabolic rate law tests (0.974 for CA on Figure 5.15 and 0.929 for CA2 on Figure 5.18) were higher all the points on the logarithmic rate law tests were within one standard deviation of the regression fit suggesting there is less error in the logarithmic rate law model tested.

$$x = k_{log} log t + C$$

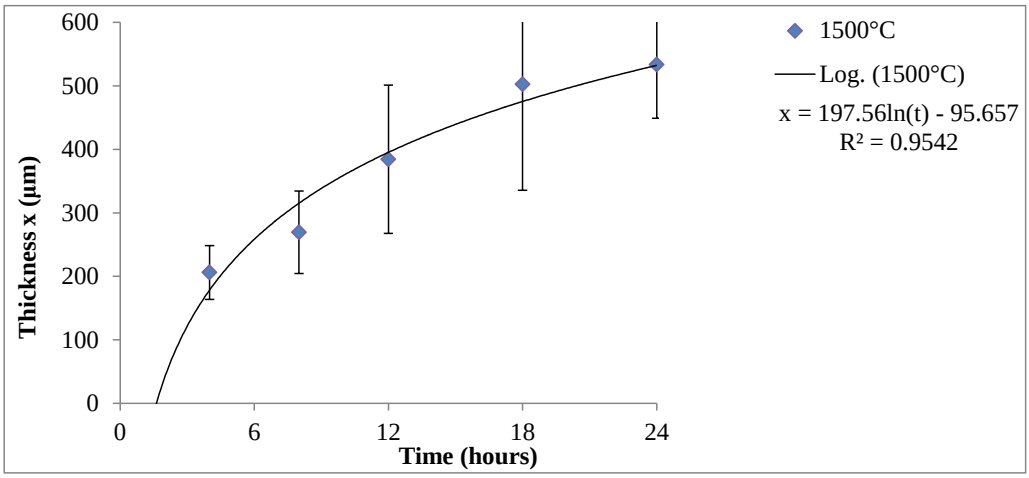

Figure 5.13: Alumina-Carbon – CA reaction couples thickness by time. The solid line represents the best fit to the logarithmic rate law.

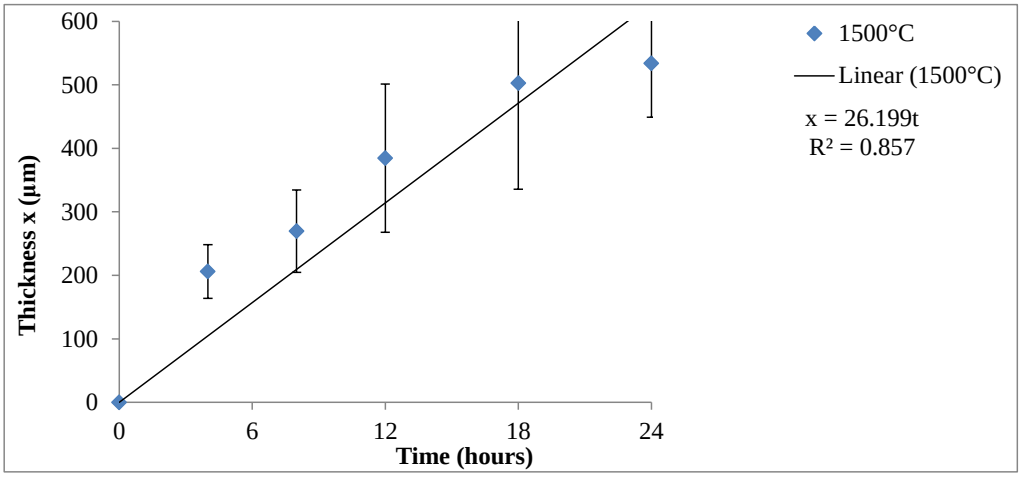

Figure 5.14: Alumina-Carbon – CA reaction couples thickness by time. The solid line represents the best fit to the linear rate law.

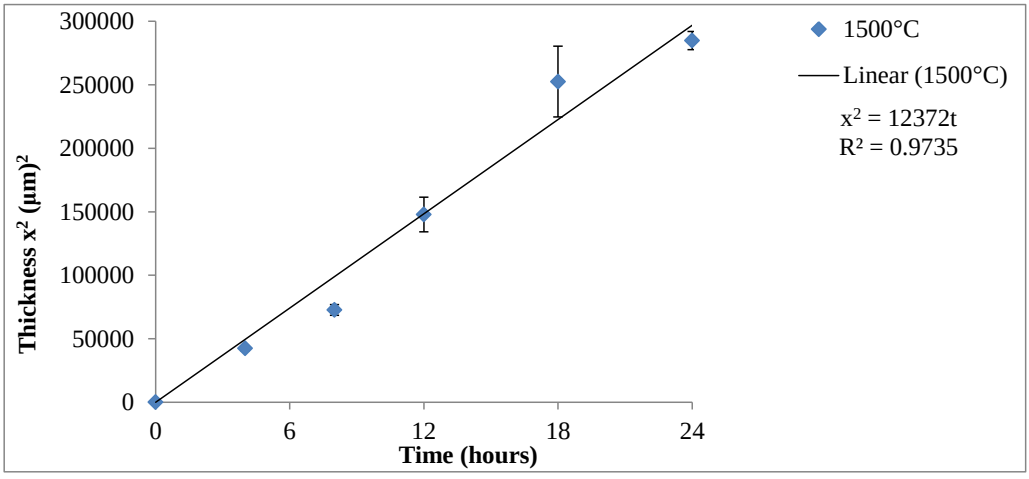

Figure 5.15: Alumina-Carbon – CA reaction couples thickness by time. The solid line represents the best fit to the parabolic rate law.

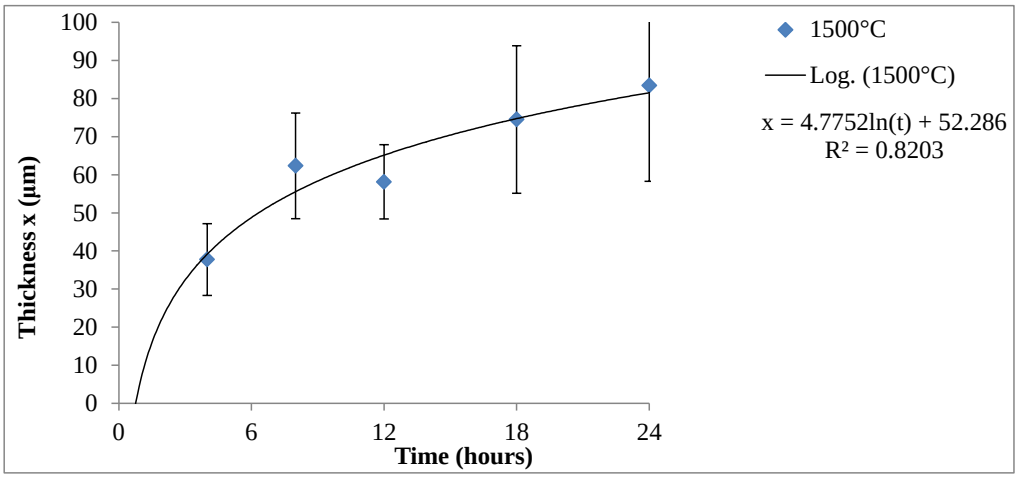

Figure 5.16: Alumina-Carbon – CA2 reaction couples thickness by time. The solid line represents the best fit to the logarithmic rate law.

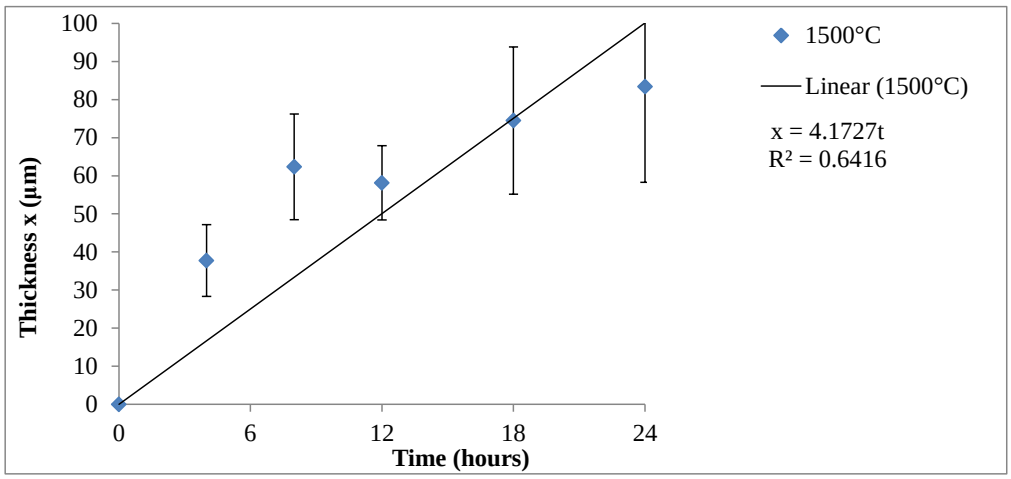

Figure 5.17: Alumina-Carbon – CA2 reaction couples thickness by time. The solid line represents the best fit to the linear rate law.

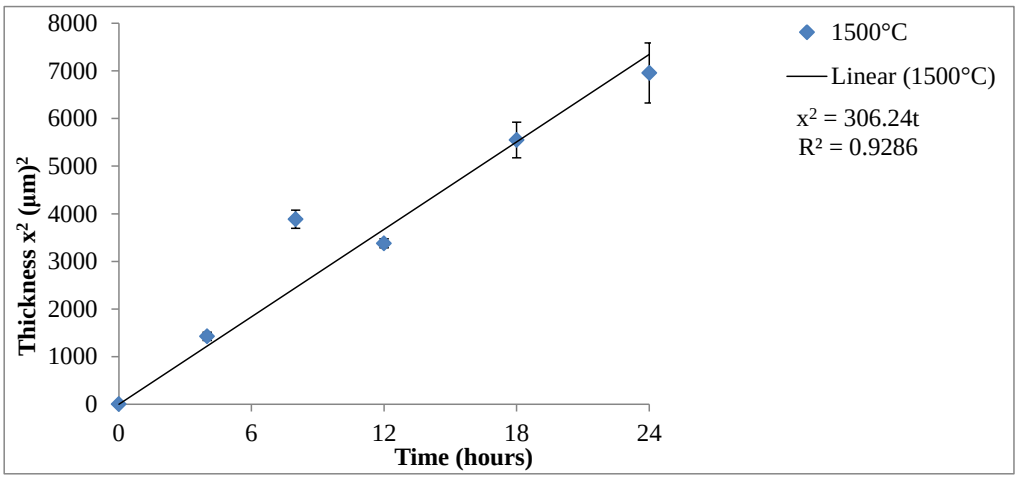

Figure 5.18: Alumina-Carbon – CA2 reaction couples thickness by time. The solid line represents the best fit to the parabolic rate law.

Logarithmic reaction kinetics in solid state systems occurs when the reaction layers consist of a continuous layer with minimal defects which slows the rate of reaction once formed. Although spalling was observed in the CA - Alumina - Carbon reaction couples the reaction layer thickness was greater and the porosity was generally lower than that observed in the Aluminosilicate reaction couple under the same conditions (Figure 4.16 and Figure 4.15 respectively). The CA2 – Alumina - Carbon reaction couples were observed to form higher density reaction layers at longer reaction times (>18hours). These observations correspond with the parabolic rate determined from the kinetic analysis.

Very little evidence of any reaction was observed in the CA6 - Alumina - Carbon reaction couples. Therefore no testing for the fit of logarithmic, linear and parabolic rates laws could be conducted. The absence of any measureable reaction layer is caused difficulties in measurement. The low reactivity of the CA6 is likely caused by low concentration gradients and contact area as discussed previously for the CA6-Aluminosilicate reaction couples (section 5.2.1).

The rate of reaction layer formation has an Arrhenius relationship with temperature due to the increased mobility of the diffusion cations, as previously discussed in section 5.1.1. Therefore the growth rate of the reaction layer increases with temperature as observed in Figure 4.5. Estimations of the k_0 and E values (given in Table 5.1) were obtained from analysis of the slope in Figure 5.4 and Figure 5.6. However, given the limited data, these values have a high uncertainty associated with them and should be only considered indicative.

Table 5.14: k_0 and Activation Energy for reaction layer formation for all CA_x – Alumina-Carbon reaction couples.

Calcium Aluminate	k_0	E
CA	$3.28\times 10^{29}\ \mu m s^{-1}$	881 kJ mol^{-1}
CA2	$2.33\times 10^{26}\ \mu m s^{-1}$	829 kJ mol^{-1}
CA6	$4.06\times 10^{27}\ \mu m s^{-1}$	919 kJ mol^{-1}

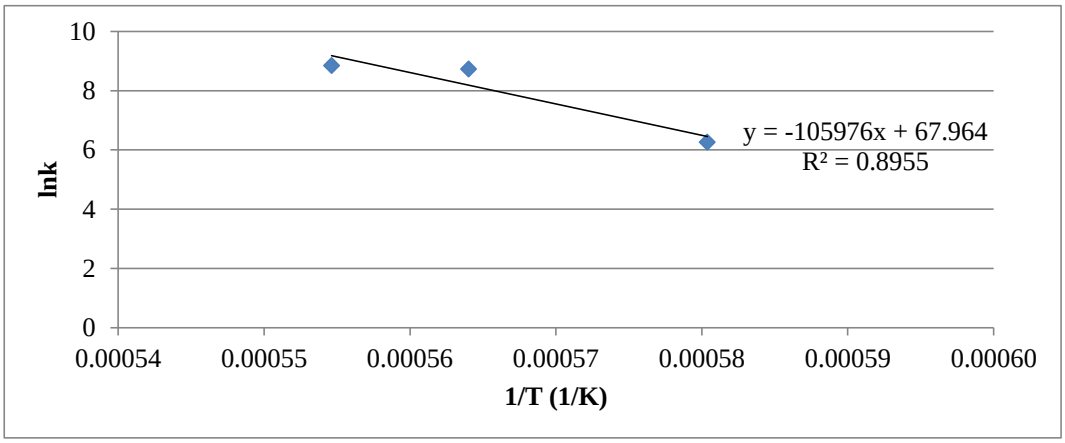

Figure 5.19: Arrhenius plot for the linear rate constant k_0 in the Alumina-Carbon – CA reaction couples

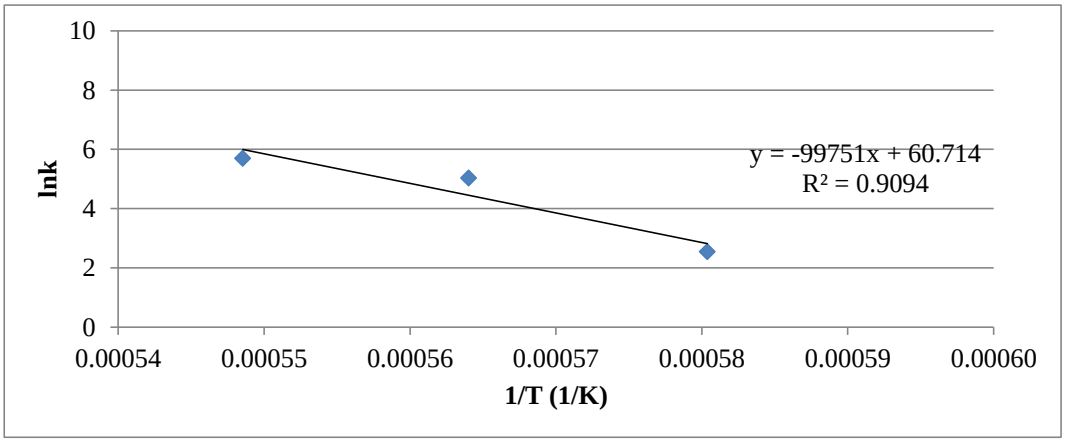

Figure 5.20: Arrhenius plot for the linear rate constant k_0 in the Alumina-Carbon – CA2 reaction couples

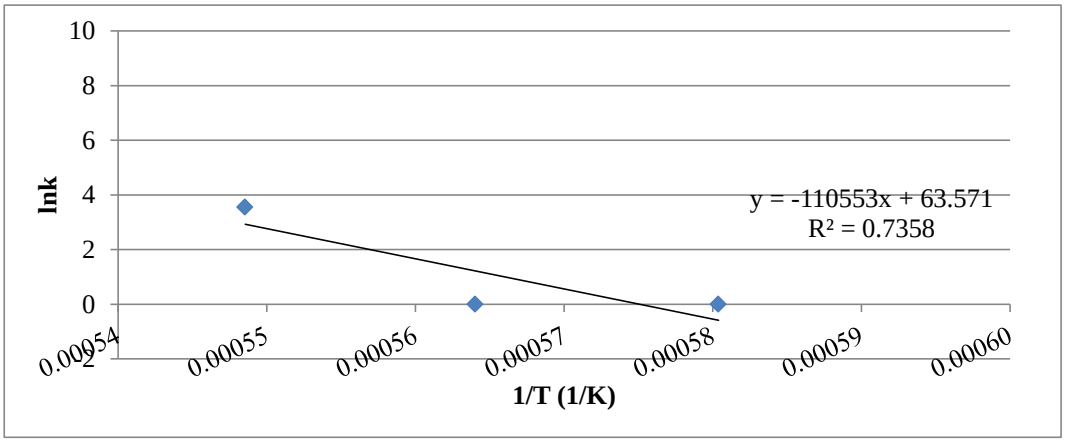

Figure 5.21: Arrhenius plot for the linear rate constant k_0 in the Alumina-Carbon – CA6 reaction couples

5.2.3. Identification of the original Reaction Couple Interface

Identification of the original interface using platinum wire was only carried out on the CA and CA2 reaction couples tested for 18 hours at 1500°C. The results of the reaction couples with platinum wire interface indicator are given in Figure 5.22. The micrographs in Figure 5.22 show the platinum wire at various stages of engulfment by the reaction layer formed predominately on the surface of the Calcium Aluminates. A representation of the Kirkendall effect consists of the inert wires moving in the opposite direction to the net direction of diffusion [70]. This indicates the rate of diffusion into the refractories is greater than the rate of diffusion into the Calcium Aluminates for all the reaction couples where a reaction layer is formed.

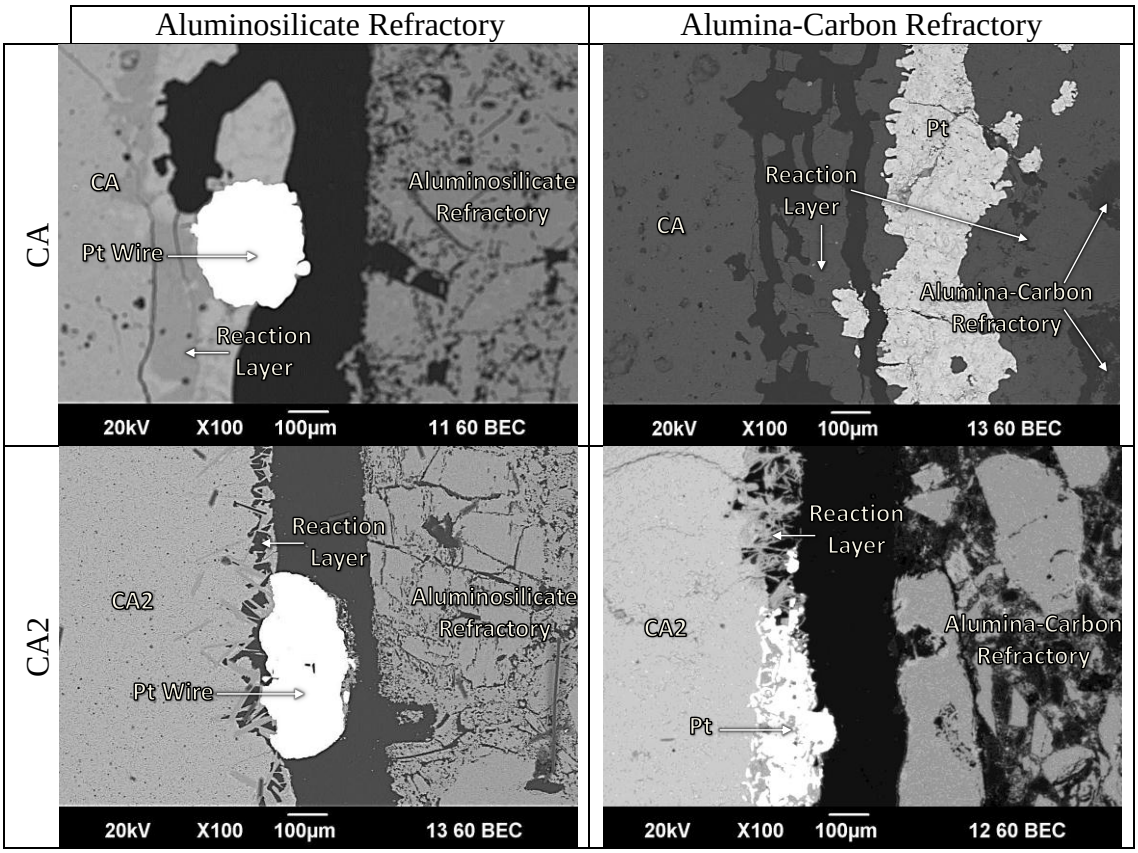

Figure 5.22: Micrographs of reaction couples tested at 1500°C for 18 hours with platinum wire located at the interface between the Calcium Aluminate and refractory.

The net direction of diffusion can also be determined by comparing the diffusion coefficients for calcium, aluminium and silicon in alumina at a given temperature, as shown in Table 2.18. It can be seen from this data that the diffusion coefficient of calcium was approximately $1x10^3$ greater than the coefficients for silicon and aluminium.

This is consistent with the results of the inert wire test of the Kirkendall effect and is further supported by the observed presence of calcium in the refractory at the higher reaction temperatures (Figure 4.6 – Figure 4.11) and longer reaction times (Figure 4.19 – Figure 4.24).

The diffusion coefficients and net direction of diffusion can be used to predict the formation of a calcium depletion zone at the surface of the Calcium Aluminates as observed in Figure 4.6 to Figure 4.11 and Figure 4.19 to Figure 4.24. The missing calcium no longer dilutes the aluminium and therefore the elemental maps show high aluminium concentrations in this region. The experimental observations of the movement of calcium and silicon were consistent with the diffusion data.

5.2.4. Refractory – Coke ash reaction kinetics in the blast furnace hearth.

The experimental methodology used for this study represents the situation in the hearth in which coke ash comes into contact with the hearth refractory without any molten iron present at the interface. Due to the non-wetting behaviour of iron melts with Calcium Aluminates [71], Aluminosilicates [72], carbonaceous refractories [66] and alumina [73], the absence of an iron melt at the interface is believed to be a good assumption for localised conditions within the hearth.

Alumina and Aluminosilicates can react with iron melts to form Hercynite ($FeAl_2O_4$) at oxygen potentials of $P_{O_2} = 4 \times 10^{-5} Pa$ [72]. However, due to the highly reducing environment in the blast furnace hearth this is unlikely to occur. The molten iron in the blast furnace hearth also contains [Si] up to 0.9% at 1550°C [74]. The [Si] may react with the Calcium Aluminates and refractory and assist in the formation of low melting point phases such as Anorthite ($CaO•Al_2O_3•2SiO_2$) and Gehlenite ($2CaO•Al_2O_3•SiO_2$) observed in some of the reaction couples. The experimental setup used did not simulate the cyclical conditions caused by the changes between a dynamic and static deadman (section 2.14). These cyclical conditions would allow the removal of any reaction products and remaining Calcium Aluminates by increases in iron flows or coke bed movement.

Any variations in iron flow or the coke bed activity may disturb the contact between the coke ash minerals and the hearth refractories causing spalling and cracking of the reaction layer. This can increase the rate of refractory degradation by exposing more unreacted refractory to the coke ash minerals. The actual rate of refractory degradation on a macro scale will therefore vary depending on the dynamics of the coke bed and iron flow across the hearth refractories.

5.3. Influence of Reaction Products Properties on Refractory Degradation

The changes in the physical properties of the refractory due to the formation of the reaction product phase will have a significant impact on the in-service properties of the refractories. The possible formation of the liquid oxide phase may accelerate the rate of refractory loss via removal of the liquid phase and reduce wear resistance of the high porosity region remaining at the refractory surface. Table 5.15 provides the unit cell volume, density and thermal expansion coefficient of all the solid phases present in the reaction layer (Mullite, Corundum, Anorthite, Gehlenite, CA, CA2, CA6).

Table 5.15: Unit cell volume, density and thermal expansion coefficent of Coke Ash and Hearth Refractory minerals [75], [36], [45], [76], [46], [77]

Phase	**Unit Cell Volume ($Å^3$)**	**Density (g/cm^3)**	**α ($10^{-6}/K$)**
CA ($CaO.Al_2O_3$)	1069.4	2.92	~26
CA2 ($CaO.2Al_2O_3$)	297.7	2.9	~24
CA6 ($CaO.6Al_2O_3$)	588.1	3.77	~21
Corundum (Al_2O_3)	84.9	3.99	19
Anorthite ($CaO.Al_2O_3.2SiO_2$)	697.64	2.76	1.6 – 2.38
Gehlenite ($2CaO.Al_2O_3.SiO_2$)	299.05	2.98	~7.2
Mullite ($3Al_2O_3.2SiO_2$)	169.7	3.08 – 3.17	~6

Volume changes due to the formation of reaction products can produce stresses and subsequent spalling of the refractory materials as seen in Figures 4.2-4.3 and Figures 4.15-4.16. In the Aluminosilicate refractory the increase change in unit cell volume is between 75% (formation of CA2) and 411% (formation of Anorthite). In the Alumina - Carbon refractory the alumina grains can react causing unit cell volume increases between 350% (formation of CA2) and 822% (formation of Anorthite).

The Calcium Aluminates, Anorthite ($CaO.Al_2O_3.2SiO_2$) and Gehlenite ($2CaO.Al_2O_3.SiO_2$) all have lower liquidus temperatures than the refractory phases (Mullite and Corundum) as shown in Figure 2.12. The Calcium Aluminates soften between 1500°C and 1600°C, which is within the range of hearth temperatures (1450°C - 1550°C). Therefore the reaction layer is likely to have a lower resistance to mechanical wear and deformation than the refractories.

The Aluminosilicate and Alumina-Carbon (alumina grains) thermal expansion coefficients (6×10^{-6}/K and 19×10^{-6}/K respectively) are significantly different to the reaction product phases (Anorthite = 1.6×10^{-6}/K, CA = 26×10^{-6}/K) as shown in Table 5.15. This difference will increase the susceptibility of the refractories to degradation by thermal spalling when exposed to cyclic temperatures.

5.4. Consequences for Blast Furnace Hearth Refractories

The consequences of these changes in the blast furnace hearth refractory properties need to be considered. The possible formation of liquid oxides and phases with liquidus temperatures within the operating temperature of the hearth are likely to increase the rate of refractory wear from the flow of molten iron across the hearth and mechanical wear from the deadman coke bed.

The combined effects of the change in volume and thermal expansion in the reaction layer will increase the susceptibility of the refractory to spalling with the changing thermal conditions in the hearth. The spalled material is removed from the refractory surface during dynamic (floating) deadman conditions which allows high liquid flows across the hearth refractory. When the hearth returns to a static deadman condition the coke ash minerals can further react with the refractory to produce more CA2 and CA6.

The static and dynamic deadman conditions produce different temperature and liquid flow throughout the hearth. The resulting variation in reaction rates and the formation of reaction products across the hearth will produce different rates of wear in localised regions of the hearth. Understanding the rates of reaction for the formation and wear mechanisms that cause degradation of the refractory surface will improve our ability to predict the campaign life of the blast furnace hearth.

6. Conclusions

The primary aim of this study was to improve the understanding of the interactions between the coke ash minerals and blast furnace hearth refractories. This has been achieved through the use of a range of experimental techniques to determine the reaction layer thickness at various reaction times and temperatures. Kinetic models were then applied to the reaction layer thickness data to determine the most appropriate model for each refractory. It was found that the Aluminosilicate refractory followed the linear rate law and the Alumina - Carbon refractory corresponded to the logarthimic rate law.

Thermodynamic modelling was conducted using the known compositions of each refractory and Calcium Aluminate reaction couple, and compared with the phases observed using scanning electron microscopy and energy dispersive spectroscopy. It was found that the formation of Melilite ($2CaO.Al_2O_3.SiO_2$) and Plagioclase (Anorthite - $CaO.Al_2O_3.2SiO_2$) were more likely in the reactions with the Aluminosilicate refractory due to the higher silicon content in the refractory. This corresponds with the observation that this refractory follows the linear rate law, which is typical of a material that forms a non-protective reaction layer with high porosity and forms liquid phase reaction products.

The main conclusions drawn from this study were:

- The Aluminosilicate refractory reactions with the coke ash minerals corresponds with the linear rate law
- The Alumina - Carbon refractory reactions with the coke ash minerals correspond with the logarithmic rate law.
- The weight loss observed in the Alumina - Carbon refractory has been attributed to the reduction of silica by the carbon contained in the refractory matrix.
- Liquid oxide formation although possible it is not clear from the information we have if this occurred.
- Plagioclase (Anorthite - $CaO.Al_2O_3.2SiO_2$) was only observed at the longer reaction times (>12 hours) in the CA reaction couples. Elemental mapping shows that some

high silicon phases were present in the reaction layer from 4 hours, suggesting Plagioclase may have formed earlier.

- Melilite (Gehlenite - $2CaO.Al_2O_3.SiO_2$) was only observed in the reaction couples containing CA at either higher reaction temperatures (1530°C) or longer reaction times of 8 hours or more.
- Grossite (CA2) formed from the reaction between CA and both the Aluminosilicate and Alumina - Carbon refractories.
- Hibonite (CA6) formed from the reaction between CA2 and both the Aluminosilicate and Alumina - Carbon refractories.
- The Alumina - Carbon refractory reacted at lower temperatures than the Aluminosilicate refractory.
- The rate of reaction was observed to be temperature dependent. An Arrhenius relation was developed to describe the effect of temperature on the reaction rate for each reaction couple.
- The net direction of mass transport was from the Calcium Aluminates into the refractory materials.
- Diffusion of calcium into the refractories formed a calcium depleted region at the surface of the CA and CA2. This implies that calcium cations have the highest diffusivity of the active species in the reaction couples.
- The rate of reaction was observed to increase with the CaO composition of the Calcium Aluminate. This is due to the higher concentration gradient increasing the rate of Ca^{2+} diffusion as described using Fick's first law of diffusion.
- The formation of Hibonite (CA6) and Grossite (CA2) is likely to increase the susceptibility of the refractory to structural and thermal spalling.
- The formation of the liquid oxide phase and the low liquidus temperature phases (Anorthite - $CaO.Al_2O_3.2SiO_2$ and Gehlenite - $2CaO.Al_2O_3.SiO_2$) are likely to increase the rate of refractory wear, limiting the ability of the refractories to form a protective reaction layer.
- The cyclic nature of the liquid flow and thermal conditions in the hearth will result in a continuous cycle of reaction layer formation, removal via spalling and subsequent reforming of the reaction layer.

In conclusion, a detailed study on the blast furnace hearth refractory and coke ash interactions has been conducted. This study has produced new data on the rate of growth and development of reaction layers consisting of liquid oxides, Melilite ($2CaO.Al_2O_3.SiO_2$), Plagioclase ($CaO.Al_2O_3.2SiO_2$) and various Calcium Aluminate phases (CA, CA2 and CA6). These results have also been used to identify the influence of temperature and Calcium Aluminate composition on the reaction layer formation.

7. Recommendations for further studies

Recommendations for further studies are outlined below:

- Investigate the effect of an iron melt bath on the formation of Melilite ($2CaO.Al_2O_3.SiO_2$) and Plagioclase ($CaO.Al_2O_3.2SiO_2$). The formation of Melilite and Plagioclase is important as these phases have a lower resistance to degradation in the blast furnace hearth.
- Investigate the effect of an iron melt bath on the rate of reaction, particularly in the Alumina - Carbon refractory where partial dissolution of the matrix phase in the iron melt is possible. The effect of sulphur on these reactions should be considered.
- Complete repeats of the experimental method using CA and CA2 across all the experimental temperatures.
- Investigate the effect of thermal cycling on the bond between the refractory and the reaction layer.

8. References

[1] Cook, S.R 2007, *No.5 Blast Furnace – 2007 Reline, Furnace, Refractories, General Arrangement,* BlueScope Steel drawing number 460373, Port Kembla, Australia.

[2] Biswas, A.K. 1981, *Principles of Blast Furnace Ironmaking*. Cootha Publishing House, Brisbane, Australia.

[3] Chapman, M.W. 2009, *Insoluble Oxide Product Formation and its Effect on Coke Dissolution in Liquid Iron*, PhD thesis, University of Wollongong, Wollongong Australia

[4] Chapman, M.W, Monaghan, B. J, Nightingale, S. A, Nightingale, R. J, Mathieson, J.G. 2008, *Formation of a Mineral Layer during Coke Dissolution into liquid Iron and its influence on the Kinetics of Coke Dissolution Rate, Metallurgical and Materials Transactions B,* vol. 39, no.3, pp. 418-430.

[5] Chapman, M.W. Monaghan, B.J. Nightingale, S.A. Mathieson, J.G. Nightingale, R.J. 2007, *Observations of the Mineral Matter Material Present at the Coke/Iron Interface During Coke Dissolution into Iron.* ISIJ International, vol.47, no.7, pp. 973-981.

[6] Chapman, M. W. Monaghan, B.J. Nightingale, S.A. Mathieson, J.G. Nightingale, R.J. 2011, *The effect of sulfur concentration in liquid iron on mineral layer formation during coke dissolution*, Metallurgical and Materials Transactions B: Process Metallurgy and Materials Processing Science, vol. 42, no. 4, pp. 642-651.

[7] Di Giorgio, N. 2007, *Blast Furnace Operations: Meeting the CO_2 Challenge*, Presentation, BlueScope Steel, Port Kembla.

[8] Omori, Y.E. ed. 1987, *Blast Furnace Phenomena and Modelling*, Elsevier Applied Science, London, pp.58, 507, 556.

[9] Croft, V. 1980, *In Situ Reduction of Blast Furnace Coke Ash*, Ironmaking and Steelmaking, pp. 116 - 122.

[10] Ozturk, B. Fruehan, R.J. 1985, *Kinetics of the Reaction of $SiO_{(G)}$ with Carbon Saturated Iron*, Metallurgical and Materials Transactions B,16B, pp. 121-127.

[11] Sano, N. Lu, W.K. Riboud, P. Maeda, M. 1997, *Advanced Physical Chemistry for Process Metallurgy,* Academic Press Limited, London, p.335.

[12] Tong, X. Miwa, T. Guillot, .J.B. Rist, A. 1991: *The Transfer of Silicon from an SiO Bearing Gas to Liquid Iron*, Second European Ironmaking Congress, The Institute of Metals, London, Glasgow, Scotland; UK, pp. 384-387

[13] Turkdogan, E.T. 1996, *Fundamentals of Steelmaking*, The Institute of Materials, Cambridge, United Kingdom.

[14] Turkdogan, E.T. 1980, *The Physical Chemistry of High Temperature, Technology*, Academic Press, New York, p.150.

[15] Nightingale, R. Zulli, P. and Tanzil, F. 2007, *Hearth Forum*, Presentation, BlueScope Steel limited, Port Kembla

[16] Chapman, M.W, Monaghan, B. J, Nightingale, R.J. 2011, *Influence of Coke Ash on Blast Furnace Hearth Behaviour*. CHEMECA 2011: Australasian Conference on Chemical Engineering (pp. 1-14). Victoria: Engineers Australia.

[17] Nightingale, R.J. Chew, S.J. Austin, P.R. Mathieson, J.G. 2002, *Assessment of Blast Furnace Deadman Condition*, International Blast Furnace Lower Zone Symposium, Wollongong, Australia.

[18] Nightingale, R.J. 27th October 2010, personal communication on the wear of hearth refractory exposed to prolonged periods of a static/sitting deadman.

[19] Díez, M.A. Alvarez, R. and Barriocanal, C. 2002, *Coal for Metallurgical Coke Production: Predictions of Coke Quality and Future Requirements for Cokemaking.* International Journal of Coal Geology. Vol. 50, no.1-4, pp. 389-412.

[20] Grigore, M. Sakurovs, R. French, D. and Sahajwalla, V. 2006, *Influence of Mineral Matter on Coke Reactivity with Carbon Dioxide*. ISIJ International vol. no.4, pp. 503-512.

[21] Gupta, S.K. Dubikova, M. French, D. Sahajwalla, V. 2007, *Characterisation of the Origin and Distribution of the Minerals and Phases in Metallurgical Cokes*, Energy and Fuel, 21, pp. 303 - 313.

[22] Hansen, M. 1958, *Constitution of Binary Alloys*, McGraw-Hill, New York.

[23] Bandyopadhyay, B. Singh, S.D. Sanyal, D. Singh, K.K. Singh, K.N. 2003: *A Study on Dissolution Kinetics of Carbon in Liquid Iron Bath*, Chemical Engineering Journal,vol.94, pp. 79-92.

[24] Mourao, M.B. Murthy, G.G.K. and Elliott, J.F. 1993, *Experimental Investigations of Dissolution Rates of Carbonaceous Materials in Liquid Iron—Carbon Melts*, Metallurgical and Materials Transactions B, vol. 24B, pp. 629- 638.

[25] Orsten, S. and Oeters, F. 1988, *Behaviour of Coal Particles Blown into Liquid Iron*, W.O. Philbrook Memorial Symposium Proceedings, Iron and Steel Society, Toronto, Ontario, Canada, pp. 27-38.

[26] Grigoryan, V.A. and Karshin, V.P. 1972, *Effect of Surface-Active Additives on the Kinetics of the Dissolution of Graphite in Liquid Iron*, Izvest Akad NaukSssr Metally, Jan-Feb, pp. 78-81.

[27] Oeters, F. 1994, *Metallurgy of Steelmaking*, VerlagStahleisenmbH, Düsseldorf, Germany, pp.209-214.

[28] Orsten, S. and Oeters, F. 1986, *Dissolution of Carbon in Liquid Iron*, Process Technology Proceedings, Iron and Steel Society, Washington, D.C, USA, pp. 143-155.

[29] Shigeno, Y. Tokuda, M. and Ohtani, M. 1985, *The Dissolution Rate of Graphite into Fe--C Melt Containing Sulphur or Phosphorus*, ISIJ International, vol.26, pp. 3-43.

[30] Shurygin, K. 1963, *On the Kinetics of Dissolution of Carbon in Liquid Iron Base Alloys*, Izv. VysshikhUchebn. ZavedeniiChernaya Met., vol.6, pp. 14-20.

[31] Sun, H. 2005, *Factors Influencing Dissolution of Carbonaceous Materials in Liquid Iron*, Metallurgical and Materials Transactions B, vol.36B, pp. 893-894.

[32] Wright, J.K. and Baldock, B.R. 1988, *Dissolution Kinetics of Particulate Graphite Injected into Iron Carbon Melts*, Metallurgical and Materials TransactionsB, 19B, pp. 375-382.

[33] Monaghan, B. Chapman, M. Nightingale, S. Mathieson, J. and Nightingale, R. 2008, *Sulphide Formation during Coke Dissolution in Liquid Iron*, presentation, SCANMET III – 3rd International Conference on Process Development in Iron and Steelmaking 8-11 June 2008, Lulea, Sweden

[34] Gudenau, H.W. Mulanza, J.P. and Sharma, D.G.R. 1990, *Carburization of Hot Metal by Industrial and Special Cokes*, Steel Research, 61, pp. 97-104.

[35] Olivares, R. 1996, *The Effect of Sulphur on the Dissolution of Graphites and Carbons in Liquid Iron-Carbon Alloys*. Department of Mechanical Engineering. PhD Thesis, University of Newcastle, Newcastle.

[36] Kowalski, M. Spencer, P.J. and Neuschutz, D. 1995, *Slag Atlas*, VDE (VDEh), ed., VerlagStahleisen GmbH, Dusseldorf, Germany, pp. 39.

[37] Kiessling, R. Lange, N. 1978, *Non Metallic Inclusions in Steel*, Vol. 2, The Metals Society, London, p.36-48

[38] Lee, W.E. and Rainforth W.M. 1994, *Ceramic Microstructures – Property control by processing*, Chapman & Hall, London

[39] Brown, G. 2005, *Testing Materials for the Blast Furnace Ceramic Cup*, Refractory Services, BlueScope Steel limited, Port Kembla. Work request No.:R1881

[40] Amdel Industrial Services Division 2005, *Certificate of Analysis*, Report No. L051892, commissioned by BlueScope Steel limited Refractory services, Port Kembla.

[41] Williams, K. 2005, *Certificate of Analysis*, Lab Reference No. X05/0943, BlueScope Steel Laboratory Services, Port Kembla.

[42] Davies, R.H. Dinsdale, A.T. Gisby, J.A. Hodson, S.M. and Ball, R.G.J, 1994, *Thermodynamic Modelling using MTDATA: A Description showing applications involving oxides, alloys and aqueous solutions*, Proc. Conf. ASM/TMS Fall meeting. "Applications of thermodynamics in the synthesis and processing of materials", Rosemont, IL, USA, pp. 371-375.

[43] Bale, C.W. Belisle, E. Chartrand, P. Decterov, Eriksson, G. Hack, K. Jung, I.H. Kang, Y.B, Melancon, J. Pelton, A.D. Robelin, C. and Petersen, S. 2009, *FactSage Thermochemical Software and Databases - Recent Developments*, CalPhad, vol. 33, pp. 295-311.

[44] Andersson J.O., Helander T., Höglund L., Shi P.F., and Sundman B. 2002, *Thermo-Calc and DICTRA, Computational tools for Materials Science.* Calphad, *vol, 26, 273-312.*

[45] Levin, E.M. Robbins, C.R. and McMurdie, H.F. 1964, *Phase Diagrams For Ceramists*, The American Ceramic Society, Columbus, Ohio

[46] Lankford, W.T. Samways, N.L. Craven, R.F. and McGannon, H.E. 1985, *Making, Shaping and Treating of Steel*, Herbick & Held, Pittsburge, p.367-441.

[47] Petaev, M.I. 2009, *Revised Thermodynamic Properties of Ca Aluminates: Implications for the Condensation Sequence*, in Proceedings of the 40th Lunar and Planetary Science Conference, Houston, USA. 23-27 March 2009

[48] Lee, H.G. 1999, *Chemical Thermodynamics for Metals and Materials*, Imperial College Press, London.

[49] Ghoroi, C. and Suresh, A.K 2007, *Intermediate Conversion Kinetics in Tricalcium Aluminate Formation*, American Institute of Chemical Engineers AIChE Journal vol. no 53, pp. 2399-2410.

[50] Kofstad, P. 1966, *High Temperature Oxidation of Metals*, John Wiley & Sons, London.

[51] Hao, Y.J and Tanaka, T. 1990, *Prediction of the Diffusing Components(s) in a Solid-Solid reaction System*, Solid State Ionics vol. 38, pp. 213-216.

[52] Hao, Y.J and Tanaka, T. 1990, *A new Experimental Method to Specify the Diffusing Component in Reacting Particulate Packing*, Canadian Journal of Chemcial Engineering Vol. 68, pp. 512-517.

[53] Tagai, H. Iseki, T. Saeki, T. and Kounosu, T. 1969, *Solid State Reaction Between Calcium Oxide and Aluminium Oxide Single Crystal*. Yogyo Kyokaishi. Vol. 77, pp. 341–347.

[54] Mohamed, B.M. and Sharp, J.H. 1997, *Kinetics and Mechanism of Formation of Monocalcium Aluminate, $CaAl_2O_4$*, J. Mater. Chem. Vol.7, pp. 1595-1599.

[55] Mohamed, B.M. and Sharp, J.H. 2002, *Kinetics and Mechanism of Formation of Tricalcium Aluminate, $Ca_3Al_2O_6$*, Thermochimica Acta, vol. 388, pp.105-114.

[56] Doremus, R.H. 2006, *Diffusion in Alumina*, Journal of Applied Physics, vol. 100, 101301.

[57] Karthikeyan, J. and Rohatgu, V.K. 1990, *Solid State Reaction Kinetics in Alumina – Slag System*, Materials Science and Engineering: A, Vol. 123, issue 1, pp. 141-144.

[58] Khanna, A.S. 2002, *Introduction to High Temperature Oxidation and Corrosion*, ASM International, USA. pp. 9-11.

[59] Poirier, D.R and Geiger, G.H. 1994, *Transport Phenomena In Materials Processing*, TMS, Warrendale, PA, pp. 444-93

[60] Lee, W.E and Zhang, S. 1999, *Melt Corrosion of Oxide and Oxide-Carbon Refractories*, International Materials Reviews, Vol. 44, No.3, pp. 77-104.

[61] Plibrico Japan Company Limited 1984, *Technology of Monolithic Refractories*, Plibrico Japan Company Limited, Tokyo

[62] *Guo, M. Parada, S. Jone, P.T. Van Dyck, J. Boydens, E. Durinck, D. Blanpain, B. and Wollants, P.* 2007, *Degradation Mechanisms of Magnesia-Carbon Refractories by High Alumina Stainless Steel Slags Under Vacuum,* Ceramics International, vol. 33, pp.1007-1018.

[63] Maldonado, M.D. Zulli, P. Guo, B.Y. and Yu, A.B. 2006, *Mathematical Modelling of Flows and Temperature Distributions in the Blast Furnace Hearth*, Proc. Fifth International Conference on CFD in the Process Industries, CSIRO, Melbourne, Australia, 13-15 December

[64] Wright, B. Zulli, P. Bierbrauer, F. and Panjkovic, V. 2003, *Assessment of Refractory Condition in a Blast Furnace Hearth Using Computational Fluid Dynamics*, Proc. Third International Conference on CFD in the Process Industries, CSIRO, Melbourne, Australia, 10-12 December

[65] Drain, P.B. 2010, *Blast Furnace Hearth Refractory and Coke Ash Interactions*, Honours thesis, University of Wollongong, Wollongong Australia, pp: 56-64, 94-97

[66] Khanna R. Sahajwalla, V. Rodgers, B. and McCarthy, F. 2006, *Dissolution of Carbon from Alumina-Carbon Mixtures into Liquid Iron: Influence of Carbonaceous Materials*, Metallurgical and Materials Transactions B, vol. 37, no. 8, pp. 623-632.

[67] Thornton, J. 1997, *Scanning Probe Microscopy Training Notebook Version 3.0*, Digital Instruments Veeco Metrology Group.

[68] Amaral, R. and Chong, L. H.2002, *Surface Roughness*, San Jose State University, http://www.sjsu.edu/faculty/selvaduray/page/papers/mate210/surface.pdf, accessed: 17/05/2012.

[69] SAA 2001, AS1774.5 *Refractories and Refractory Materials - Physical Test Methods*, in *Method 5: The Determination of Density, Porosity and Water Absorption*.

[70] Smigelskas, A.D, and Kirkendall, E.O. 1947, *Zinc Diffusion in Alpha Brass*, Trans. Met. Soc. AIME, vol. 171, pp. 130-142.

[71] Monaghan, B.J. Chapman, M.W. Nightingale, S.A. 2010, *Liquid Iron Wetting of Calcium Aluminates*, ISIJ International, vol. 50, no.11, pp. 1707-1712.

[72] Kapilashrami, E. Sahajwalla, V. and Seetharaman, S. 2004, *Investigation of the Wetting Characteristics of Liquid Iron on Mullite by Sessile Drop Technique*, ISIJ International, vol. 44, no.4, pp. 653-659.

[73] Kapilashrami, E. Jakobsson, A. Lahiri, A.K. and Seetharaman, S. 2003, *Studies of the Wetting Characteristics of Liquid Iron on Dense Alumina by the X-ray Sessile Drop Technique*, Metallurgical and Materials Transactions B, vol. 34, no. 2, pp. 193-199.

[74] Kequin, M. I. 1992, *Reduction and Re-oxidation of Silicon in the Blast Furnace*, Chin. J. Met. Sci. Tech, vol. 8, pp. 435-439

[75] Carter, C B, Norton, M. 2007, *Ceramic Materials Science and Engineering*, Springer

[76] Hofmeister, A.M. 2004, *Physical Properties of Calcium Aluminates from Vibrational Spectroscopy*, Geochimica et Cosmochimica Acta, Vol. 68, No. 22, pp.4721-4726,

[77] Tribaudino, M. Angel, R.J. Camara, F. Nestola, F. Pasqual, D. and Margiolaki, I. 2010, *Thermal Expansion of Plagioclase feldspars*, Contributions to Mineralogy and Petrology, Vol. 160, No. 6, pp.899-908

Appendix I - Atomic Force Microscopy and Roughness Results

The roughness parameters measured using the atomic force microscope for each of the reaction couple materials are shown in Table A-1. The area over which each of these measurements was taken is shown in the atomic force micrographs indicated in Table A-1.

Table A-1: Atomic Force Microscopy Roughness Results

Material	Rms (R_q) (nm)	R_a (nm)	Micrograph
Alumina-Carbon Matrix	279.0	226.0	Figure A-1 a
Alumina-Carbon Matrix	296.0	244.0	Figure A-1 a
Alumina-Carbon Matrix	236.0	197.0	Figure A-1 b
Alumina-Carbon Matrix	240.0	185.0	Figure A-1 b
Alumina-Carbon (alumina Grains)	51.0	41.0	Figure A-1 a
Alumina-Carbon (alumina Grains)	76.0	65.0	Figure A-1 a
Alumina-Carbon (alumina Grains)	34.0	25.0	Figure A-1 b
Alumina-Carbon (alumina Grains)	44.0	35.0	Figure A-1 b
Alumina-Carbon (alumina Grains)	61.1	44.0	Figure A-1 c
Alumina-Carbon (alumina Grains)	62.3	43.7	Figure A-1 c
Aluminosilicate	40.9	20.7	Figure A-2 a
Aluminosilicate	32.6	20.3	Figure A-2 b
Aluminosilicate	22.2	13.7	Figure A-2 c
Aluminosilicate	69.0	56.0	Figure A-2 d
Aluminosilicate	44.7	25.6	Figure A-2 e

Table A-1: Atomic Force Microscopy Roughness Results (continued)

Material	Rms (R_q) (nm)	R_a (nm)	Micrograph
CA	47.8	32.8	Figure A-3 a
CA	53.9	41.7	Figure A-3 b
CA	57.3	41.3	Figure A-3 c
CA	42.1	29.9	Figure A-3 d
CA	43.3	33.7	Figure A-3 e
CA2	29.6	18.6	Figure A-4 a
CA2	31.9	19.3	Figure A-4 b
CA2	37.9	19.6	Figure A-4 c
CA2	31.8	18.0	Figure A-4 d
CA2	39.3	27.9	Figure A-4 e
CA6	846	716	Figure A-5 a
CA6	843	614	Figure A-5 b
CA6	868	672	Figure A-5 c
CA6	603	492	Figure A-5 d
CA6	810	660	Figure A-5 e

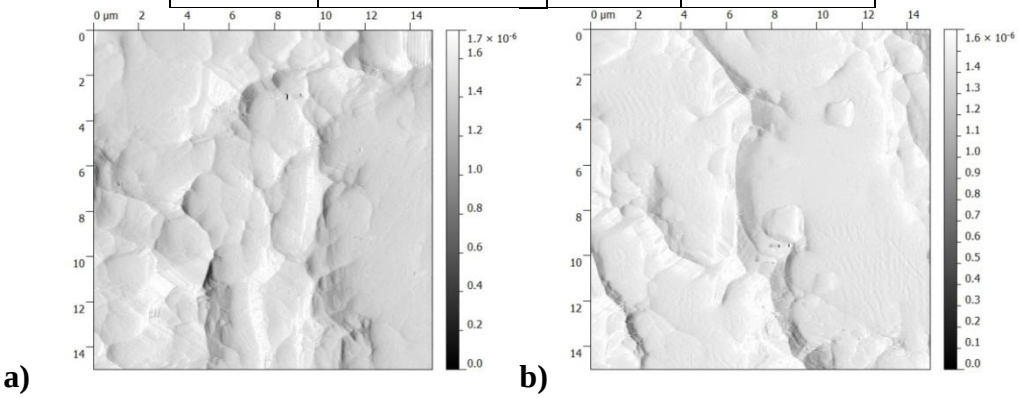

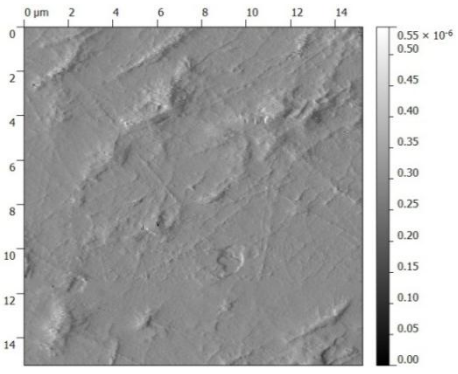

Figure A-1: Atomic Force Micrographs of the Alumina - Carbon refractory samples.

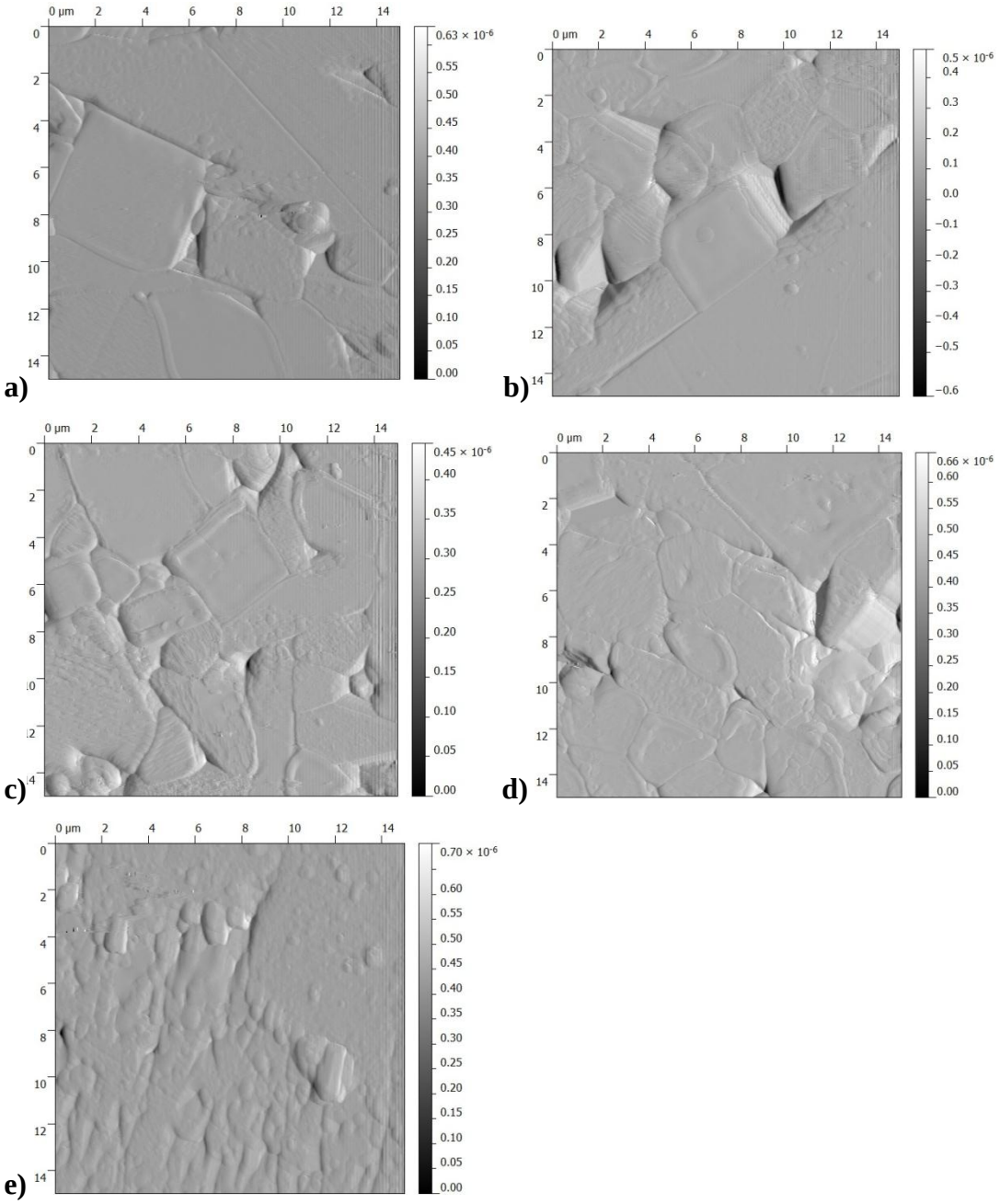

Figure A-2: Atomic Force Micrograph of the Aluminosilicate refractory samples.

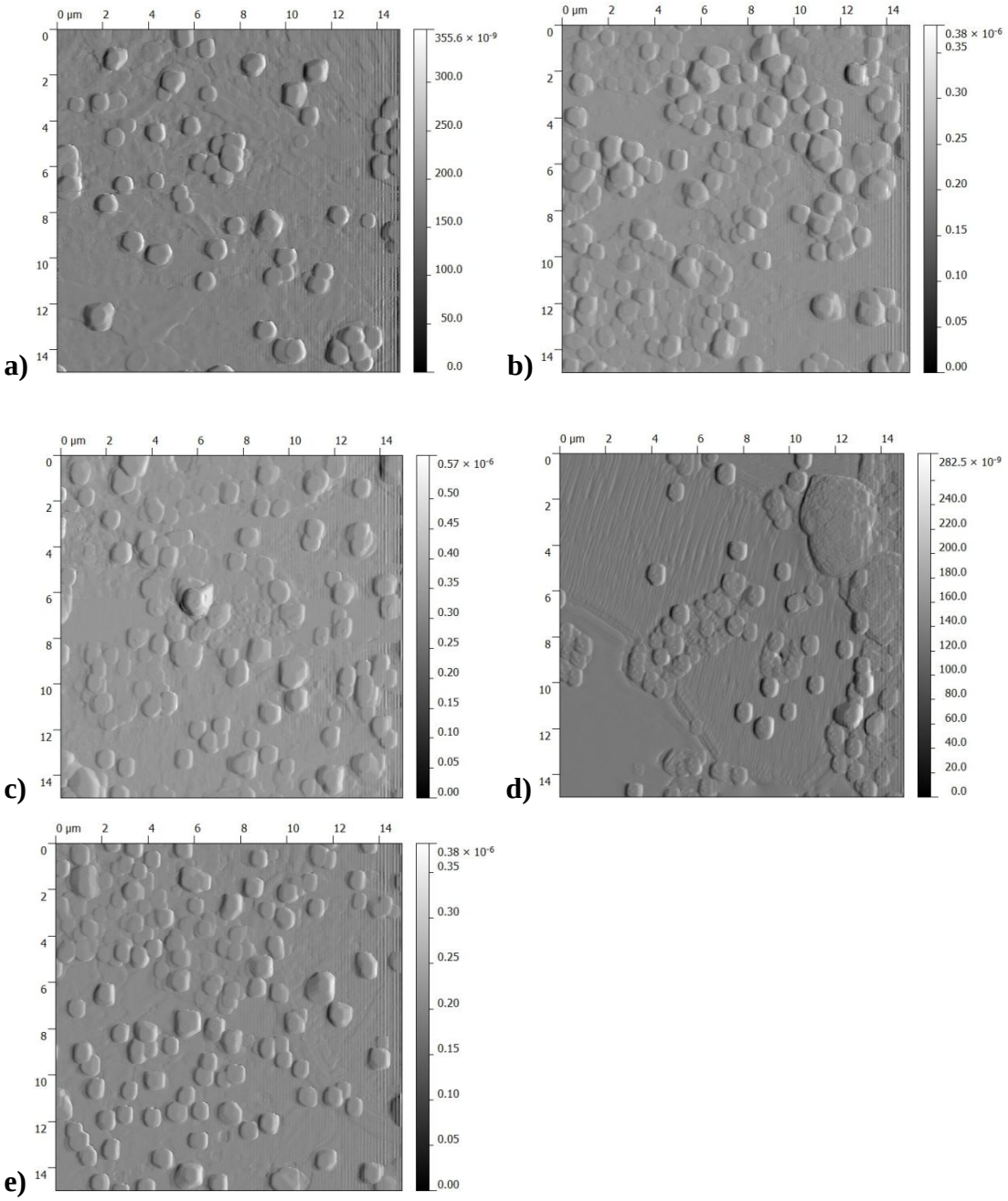

Figure A-3: Atomic Force Micrograph of the CA samples.

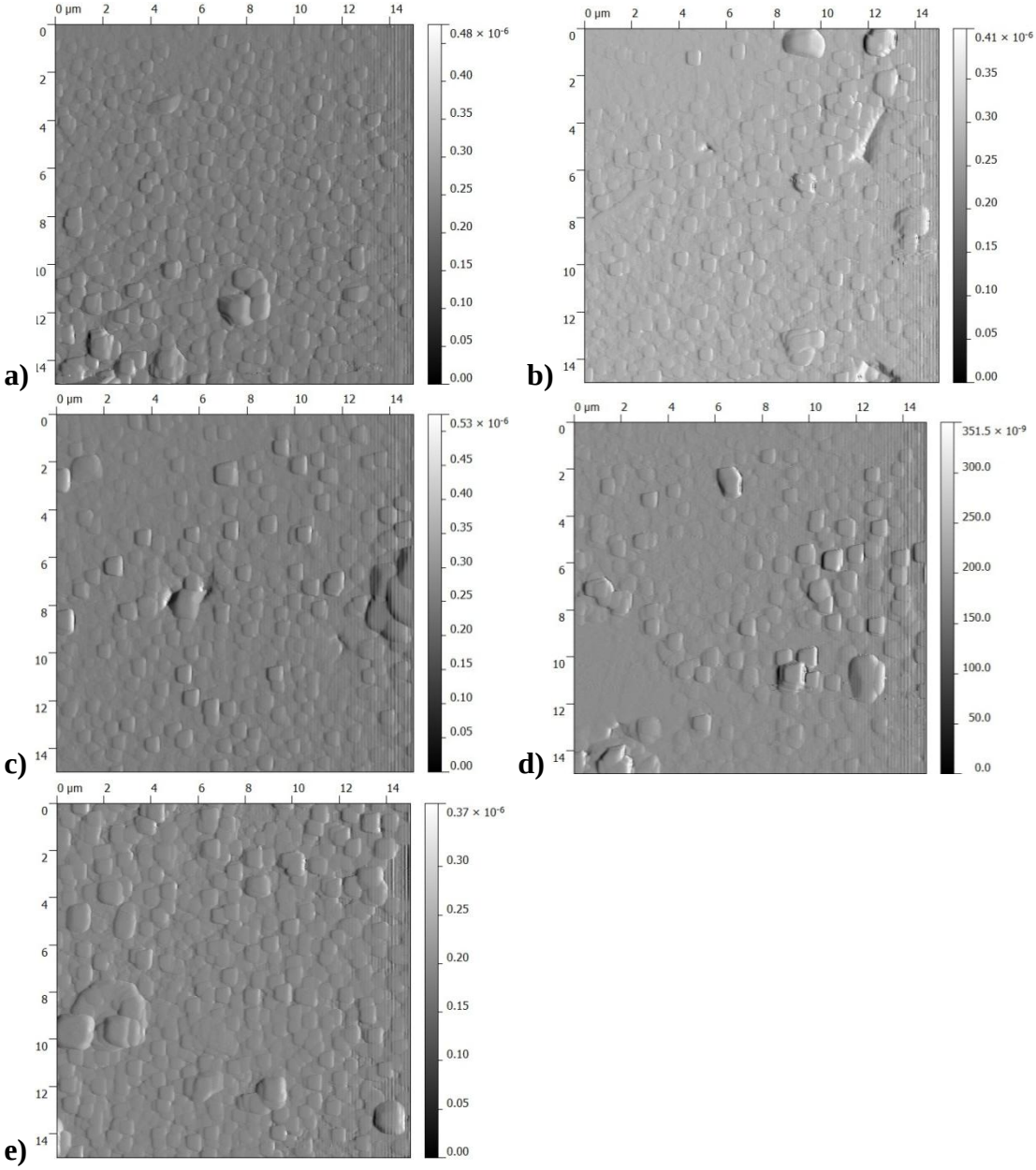

Figure A-4: Atomic Force Micrograph of the CA2 samples.

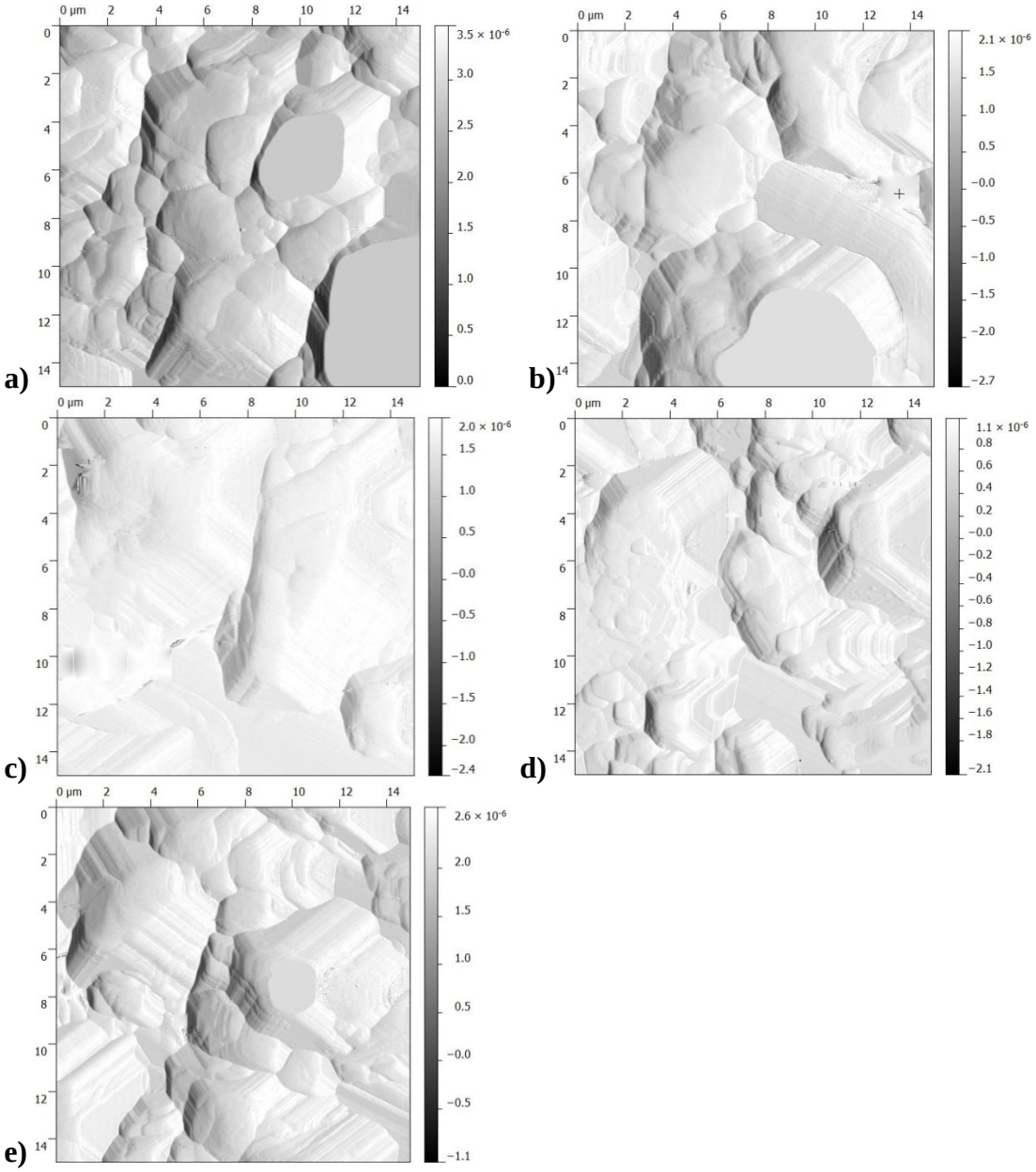

Figure A-5: Atomic Force Micrograph of the CA6 samples.

Appendix II - AS1774.5-2001: The Determination of Density and Porosity

Australian Standard™

AS 1774.5

Refractories and refractory materials— Physical test methods

Method 5: The determination of density, porosity and water absorption

Standard below removed for copyright reasons, please refer to the citation: Standards Australia 2001, Refractories and refractory materials - Physical test methods: Method 5: the determination of density, porosity and water absorption, AS1774.5-2001, Standards Australia.

Standard below removed for copyright reasons, please refer to the citation: Standards Australia 2001, Refractories and refractory materials - Physical test methods: Method 5: the determination of density, porosity and water absorption, AS1774.5-2001, Standards Australia.

Standard below removed for copyright reasons, please refer to the citation: Standards Australia 2001, Refractories and refractory materials - Physical test methods: Method 5: the determination of density, porosity and water absorption, AS1774.5-2001, Standards Australia.

Standard below removed for copyright reasons, please refer to the citation: Standards Australia 2001, Refractories and refractory materials - Physical test methods: Method 5: the determination of density, porosity and water absorption, AS1774.5-2001, Standards Australia.

Standard below removed for copyright reasons, please refer to the citation: Standards Australia 2001, Refractories and refractory materials - Physical test methods: Method 5: the determination of density, porosity and water absorption, AS1774.5-2001, Standards Australia.

Appendix III - Reaction Couple Mass Change Results

The reaction couples before and after heating to the reaction temperature were used to calculate the percentage mass change during testing using Equation 3-1. This data is given in Table A-2, a negative mass change indicates a mass loss and a positive change indicates a mass gain.

Table A-2: Temperature Series Reaction Couple mass change data

Reaction Couple Materials		**°C**	**Time**	**%ΔMass**		
Refractory	**Calcium Aluminate**		**(Hours)**	**Refractory**	**CA_x**	**Total**
Aluminosilicate	CA	1450	4	-0.03	0.58	0.05
Aluminosilicate	CA	1500	4	Reaction couple Bonded		-0.13
Aluminosilicate	CA	1530	4	100.00	100.00	-0.25
Aluminosilicate	CA2	1450	4	0.17	0.13	0.16
Aluminosilicate	CA2	1500	4	-0.26	-0.35	-0.27
Aluminosilicate	CA2	1530	4	-1.03	0.12	-0.82
Aluminosilicate	CA2	1530	4	-0.28	-0.27	-0.28
Aluminosilicate	CA2	1550	4	Reaction couple Bonded		-0.31
Aluminosilicate	CA6	1450	4	0.18	1.06	0.24
Aluminosilicate	CA6	1450	4	0.01	-0.05	-0.01
Aluminosilicate	CA6	1450	4	-0.02	-0.27	-0.06
Aluminosilicate	CA6	1450	4	0.01	-0.26	-0.04
Aluminosilicate	CA6	1500	4	-0.18	1.26	-0.09
Aluminosilicate	CA6	1550	4	-0.20	-0.23	-0.20
Alumina-Carbon	CA	1450	4	Reaction couple Bonded		3.96
Alumina-Carbon	CA	1500	4	Reaction couple Bonded		3.44
Alumina-Carbon	CA	1530	4	Reaction Couple Bonded		4.84
Alumina-Carbon	CA2	1450	4	3.67	-0.44	2.85
Alumina-Carbon	CA2	1500	4	Reaction couple Bonded		3.99
Alumina-Carbon	CA2	1550	4	Reaction Couple Bonded		4.09
Alumina-Carbon	CA6	1450	4	3.88	0.22	3.28
Alumina-Carbon	CA6	1450	4	4.30	-0.13	3.56
Alumina-Carbon	CA6	1450	4	3.65	-0.21	3.00
Alumina-Carbon	CA6	1450	4	4.39	0.26	3.87
Alumina-Carbon	CA6	1500	4	4.69	-0.31	4.29
Alumina-Carbon	CA6	1550	4	5.23	-0.24	4.80

The time series reaction couple mass change data is given in Table A-3.

Table A-3: Time Series Reaction Couple mass change data

Reaction Couple Materials		**Time**	**%ΔMass**		
Refractory	**Calcium Aluminate**	**(Hours)**	**Refractory**	**CA_x**	**Total**
Aluminosilicate	CA	4	Reaction couple Bonded		-0.13
Aluminosilicate	CA	8	0.06	-0.57	-0.04
Aluminosilicate	CA	12	0.14	-3.22	-0.18
Aluminosilicate	CA	18	0.22	0.11	0.20
Aluminosilicate	CA	24	Reaction couple Bonded		-0.04
Aluminosilicate	CA2	4	-0.26	-0.35	-0.27
Aluminosilicate	CA2	8	0.08	0.23	0.11
Aluminosilicate	CA2	12	-0.22	0.40	-0.16
Aluminosilicate	CA2	18	0.30	0.30	0.30
Aluminosilicate	CA2	24	0.26	-1.80	0.10
Aluminosilicate	CA6	4	-0.18	1.26	-0.09
Aluminosilicate	CA6	8	-0.01	2.71	0.15
Aluminosilicate	CA6	12	-0.03	-3.23	-0.19
Aluminosilicate	CA6	18	0.18	3.53	0.38
Aluminosilicate	CA6	24	-0.13	-1.16	-0.18
Alumina-Carbon	CA	4	Reaction couple Bonded		3.44
Alumina-Carbon	CA	8	Reaction couple Bonded		4.07
Alumina-Carbon	CA	12	Reaction couple Bonded		4.17
Alumina-Carbon	CA	18	Reaction couple Bonded		4.13
Alumina-Carbon	CA	24	Reaction couple Bonded		4.53
Alumina-Carbon	CA2	4	Reaction couple Bonded		3.99
Alumina-Carbon	CA2	8	4.99	-0.13	3.99
Alumina-Carbon	CA2	12	5.61	-0.38	5.31
Alumina-Carbon	CA2	18	4.85	0.52	4.02
Alumina-Carbon	CA2	24	Reaction couple Bonded		4.80
Alumina-Carbon	CA6	4	4.69	-0.31	4.29
Alumina-Carbon	CA6	8	4.62	-6.28	4.49
Alumina-Carbon	CA6	12	6.12	2.89	6.05
Alumina-Carbon	CA6	18	5.48	5.20	5.47
Alumina-Carbon	CA6	24	6.39	-0.26	6.13

Appendix IV - Reaction Layer Thickness Measurements

The average reaction layer thickness for each interface micrograph in the temperature series are given in Table A-4. Table A-5 shows the reaction couples for which no reaction layer was observed.

Table A-4: Reaction Layer Thickness Measurements for Temperature Series

Reaction Couple Materials		˚C	**Reaction Layer thickness (µm)**		
Refractory	**Calcium Aluminate**		**Interface 1 Micrograph**	**Interface 2 Micrograph**	**Interface 3 Micrograph**
Aluminosilicate	CA	1450	6.63	8.62	7.02
Aluminosilicate	CA	1500	63.12	21.93	86.08
Aluminosilicate	CA	1530	104.40	81.59	44.01
Aluminosilicate	CA2	1450	4.34	3.94	2.74
Aluminosilicate	CA2	1500	8.18	8.94	8.93
Aluminosilicate	CA2	1530	15.51	20.87	40.89
Aluminosilicate	CA2	1550	24.37	29.34	36.21
Aluminosilicate	CA6	1550	10.78	31.35	6.21
Alumina-Carbon	CA	1450	92.02	54.55	47.66
Alumina-Carbon	CA	1500	193.55	217.45	207.10
Alumina-Carbon	CA	1530	224.01	229.03	253.64
Alumina-Carbon	CA2	1450	11.77	9.61	8.82
Alumina-Carbon	CA2	1500	36.47	39.94	56.93
Alumina-Carbon	CA2	1550	50.87	54.39	41.29
Alumina-Carbon	CA6	1550	0.00	0.00	50.17

Table A-5: Temperature Series Reaction couples with no observable reaction layer

Refractory Material	**Calcium Aluminate**	**Reaction Time**	**Temperature**
Aluminosilicate	CA6	4 Hours	1450 ˚C 1500 ˚C
Alumina-carbon	CA6	4 Hours	1450 ˚C 1500 ˚C

The average reaction layer thickness for each interface micrograph in the time series are given in Table A-6.

Table A-6: Reaction Layer Thickness Measurements for Time Series

Reaction Couple Materials		**Time (Hours)**	**Reaction Layer thickness (µm)**		
Refractory	**Calcium Aluminate**		**Interface 1 Micrograph**	**Interface 2 Micrograph**	**Interface 3 Micrograph**
Aluminosilicate	CA	4	63.12	21.93	86.08
Aluminosilicate	CA	8	86.56	52.22	50.82
Aluminosilicate	CA	12	307.73	173.98	87.01
Aluminosilicate	CA	18	358.62	275.47	281.70
Aluminosilicate	CA	24	625.30	391.87	379.41
Aluminosilicate	CA2	4	8.18	8.94	8.93
Aluminosilicate	CA2	8	18.72	20.24	24.01
Aluminosilicate	CA2	12	15.68	56.34	61.01
Aluminosilicate	CA2	18	122.68	74.93	91.67
Aluminosilicate	CA6	4	0	0	0
Aluminosilicate	CA6	8	0	0	0
Aluminosilicate	CA6	12	0	0	0
Aluminosilicate	CA6	18	49.97	61.79	59.74
Alumina-Carbon	CA	4	193.55	217.45	207.10
Alumina-Carbon	CA	8	252.10	277.63	278.75
Alumina-Carbon	CA	12	416.76	412.22	324.38
Alumina-Carbon	CA	18	609.87	315.24	582.43
Alumina-Carbon	CA	24	487.68	523.47	589.94
Alumina-Carbon	CA2	4	36.47	39.94	36.84
Alumina-Carbon	CA2	8	62.66	70.71	53.65
Alumina-Carbon	CA2	12	56.73	60.39	57.29
Alumina-Carbon	CA2	18	82.01	78.40	63.10
Alumina-Carbon	CA2	24	89.63	82.22	78.37

Table A-7 shows the reaction couples in the time series for which no reaction layer was observed.

Table A-7: Time Series Reaction couples with no observable reaction layer

Refractory Material	**Calcium Aluminate**	**Reaction Times**	**Temperature**
Aluminosilicate	CA6	4 hours 8 hours 12 hours	1500 ˚C
Alumina-carbon	CA6	4 hours 8 hours 12 hours 18 hours 24 hours	1500 ˚C

Appendix V - Reaction Couple SEM Micrographs

All the SEM micrographs produced for the temperature series of experiments in this study are shown below in Figure A-6 to Figure A-9. The calcium aluminates are to the left of each micrograph and refractory material to the right.

Figure A-6: Aluminosilicate refractory Temperature Series reaction couples. 100µm scale bar.

	CA – 1450°C	CA – 1500°C	CA – 1530°C	CA2– 1450°C	CA2 – 1500°C	CA2 – 1550°C
Interface 1 Micrograph	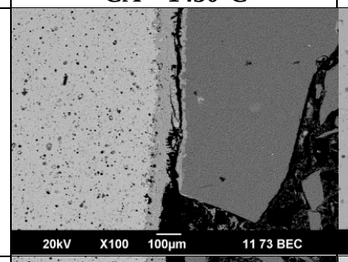	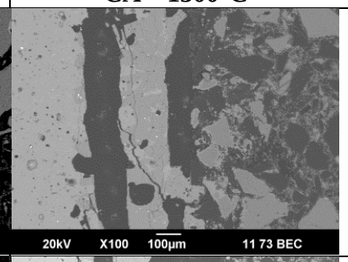	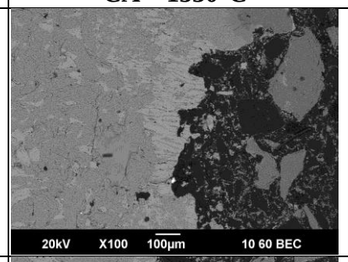	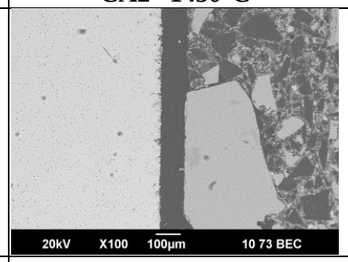	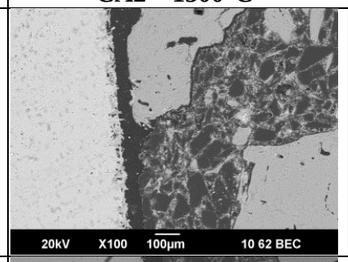	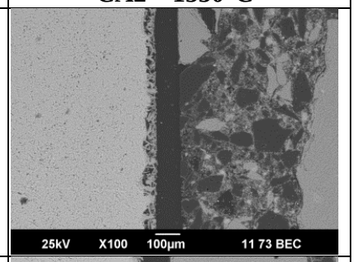
Interface 2 Micrograph	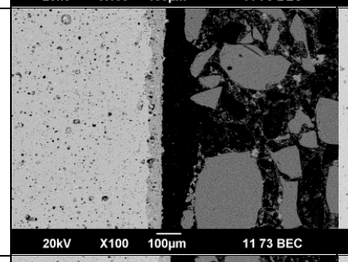	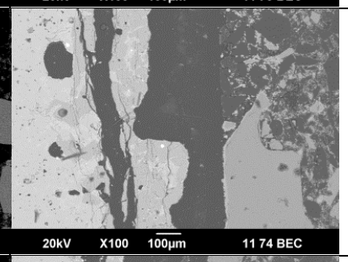	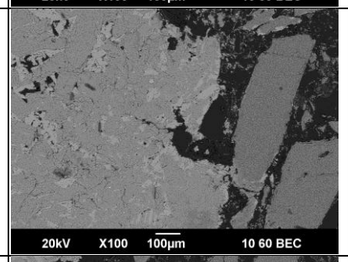	Only 1 Micrograph	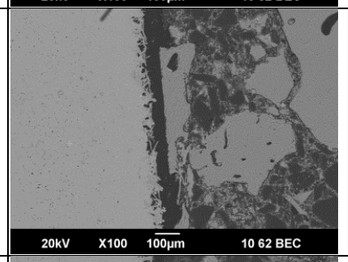	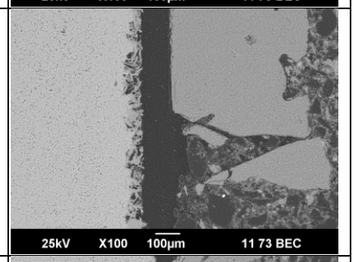
Interface 3 Micrograph	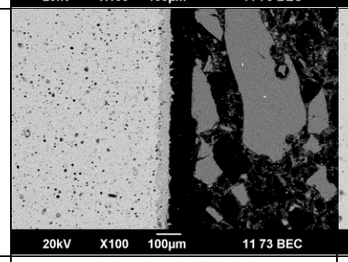	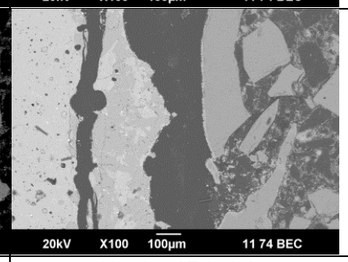	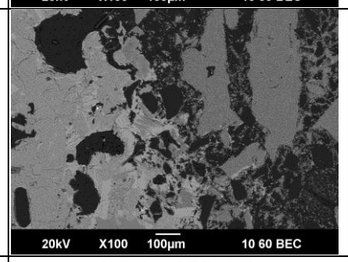	Only 1 Micrograph	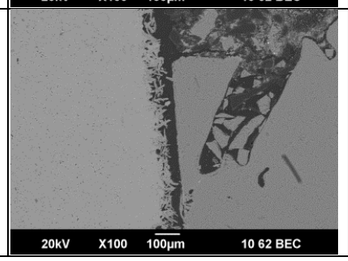	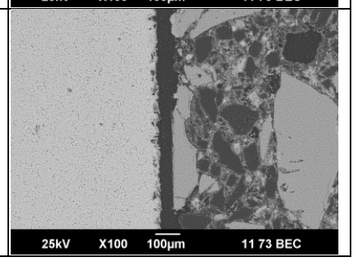

	CA6 – 1450°C	CA6 – 1500°C	CA6 – 1550°C
Interface 1 Micrograph	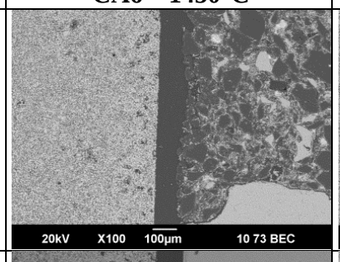	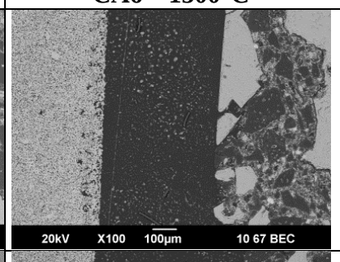	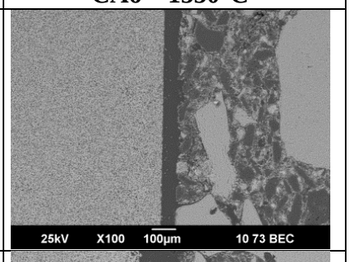
Interface 2 Micrograph	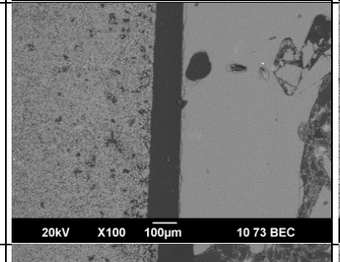	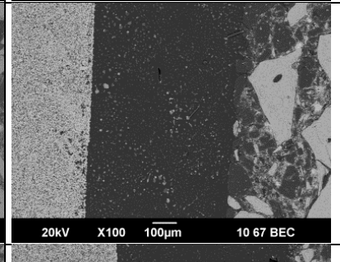	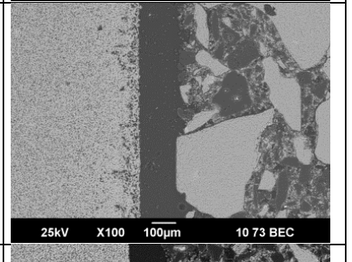
Interface 3 Micrograph	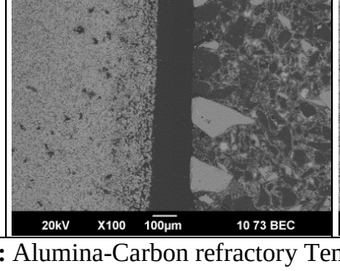	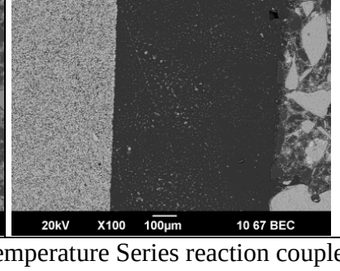	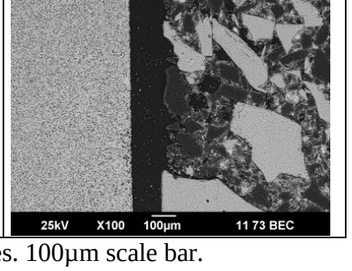

Figure A-7: Alumina-Carbon refractory Temperature Series reaction couples. 100µm scale bar.

All the SEM micrographs produced for the time series of experiments in this study are shown below in Figure A-8 to Figure A-13. The calcium aluminates are to the left of each micrograph and refractory material to the right.

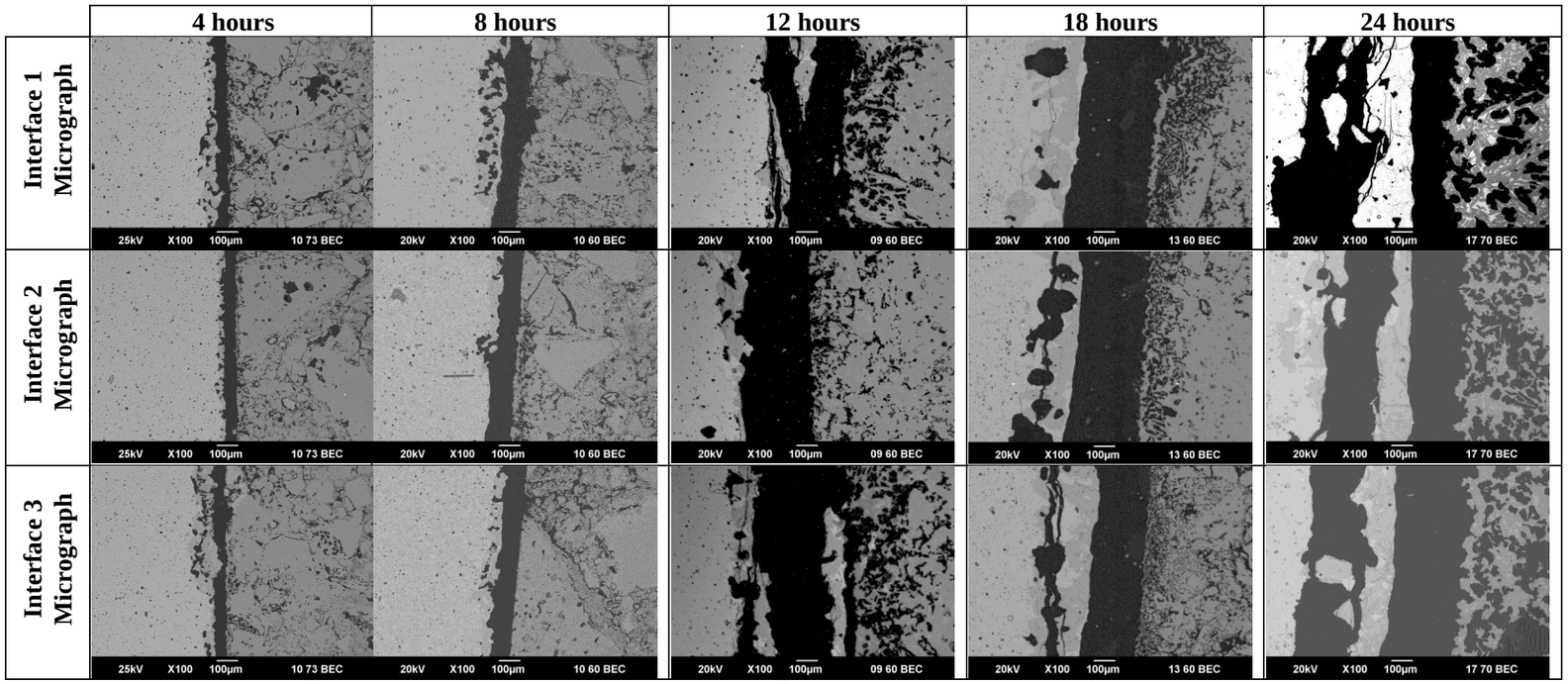

Figure A-8: Aluminosilicate - CA refractory Time Series reaction couples. 100µm scale bar.

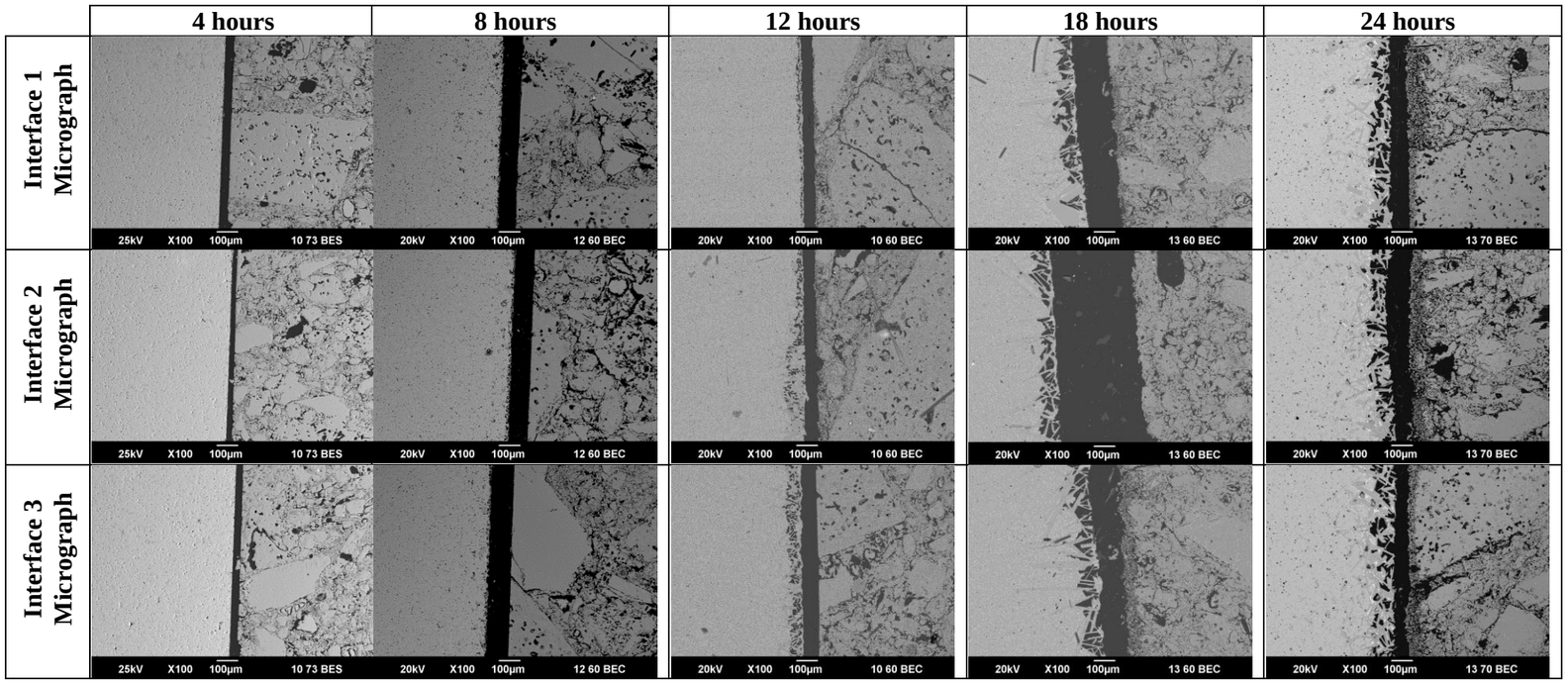

Figure A-9: Aluminosilicate – CA2 refractory Time Series reaction couples. 100µm scale bar.

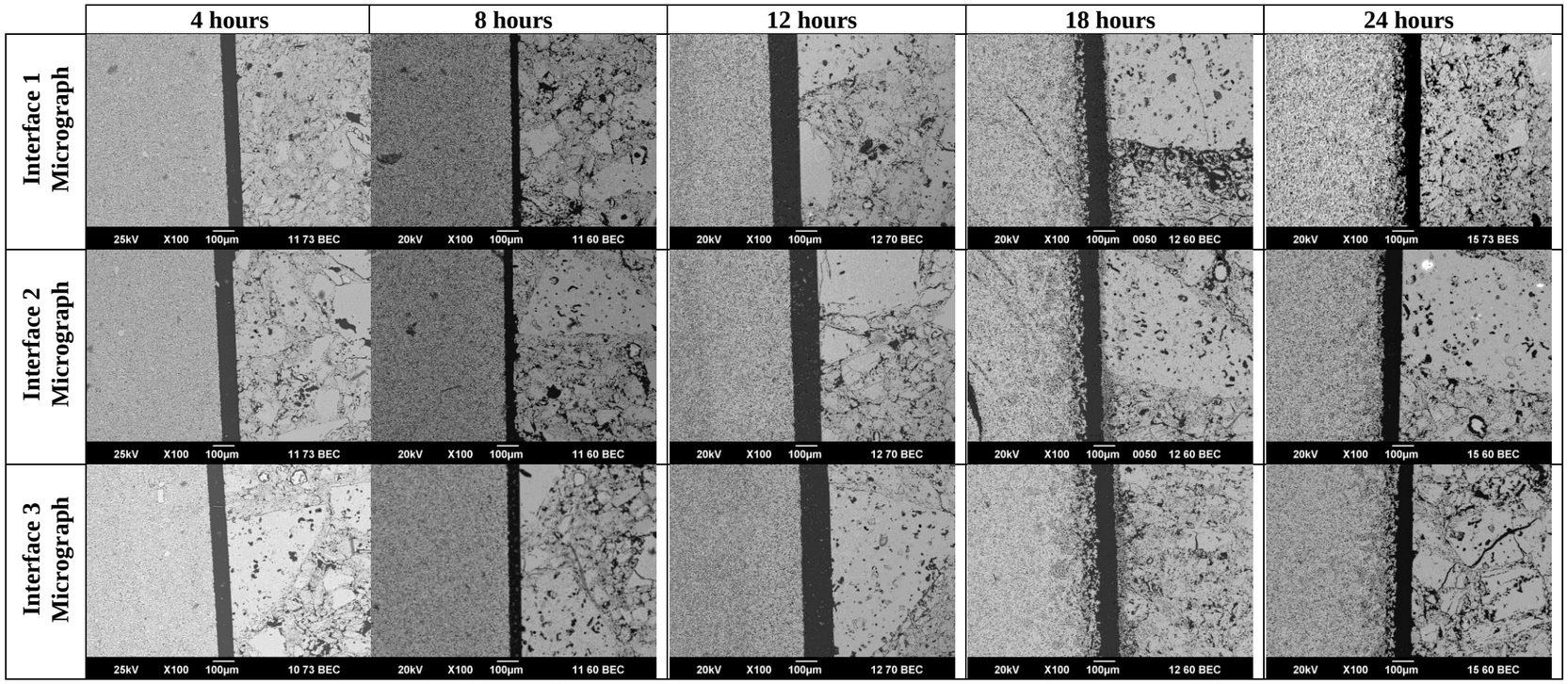

Figure A-10: Aluminosilicate – CA6 refractory Time Series reaction couples. 100µm scale bar.

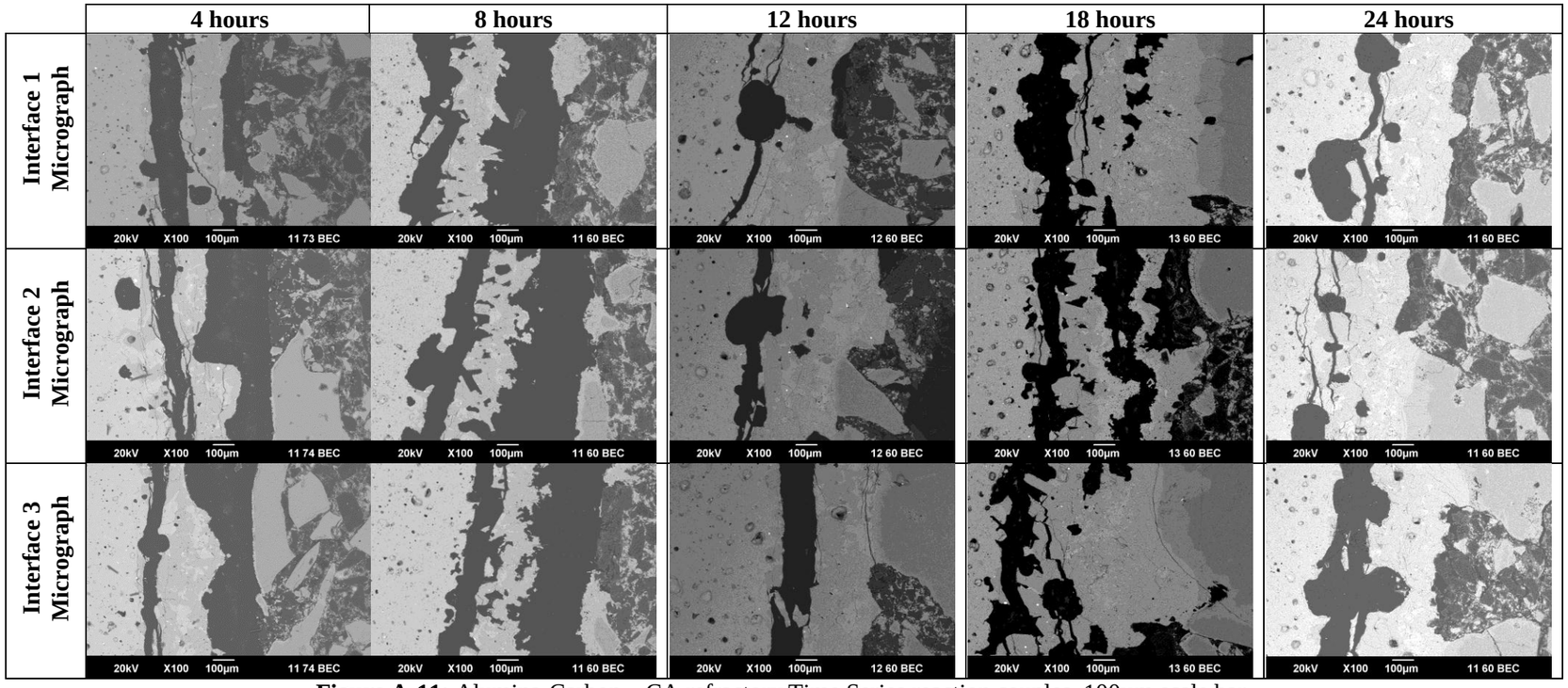

Figure A-11: Alumina-Carbon – CA refractory Time Series reaction couples. 100µm scale bar.

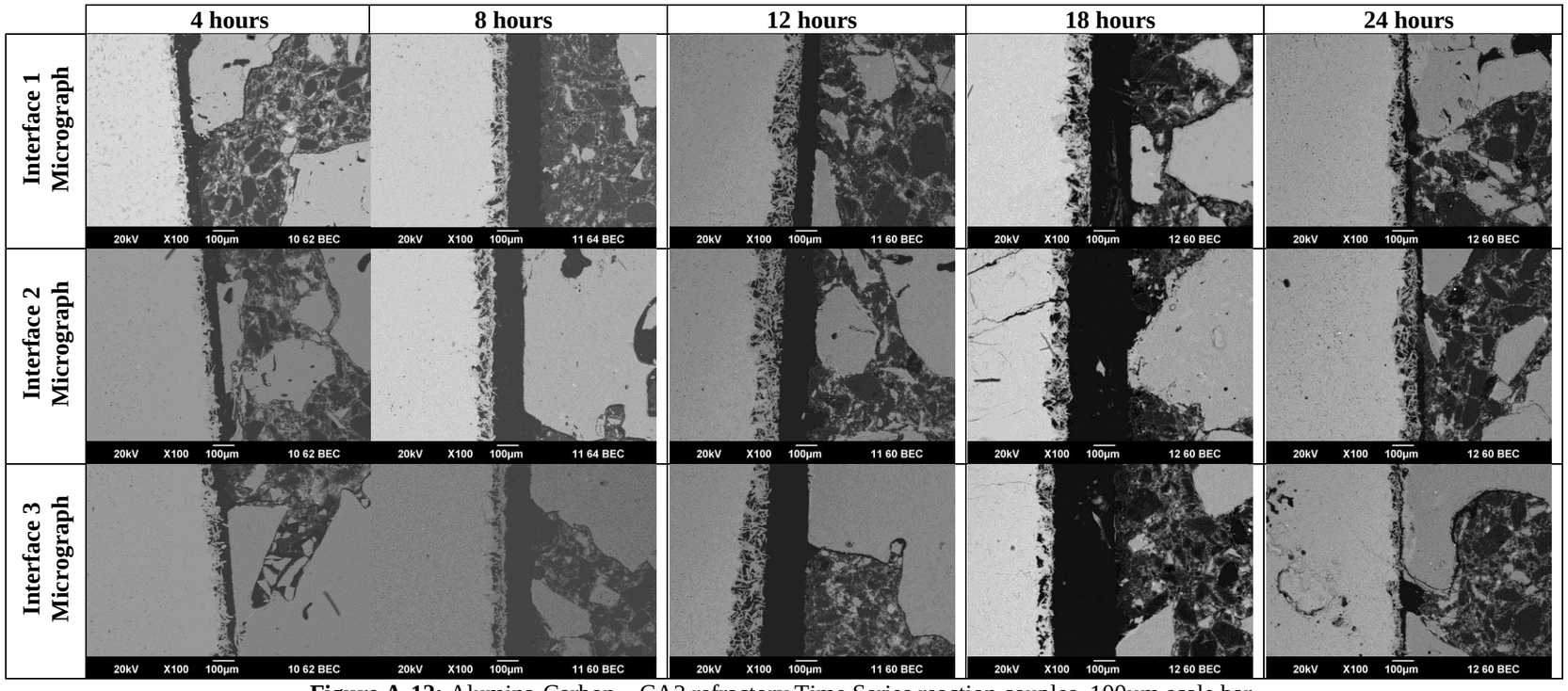

Figure A-12: Alumina-Carbon – CA2 refractory Time Series reaction couples. 100µm scale bar.

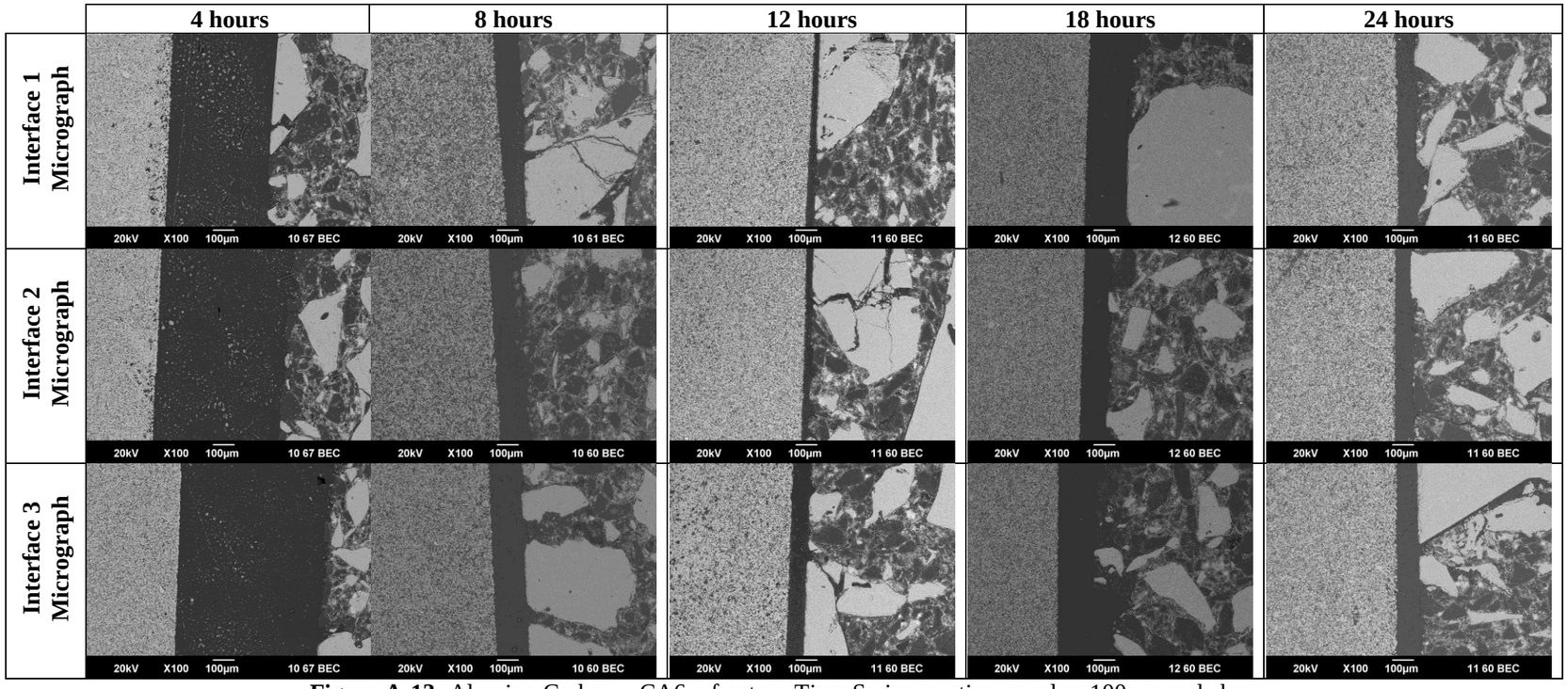

Figure A-13: Alumina-Carbon – CA6 refractory Time Series reaction couples. 100µm scale bar.

Appendix VI - Energy Dispersive Spectroscopy Line Analysis Results

EDS line analysis results for all the reaction couples are given in Figure A-14 to Figure A-18

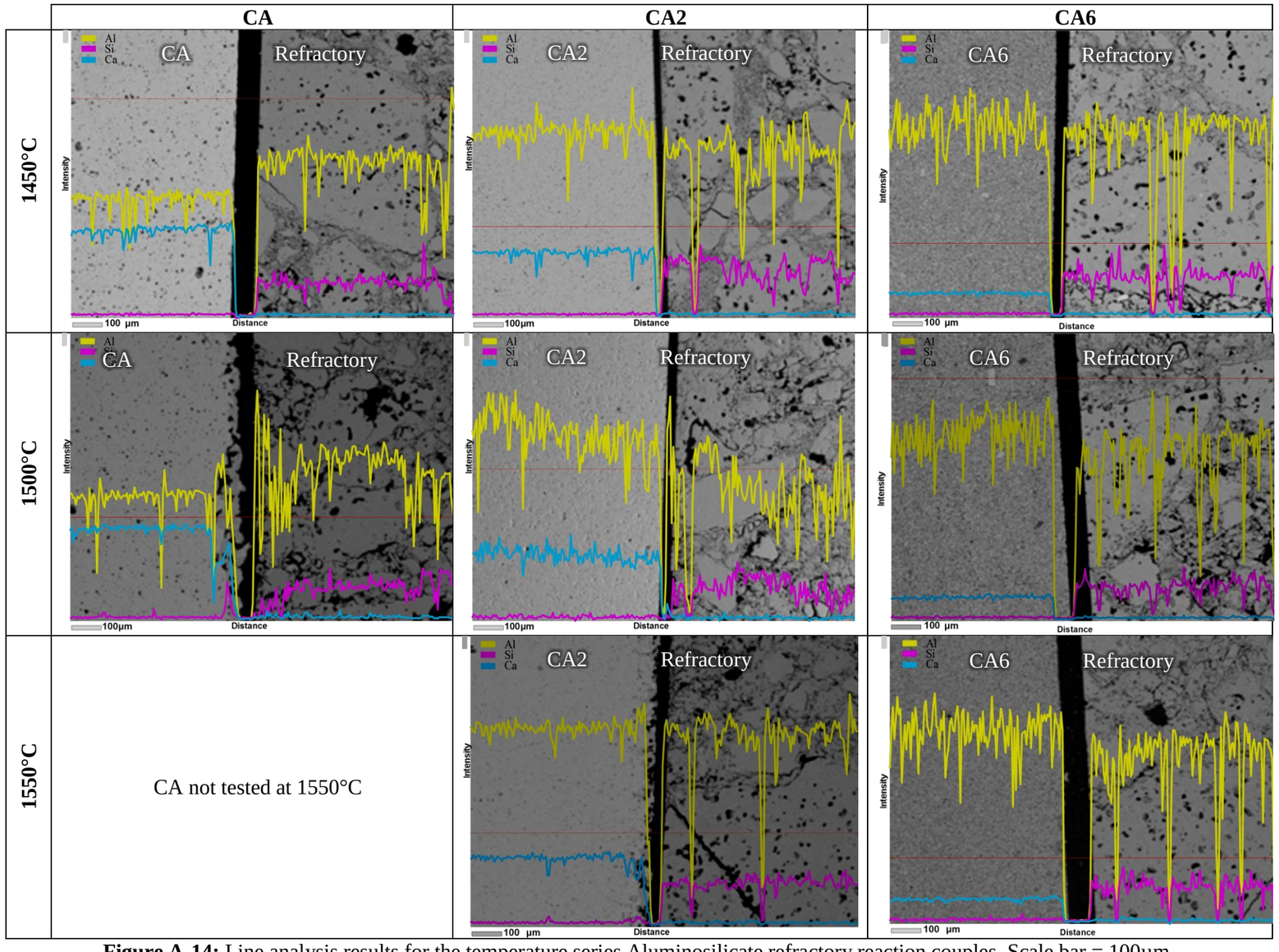

Figure A-14: Line analysis results for the temperature series Aluminosilicate refractory reaction couples. Scale bar = 100µm.

	CA	CA2	CA6
1450°C	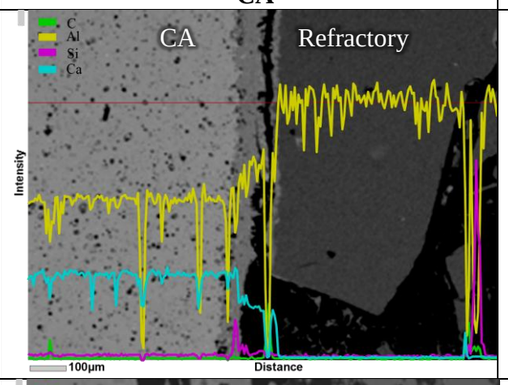	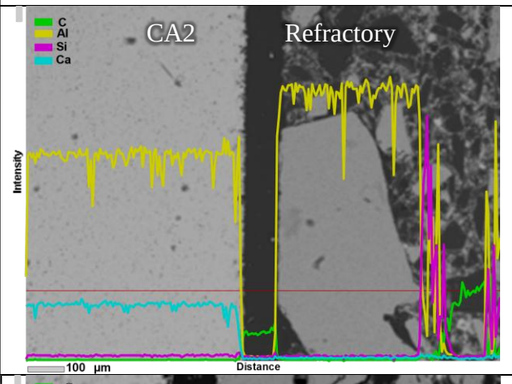	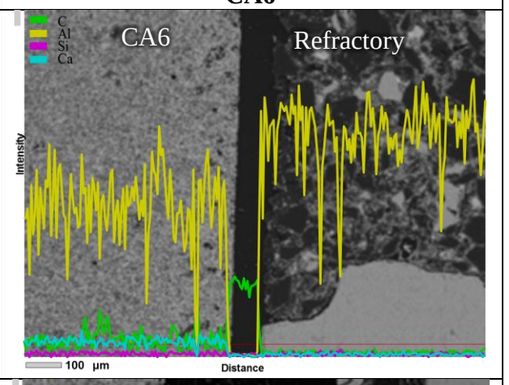
1500°C	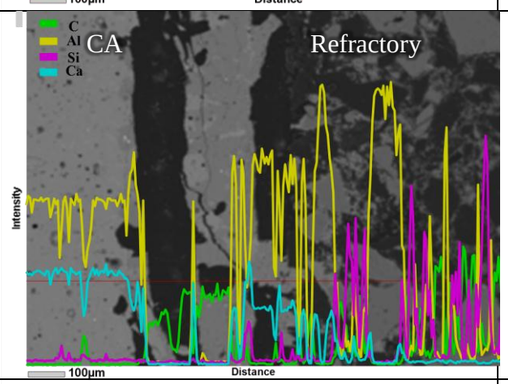	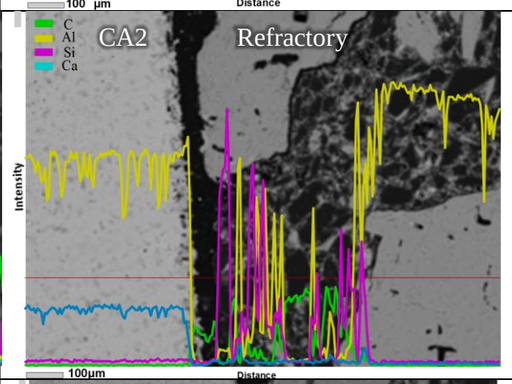	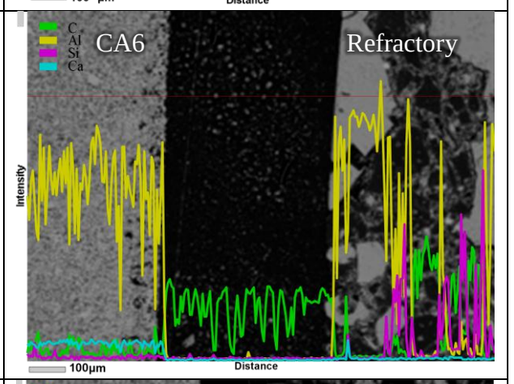
1550°C	CA not tested at 1550°C	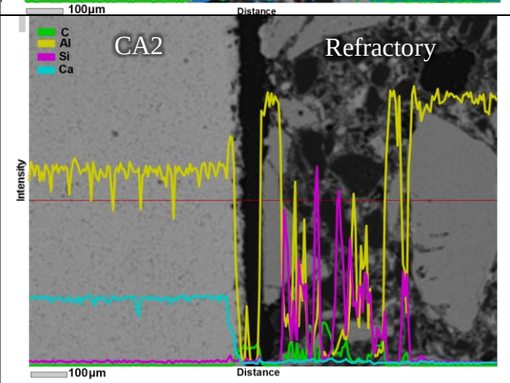	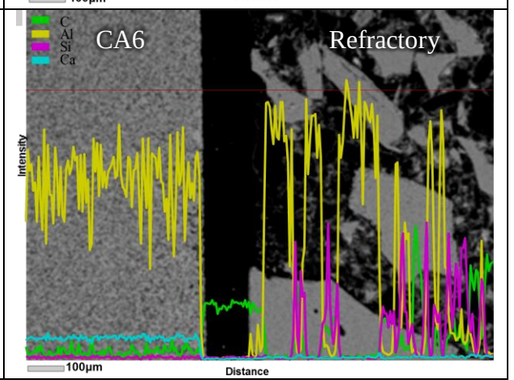

Figure A-15: Line analysis results for the temperature series Alumina-Carbon refractory reaction couples. Scale bar = 100µm.

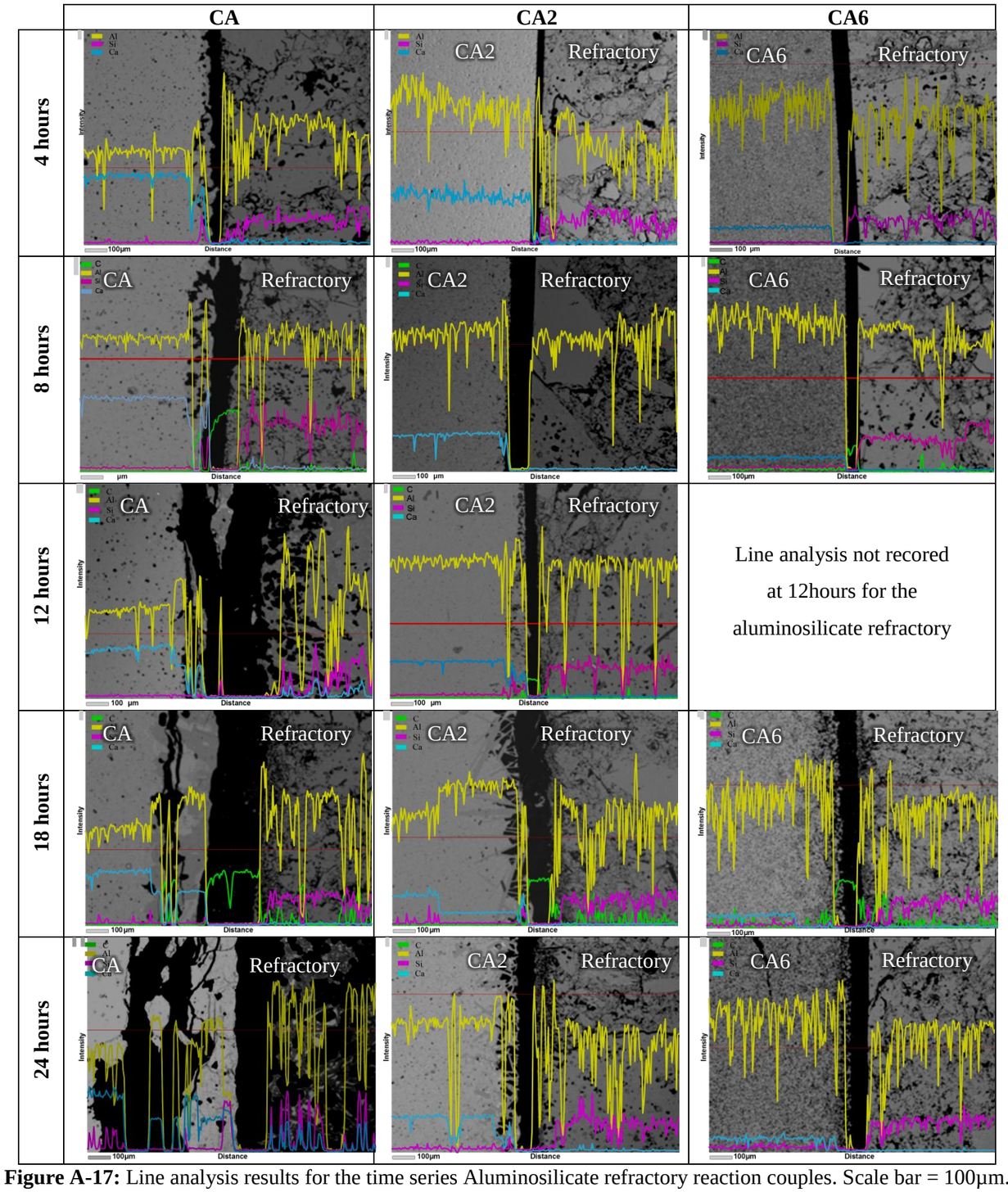

Figure A-17: Line analysis results for the time series Aluminosilicate refractory reaction couples. Scale bar = 100µm.

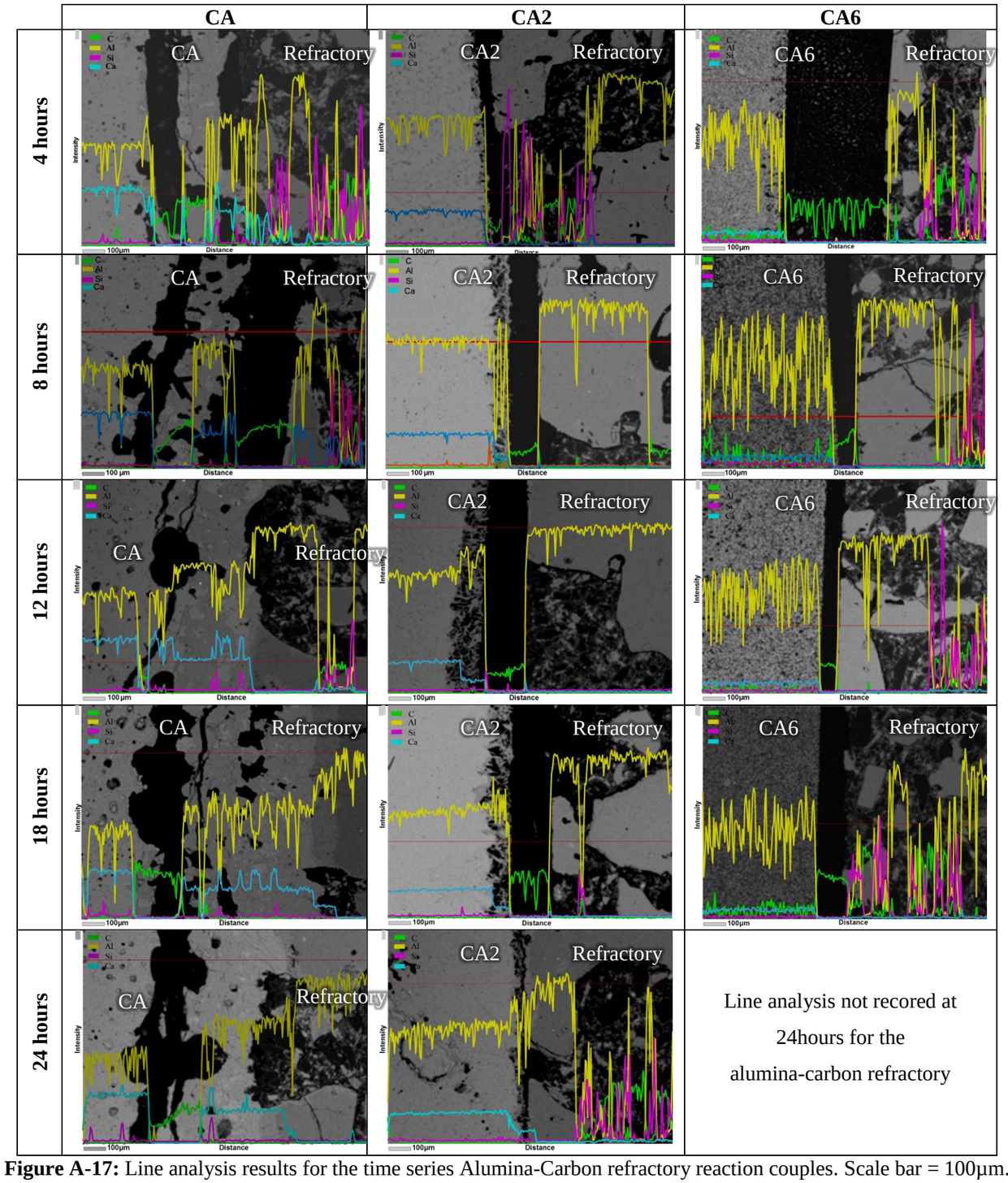

Figure A-17: Line analysis results for the time series Alumina-Carbon refractory reaction couples. Scale bar = 100µm.